



UNIVERSITÀ DEGLI STUDI DI MESSINA
Corso di Dottorato di Ricerca in
“Ingegneria e chimica dei materiali e delle
costruzioni”
XXX Ciclo

Novel devices and strategies in
earthquake protection of structures

Coordinatore:
Prof. Signorino GALVAGNO

Tutor:
Prof. Ing. Antonino RECUPERO

Co-Tutor:
Prof. Ing. Giuseppe RICCIARDI

Dott. Ing. Dario DE DOMENICO

Tesi di dottorato di:
Isabella FAILLA

Triennio 2014/2017

To my father

ACKNOWLEDGEMENTS

A few years ago I fell in love with *seismic engineering* but, I have to admit, it was not love at first sight; it has been a love that has matured over the years thanks to the meeting with my Professors who have sent me their love for this wonderful discipline.

Among all, I sincerely thank Professor Ricciardi who has followed me during my scientific growth and supported me in these years of Doctorate giving always precious advices and has transmitted to me his great passion for research. I thank Professor Recupero for the useful discussions about the construction technique and for his encouragement to continue the study of this research. I also thank Professor Muscolino and Professor Falsone because, being the first I met on my journey, they were the first who made me fall in love with seismic engineering and feed my passion.

An important thank goes to my family, my father who has always believed in me, my mother who is for me an example of life and my sister who is my strength. Finally, I would like to thank my husband, Stefano, who made all this possible by helping and supporting me in these years and my daughter, Vita, because she pushes me every day to improve to be an example for her.

Index

List of figures	v
List of tables	xvii
INTRODUCTION	1
LITERATURE REVIEW	5
1.1 Historical development of base isolation system.....	6
1.1.1 From 1900 to nowadays	9
1.2 Basic concepts in seismic isolation.....	17
1.2.1 Theory of base isolation	17
1.2.2 The Italian code for base isolated structures	23
1.3 Main features of commercial devices	25
1.3.1 Elastomeric-based devices.....	25
1.3.1.1 Low Damping Rubber Bearing (LDRB).....	25
1.3.1.2 High Damping Rubber Bearing (HDRB).....	26
1.3.1.3 Lead Rubber Bearing (LRB).....	27
1.3.1.4 Fiber Reinforced Elastomeric Isolator (FREI).....	29
1.3.2 Friction based device	31
1.3.2.1 Pure Sliding Device (SD).....	31
1.3.2.2 Friction Pendulum System (FP).....	33
1.3.2.3 Resilient-Friction Base Isolation system (RFBI)	35
1.3.2.4 Electricité De France base isolation system (EDF).....	36
1.3.2.5 Sliding Resilient-Friction Base Isolation system (SR-F)	37
1.3.2.6 Earthquake Engineering Research Center Base Isolation	
system (EERC)	38
1.3.2.7 Taisei Shake Suppression (TASS) base isolation system	
40	

1.3.2.8	Variable Friction Pendulum Isolation (VFPI) system	41
1.3.2.9	The RoGlider Isolation system	42
1.3.2.10	High Damping Hybrid Seismic Isolator (HDHSI)	44
1.3.3	Advantages and disadvantages.....	46
1.4	Vertical isolation devices	48
BEHAVIOR OF MATERIALS USED IN ISOLATION DEVICES		53
2.1	Preliminary definitions	54
2.1.1	Deformation gradient	56
2.1.2	Strain	58
2.1.3	Velocity and velocity gradient	63
2.1.4	Deformation rate	65
2.1.5	Stress representation	67
2.1.5.1	Cauchy stress tensor	67
2.1.5.2	The Kirchhoff stress tensor.....	68
2.1.5.3	The First Piola–Kirchhoff stress tensor	69
2.1.5.4	The Second Piola–Kirchhoff stress tensor.....	70
2.2	ELASTOMER: an hyperelastic material.....	71
2.2.1	Shape of the elastic potential	77
2.2.1.1	Polynomial shape.....	77
2.2.1.2	Mooney-Rivlin model.....	78
2.2.1.3	Reduced polynomial shape	79
2.2.1.4	Ogden model.....	80
2.2.1.5	Arruda-Boyce model	80
2.2.2	Hyperelastic material models in Finite Element analysis ..	82
2.2.2.1	Simple tension strain state	83
2.2.2.2	Pure shear strain state	86
2.2.2.3	Simple compression strain state.....	87

2.2.2.4	Equal biaxial strain state	88
2.2.2.5	Volumetric compression	89
2.2.2.6	Creating a consistent data set	89
2.2.2.7	Elastomer characterization	93
2.3	PTFE: a fluoropolymer with thermo-mechanical behavior	98
2.3.1	Experimental test for characterization of compressive mechanical behavior.....	107
2.3.2	Friction sliding.....	114
2.3.2.1	Basic mechanism of friction	115
2.3.2.2	Static and sliding friction	118
2.3.2.3	PTFE- polished stainless steel sliding	121
2.3.3	Theory of frictional heating.....	123
2.4	STEEL: an elastoplastic material.....	128
2.4.1	Material main features	128
FINITE ELEMENT MODELING OF EXISTING DEVICES		131
3.1	Finite Element Model (FEM) of HDRB device.....	131
3.2	Finite Element Model of Friction Pendulum devices	140
3.2.1	Mechanical behavior.....	142
3.2.2	Macroscale phenomenological model	147
3.2.3	Thermo Mechanical Coupled FE model.....	151
NEW ISOLATION DEVICES		167
4.1	Design criteria.....	178
4.1.1	Behavior of rubber in pure shear	178
4.1.2	Behavior of multilayer rubber in compression	178
4.1.3	Kinematics of VID	188
4.1.4	Analogies between horizontal and vertical spectra	193
4.1.5	Standard Code for the design	197
4.2	Finite Element model.....	201

4.2.1	Geometric model.....	202
4.2.2	Finite element for the calibration of the model.....	205
4.2.3	Constitutive law of the materials used	205
4.2.4	Modeling contact interaction surfaces	206
4.2.5	Boundary conditions and loads	208
4.3	Hybrid Friction Rubber Isolator FE model	209
4.4	Vertical Isolation Device FE model	222
4.4.1	Numerical application on a steel tank	226
4.5	Advantaged of the proposed isolation devices	230
4.5.1	HRFI.....	230
4.5.2	VID.....	231
	TUNED MASS DAMPER INERTER.....	233
5.1	Equation of motion of systems with TMDI.....	235
5.1.1	Numerical application on a 5-story building	241
5.2	Methods to realize of an inerter device	246
5.3	Design of a rack pinion inerter device.....	252
5.4	Design of a fluid inerter device	257
	FIBER REINFORCED PTFE.....	267
6.1	Manufacturing process and compression tests	268
6.2	Finite element model of the new proposed material	274
	CONCLUSIONS.....	277
	REFERENCES.....	279

List of figures

Figure 1.1 First application of seismic isolation: (a) Cnósso Palace; (b) Troia's walls	6
Figure 1.2 Diana Temple in Efeso.....	7
Figure 1.3 Dikilitash obelisk: a) base of the real structure, b) base model	8
Figure 1.4 Dikilitash obelisk: a) real structure, b) Finite Element Model..	8
Figure 1.5 Temple of Sanjusangendo.....	9
Figure 1.6 First patents on isolation: a) Touaillon; b) Kawai.....	10
Figure 1.7 First patents on isolation: a) Bechtold b) Calentarients	11
Figure 1.8 First patents on isolation: Martel	12
Figure 1.9 First patents on isolation: Lodà.....	13
Figure 1.10 The Pestalozzi School	14
Figure 1.11 Schematic sketch of a base isolated structure: a) structural scheme with the base isolation system b) useful scheme for the definition of the equation of motion (Muscolino 2002).....	18
Figure 1.12 Response function, in terms of relative displacement, in the time domain and in the frequency domain of an SDOF system: a) fixed system; b) isolated system (Muscolino 2002)	22
Figure 1.13 LDRB device.....	25
Figure 1.14 HDRB device	26
Figure 1.15 Experimental hysteresis loops of a HDRB at frequency of 0.5 Hz, shear strain $\pm 100\%$ (FIP INDUSTRIALE)	26
Figure 1.16 Lead-plug isolator (Naeim et al. 1999)	27
Figure 1.17 LRB device	28
Figure 1.18 Experimental hysteresis loops of a LRB at frequency of 0.5 Hz, shear strain $\pm 100\%$ (FIP INDUSTRIALE)	28
Figure 1.19 Modeling of isolators: (a) Classical layer of steel and rubber ; (b) Fiber Reinforced Elastomeric Isolator	29
Figure 1.20 Manufacturing of FREI: (a) schematic diagram of dipping process to improve bonding characteristic between rubber and fiber; (b) dipping process; (c) FREI in final form (Moon et al. 2002).....	30

Figure 1.21 Hysteresis loops for SREI and FREI at 50% shear strain (Moon et al. 2002)..... 30

Figure 1.22 Schematic schetk of a SD 31

Figure 1.23 Pure Sliding Device (FIP INDUSTRIALE) 32

Figure 1.24 Force-displacement loop result of a static test (speed 4mm/min) at maxium design vertical load (14000 kN)(FIP INDUSTRIALE) 32

Figure 1.25 FP schematic sketch..... 33

Figure 1.26 FP schematic sketch..... 33

Figure 1.27 A double concave curved surface slider (FIP INDUSTRIALE) 34

Figure 1.28 Experimental hysteresis loops of a double curved surface slider (FIP INDUSTRIALE)..... 34

Figure 1.29 The R-FBI system (Mostaghel 1984) 35

Figure 1.30 The EDF system (Gueraud,et al, 1985) 36

Figure 1.31 Schematic diagram of non uniform shear-beam structure with SR-F base isolator (Su et al. 1991) 37

Figure 1.32 EERC isolation system (Chalhoub and Kelly 1990) 38

Figure 1.33 Tension restrain showing dimensions (Chalhoub and Kelly 1990) 39

Figure 1.34 Effect of tension device in horizontal stiffness (Chalhoub and Kelly 1990) 39

Figure 1.35 Schematic figure of TASS system (Nagashima et al. 1987) 40

Figure 1.36 Details and operation of VPFS (Panchal and Jangid 2008).. 41

Figure 1.37 The RoGLider device (Robinson et al. 2006)..... 42

Figure 1.38 RoGLider during test displacement +575mm, vertical force of 110kN (Robinson et al. 2006) 42

Figure 1.39 RoGLider force displacement curve – vertical force of 850 kN (Robinson et al. 2006)..... 43

Figure 1.40 RoGLider force displacement curve – vertical force of 110 kN (Robinson et al. 2006)..... 43

Figure 1.41 HDHSI system (Cancellara and Pasquino 2011)..... 44

Figure 1.42 Hysteretic cycles of single components and the HDHSI device (Cancellara and Pasquino 2011) 45

Figure 1.43 Xueyuan et al. service:combined shape of disk spring (left); Section of the vertical isolation system (right) 49

Figure 1.44 Magnetic leakage system schematic sketch (Tsuda et al. 2009)	49
Figure 1.45 Model with non linear springs and magnetic damping (Masaharu et al. 2007)	50
Figure 1.46 Steel elicoidal spring (left) – Viscous damper (right)	50
Figure 1.47 Tridimensional Seismic Device	51
Figure 2.1 General Motion of a deformable body (Bonet and Wood 2008)	55
Figure 2.2 General motion in the neighborhood of a particle (Bonet and Wood 2008)	57
Figure 2.3 Change in length (Bonet and Wood 2008)	60
Figure 2.4 Volume change (Bonet and Wood 2008)	62
Figure 2.5 Rate of deformation (Bonet and Wood 2008)	65
Figure 2.6 Traction vector (Bonet and Wood 2008)	68
Figure 2.7 Constitutive law with locking stretch	79
Figure 2.8 Schematic Arruda-Boyce model	81
Figure 2.9 A typical final data set for input into a curve fitter (Miller 1999)	82
Figure 2.10 Dumbell specimen with 2mm thickness	83
Figure 2.11 Analysis of a tension specimen (Miller 1999)	84
Figure 2.12 A tension experiment using video extensometer (Miller 1999)	85
Figure 2.13 A pure shear experiment using a laser extensometer	86
Figure 2.14 A lubricated compression specimen showing lateral constraining from friction at the surface	87
Figure 2.15 Analysis of a biaxial specimen	88
Figure 2.16 A biaxial extension experiment	88
Figure 2.17 Volumetric compression fixture with specimen	89
Figure 2.18 Cyclic loading of filled natural rubber (Miller 1999)	91
Figure 2.19 1 st loading of a thermoplastic elastomer (Miller 1999)	91
Figure 2.20 Multiple strain cycles of a thermoplastic elastomer (Miller 1999)	92
Figure 2.21 Multiple strain cycles of a thermoplastic elastomer at two maximum strain levels (Miller 1999)	92

Figure 2.22 Uniaxial test on elastomer: first series with dashed line, second series with continuous line (Cuomo 2007) 93

Figure 2.23 Planar test on elastomer: first series with dashed line, second series with continuous line (Cuomo 2007) 94

Figure 2.24 Volumetric test on elastomer: first series with dashed line, second series with continuous line (Cuomo 2007) 94

Figure 2.25 Biaxial test on elastomer: second series with continuous line (Cuomo 2007) 95

Figure 2.26 Uniaxial test curves from ABAQUS 95

Figure 2.27 Biaxial test curves from ABAQUS 96

Figure 2.28 Planar test curves from ABAQUS 96

Figure 2.29 Volumetric test curves from ABAQUS 97

Figure 2.30 Stress-strain curve for different temperature (DuPont-Fluoroproducts 1996) 99

Figure 2.31 Tensile stress-strain curves (DuPont-Fluoroproducts 1996) 100

Figure 2.32 Variation of tensile stress with temperature (DuPont-Fluoroproducts 1996) 101

Figure 2.33 Variation of compression stress-strain curves with temperature (DuPont-Fluoroproducts 1996) 102

Figure 2.34 Tensile and Compression behavior (DuPont-Fluoroproducts 1996) 103

Figure 2.35 Stress-strain curves for shear (DuPont-Fluoroproducts 1996) 104

Figure 2.36 Basic creep testing equipment (Physical properties of Fluon unfilled and filled PTFE 2007) 105

Figure 2.37 Compressive creep (Physical properties of Fluon unfilled and filled PTFE 2007) 105

Figure 2.38 Isochronous stress-strain relationship in compression, at 25°C (Physical properties of Fluon unfilled and filled PTFE 2007) 106

Figure 2.39 Recovery for creep in compression, at 25°C (Physical properties of Fluon unfilled and filled PTFE 2007) 107

Figure 2.40 Heat treatment 108

Figure 2.41 The PTFE virgin dust into the mold 109

Figure 2.42 The molding equipment 109

Figure 2.43 The printing process: preforming pressure 110

Figure 2.44 Equipment for the heat treatment.....	110
Figure 2.45 Printed disk of vergin PTFE.....	111
Figure 2.46 Compression test machine	111
Figure 2.47 Compression testing machine	112
Figure 2.48 Disk of vergin PTFE during the test	112
Figure 2.49 Disk of vergin PTFE after the compression test	113
Figure 2.50 Stress-strain experimental curve in compression for the vergin PTFE.....	113
Figure 2.51 Schematic illustration of an interface, showing the apparent and real areas of contact	115
Figure 2.52 Schematic illustration of the roughness of sliding surface. Positive and negative θ coexist.....	116
Figure 2.53 Schematic illustration of a cone pressed into a flat surface. The asperity moving horizontally creates a groove which is swept out of A_p	117
Figure 2.54 Typical friction force-sliding loop of polymer-stainless steel interface without the contribution of restoring stiffness W/R (pressure=15 MPa, peak velocity=1.27 mm/sec) (Trovato 2013).....	118
Figure 2.55 Schematic representation of a friction apparatus.	119
Figure 2.56 (a) A schematic hypothetical force displacement plot. (b) Friction record corresponding to the force displacement plot.....	120
Figure 2.57 Schematic variation of real area of contact, Pressure and coefficient of sliding friction.	122
Figure 2.58 Semi-infinite solid with constant heat flux at the surface (Carslaw and Jager 1959)	126
Figure 2.59 Schematic illustration of the sliding contact surface problem (Carslaw and Jager 1959)	127
Figure 2.60 – Typical steel constitutive law for structural use.....	129
Figure 2.61 – Schematic steel constitutive law	130
Figure 3.1 Maxwell model for elastomer viscoelasticity used in ADINA	133
Figure 3.2 HDRB experimentally tested (model).....	135
Figure 3.3 Model of the HDRB	135
Figure 3.4 Mesh of the HDRB	136

Figure 3.5 Load displacement curve for elastomer seismic isolator (case 1- $p_m=22.5$ MPa) 137

Figure 3.6 Deformed shape for the load case 1..... 137

Figure 3.7 Load displacement curve for elastomer seismic isolator (case 2- $p_m=22.5$ MPa and $\gamma=180\%$) 138

Figure 3.8 Deformed shape for the load case2..... 138

Figure 3.9 Simple compression test (comparison FEM model and experimental results (Cuomo 2007))..... 139

Figure 3.10 Combined compression and shear test (comparison FEM model and experimental results (Cuomo 2007))..... 139

Figure 3.11 Section through a FP bearing: a) constituting elements and materials; b) kinematic analysis (De Domenico et al. 2018) 143

Figure 3.12 Sketch at two time-instants of in-plane motion of the slider with the resulting forces highlighted (De Domenico et al. 2018)..... 146

Figure 3.13 Heat flux generated during the time interval dt : a) actual; b) equivalent uniformly distributed (Lomiento et al. 2013)..... 148

Figure 3.14 FE-model of the FP: a) isometric view; b) exploded drawing with contact surface labels 152

Figure 3.15 Cloverleaf test: a) in-plane trajectory; b) longitudinal (u_x) and lateral (u_y) components of motion (De Domenico et al. 2018) 155

Figure 3.16 Comparative analysis of the trajectories traveled by the FP during the cloverleaf test (De Domenico et al. 2018)..... 157

Figure 3.17 Contact force distribution: a) vector plot of the f_i forces; b) band plot of f_{zi} on the sliding surface 158

Figure 3.18 Angular shift $\Delta\varphi$ between the force vector and velocity for bidirectional cloverleaf test..... 159

Figure 3.19 Force-displacement loops for cloverleaf test: a) and b) bidirectional; c) and d) monodirectional..... 160

Figure 3.20 Plot of the friction coefficient versus time: a) bidirectional test; b) and c): monodirectional tests 161

Figure 3.21 Force displacement loops from the TMC-FE model: a) longitudinal; b) lateral 162

Figure 3.22 Temperature distribution on the sliding plate for bidirectional cloverleaf test 163

Figure 3.23 Temperature distribution on the sliding PTFE pad for bidirectional cloverleaf test	163
Figure 3.24 Temperature for monodirectional test (lateral) on: a) sliding plate; b) PTFE pad	164
Figure 3.25 Average temperature histories during the test: a) bidirectional test; b) monodirectional test (CS stands for “contact surface”; TIFC stands for “Temperature-Independent Friction Coefficient”) (De Domenico et al. 2017).....	164
Figure 3.26 Bidirectional orbits analyzed in the parametric study: a) Durer’s folium; b) straight cloverleaf; c) twelve-leaf clover; d) circular orbit; e) oblique cloverleaf; f) spiral orbit	166
Figure 4.1 Schematic section of the Hybrid Friction Rubber Isolator....	168
Figure 4.2 Part 1 and 2 of the Hybrid Friction Rubber Isolator	169
Figure 4.3 Part 3 and 4 of the Hybrid Friction Rubber Isolator	169
Figure 4.4 Part 5 and 6 of the Hybrid Friction Rubber Isolator	170
Figure 4.5 Part 7 and 8 of the Hybrid Friction Rubber Isolator	170
Figure 4.6 Schematic section of the Vertical Isolation Device	172
Figure 4.7 Part 1 and 2 of the Vertical Isolation Device	173
Figure 4.8 Part 3 and 4 of the Vertical Isolation Device	174
Figure 4.9 Part 5 of the Vertical Isolation Device.....	175
Figure 4.10 The tridimensional isolation device made by the two proposed devices	176
Figure 4.11 The tridimensional isolation device made by the vertical proposed device and a classic elastomeric isolation device	177
Figure 4.12 (a) Cartesian coordinate system on an arbitrarily shaped pad; (b) displacement fields of an arbitrarily shaped pad (Kelly and Konstantinidis 2011)	180
Figure 4.13 Coordinates system for a rectangular pad with side lengths l_1 and $2b$ (Kelly and Konstantinidis 2011).....	186
Figure 4.14 Effect of bulk compressibility on E_c for rectangular pads with different length-to-width ratios, ρ (Kelly and Konstantinidis 2011)	187
Figure 4.15 Schematic sketch of the VID.....	188
Figure 4.16 Equilibrium of the ascending phase	189
Figure 4.17 Equilibrium of the descending phase	190

Figure 4.18 Elastic spectrum of the horizontal component 194

Figure 4.19 Elastic spectrum of the vertical component..... 195

Figure 4.20 Details of PTFE recess and relief (UNI EN 1337-2)..... 199

Figure 4.21 Pattern of dimples in recessed PTFE sheet (UNI EN 1337-2)
..... 199

Figure 4.22 Degradation of the friction coefficient with temperature ... 208

Figure 4.23 Schematic sketch of the HFRI with the representation of the
dimensions 209

Figure 4.24 ABAQUS-3D model of the horizontal device..... 210

Figure 4.25 ABAQUS-3D model highlighting the different material with
different colors 211

Figure 4.26 ABAQUS-3D Section model highlighting the different part
with different colors 211

Figure 4.27 ABAQUS-3D model of the PTFE pad 212

Figure 4.28 Time history of the horizontal displacement with A=100 mm,
vp=250 mm/sec 213

Figure 4.29 Deformed shape of HDRI at the final step 213

Figure 4.30 Stress distribution at the final step..... 214

Figure 4.31 Stress distribution at the final step in the rubber part 214

Figure 4.32 Force-displacement loop from the FE model 215

Figure 4.33 Time history of the horizontal displacement with A=100 mm,
vp=100 mm/sec 215

Figure 4.34 Force-displacement loop from the FE model 216

Figure 4.35 Trajectories of the clover leaf test 218

Figure 4.36 Force displacement loop for the clover leaf test in direction x:
comparison between simple analysis and TMC analysis..... 218

Figure 4.37 Force displacement loop for the clover leaf test in direction y:
comparison between simple analysis and TMC analysis..... 219

Figure 4.38 Force displacement loop for the clover leaf test in direction x:
comparison between simple analysis and experimental test..... 219

Figure 4.39 Force displacement loop for the clover leaf test in direction y:
comparison between simple analysis and experimental test..... 220

Figure 4.40 Temperature distribution on the sliding plate for bidirectional
cloverleaf test of HFRI..... 220

Figure 4.41 Average temperature histories during the bi-directional test
..... 221

Figure 4.42 Schematic sketch of the VID with the representation of the dimensions.....	222
Figure 4.43 ABAQUS-3D model of the vertical device	223
Figure 4.44 ABAQUS-3D model of the inner part of the vertical device	224
Figure 4.45 ABAQUS-3D model of the vertical device	224
Figure 4.46 Deformed shape after ONE cycle	225
Figure 4.47 Force-displacement loop for the VID	225
Figure 4.48 Circular cylindrical steel storage tanks of 150 thousands barrels	226
Figure 4.49 SAP model of the structures without the VID	228
Figure 4.50 SAP model of the structures with the VID	228
Figure 4.51 Displacement of the central point: fixed vs isolated structure	229
Figure 4.52 Normal strength of a beam: fixed vs isolated structure.....	229
Figure 5.1 Sketch of a base-isolated one-story building with attached TID (De Domenico and Ricciardi 2017)	236
Figure 5.2 Schematic arrangement of the proposed enhanced base-isolation system.	239
<i>Figure 5.3 Enhanced base-isolation system (BIS) for different ζ_b values. A,B, normalized displacement variance of the conventional BIS and of the auxiliary BIS (TMDI). C,D, corresponding optimal TMDI parameters (De Domenico and Ricciardi 2018).</i>	240
Figure 5.4 Multistory building with proposed enhanced base-isolation system.	242
Figure 5.5 PSD function according to Eurocode 8 ground type A spectrum-compatible base acceleration.	244
Figure 5.6 Time histories responses of the last floor displacements	245
Figure 5.7 Time histories responses of the proposed TID displacements	245
Figure 5.8 Schematic of a mechanical model of an inerter (Smith 2002)	246
Figure 5.9 – Rack-Pinion inerter device with several gears (Mirza Hessabi and Mercan 2016).....	247

Figure 5.10 The small scale prototype gears (Mirza Hessabi and Mercan 2016) 247

Figure 5.11 Measured force vs measured displacement for the prototype with $b = 29.87$ kg (Mirza Hessabi and Mercan 2016). 248

Figure 5.12 Schematic of a mechanical model of a ballscrew inerter (Smith 2008) 249

Figure 5.13 Ballscrew inerter made at Cambridge University Engineering Department; Mass < 1 kg, Inertance (adjustable) = 60–240 kg. (a) Complete with outer case, (b) ballscrew, nut and flywheel, (c) flywheel removed, (d) thrust bearing. (Smith 2002) 249

Figure 5.14 Schematic of a mechanical model of a hydraulic inerter (Smith 2008) 250

Figure 5.15 A prototype of the hydraulic inerter (Wang et al. 2010).... 250

Figure 5.16 The working principle of an hydraulic inerter (Wang et al. 2010) 251

Figure 5.17 Schematic of a mechanical model of a fluid inerter (Swift et al. 2013) 251

Figure 5.18 Fluid inerter device designed and tested in Smith and Wagg (2016). 252

Figure 5.19 Schematic sketch of the inerter damper proposed 253

Figure 5.20 Part of the rack pinion inerter device..... 253

Figure 5.21 Theoretical mechanical model of a part of the proposed rack pinion inerter device..... 256

Figure 5.22 Cross and longitudinal sections of the proposed inerter device 257

Figure 5.23 Pro-RST Silkolene oil density versus temperature (assuming a linear extrapolation). 258

Figure 5.24 Inertance of the proposed device versus temperature..... 259

Figure 5.25 Plant of the proposed device..... 260

Figure 5.26 Parasitic damping force 263

Figure 5.27 Total force of the proposed device (total force in black; inertance part in dashed green; viscosity of the fluid in blue; inlet and outlet part in dashed brown)..... 263

Figure 5.28 Force-displacement loop for the proposed device (frequency of 0.5 Hz; displacement of 120 mm) 264

Figure 5.29 Force-displacement loops for the proposed device (frequency of 0.5 Hz; displacement of 120 mm): total inerter force (black line), inertance contribution plus linear part of the parasitic force (red line), inertance contribution to the total inerter force (blue line).....	264
Figure 5.30 3D mechanical model of the proposed fluid inerter device from SolidWorks	265
Figure 6.1 Disk of PTFE filled with glass fiber	268
Figure 6.2 Disk of PTFE filled with glass fiber after the compression test	268
Figure 6.3 Stress-strain behavior of the disk of PTFE filled with glass fiber	269
Figure 6.4 Disk of PTFE filled with bronze	269
Figure 6.5 Disk of PTFE filled with bronze after the compression test .	270
Figure 6.6 Stress-strain behavior of the disk of PTFE filled with bronze	270
Figure 6.7 Glass fiber used for the proposed new material	271
Figure 6.8 The inclusion of the fiber inside the the stamp	271
Figure 6.9 Fiber reinforced PTFE after the compression test	271
Figure 6.10 Stress-strain behavior of the disk of reinforced vergin PTFE	272
Figure 6.11 Comparison between the two disks after the compression test (vergin PTFE on the left; reinforced PTFE on the right)	272
Figure 6.12 Comparison between the stress–strain curve of the two disks	273
Figure 6.13 Comparison between the stress–strain curve of the four printed disks.....	273
Figure 6.14 3D model of the reinforced disk realized with ABAQUS	6.14
.....	274
Figure 6.15 Section of the 3D model of the reinforced disk realized with ABAQUS	6.14.....
.....	274
Figure 6.16 Mesh of the reinforced disk.....	275
Figure 6.17 Stress-strain curve from the FE model.....	275
Figure 6.18 Comparison between experimental and FE model	276

List of tables

Table 1.1 Advantage and disadvantage of commercial devices	47
Table 2.1 Rubber mechanical properties	78
Table 2.2 Yield values for different temperature (DuPont-Fluoroproducts 1996).....	99
Table 2.3 Thermal properties of PTFE and stainless steel	124
Table 2.4 Thermal diffusivity of various metals.	125
Table 2.5 Mechanical characteristic of Steel.....	130
Table 3.1 Geometrical characteristics of the HDRB experimentally tested (Cuomo 2007).....	134
Table 3.2 Mechanical characteristics of the HDRB experimentally tested (Cuomo 2007).....	135
Table 3.3 Geometrical data of the analyzed FP (after Lomiento et al.2013)	151
Table 3.4 Mechanical Parameters of the materials.....	153
Table 3.5 Thermal Parameters of the materials.....	153
Table 3.6 Numerical parameters defining the analytical model and the TMC FE subroutine	160
Table 4.1 Characteristic compressive strength for PTFE (UNI EN 1337-2)	201
Table 4.2 Geometrical characteristic of the HRFI studied	210
Table 4.3 Geometrical characteristic of the HRFI studied in case 2	217
Table 4.4 Geometrical characteristic of the VID studied	223
Table 4.5 Mechanical characteristics of materials of circular cylindrical steel storage tanks	227
Table 4.6 – Geometrical characteristics of the circular cylindrical steel storage tanks	227
Table 5.1 Mechanical and geometrical characteristic of the designed rack pinion inerter device	255
Table 5.2 Dimension of the proposed fluid inerter device	259

INTRODUCTION

The base isolation technique provides the foundations for many advanced techniques for computing and applications, in the framework of buildings, bridges, etc... In view of ubiquity of scientific problems modeled by this system, the subject is of interest for an increasing number of scientists and engineers. The study of this system is reflected by the specific applications (over 24000) appearing in the worldwide. The basic idea of this system is to disconnect the superstructure response from ground motion. Since the significant component of the seismic action is predominantly the wave one, the isolation effect is achieved by using devices generally characterized by a low horizontal rigidity (high flexibility) combined with a high vertical stiffness to support the static loads. The high vertical stiffness is dictated by the need to avoid oscillations of the structure under the action of only static design loads. However, it is widely documented in the scientific literature, as well as confirmed by recent earthquakes, for example the 2009 Aquila earthquake and the 2016 Norcia earthquake, that, if the structure is near the earthquake's hypocenter (near fault seismic event), the vertical component of seismic waves is significant and may represent the main cause of damage to structures. It is therefore necessary to reduce the vulnerability of the structures not only with regard to the ondulatory component of the seismic action, but also to envisage seismic protection strategies with regard to the subsidiary component.

Concerning horizontal isolation devices, the existing systems are classified according to how the high deformability in the horizontal direction is obtained at the base of the structure; on the market there are two main types of isolators: (i) isolator made of elastomeric material and (ii) sliding isolators. The former are generally made of natural rubber or synthetic elastomer or neoprene while the latter are sliding supports of steel-PTFE (steel-Teflon).

The elastomeric isolators consist of alternating layers of rubber and steel solidarized by hot vulcanization. The layers of steel perform the function of confinement of the rubber, reducing the deformability by orthogonal loads to lay the layers, leaving them free to deform by parallel loads exploiting the high tangential deformability of the rubber (deformations greater than 300%), also because the elastomer has a low lift for vertical loads.

The sliding isolator consists respectively of sliding bearings (steel-Teflon) characterized by low friction resistance values in order to transmit the lowest possible seismic load to the structure. Within this typology the most used are the pendulum isolators (FP-Friction Pendulum System), consisting of a sliding slide lower than the concave surface, whose radius of curvature determines, by analogy with the mechanism of a simple pendulum, the period of oscillation and allows horizontal displacement. Between the two surfaces there is interposed a central "scroll" in steel (slider) whose upper and lower faces, both convex and appropriately shaped to mate with the concave ones of the above plates, are covered with suitably treated materials (generally polished stainless steel and fluoropolymers such as PTFE or high-strength polymers) that exhibit low friction resistance but at the same time offer a high load-bearing capacity with respect to the vertical loads transmitted by the structure. To ensure adequate energy dissipation and to limit large displacements to the base, the isolation system must have adequate damping. In the case of isolator made of elastomeric material this condition is guaranteed by the hysteretic behavior of the materials composing these devices. In the case of sliding isolators, the dissipation mechanism is due to the friction between the sliding interfaces. Both existing devices, however, present problems related to potential instability phenomena due to high lateral deformations, uplifting phenomena that may occur both in the case of sliding isolators (lifting) and in the case of elastomeric isolators (lowering). They also present insufficient geometry re-centering for the pendulum isolators and effects attributed to the multidirectionality of the motion for which we observe a difference between the experimental behavior and the theoretical one based on monodirectional idealizations.

Concerning vertical isolation protection, there are devices, generally consisting of springs and / or elastic elements (such as rubber or elastomers)

in series or in parallel, characterized by a high vertical flexibility and therefore potentially capable of isolation in respect of vertical seismic action. These devices have been widely used in the isolation of mechanical vibrations produced by machinery such as motors, current generators, chillers, AHUs. The use of such devices in the framework of civil engineering structures (buildings, bridges, reservoirs, nuclear power plants) for the isolation from vertical seismic excitation has not had the same diffusion. This is presumably due to the absence of an effective and valid technology, of simple realization that can be introduced into the construction market.

My PhD scholarship has been sponsored by Bosch Rexroth S.P.A., that suggested me a research project focused on the “design of innovative isolation device”. For this reason, the main goal of my thesis centers around the requirement, hence the proposal, of novel devices and strategies that could overcome the problems of existing isolation devices that are currently more widespread and also fill the technological vacuum currently present in the field of isolation with respect to the vertical component of the seismic action.

The chapters of this thesis are organized as follows: in Chapter 1 a careful and focused bibliographic research was carried out, aimed at the knowledge of the existing devices on the trade and their main problems.

In Chapter 2, attention is focused on the behavior characterization of materials that are used in isolation devices, such as steel, elastomer and PTFE (polytetrafluoroethylene). To better characterize the compression behavior of PTFE, laboratory specimens were made from the virgin product and with addition of filled parts in the chemical composition, and they underwent compression tests.

In Chapter 3, we venture into modeling through Finite Elements of the existing devices, e.g. Elastomeric HDRB (High Damping Rubber Bearing) and Friction Pendulum. This step has been of fundamental importance to highlight all the problems, already known in the literature, related to the devices already present on the market.

Once the study on existing devices was completed, the Chapter 4 was dedicated to the design of a new isolation device for the horizontal component of the seismic action, called HFRI (Hybrid Friction Rubber Isolator), and an isolation device for the component vertical, called VID

(Vertical Isolation Device). After an initial design, obtained following the UNI standards in this regard, the finite element models were processed using the Abaqus CAE calculation code, using them it was possible to study the hysteretic behavior of devices that are both based on a dissipation mechanism by friction between PTFE and lubricated stainless steel. With these models it was also possible to study the tension state that develops in the devices. From these analysis it has been found that both devices are feasible and valid for use in the seismic protection of structures; in particular, the HRFI device is comparable, in terms of performance and size in plan, to a Friction Pendulum while for what concerns the VID device, since it is completely innovative and there are no similar products on the market, it was not possible to compare it with any other product.

As part of this research, a seismic isolation system was also studied, illustrated in Chapter 5, which includes the addition of a device called *Inerter* combined with a dissipator and an elastic element, thanks to which it is possible to significantly reduce the displacements of the isolated structure, exploiting a peculiar effect that exploits the concept of damper to mass tuned but using small amounts of mass. Then, for a particular numerical application, two kind of inerter device has been designed, a rack-pinion one and a fluid inerter one, from which it is possible to demonstrate that the fluid inerter device is the one that better increase the mass. Finally, in Chapter 6, in order to improve the performance of the two designed devices (HFRB and VID), a glass fiber reinforcement was studied for the PTFE part, and, in particular, experimental test on two filled printed PTFE disk and one reinforced PTFE have been carried out. For better understand the behavior of the reinforced PTFE, numerical simulation with FE software has been conducted in the reinforced part. Both the experimental test and the FE simulation have demonstrate that the reinforcement improves the compressive behavior of the vergin PTFE. The research activity carried out during the three-year period led to the presentation of two patent applications for the devices studied, which are currently being processed.

Chapter 1

LITERATURE REVIEW

This chapter presents the principles of seismic isolation and the evolution that affected design applications. Criteria for this technology from ancient to nowadays are done mainly to furnish the motivations for grasping the rest of the thesis. The basic theory of seismic isolation is also illustrated and the main features of commercial devices are studied to highlight their advantages and disadvantages.

The chapter is organized as follows:

- Section 1 is just an opening, yet rigorous, a pleasant, friendly and not too technical introduction on the massive interest raised over the last years on the subject.
- Section 2 can be seen as a review of the basic background regarding seismic isolation and collects some applications.
- Section 3 includes the main features of different devices in order to do a comparison between them and understand better similarities and rules.

The exposition of the chapter is however carried out in the perspective of revisiting different topics within a unified framework.

1.1 Historical development of base isolation system

Historical studies and archaeological campaigns have revealed that ancient civilizations were facing the problem of building structures that could resist to the earthquake. Important buildings, of many ancient civilizations, have survived several earthquakes, even of big magnitude. It seems that over 2000 years ago, builders had realized the importance of inserting "elements" that had the property of attenuating the effect of earthquakes.

In ancient Crete (2000-1200 b.C.) is possible to find symmetrical buildings consisting of monocellular nuclei. The structure was made up of stone blocks interconnected by wooden elements which, in addition to ensuring the connection between the elements, provided "plasticity" to the entire building, compensating for the "fragility" of the stone. These buildings were also resting on a layer of sand and gravel that, apart from smoothing soil irregularities, produced a filtering action against soil vibration during an earthquake.

Under the foundations of the Troy Walls (1500 b.C.), according to US archeologist Carl Blegen, was deliberately left a layer of compact earth between the foundation plan and the base rock. According to the archaeologist, the builders wanted to create a ground cushion in such a way as to protect the wall from the effects of the earthquake.



(a)



(b)

Figure 1.1 First application of seismic isolation: (a) Cnossos Palace; (b) Troia's walls

In ancient Greece, the idea of protecting the structure was widespread by disconnecting it from the ground, interposing between it and the foundations some layers of material that could "translate" the construction against the ground in the event of an earthquake. In some cases, they lay under the firm foundation of the ceramic and clay layer walls. The ceramic protected the clay layer from moisture and dehydration, maintaining the plastic properties that dampened ground vibrations during the earthquake. We find concrete evidence of the application of seismic damping in antiquity in a classic passage of *Naturalis Historia* of Plinio il Vecchio quoting:

“Graecae magnificentiae vera admiratio exstat templum Ephesiae Dianae CXX annis factum a tota Asia. In solo id palustri fecere, ne terrae motus sentiret aut hiatus timeret, rursus ne in lubrico atque instabili fundamenta tantae molis locarentur, calcatis ea substravere carbonicus, dein velleribus lanae.” (n.h., 36,95)



Figure 1.2 Diana Temple in Efeso

Archaeological excavations have shown that trenches wider than the size of the foundations were excavated for substructures, and a layer of 20 cm thick limestone gravel was laid on the ground. On this layer the walls were raised and the lateral voids were filled with waste material from stone processing. It is important to note that the material was not used again for filling. In this way the foundation walls were insulated and lined on all

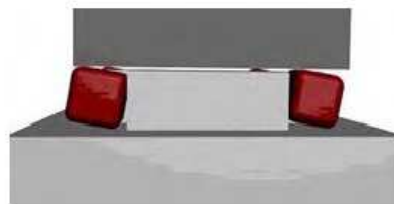
faces, from the wet ground. Filis of Byzantium, about the construction of this temple, wrote:

"The architect released the bottom of the underworld, then dug ditches to great depths and laid the foundations. The amount of masonry used for underground structures was the entire mountain quarry. He insisted on his unmistakable stability..."

In antiquity another example of seismic isolation is the Dikilitash obelisk located in Turkey. It is a stone block of 18.69 m high, carved in Egypt in 1450 b.C and was erected in Instabul in 379-395 a.C. It is mounted on a marble base of $3 \times 3 \times 3 \text{m}$ through 4 cubes (50x50cm) of bronze placed in the edges. It has been calculated that it can collapse with an earthquake of magnitude greater than 7.6 and having an epicenter at a distance of 5 km.



(a)



(b)

Figure 1.3 Dikilitash obelisk: a) base of the real structure, b) base model



(a)



(b)

Figure 1.4 Dikilitash obelisk: a) real structure, b) Finite Element Model

There are certain references to a primal application of isolation to the base also in Kyoto for Sanjusangendo, a Buddhist temple built in 1266 a.C., containing a famous building built to accommodate 1000 statues. Below the foundations were laid layers of coal, woolen yarns, sand, so that it could favor the sliding of the structure with respect to the ground. The temple did not suffer damage following the 1995 Kobe earthquake (only 4 statues were slightly damaged).



Figure 1.5 Temple of Sanjusangendo

1.1.1 From 1900 to nowadays

In 1870 thanks to Jules Touaillon we have the first document attesting to the idea of designing a building with a system that decouples the motion of the structure from the ground (Figure 1.6 a)). The patent was based on the use of spheres interposed between the foundation of the structure and foundations, but never had any practical application.

More than a century ago, in 1885, John Milne, a professor of engineering in Japan, built a small wooden house on balls in cast-iron plates with saucer-like edges on the heads of piles, to demonstrate that a structure could be isolated from earthquake shaking (Housner et al. 1997). However, the building behavior under wind loads was not satisfactory. So, he reduced

the balls diameter from 10 inch to 1/4 inch. By this mean, the building became stable against wind loads and was evidently successful under actual earthquake action. In 1891, after Narobi earthquake, the Japanese Kawai, proposed a base isolated structure with timber logs placed in several layers in the longitudinal and transverse direction (Figure 1.6 b)) (Izumi 1988).

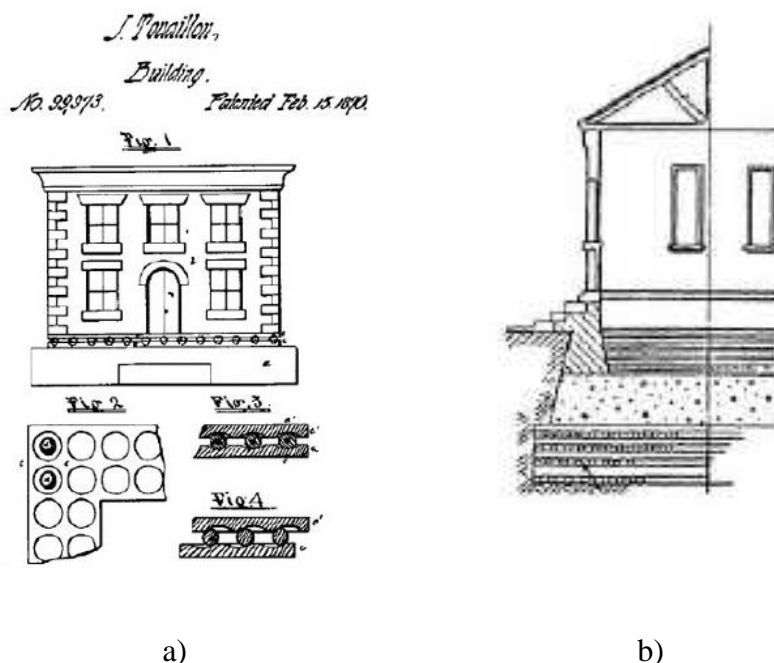
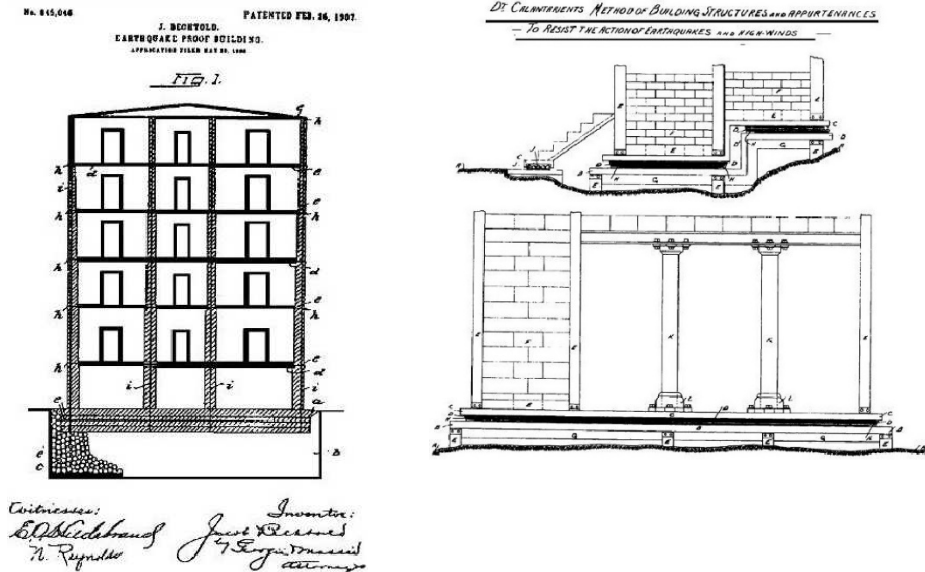


Figure 1.6 First patents on isolation: a) Touaillon; b) Kawai

In 1906, Jacob Bechtold of Germany applied for a U.S. patent in which a seismic-resistant building has to be placed on rigid plate supported on spherical bodies of hard material (Figure 1.7 a)) (Buckle and Mayes1990).

In 1909, a medical doctor from England, Calentarients, had submitted a patent application to the British patent office for a method of building construction. In his method, a building is constructed on a layer of fine sand or talc that would allow the building to slide in an earthquake, there by reducing the force transmitted to the building itself (Figure 1.7 b))(Kelly 1986).



a)

b)

Figure 1.7 First patents on isolation: a) Bechtold b) Calentarients

He also invented ingenious connections for gas and sewer networks, so as to avoid damage during ground vibrations. A patent that never had a practical application.

Following the earthquake of 1908, resulting in a tsunami that hit Messina and Reggio Calabria causing between 80,000 and 120,000 deaths and the collapse of 90% of Messina's buildings, the City Reconstruction Commission proposed two intervention techniques that provided for decoupling the building from the foundations by inserting a layer of sand or rollers under the columns that allowed the building to move horizontally. The second one was recommended between the two approaches. Unfortunately, these proposals were never accepted.

In 1911, the scholar Domenico Lodà invented the first "seismic isolator" in history (see Figure 1.9). This patent provided a support system that prevented the transmission of seismic movements and anticipated modern isolator solutions. This device can be considered as the ancestor of current isolators.

One notable historic structure, however, is Frank Lloyd Wright's Imperial Hotel in Tokyo, completed in 1921. This building was founded on a willow layer of firm soil which in turn was supported by an underlying layer of mud. Cushioned from devastating ground motion, the hotel survived the 1923 Tokyo earthquake and later Wright wrote in his autobiography (Wright 1977) of the "merciful provision" of 60 to 70 feet of soft mud below the upper 8 foot thick surface soil layer which supported the building. The Imperial Hotel is an evidence that base isolation works and seismic protection can be achieved by relatively simple means. Even though the building suffered damage, Wright is worthy of having completed a work, integrating architecture and anti-seismic engineering, which still puts it at the forefront for that period.

In 1929, Robert de Montalk of New Zealand filed a patent application for an invention comprising a means whereby a bed is placed and retained between the base of a building and its solid foundation. The bed was being composed of material which will absorb or minimize seismic shocks (DeMontalk 1932).

Again in 1929, R. R. Martel proposed the so-called "Flexible first story concept", which consisted in the introduction of flexible columns on the first floor to lengthen the natural structure of the structure (Figure 1.8). It was proposed that the first-story columns should be designed to yield during an earthquake to produce isolation and energy-absorbing actions. However, to produce enough damping, several inches of displacements is required, and a yielded column has greatly buckling loads, proving the concept to be impractical.

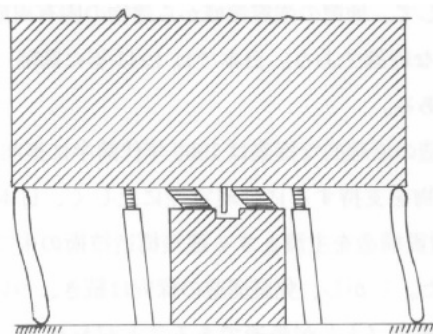


Figure 1.8 First patents on isolation: Martel

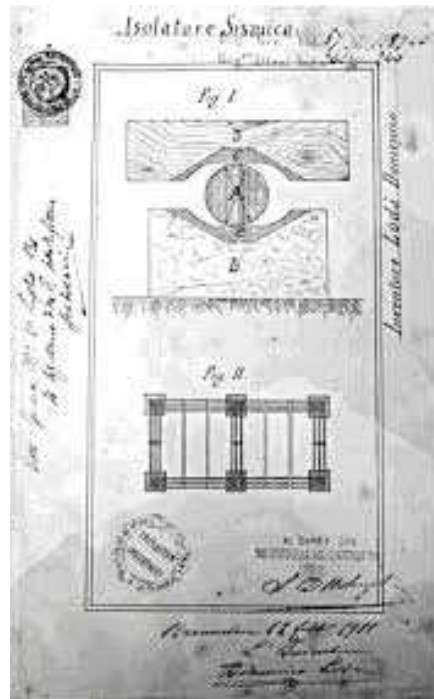


Figure 1.9 First patents on isolation: Lodà

To prevent the structure from moving too far, the first story is constructed underground and energy dissipators are installed at the top of this story (Arnold 2001). To overcome the inherent dangers of soft supports at the base, many types of roller bearing systems have been proposed. The rollers and spherical bearings are very low in damping and have no inherent resistance to lateral loads, and therefore some other mechanisms are needed to provide wind restraint and energy absorbing capacity. A long duration between two successive earthquakes may result in the cold welding of bearings and plates, thus causing the system to become rigid after a time. Therefore, the application of the rolling supports was restricted to the isolation of special components of low or moderate weight (Caspé 1984).

Other developments were with Green (1935) and Jacobsen (1938) studies, which led to the introduction of the concept of energy absorption by plasticization. The Los Angeles Olive View Hospital was built using this concept, but the system shown itself to be inadequate, undergoing the soft floor mechanism, which was instead a virtuosity of the structure. In 1971, shortly after the end of the construction work, the San Fernando earthquake tested the new structure, causing 4 victims and extensive

damage. It was noted that it was not possible to absorb the earthquake energy only with a column plan. Analyzing, in fact, the behavior of the Olive View Hospital Anil K. Chopra concluded: *"Though the buildings with soft planes are obviously unsuitable for the seismic regions, their response during the earthquake past suggests the possibility of reducing damage to the building Through a base isolation system that acts as a kind of soft floor"*.

Simultaneously to the development of the soft first-story approach, the flexibility of natural rubber was also seen to be another solution for increasing the flexibility of the system. The first use of a rubber isolation system was in 1969 to protect a structure from earthquake, and it was an elementary school in Skopje, Yugoslavia. The Pestalozzi School, a three story concrete structure designed and built by Swiss engineers, is isolated by a system known as the Swiss Full Base Isolation-3D System (Staudacher et al. 1970). The rubber bearings used in this application were completely unreinforced so that the weight of the building causes them to bulge sideways. To improve the building stability under minor vibrations, glass blocks acting as seismic fuzes are intended to break when the seismic loading exceeds a certain threshold. Owing to have the same stiffness of the isolation system in all directions, the building bounces and rocks backwards and forwards (Jurukovski and Rakicevic 1995). Because of this, the adoption of these devices turned out to be unsatisfactory and they were no longer used in others application.



Figure 1.10 The Pestalozzi School

Seismic isolation became a reality in the seventies in England, where were produced the first elastomeric bearings by the MRPRA (Malaysian Rubber Producers' Association Research), who devised a process for vulcanizing rubber layers with a stainless steel. These bearings are very stiff in the vertical direction to carry the structural weight but they are very flexible horizontally to enable the isolated structure to move laterally under strong ground motion.

The first application was made in France in the early 70s, in order to safeguard a series of nuclear power stations and plant facilities. The utility developed a standard nuclear power plant with the safety grade equipment qualified for 0.2g acceleration. The system combines laminated neoprene bearings with lead-bronze alloy in contact with stainless steel, the sliding surface being mounted on top of the elastomeric bearing. The coefficient of friction of the sliding surface is supposed to be 0.2 over the service life of the isolator (Electricité-de- France System).

In the early 1980s, developments in rubber technology led to new rubber compounds which were termed high damping rubber (HDR) (Derham and Kelly al. 1985)

In the 80s the seismic isolation technique spread throughout the world with important applications in bridges and strategic buildings, especially in the U.S. and New Zealand, elastomeric isolators with high damping rubber using high dissipation (High Damping Rubber Bearing) or isolators with lead plug, Lead Rubber Bearing (LRB) (Tarics et al. 1984; Anderson 1989, Charlerson. 1987, Reaveley et al. 1988); in Japan the solution initially more adopted involved the use of low-damping elastomeric devices, Low Damping Rubber Bearing (LDRB) with the addition of viscous or hysteretic dampers (Kelly 1988).

Later, a large number of isolation devices were developed including rollers, springs, friction slip plates, capable suspension, sleeved piles, and rocking foundations. Now seismic isolation has reached the stage of gaining acceptance and replacing the conventional construction, at least for important structures.

Moreover, after the two catastrophic events such as the 1994 Northridge and the 1995 Kobe earthquake, which struck respectively California and Japan, the development of seismic isolation had an

additional input. Indeed in those events the isolated structures turned out to be an excellent performance than that one of the equivalent fixed base structures located in the same affected area (Asher et al. 1995).

After these events, the number of applications of seismic isolation has undergone considerable development particularly in Japan. The interest for this application is remarkable in existing buildings, in which the seismic isolation can reach levels of security significantly higher than those achieved by the traditional type of retrofitting.

In USA the first examples of seismic retrofitting of existing buildings by basic isolation go back to the mid-90s. The structures were large buildings such as City Hall in Oakland, San Francisco and Los Angeles. In all above cases it have been used rubber devices with lead plugs or high damping bearing (LRB or HDRB). Recently, important applications of sliding isolators with curved (Amin and Mokha 1995) or flat surface have been applied in the U.S.A., with the addition of auxiliary devices re-centering rubber (Way and Howard 1990).

In the last 40 years in Italy, especially after the earthquake in Friuli (1976) where the viaduct Somplago, protected with a seismic isolation system relatively simple but effective, was the only viaduct without damage, the use of seismic isolation has experienced a constant development. In particular in the decade from 1983 to 1993 seismic isolation was widely used in Italy for the protection of highway bridges and viaducts (Medeot 1991).

For this reason, important national and international research programs, involving companies, research institutes and Italian universities, have been carried out in order to develop the efficacy of the seismic devices and new technologies for devices and isolation systems.

Seismic isolation has been studied at different scale levels and for different devices, in the last years has been carried out dynamic tests on isolators individual small-scale (Kelly and Quiroz 1992) and real scale (Braga et al. 1997), or the performance of dynamic shaking table tests on scale models of isolated structures (Dolce et al. 2001 and 2008).

1.2 Basic concepts in seismic isolation

Base isolation is the most effective technique to mitigate the effect of seismic action. It is generally realized by some device. A seismic event is manifested by the vibrations induced by the movement of the ground and generates in the structure forces inertia equal to the product of its masses for accelerations. To avoid structural damage during an earthquake, it would be necessary to increase the resistance of the structure proportionally with the intensity of the earthquake.

The underlying principle of seismic isolation it is to avoid the earthquake, rather than to resist, and it is applied decoupling the dynamic response of the building from the ground motion. Decoupling is obtained through the interposition of devices, between structure and foundations, with low horizontal stiffness and high dissipative behavior in order to provide a lower fundamental frequency of the structure and to increase the overall damping of the structure.

1.2.1 Theory of base isolation

The linear theory of seismic isolation is provided in detail in Kelly 1993. Likewise, as for fixed-frame structures, where the study of dynamic behavior starts from the study of the simple SDOF system, the characteristic aspects of the dynamic behavior of base isolated structures can be derived from the analysis of a simplified model, with only two degrees of freedom.

The study of the n degree of freedom system, with lumped mass, linear springs and linear viscous damping, is developed with the technique of modal analysis that allows to identify changes in dynamics features, vibration frequencies and modal shapes determined by the isolation system on the elevation structure. The equation of motion of the structure can be written in the following form:

$$\hat{\mathbf{M}}\ddot{\mathbf{u}}(t) + \hat{\mathbf{C}}\dot{\mathbf{u}}(t) + \hat{\mathbf{K}}\mathbf{u}(t) = -\hat{\mathbf{M}}[\ddot{u}_g(t) + \ddot{u}_b(t)] \quad (1.1)$$

$$m_{tot} \ddot{u}_b(t) + c_b \dot{u}_b(t) + k_b u_b(t) = -m_{tot} \ddot{u}_g(t) - \boldsymbol{\tau}^T \hat{\mathbf{M}} \ddot{\mathbf{u}}(t) \quad (1.2)$$

and in matrix form:

$$\begin{bmatrix} \hat{\mathbf{M}} & \hat{\mathbf{M}}\boldsymbol{\tau} \\ \boldsymbol{\tau}^T \hat{\mathbf{M}} & m_{tot} \end{bmatrix} \begin{bmatrix} \ddot{\mathbf{u}}(t) \\ \ddot{u}_b(t) \end{bmatrix} + \begin{bmatrix} \hat{\mathbf{C}} & \mathbf{0} \\ \mathbf{0} & c_b \end{bmatrix} \begin{bmatrix} \dot{\mathbf{u}}(t) \\ \dot{u}_b(t) \end{bmatrix} + \begin{bmatrix} \hat{\mathbf{K}} & \mathbf{0} \\ \mathbf{0} & k_b \end{bmatrix} \begin{bmatrix} \mathbf{u}(t) \\ u_b(t) \end{bmatrix} = - \begin{bmatrix} \hat{\mathbf{M}}\boldsymbol{\tau} \\ m_{tot} \end{bmatrix} \ddot{u}_b(t) \quad (1.3)$$

where $\hat{\mathbf{M}}$, $\hat{\mathbf{C}}$ and $\hat{\mathbf{K}}$ are the n -dimensional matrices of mass, damping and stiffness of the superstructure as if it was on a fixed base, $\boldsymbol{\tau}$ is the $n \times 1$ influence vector of the substructure associated with the ground motion $\ddot{u}_g(t)$ and $\mathbf{0}$ is a $n \times 1$ vector of zero terms; $\mathbf{u}(t)$, $\dot{\mathbf{u}}(t)$ and $\ddot{\mathbf{u}}(t)$ are, respectively, vectors of displacements, velocities and accelerations of the significant D.O.F. of the structure relative to the base isolation system while $u_b(t)$ is the displacement of the base isolation system; c_b , k_b are respectively the damping coefficient and the stiffness of the base isolation system.

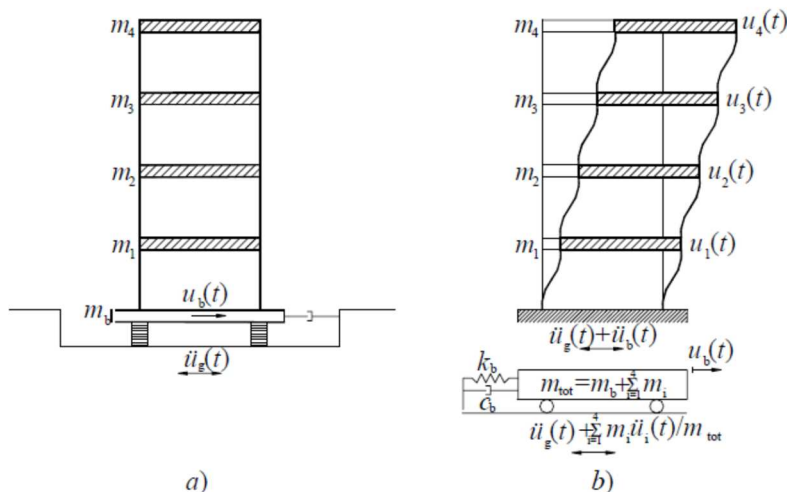


Figure 1.11 Schematic sketch of a base isolated structure: a) structural scheme with the base isolation system b) useful scheme for the definition of the equation of motion (Muscolino 2002)

The total mass m_{tot} is defined as follows:

$$m_{tot} = m_b + \boldsymbol{\tau}^T \hat{\mathbf{M}} \boldsymbol{\tau} = m_b + \sum_{i=1}^n m_i \quad (1.4)$$

being m_b the mass of the isolation system and m_i the mass of the generic storey of the structure.

In the spirit of the substructure approach, two subsystems can be identified from Figure 1.11, the primary system is the (linear) superstructure, which is subject to the ground motion along with the inertia forces transferred by the secondary system, the base isolation system, which is in turn excited by a feedback of the primary system. Since we have written the equations in relative displacements, the resulting Equation (1.1) are decoupled in terms of elastic and viscous forces but coupled in terms of inertia forces due to the off-diagonal terms of the $\hat{\mathbf{M}}$ matrix in Equation(1.3). The latter terms characterize the dynamic interaction of the two subsystems. It is easy to observe that while the superstructure can realistically be considered a classically damped system, the Caughey and O’Kelly condition (Caughey 1965) being generally satisfied, due to the high contrast in damping between the superstructure and the BIS, the base-isolated building is a non-classically damped system (Chopra 2012). Natural frequencies and modes of vibration of such systems are different in the undamped and damped cases; in fact, one should solve a complex-value eigenproblem (including the damping matrix) to decouple the equations of motion in the modal subspace. This fact significantly complicates the mathematical aspects making the derivation of the eigenvalues and eigenvectors computationally more demanding. The conventional response spectrum method neglects this complication and indeed deals with the base isolation building as a classically damped structure, thus solving the following real-value eigenproblem associated with the stiffness and mass matrices reported in equation (1.3):

$$\mathbf{K}\Phi = \mathbf{M}\Phi\Omega^2 \quad (1.5)$$

where Φ and Ω^2 are the modal matrix and spectral matrix, respectively, collecting the first m (with $m \leq n+1$) eigenvectors ϕ_i and eigenvalues ω_i^2 . Generally, the arbitrary multiplicative factor of the natural modes ϕ_i is chosen such that the modal matrix is orthonormal to the mass matrix, $\Phi^T \mathbf{M} \Phi = \mathbf{I}_m$, being \mathbf{I}_m the identity matrix of order m .

In order to make some considerations on the advantages of seismic base isolation, we evaluate the frequencies of an isolated single degree of freedom structure. The equations of the motion of this structure are:

$$\begin{aligned} m\ddot{u}(t) + m\ddot{u}_b(t) + c\dot{u}(t) + ku(t) &= -m\ddot{u}_g(t) \\ m\ddot{u}(t) + m_{tot}\ddot{u}_b(t) + c_b\dot{u}_b(t) + k_b u_b(t) &= -m_{tot}\ddot{u}_g(t) \end{aligned} \quad (1.6)$$

Making the following position

$$\begin{aligned} \omega_0^2 &= \frac{k}{m} & \zeta_0 &= \frac{c}{2\sqrt{km}} & \omega_{iso}^2 &= \frac{k_b}{m_{tot}} \\ \zeta_{iso} &= \frac{c_b}{2\sqrt{k_b m_{tot}}} & \gamma &= \frac{m}{m_{tot}} \end{aligned} \quad (1.7)$$

we obtain:

$$\begin{aligned} \ddot{u}(t) + \ddot{u}_b(t) + 2\zeta_0\omega_0\dot{u}(t) + \omega_0^2 u(t) &= -\ddot{u}_g(t) \\ \gamma\ddot{u}(t) + \ddot{u}_b(t) + 2\zeta_{iso}\omega_{iso}\dot{u}_b(t) + \omega_{iso}^2 u_b(t) &= -\ddot{u}_g(t) \end{aligned} \quad (1.8)$$

The natural frequencies can be calculated by solving the eigenvalues problem defined in equation (1.5) that leads to the following characteristic equation:

$$\left. \begin{matrix} \omega_1^2 \\ \omega_2^2 \end{matrix} \right\} = \frac{1}{2(1-\gamma)} \left\{ (\omega_0^2 + \omega_{iso}^2) \pm [(\omega_0^2 + \omega_{iso}^2)^2 - 4(1-\gamma)\omega_0^2\omega_{iso}^2]^{1/2} \right\} \quad (1.9)$$

Assuming that $\omega_{iso}^2 \ll \omega_0^2$ the equation (1.9) can be written as follows:

$$\begin{aligned}\omega_1^2 &\equiv \omega_{\min}^2 \approx \omega_{iso}^2 \left(1 - \gamma \frac{\omega_{iso}^2}{\omega_0^2} \right) \\ \omega_2^2 &\equiv \omega_{\min}^2 \approx \frac{\omega_0^2}{1 - \gamma} \left(1 + \gamma \frac{\omega_{iso}^2}{\omega_0^2} \right)\end{aligned}\tag{1.10}$$

Taking into account that $\omega_{iso}^2 / \omega_0^2 \ll 1$ and that $\gamma < 1$, it can be seen that the first frequency of the isolation-SDOF system is close to the frequency of the isolation system and that the second frequency is greater than that of the SDOF due to the presence of the basement.

This implies that the fundamental mode is associated with the isolation system and this can be designed to reduce stress on the structure. In the Figure 1.12 the responses are plotted in the time and frequency domain of fixe ($\omega_0 = 14.14$ rad/s, $\zeta_0 = 0.05$, $m = 5000$ kg) and isolated SDOF

($\omega_{iso} = 3.14$ rad/s, $\zeta_{iso} = 0.1$, $\gamma = 0.45$), subjected to $f(t) = \sum_{k=3}^7 \exp(-kt / 30) \sin(3kt)$,.

In the latter case the system is not classically damped and the transfer function of the relative displacements of the SDOF system has two peaks near the pulsations, equation (1.10).

From the exam of the response in the time domain, it can be seen that, due to the introduction of the base isolation system, the relative displacements of the structure are strongly reduced with respect to the base. Instead, looking on the response in the frequency domain it is shown that in the case of the fixed SDOF system, the predominant circular frequency is near the natural oscillation pulsation. In the case of the isolated structure, however, this does not occur because the ordinate of the first peak, close to the frequency of the isolation system, is smaller than that of the forcing and of the second natural vibration of the composed system.

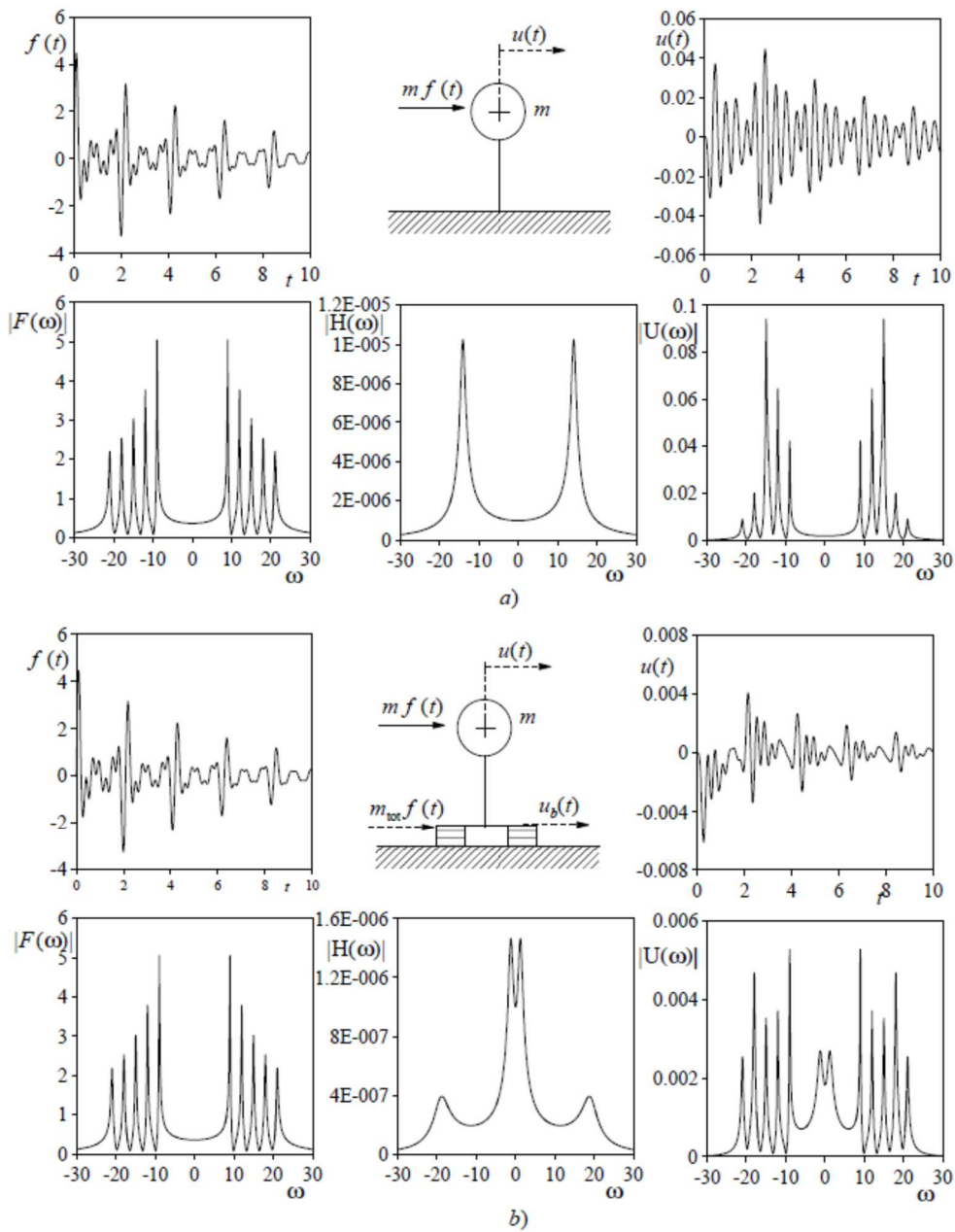


Figure 1.12 Response function, in terms of relative displacement, in the time domain and in the frequency domain of an SDOF system: a) fixed system; b) isolated system (Muscolino 2002)

1.2.2 The Italian code for base isolated structures

A first specific legislation to regulate the construction of buildings in concrete and masonry dates back in Italy to 1996, with a minister ordinance. Immediately after the earthquake of 31 October 2002, which affected the territory on the border between Molise and Puglia, the Department of Civil Protection has adopted the ordinance of Council of Ministers no. 3274 of 20.03.2003, which includes two chapters on seismic isolation of buildings and bridges, in order to provide an immediate response to the need to update the classification of seismic and earthquake regulations.

This seismic code has been for a long time not mandatory but only indicative of the basics of seismic design requirements. Only in 2008 it was published in the "Gazzetta Ufficiale", the last Italian seismic code, called "Nuove Norme Tecniche delle Costruzioni". The new technical regulations are based on the European standards related to Eurocode 8 and in particular the parts relating to the evaluation of the seismic horizontal forces and the seismic isolation design. In Chapter 7 the New Italian Code introduce the seismic design rule action. Paragraph 7.10 provides criteria and rules for construction, bridges design and for the retrofitting of existing structures in which an isolation system is placed below the construction. The legislation introduces the terms "isolation" and "dissipation" referring to innovative techniques that propose the use of devices in the structure of the constructions in order to protect them from seismic loads.

The reduction of the horizontal seismic response can be obtained by two strategies of isolation, or through their appropriate combination:

- a) increasing the fundamental period of the construction to bring it in the field of minors acceleration response;
- b) limiting the maximum horizontal force transmitted.

In both the strategies, the isolation performance can be improved through the dissipation in the isolation system of a substantial portion of the mechanical energy transmitted from the ground to the building. Italian code includes provisions concerning the devices. Isolation devices and their connection to the structure must be designed to ensure the access and to make the devices inspected and replaced. To minimize the torsion effects,

the projection of the center of mass of the superstructure and the center of rigidity of the isolation devices must be, as far as possible, coincident. Also, where the isolation system includes a dissipative and self centering function, it is necessary that such devices are arranged in a way that minimizes the torsion effects (e.g. increasing the perimeter) and are in number statically redundant. To minimize the differences in behavior of the isolators, the compressive strength should be as uniform as possible. In the case of isolation systems that use different types of isolators, special attention must be paid to the possible effects of different vertical deformation under static and seismic actions. To prevent or limit tensile strength that could occur in the isolators, the vertical load on an individual isolator should be zero or positive under the seismic actions. When the analysis proves that the vertical load are negative, it is should be proved with appropriate tests which the isolators are able to support such a condition.

1.3 Main features of commercial devices

1.3.1 Elastomeric-based devices

The elastomeric-based devices are made by vulcanization bonding of successive rubber and steel reinforcing plate (Kelly 1990), this procedure of manufacture is relatively simple. The bearing have high stiffness in vertical direction, due to the steel plate, and are sufficient flexible in horizontal direction. Commonly it is used natural rubber for the elastomer because its main mechanical characteristics are superior to that ones of synthetic elastomer, such us neoprene rubber, butyl rubber and nitrile rubber (Taylor and Lin 1992). This kind of bearings are distinguishable in three main categories: Low- Damping Rubber Bearings, High-Damping Rubber Bearings and Lead Rubber Bearings.

1.3.1.1 *Low Damping Rubber Bearing (LDRB)*

The LDRBs bearings have a low damping ratio, produced only by the elastomer, in the order of 2 % to 4%, and so usually they are used with an other element that produce suitable damping. The behavior of the rubber material in shear is linear up to shear strains of above 100%. This bearing are easy to manufacture, simple to model and are unaffected by rate, temperature or aging (Naeim and Kelly 1999).

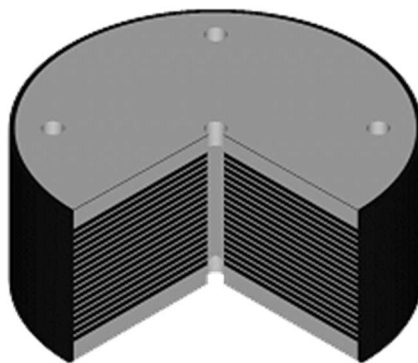


Figure 1.13 LDRB device

1.3.1.2 High Damping Rubber Bearing (HDRB)

Thanks to the developments in rubber technology, in 1980 had been produced bearing that had a high stiffness at low shear strains but a reduced stiffness at high strain levels. With this bearings, named “ High Damping Rubber Bearings” the damping is increased to levels between 10 and 20 % at 100% shear strain (Naeim et Kelly 1999, Kelly 2002). This increment is due to the use of a rubber with a high damping behavior.

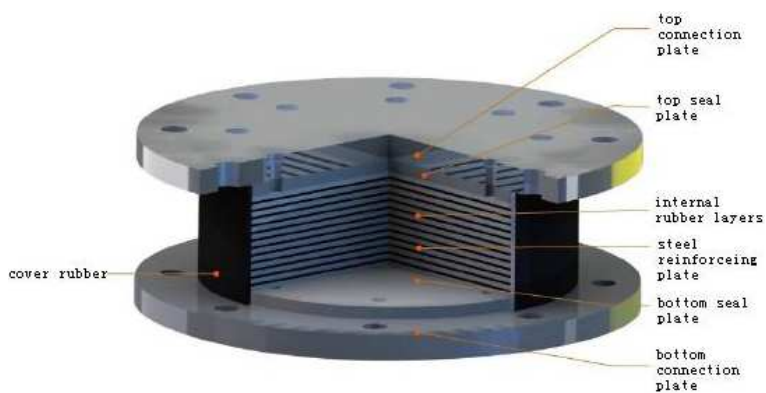


Figure 1.14 HDRB device

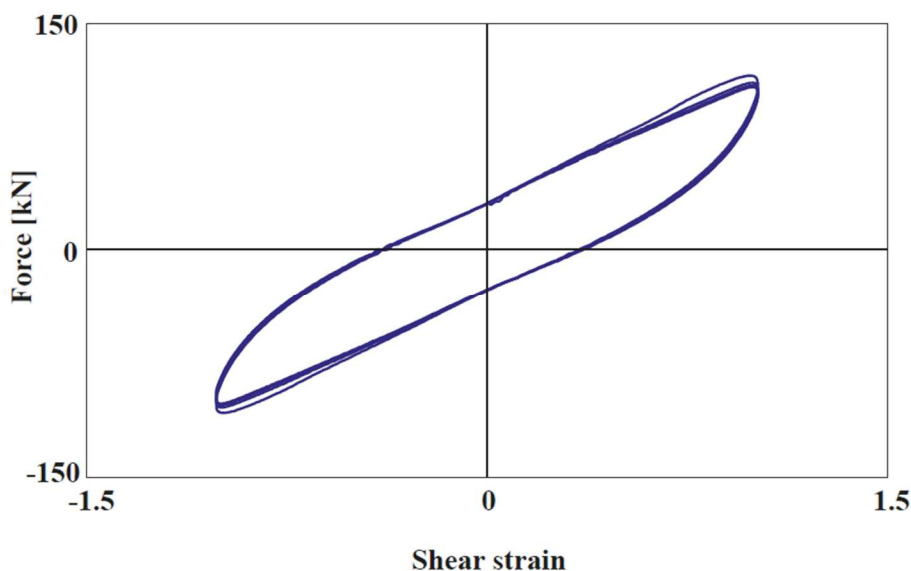


Figure 1.15 Experimental hysteresis loops of a HDRB at frequency of 0.5 Hz, shear strain $\pm 100\%$ (FIP INDUSTRIALE)

1.3.1.3 Lead Rubber Bearing (LRB)

The LRB are based on a laminated rubber bearing but in which there is a central lead core to provide an additional means of energy dissipation. The lead plug produce an increase in damping to about 15%, reduces the lateral displacement and increases also the resistance to minor earthquake or wind. The lead-plug bearing was invented in New Zealand in 1975 (Robinson and Tucker 1977, Robinson and Tucker 1983) and has been used extensively in New Zealand. The lead must fit tightly in the elastomeric bearing, and this is achieved by making the lead plug slightly larger than the hole and forcing it in. The lead core has a good fatigue behavior during cyclic loading at plastic strain, generally the lead yields at low stress (about 10 MPa) in shear and exhibits an elasto-plastic behavior. Substantially the LRB behaves essentially as an hysteretic damper (Kelly et al. 1972; Kelly et al. 1977; Skinner 1975).

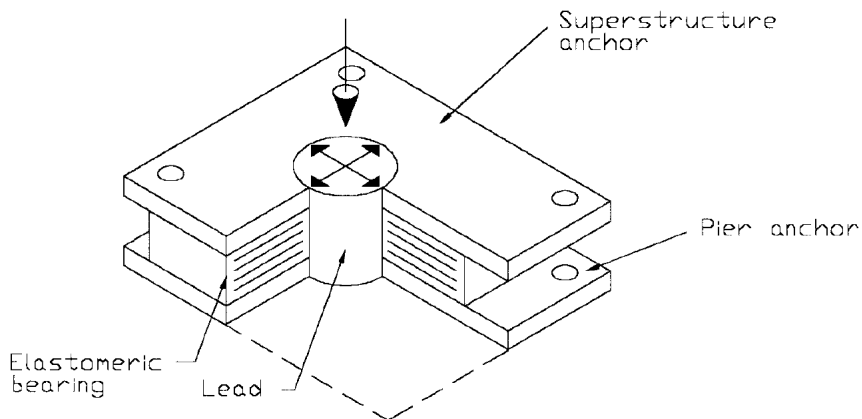


Figure 1.16 Lead-plug isolator (Naeim et al. 1999)

Because the effective stiffness and effective damping of the lead-plug bearing is dependent on the displacement, it is important to state the displacement at which a specific damping value is required.

Lead-plug bearings have been extensively tested and there are very complete guidelines on their design and modeling.



Figure 1.17 LRB device

In Figure 1.17 is represented a classic LRB device and in Figure 1.18 is shown the hysteretic cycle of a LRB at frequency 0.5 Hz.

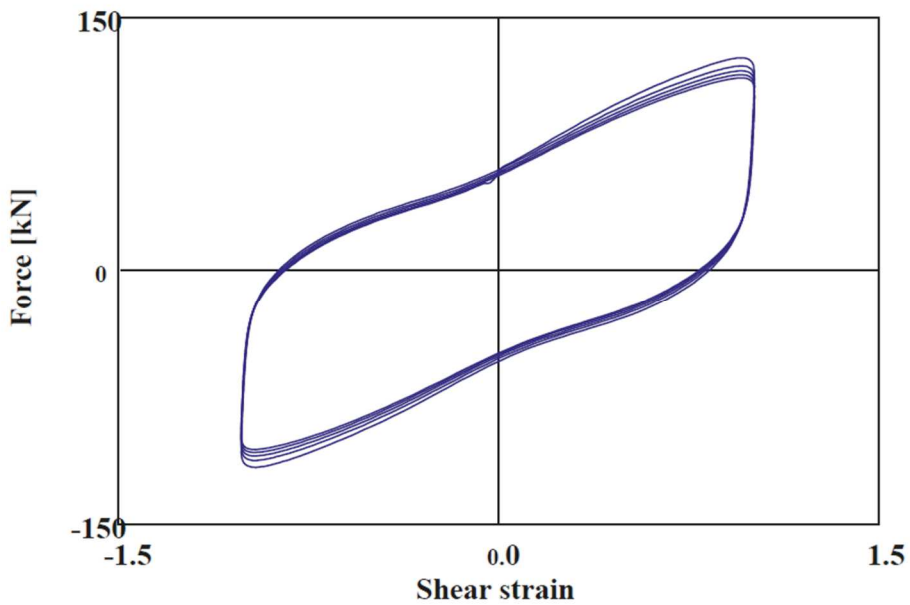


Figure 1.18 Experimental hysteretic loops of a LRB at frequency of 0.5 Hz, shear strain $\pm 100\%$ (FIP INDUSTRIALE)

1.3.1.4 Fiber Reinforced Elastomeric Isolator (FREI)

In this device, the use of steel plate is replaced by fiber mesh that are lighter, easy to be manufactured and so economically better (Kelly 2001). In terms of weight the reduction is possible because fiber materials are available with an elastic stiffness that is of the same order as steel. Thus the reinforcement needed to provide the vertical stiffness may be obtained by using a similar volume of a very much lighter material, manufacturing costs may also be reduced if the use of fiber allows a simpler, less labor-intensive process. It is also possible that the current approach of vulcanization under pressure in a mold with steam heating can be replaced by microwave heating in an autoclave. Another benefit of using fiber reinforcement is that it would then be possible to built isolators in long rectangular strips, whereby individual isolators could then be cut to the required size.

In Figure 1.21 is shown the comparison between the force displacement loop of a classical Steel Reinforced Elastomeric Isolator (SREI) and a Fiber Reinforced Elastomeric Isolator (FREI) realized with carbon fiber (Moon et al. 2002). The test results of the FREI revealed the effective stiffness of 330 kg_f/mm and the equivalent damping of 15.85%. The test results of the SREI revealed an effective stiffness of 350 kg_f/mm and the equivalent damping of 6.20%. The horizontal test results showed that carbon reinforcement elastomers were over two times higher in damping than steel reinforcement elastomers.

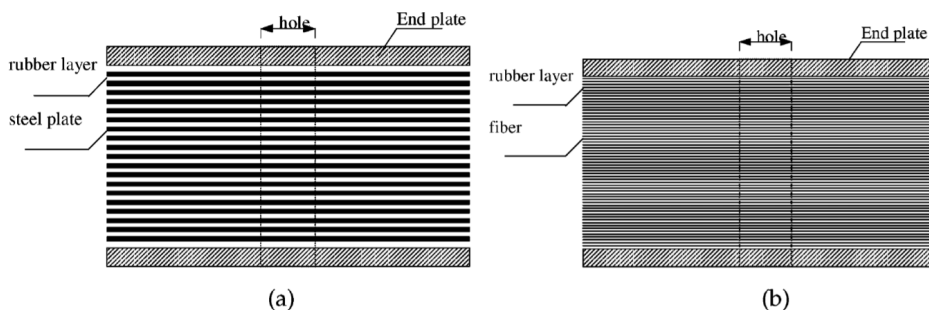


Figure 1.19 Modeling of isolators: (a) Classical layer of steel and rubber ; (b) Fiber Reinforced Elastomeric Isolator

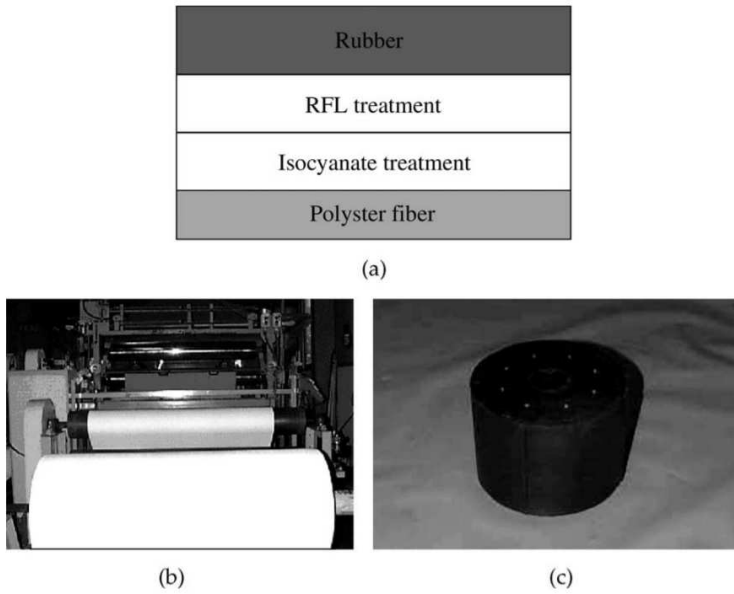


Figure 1.20 Manufacturing of FREI: (a) schematic diagram of dipping process to improve bonding characteristic between rubber and fiber; (b) dipping process; (c) FREI in final form (Moon et al. 2002)

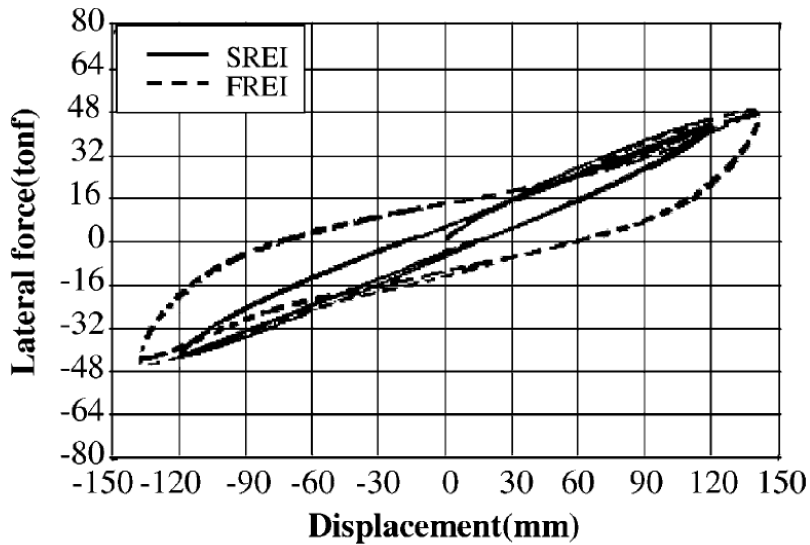


Figure 1.21 Hysteresis loops for SREI and FREI at 50% shear strain (Moon et al. 2002)

1.3.2 Friction based device

Sliding friction based devices are composed of sliding bearings (Teflon-steel), which are characterized by low friction resistance values to transmit the least possible seismic load to the structure.

1.3.2.1 *Pure Sliding Device (SD)*

The simplest isolation systems to be proposed is the purely sliding one, in fact these devices have no inherent natural period and therefore are insensitive to variations in frequency content of seismic excitations. The SD are made up of two flat disks of different diameters flowing one on the other. The materials used are chosen so that they can developed a low friction resistance, than the acceleration transmitted to the structure can be reduced. The materials used typically are polished stainless steel and PTFE (Teflon). The main problems of these devices are the absence of restoring force and the deterioration of sliding surface due to the number of cycle of the seismic load (Skinner et al. 1993).

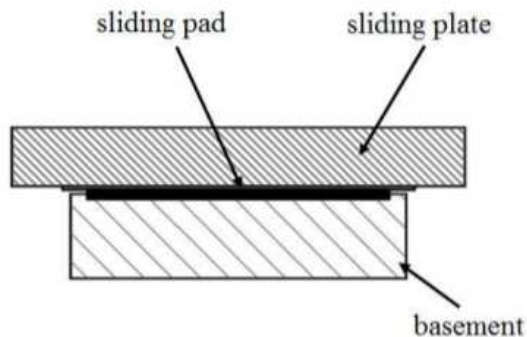


Figure 1.22 Schematic schetk of a SD



Figure 1.23 Pure Sliding Device (FIP INDUSTRIALE)

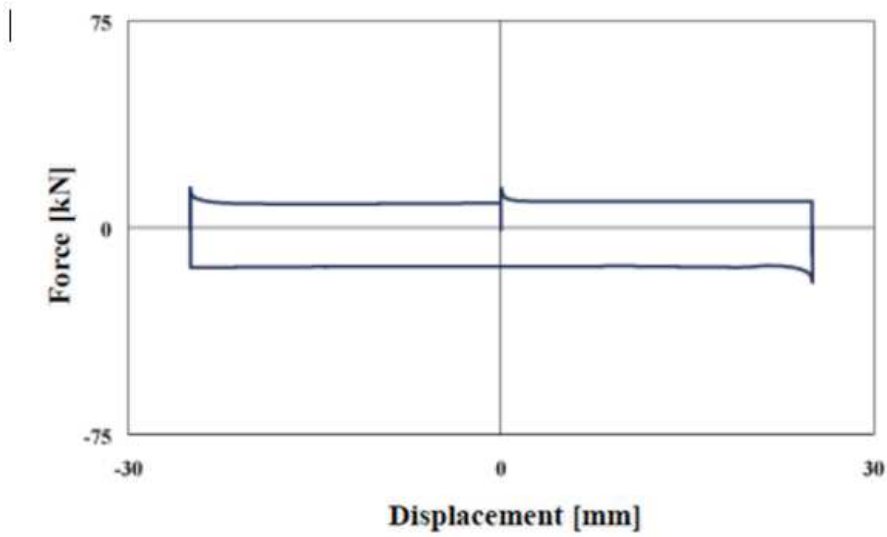


Figure 1.24 Force-displacement loop result of a static test (speed 4mm/min) at maximum design vertical load (14000 kN)(FIP INDUSTRIALE)

1.3.2.2 Friction Pendulum System (FP)

The Friction Pendulum system is an isolation system that has at same time a restoring force, due to the geometry, and a dissipative behavior, due to the friction between the sliding surfaces (Zayas et al. 1987). In these devices, the lateral force is opposed to the friction force due to the fact that a surface is flowing over the other one. The recentering function is obtained through the curved surface, which allows the device to return in position once that it is finished the external action.

The vertical load, in fact, produces a component in the tangential direction to the spherical surface allowing the recentering. The choice of curvature is very important because it is close to the rigidity of the device, and therefore to the period of vibration of the isolated structure (the period is inversely proportional to the stiffness). Usually the slider is faced with a Teflon type material, such us PTFE, for which the coefficient of friction depends on velocity of sliding, on the vertical load, on the temperature, etc.. (Mokha 1980). In fact when the slider slips on the polished chrome surface of the sliding it is reached a maximum sliding friction coefficient of the order of 0.1 or less, at high velocity of sliding, and a minimum friction coefficient of the order of 0.05 or less, for very low velocity of sliding. One advantage of these devices is low maintenance; in fact, teflon effectively protects the surface from corrosion.

These devices usually have a dimension contained in height while very large in plan, to allow the horizontal displacements. If it is necessary to reduce the size of the plan or if there is a particular constructive need, they can be produced with two concave sliding surfaces with equal or different radius (concave double-surface sliding device).

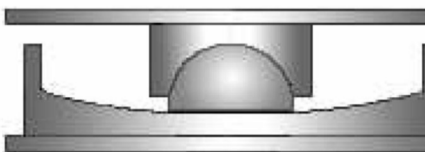


Figure 1.25 FP schematic sketch

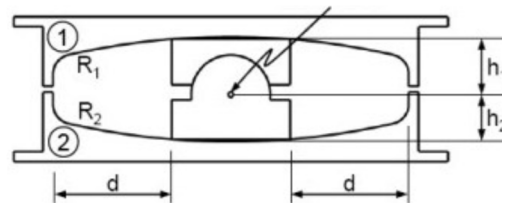


Figure 1.26 FP schematic sketch



Figure 1.27 A double concave curved surface slider (FIP INDUSTRIALE)

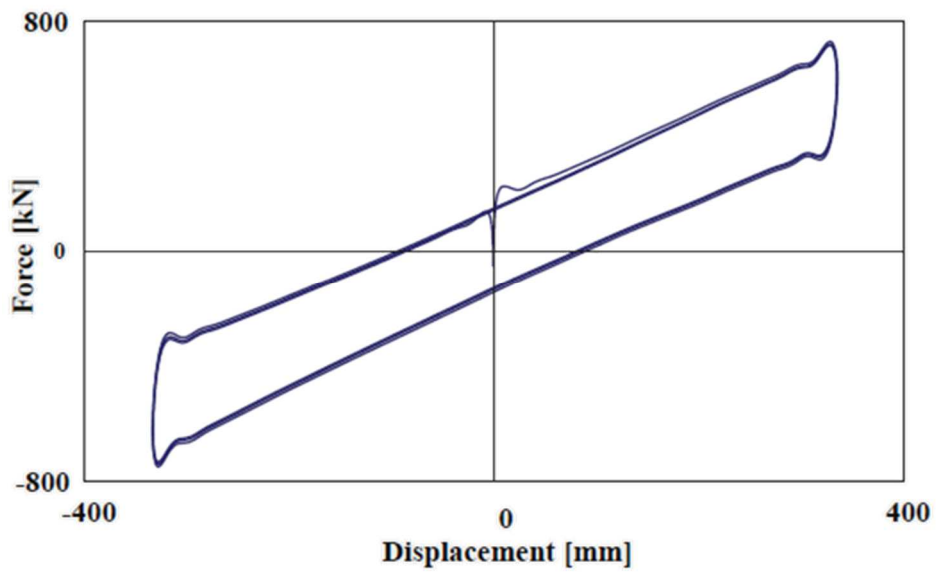


Figure 1.28 Experimental hysteresis loops of a double curved surface slider (FIP INDUSTRIALE)

1.3.2.3 Resilient-Friction Base Isolation system (RFBI)

The R-FBI device consists of a set of flat rings which can slide on each other with a central rubber core and/or peripheral rubber cores. Also, there is a very flexible rubber cover which protects the sliding rings from corrosion and dust. In order to reduce the friction, the sliding rings are teflon coated. The rubber cores help to distribute the lateral displacement and velocity along the height of the isolator, so that the velocity at each face is small, maintaining a low friction coefficient. The R-FBI is designed such that all the vertical load is carried entirely by the sliding elements, and no vertical load is carried by the rubber cores. Therefore, the R-FBI is very rigid in the vertical direction (Mostaghel et al. 1987).

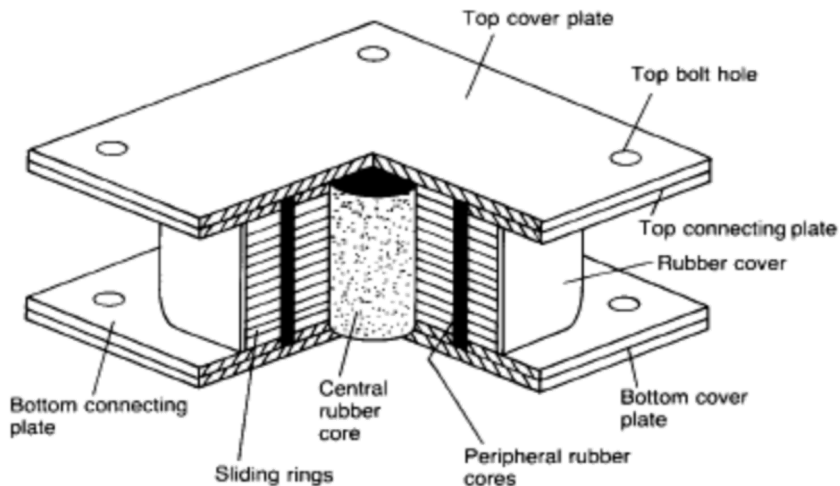


Figure 1.29 The R-FBI system (Mostaghel 1984)

1.3.2.4 *Electricité De France base isolation system (EDF)*

The EDF. system developed by “Electricité de France” (Gueraud et al. 1985) is constituted by an elastomeric device coupled to the top with a Pure Sliding Friction device design to have a coefficient of friction of 0.2 during the service life of the base isolation system. These devices were widely used in the 80s for protection of nuclear power plants in region of high seismicity. A peculiar behavior of these devices is that in the case of medium-low intensity earthquakes, only elastomeric activation is planned, while in the presence of earthquakes of greater intensity or abnormal earthquakes it is expected to activate FS device too.

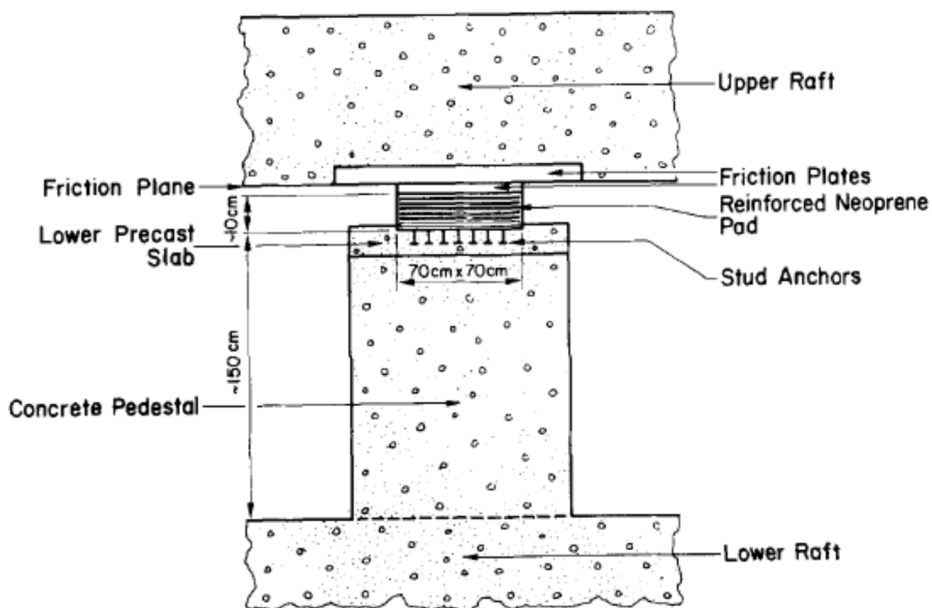


Figure 1.30 The EDF system (Gueraud, et al, 1985)

1.3.2.5 Sliding Resilient-Friction Base Isolation system (SR-F)

The SR-F device, designed in 1991 (Su et al. 1991), is the couple of an EDF and a R-FBI system. Practically, the elastomeric bearings of the EDF system is replaced by the R-FBI units so that the friction plate take the place of the upper surface of the R-FBI system. As a result, the structure can slide on its foundation just as in the EDF base-isolation system. The behavior of this base isolator, referred to as the sliding resilient-friction (SRF) base-isolation system, is schematically shown in Figure 1.31. For low level of seismic excitation, the system behaves as an R-FBI unit. The sliding at the top friction plate occurs only for very high levels of ground acceleration. This provides an additional safety measure for unexpectedly severe ground excitations.

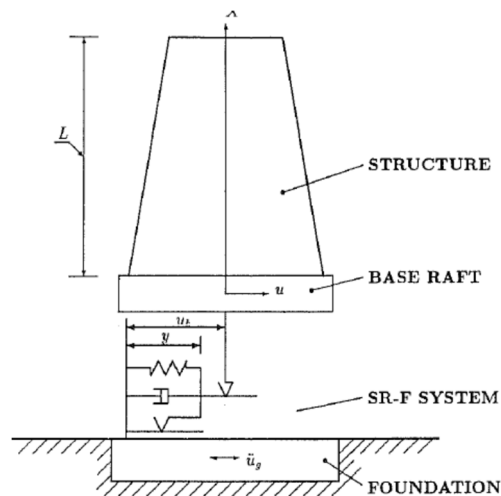


Figure 1.31 Schematic diagram of non uniform shear-beam structure with SR-F base isolator (Su et al. 1991)

1.3.2.6 Earthquake Engineering Research Center Base Isolation system (EERC)

A new base isolation system combining sliders, rubber bearings and tension devices was developed in 1990 (Chalhoub et al. 1990). The system was tested on the earthquake simulator at the University of California at Berkeley by installing it under the base of a one-fourth scale nine-story steel structure and subjecting it to different earthquake inputs. When sliding starts the rubber bearings provide additional stiffness and recentering. Under very severe inputs, the tension devices reach their locking limit and cause a large increase in the stiffness of the system. Areas of base shear hysteresis loops are drastically enlarged by the addition of sliders. Displacements are better controlled than the ones for a purely elastomeric isolation system. Vertical deflections due to large horizontal drift encountered in solely rubber systems are eliminated. The fail-safe capacity is provided by the tension restrainers and by the constant contact of the sliders with the base.

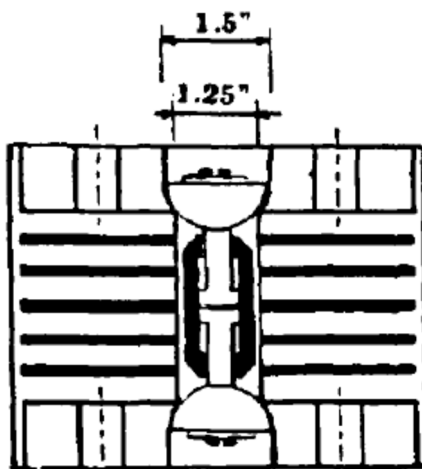


Figure 1.32 EERC isolation system (Chalhoub and Kelly 1990)

The tension device is better illustrated in Figure 1.33. The effect of the tension device on the force displacement loop is shown in Figure 1.34.

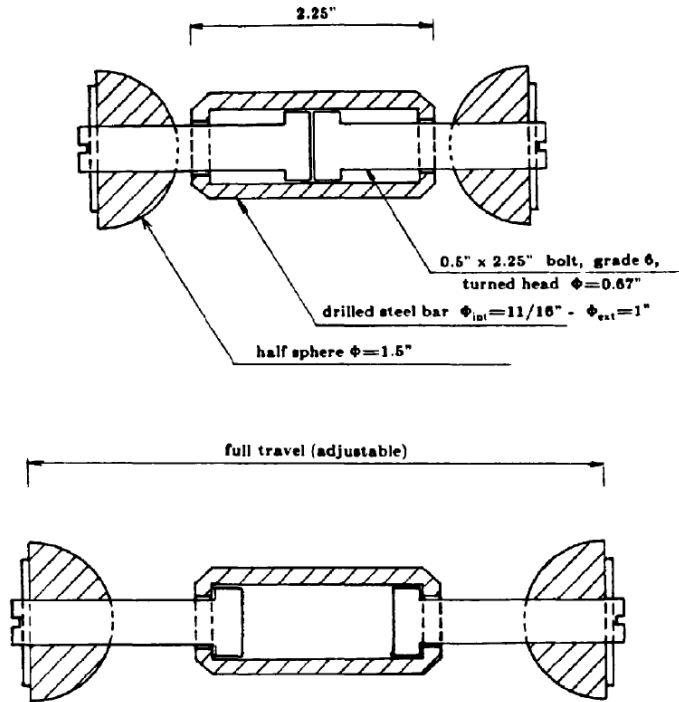


Figure 1.33 Tension restraint showing dimensions (Chalhoub and Kelly 1990)

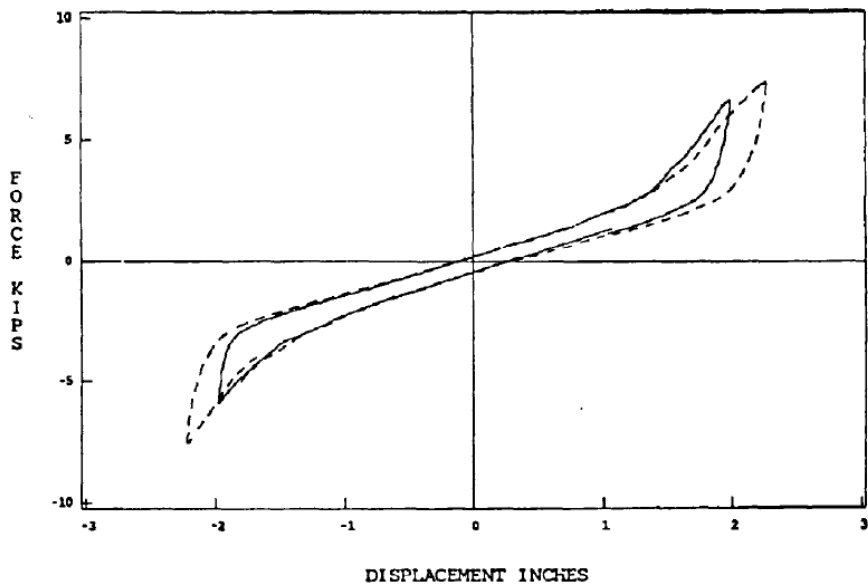


Figure 1.34 Effect of tension device in horizontal stiffness (Chalhoub and Kelly 1990)

1.3.2.7 Taisei Shake Suppression (TASS) base isolation system

The TAISEI Shake Suppression (TASS) system, developed by Taisei Corporation in Japan (Nagashima et al. 1987) is composed of a sliding bearings and horizontal spring beams (see Figure 1.35). Sliding bearing support the vertical loads on it and scarcely resists against horizontal force. Teflon or ball bearings are used for sliding bearings. Steel plates or bars are used for horizontal spring beams, horizontal spring beams connect the sliding floor to the base frame or building floor, and add the smack horizontal stiffness to the sliding floor. The system can be realized also with an elastic sliding bearings (the sliding surface is bonded to an elastomeric bearing) and neoprene bearings to provide the restoring force (Kelly 1990). The friction coefficient of the sliding interface is 0.1.

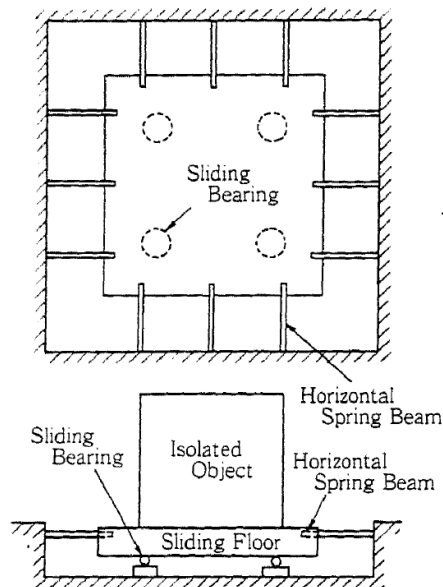


Figure 1.35 Schematic figure of TASS system (Nagashima et al. 1987)

1.3.2.8 Variable Friction Pendulum Isolation (VFPI) system

The VFPI is a modified form of FP that has oscillation frequency decreasing with sliding displacement, and the restoring force has an upper bound so that the force transmitted to the structure is limited (Panchal and Jangid 2008). The difference between FP and VFP is that the friction coefficient of FP is considered to be constant whereas the friction coefficient of VFP is varied in the form of a curve. Such variation of friction coefficient in VFP can be achieved by gradually varying the roughness of spherical surface. This isolation system retains the advantages of both PF isolation system and FP. The geometry of the isolator can be chosen to achieve a progressive period shift at different response levels. The VFPI thus combines the advantages of both FP and SD system. It is also found that VFPI behavior is stable at low intensity of excitations (as a high initial stiffness can be chosen). Furthermore, due to its force-softening characteristics, VFPI provides a fail-safe mechanism at high intensity of excitations without losing the ability to restore the structure close to its initial position.

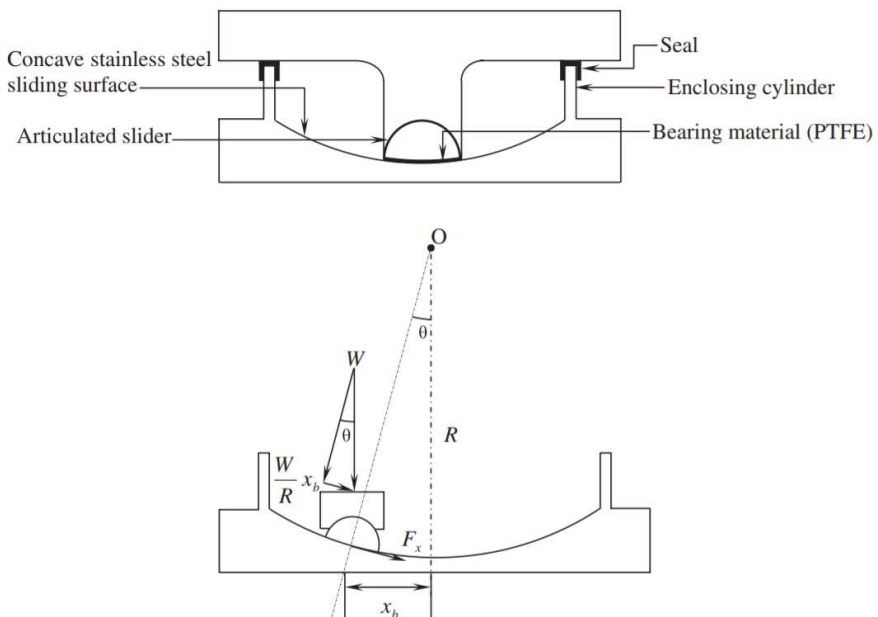


Figure 1.36 Details and operation of VFPI (Panchal and Jangid 2008)

1.3.2.9 The RoGlider Isolation system

The RoGlider is a sliding bearing which includes an elastic restoring force (Robinson 2006). The device is composed by two stainless steel plates with a PTFE ended puck sitting between the plates. Attached to the puck with each being joined to the top or bottom plates there are two rubber membranes. When the top and bottom plates slide away with respect to each other, the opposite parts of the rubber membrane goes in tension or in compression. The tension components is responsible of the restoring force between the plates while the rubber buckle when there is compression.

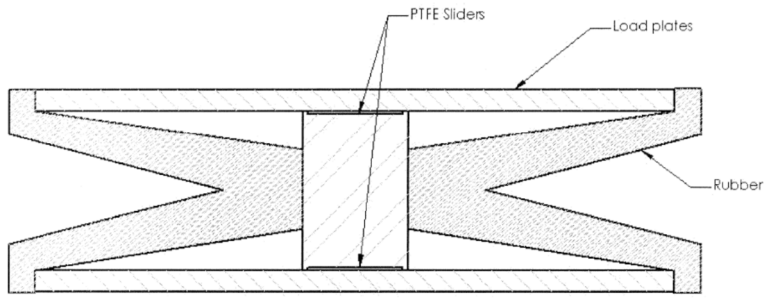


Figure 1.37 The RoGlider device (Robinson et al. 2006)

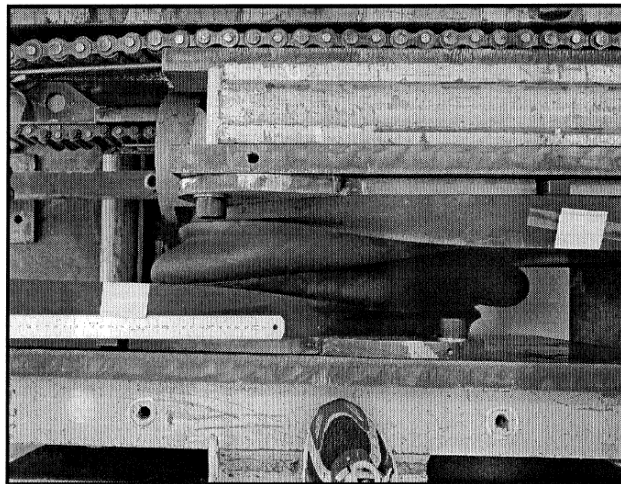


Figure 1.38 RoGlider during test displacement +575mm, vertical force of 110kN (Robinson et al. 2006)

As we can see from Figure 1.38, when the device is in use the elastomeric part is partially under a traction state. This is a very dangerous situation for the stability of the device. In Figure 1.39 and Figure 1.40 the force displacement loop of the RoGlider is shown for different values of the vertical force.

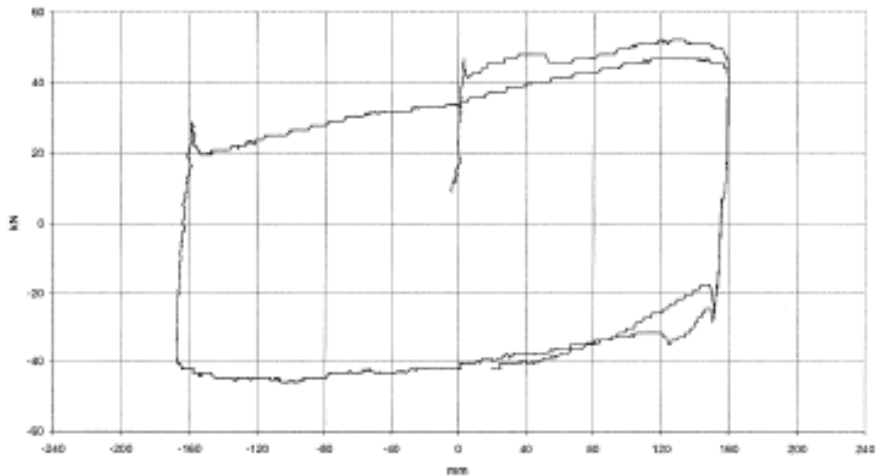


Figure 1.39 RoGlider force displacement curve – vertical force of 850 kN (Robinson *et al.* 2006)

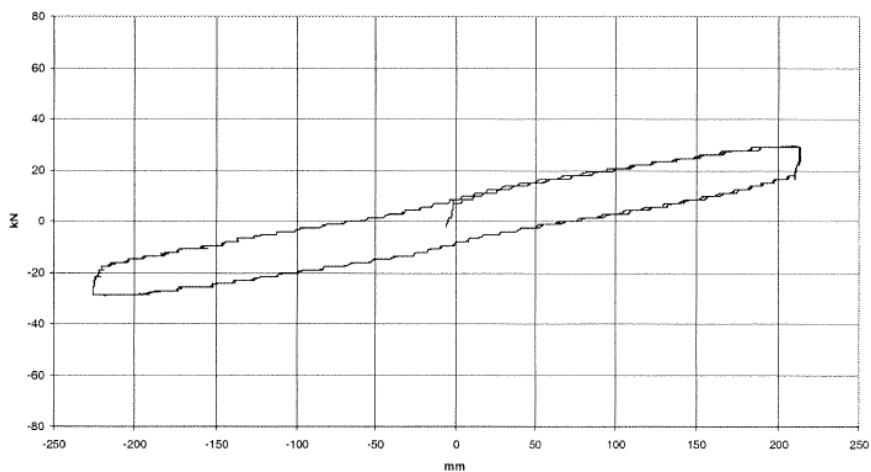


Figure 1.40 RoGlider force displacement curve – vertical force of 110 kN (Robinson *et al.* 2006)

1.3.2.10 High Damping Hybrid Seismic Isolator (HDHSI)

The HDHSI device is obtained by the assembly in series of a LRB and a FS with high friction coefficient (Cancellara and Pasquino 2011). The HDHSI device is in contrast to the R-FBI (Resilient-Friction Base Isolation) isolator and is the optimization of the EDF (Electricité De France) system. HDHSI devices can handle seismic events either expected that abnormal characterized as well as high intensity as well by impulsive actions such as earthquakes with near fault phenomena.

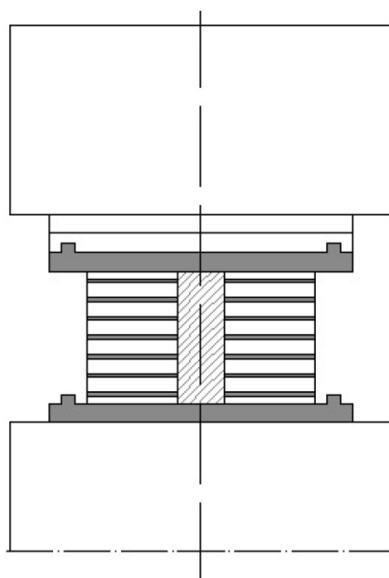


Figure 1.41 HDHSI system (Cancellara and Pasquino 2011)

It is interesting to note that this system is not a re-centering system. In presence of medium-low intensity earthquakes, it is predicted the activation only the LRB, whereas in presence of higher intensity earthquakes (included eventual anomalous seismic events which are not among those of design predicted by the rule for Ultimate Limit State) it is predicted the activation of FS isolator. The friction coefficient of FS will be chosen by the horizontal force limitation value which is transmitted to the superstructure (preferably between 10 and 20% of weight force of the whole structure). In Figure 1.42 the hysteretic cycles of the HDHSI are

shown starting from hysteretic cycles of single LRB and FS devices which compose it.

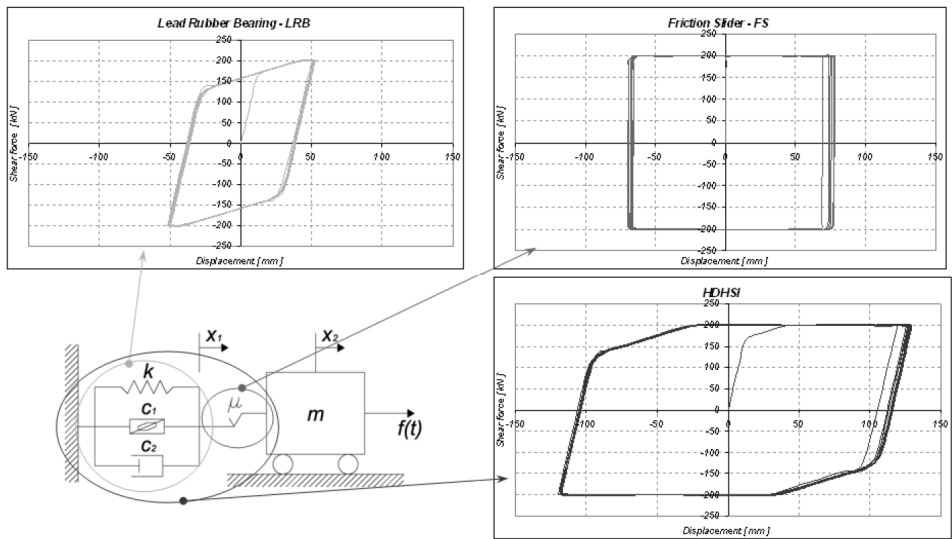


Figure 1.42 Hysteretic cycles of single components and the HDHSI device (Cancellara and Pasquino 2011)

1.3.3 Advantages and disadvantages

Table 1.1 summarizes the advantages and disadvantages of the most commonly used device types.

Device	Advantages	Disadvantages
Elastomeric	<ul style="list-style-type: none"> - Sufficient horizontal flexibility to increase the structural period - Low cost 	<ul style="list-style-type: none"> - Low resistance to service load - Low damping - Large displacement - No recentering mechanism - P-Delta influence
LRB	<ul style="list-style-type: none"> - High Damping due to the lead core - Resistance to service load - No need of other additional device - Sufficient horizontal flexibility to increase the structural period - Simple maintenance - Well known technology with many experimental applications - Wide range of stiffness and damping 	<ul style="list-style-type: none"> - Low Rubber durability - Cyclic change in properties - P-Delta influence - Recentering proprieties - Not for low-mass structures
HDRB	<ul style="list-style-type: none"> - High damping due to the additive proprieties of the rubber - Resistance to service load 	<ul style="list-style-type: none"> - Low Rubber durability - Strain dependent stiffness - Strain dependent damping - Limited choice of stiffness and damping

	<ul style="list-style-type: none"> - No need of other additional device - Sufficient horizontal flexibility to increase the structural period - Simple maintenance - Well known technology with many experimental applications - Recentering properties 	<ul style="list-style-type: none"> - P-Delta Influence - Complicated nonlinear analysis
Curved Sliders	<ul style="list-style-type: none"> - Period is independent from the mass of the structure - Good also for low-mass structures - High damping levels - Recentering proprieties - Resistance to service load - Relative wide range of damping - Small size - Low cost 	<ul style="list-style-type: none"> - Changing friction coefficient with temperature - Changing friction coefficient with vertical load - Increasing of the friction coefficient at the beginning and at the inversion of the motion - Uplifted structure with motion - High initial stiffness - Not uniform distribution of temperature on the sliding surface

Table 1.1 Advantage and disadvantage of commercial devices

1.4 Vertical isolation devices

Despite today's awareness that even vertical seismic action is not to be underestimated, vertical isolation devices are not diffused, but the need to protect particular structures, such as, for example, nuclear power plants, pushed researchers to be interested in the subject, producing ideas for the realization of studies or prototypes to solve this problem. Problems related to the development of this technology are related to large displacements, also induced in the only static condition, and to the introduction of a degree of vertical freedom and consequent rocking phenomenon (Forni 2011). To date, various vertical isolation devices have been proposed. These are mainly classified into three groups:

1. Active and semi-active devices that utilize hydraulic mechanisms or pneumatic suspension, which are expensive and bulky.
2. Passive devices with motion transformation, which alter the direction of motion, the period of such devices are limited within 2 seconds.
3. Passive devices with Euler springs, which reach a period of 3 seconds.

Among the various models and prototypes present in the literature we find:

- A passive pulse hydraulic device proposed in 2012 by Hui Zeng, Jingyi Zhao, and Kai Wang with auxiliary support function. During seismic action, the hydraulic fluid flows inside the system, thus dimming the system.(Zeng and al 2013).
- Xueyuan Yan, Jianping Wang, studied in 2014 a device that uses disk springs with external guide (Xueyuan at al 2014).

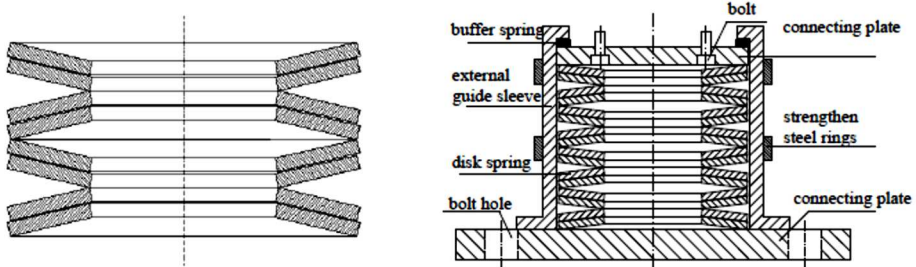


Figure 1.43 Xueyuan et al. service:combined shape of disk spring (left); Section of the vertical isolation system (right)

- In 2008, Takehiko Asai, Kyoto-Daigaku, Yoshikazu Araki, Takeshi Masui, Nobutoshi Yoshida proposed a device that leverages the combination of a constant and soft load (Asai et al. 2008).
- Magnetic leakage system proposed by Tsuda et al. in 2009.

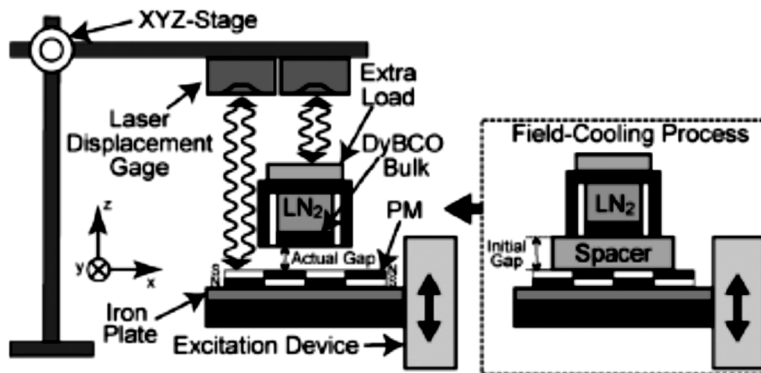


Figure 1.44 Magnetic leakage system schematic sketch (Tsuda et al. 2009)

- A nonlinear spring mechanism and magnetic damping on a guide designed by Masaharu et al. in 2007.

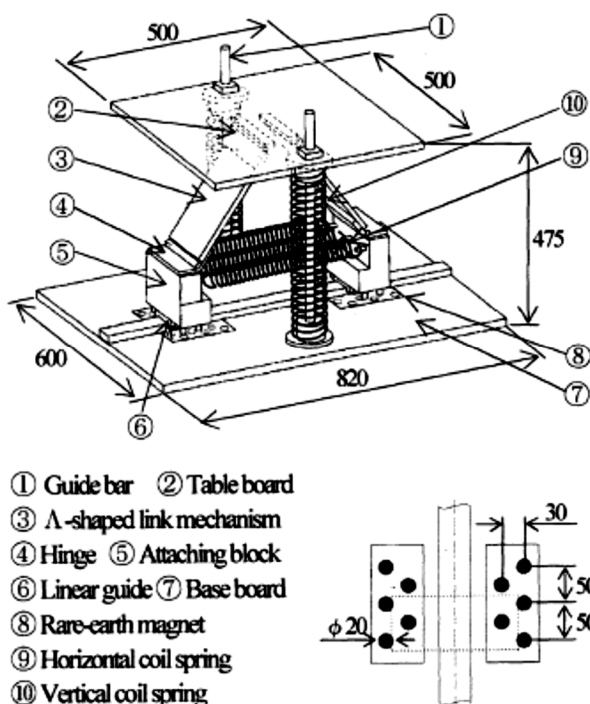


Figure 1.45 Model with non linear springs and magnetic damping (Masaharu et al. 2007)

A three-dimensional control system with helical springs and viscous dampers: the system has high flexibility both vertically and horizontally, which are independent of each other. The system has been applied to existing structures and produced a reduction in horizontal and vertical accelerations of 70% and 40%, respectively (Celia Gómez 2013, Daniel Siepe 2015).



Figure 1.46 Steel elicoidal spring (left) – Viscous damper (right)

In 2008 A. Kashiwazaki, R. Mita, T. Enomoto, M. Akimoto, proposed an improvement on a study of a 3D isolation system to be applied to nuclear power plants. The prototype was never applied causes vertical capacity and rocking phenomenon problems. The authors proposed to resolve it by integrating a hydraulic mechanism for reducing the phenomenon of rocking (Kashiwazaki et al. 2008).

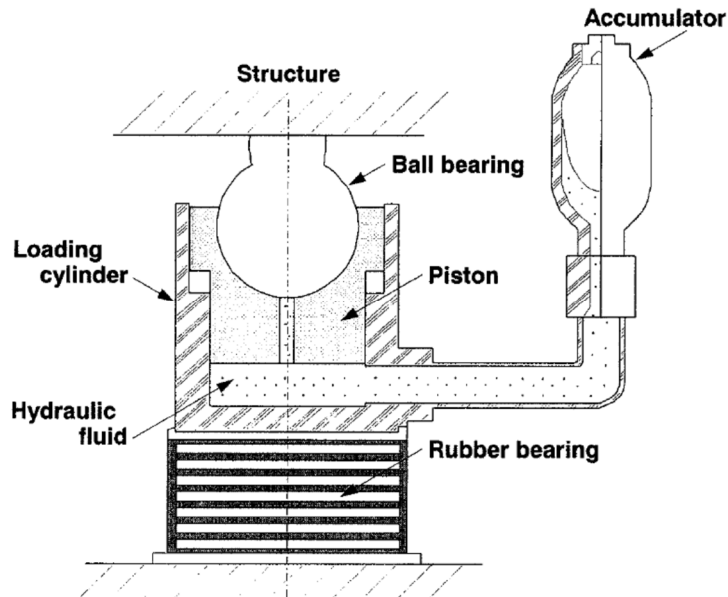


Figure 1.47 Tridimensional Seismic Device

Chapter 2

BEHAVIOR OF MATERIALS USED IN ISOLATION DEVICES

This chapter provides a description of the mechanical behavior of the material that are usually used for the commercial device. First of all, we give a short collects of preliminary definitions (Bonet and Wood 2008). We focus the attention, secondly, on hyperelastic materials, such us elastomers that are the main components of elastomeric devices, and thermoplastic materials, such us PTFE used in friction pendulum system.

Natural rubber is obtained by coagulation of a latex from a tree called *Hevea Brasiliensis*. It consists predominantly of *cis*-1,4-polyisoprene. Fossilised natural rubber discovered in Germany in 1924 stems back about 50 million years. Columbus learned during his second voyage to America about a game played by the natives of Haiti in which balls of an elastic ‘tree-resin’ were used. The word ‘rubber’ is derived from the ability of this material to remove (rub off) marks from paper, which was noted by Joseph Priestley in 1770. Rubber materials are not restricted to natural rubber. They include a great variety of synthetic polymers of similar properties. An elastomer is a polymer that exhibits rubber elastic properties, i.e. a material that can be stretched several times to its original length without breaking and which, upon release of the stress, immediately returns to its original length. Rubbers are almost elastic materials, i.e. their deformation is instantaneous and they show almost no creep.

Polytetrafluoroethylene (PTFE) is a synthetic polymer of tetrafluoroethylene. On the market it is possible to identify various brands of PTFE products, the most well-known is the Chemours Teflon. This material is a solid fluorocarbene because it is characterized by a high

molecular weight and is made up entirely of carbon and fluoride, furthermore it is hydrophobic. Being classifiable as a solid lubricant, of course, PTFE has a low friction coefficient which is one of the lowest coefficients of solid materials. It is less reactive due to the carbon-fluoride bond strength, so it is often used in chemical, reactive and corrosive chemical containers and pipes. The low coefficient of friction also makes this material suitable for reducing friction, wear and dissipation of energy in the industrial environment, although its applications are varied. PTFE was accidentally discovered in 1938 by Roy Plunkett while working in New Jersey for the DuPont company. The original goal was to create a new refrigerant clofluorocarbon. The main features of PTFE are:

- chemical inertia, so it is not attacked by almost all chemical compounds, except for some exceptions;
- insolubility in water and in organic solvents;
- excellent dielectric quality;
- fire resistant;
- lubricating properties;
- aging resistance;
- anti-adhesion and non-stick surface.

Therefore, it has great resistance to external agents and a high degree of resistance to low and high temperatures ($-200\text{ }^{\circ}\text{C}$ to $+260\text{ }^{\circ}\text{C}$). It is one of the most stable thermoplastic materials, since up to $260\text{ }^{\circ}\text{C}$ no particular structural decompositions are detected.

2.1 Preliminary definitions

A proper description of motion is fundamental to finite deformation analysis. We must always keep in mind that deformation is an aspect of kinematics and it must be studied in a manner completely independent from the causes of the motion. Deformation is typically seen as something "caused by stresses". This is a distorted view, which prevents a deep understanding of deformation and strain as kinematical quantities.

Kinematics is indeed the study of motion and deformation regardless of their causes. Thus, the study of the kinematics of continuum bodies (i.e., of motion and deformation) is completely independent of stress and external forces, exactly as the kinematics of particles is completely independent of forces.

Figure 2.1 shows the general motion of a deformable body. The body is imagined as being an assembly of material particles that are labeled by the coordinates X , with respect to Cartesian basis E_i , at their initial positions at time $t=0$. Generally, the current positions of these particles are located, at time t , by the coordinates x with respect to an alternative Cartesian basis e_i . In the remainder of this chapter we assume that the bases E_i and e_i will be coincident. However, the notational distinction between E_i and e_i will be retained in order to identify the association of quantities with initial or current configurations.

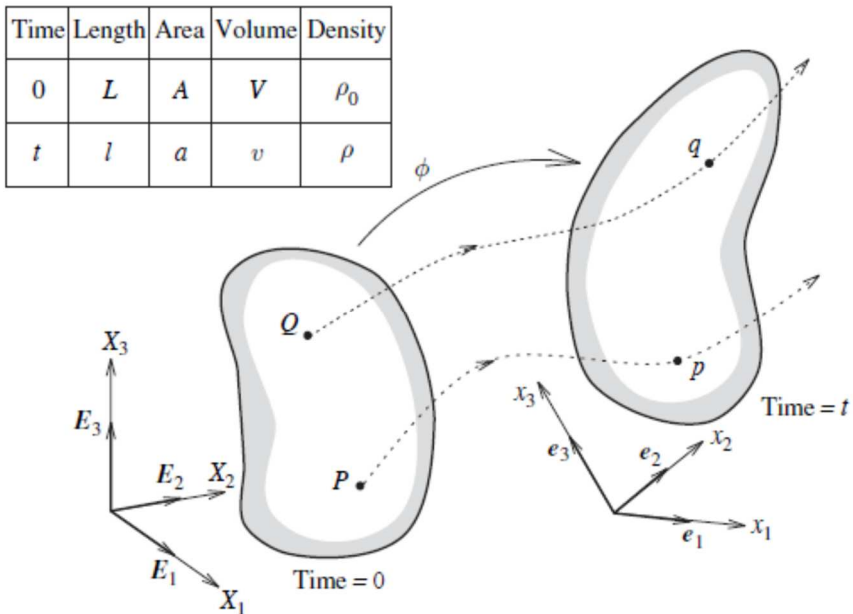


Figure 2.1 General Motion of a deformable body (Bonet and Wood 2008)

The motion can be mathematically described by a mapping ϕ between initial and current particle positions as

$$x = \phi(\mathbf{X}, t) . \quad (2.1)$$

For a fixed value of t the above equation represent a mapping between the undeformed and deformed bodies. Additionally, for a fixed particle \mathbf{X} , equation (2.1) describes the motion or trajectory of this particle as a function of time. In finite deformation analysis no assumptions are made regarding the magnitude of the displacement $\mathbf{x} - \mathbf{X}$, indeed the displacement may well be of the order or even exceed the initial dimensions of the body as is the case, for example, in metal forming. In infinitesimal deformation analysis the displacement $\mathbf{x} - \mathbf{X}$ is assumed to be small in comparison with the dimensions of the body, and geometrical changes are ignored.

2.1.1 Deformation gradient

In finite deformation analysis a key quantity is the deformation gradient \mathbf{F} , which is involved in all equations relating quantities before deformation to corresponding quantities after deformation. The deformation gradient tensor enables the relative spatial position of two neighboring particles after deformation, to be described in terms of their relative material positions before deformation. Consequently, it is central for the description of deformation and hence strain.

Consider two material particles Q_1 and Q_2 in the neighborhood of a material particle P (Figure 2.2). The positions of Q_1 and Q_2 relative to P are given by the elemental vectors $d\mathbf{X}_1$ and $d\mathbf{X}_2$ as:

$$d\mathbf{X}_1 = \mathbf{X}_{Q_1} - \mathbf{X}_P; \quad d\mathbf{X}_2 = \mathbf{X}_{Q_2} - \mathbf{X}_P . \quad (2.2)$$

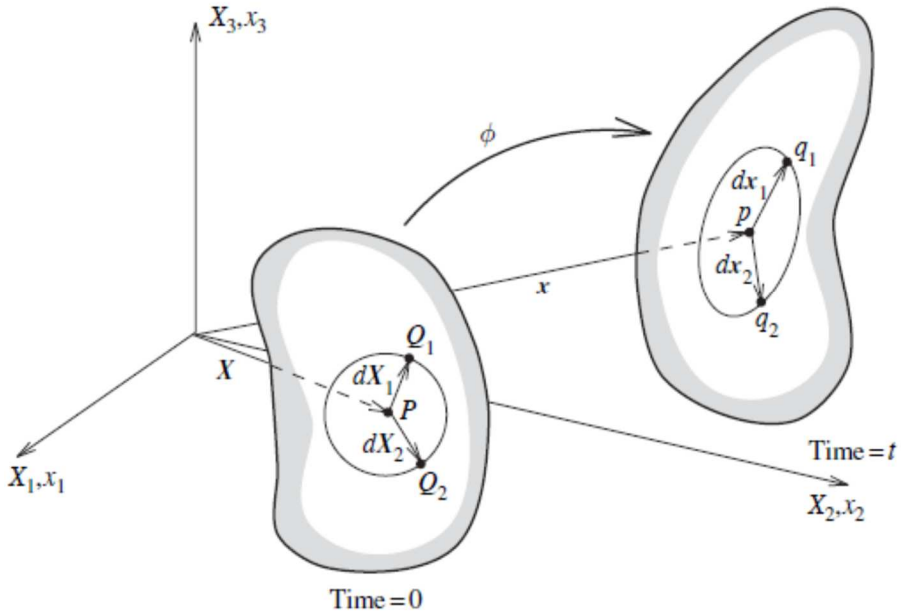


Figure 2.2 General motion in the neighborhood of a particle (Bonet and Wood 2008)

After deformation, the material particles P , Q_1 and Q_2 have been deformed to current spatial positions given by the mapping (Figure 2.2) as

$$\mathbf{x}_p = \phi(\mathbf{X}_p, t); \quad \mathbf{x}_{q_1} = \phi(\mathbf{X}_{q_1}, t); \quad \mathbf{x}_{q_2} = \phi(\mathbf{X}_{q_2}, t); \quad (2.3)$$

and the corresponding elemental vectors become

$$d\mathbf{x}_1 = \mathbf{x}_{q_1} - \mathbf{x}_p = \phi(\mathbf{X}_p + d\mathbf{X}_1, t) - \phi(\mathbf{X}_p, t) \quad (2.4)$$

$$d\mathbf{x}_2 = \mathbf{x}_{q_2} - \mathbf{x}_p = \phi(\mathbf{X}_p + d\mathbf{X}_2, t) - \phi(\mathbf{X}_p, t). \quad (2.5)$$

Defining the *deformation gradient tensor* \mathbf{F} as:

$$\mathbf{F} = \frac{\partial \phi}{\partial \mathbf{X}} = \nabla_0 \phi, \quad (2.6)$$

where ∇_0 denotes the gradient with respect to the material configuration. The elemental vectors $d\mathbf{x}_1$ and $d\mathbf{x}_2$ can be obtained in terms of $d\mathbf{X}_1$ and $d\mathbf{X}_2$ as:

$$d\mathbf{x}_1 = \mathbf{F}d\mathbf{X}_1; \quad d\mathbf{x}_2 = \mathbf{F}d\mathbf{X}_2. \quad (2.7)$$

Note that \mathbf{F} transforms vectors in the initial or reference configuration into vectors in the current configuration and it is therefore said to be a *two-point* tensor.

2.1.2 Strain

As a general measure of deformation, we will consider the change in the scalar product of the two elemental vectors $d\mathbf{X}_1$ and $d\mathbf{X}_2$ shown in Figure 2.2 as they deform to $d\mathbf{x}_1$ and $d\mathbf{x}_2$. This change will involve both the stretching (that is, change in length) and changes in the enclosed angle between the two vectors. Recalling Equation (2.7) the spatial scalar product $d\mathbf{x}_1 \cdot d\mathbf{x}_2$ can be found in terms of the material vectors $d\mathbf{X}_1$ and $d\mathbf{X}_2$ as:

$$d\mathbf{x}_1 \cdot d\mathbf{x}_2 = d\mathbf{X}_1 \cdot \mathbf{B} d\mathbf{X}_2 \quad (2.8)$$

where \mathbf{B} is the right *Cauchy–Green deformation tensor*, which is given in terms of the deformation gradient as \mathbf{F}

$$\mathbf{B} = \mathbf{F}^T \mathbf{F}. \quad (2.9)$$

Note that in Equation (2.9) the tensor \mathbf{B} operates on the material vectors $d\mathbf{X}_1$ and $d\mathbf{X}_2$ and consequently \mathbf{B} is called a material tensor quantity.

Alternatively, the initial material scalar product $d\mathbf{X}_1 \cdot d\mathbf{X}_2$ can be obtained in terms of the spatial vectors dx_1 and dx_2 via the *left Cauchy–Green* or *Finger tensor* \mathbf{b} as

$$d\mathbf{X}_1 \cdot d\mathbf{X}_2 = dx_1 \cdot \mathbf{b}^{-1} dx_2, \quad (2.10)$$

where \mathbf{b} is:

$$\mathbf{b} = \mathbf{F}\mathbf{F}^T. \quad (2.11)$$

In equation (2.10) \mathbf{b}^{-1} operates on the spatial vectors dx_1 and dx_2 , and consequently \mathbf{b}^{-1} , or indeed \mathbf{b} itself, is a spatial tensor quantity. Now the change in scalar product can be found in terms of the material vectors $d\mathbf{X}_1$ and $d\mathbf{X}_2$ and the *Lagrangian or Green strain tensor* \mathbf{E} as:

$$\frac{1}{2}(dx_1 \cdot dx_2 - d\mathbf{X}_1 \cdot d\mathbf{X}_2) = d\mathbf{X}_1 \cdot \mathbf{E} d\mathbf{X}_2, \quad (2.12)$$

where \mathbf{E} is the material tensor, defined as:

$$\mathbf{E} = \frac{1}{2}(\mathbf{B} - \mathbf{I}). \quad (2.13)$$

Alternatively, the same change in scalar product can be expressed with reference to the spatial elemental vectors dx_1 and dx_2 and the *Eulerian or Almansi strain tensor* \mathbf{e} as:

$$\frac{1}{2}(dx_1 \cdot dx_2 - d\mathbf{X}_1 \cdot d\mathbf{X}_2) = dx_1 \cdot \mathbf{e} dx_2, \quad (2.14)$$

where \mathbf{e} is the material tensor, defined as:

$$\mathbf{e} = \frac{1}{2}(\mathbf{I} - \mathbf{b}^{-1}). \quad (2.15)$$

The general nature of the scalar product as a measure of deformation can be clarified by taking $d\mathbf{X}_1$ and $d\mathbf{X}_2$ equal to $d\mathbf{X}$ and consequently dx_1 and dx_2 equal to $d\mathbf{x}$.

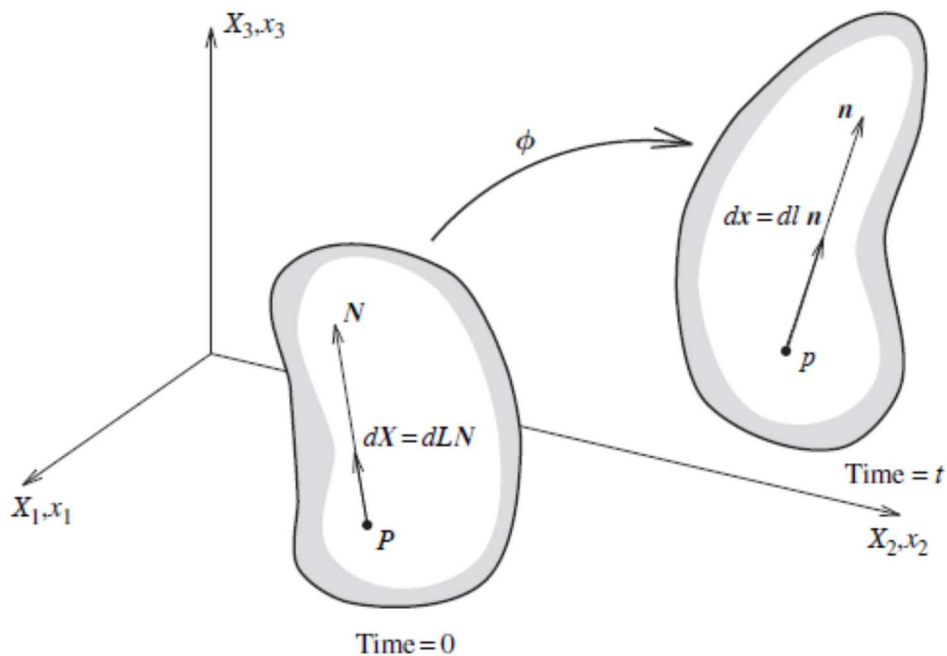


Figure 2.3 Change in length (Bonet and Wood 2008)

This enables initial (material) and current (spatial) elemental lengths squared to be determined as (Figure 2.3):

$$dL^2 = d\mathbf{X} \cdot d\mathbf{X}; \quad dl^2 = d\mathbf{x} \cdot d\mathbf{x}. \quad (2.16)$$

The change in the squared lengths, that occurs as the body deforms from the initial to the current configuration, can now be written in terms of the elemental material vector $d\mathbf{X}$ as:

$$\frac{1}{2}(dl^2 - dL^2) = d\mathbf{X} \cdot \mathbf{E} d\mathbf{X}; \quad (2.17)$$

which, after division by dL^2 , gives the scalar *Green's strain* as:

$$\frac{dl^2 - dL^2}{2dL^2} = \frac{d\mathbf{X}}{dL} \cdot \mathbf{E} \frac{d\mathbf{X}}{dL}; \quad (2.18)$$

where $d\mathbf{X}/dL$ is a unit material vector \mathbf{N} in the direction of $d\mathbf{X}$, hence, finally:

$$\frac{1}{2} \frac{dl^2 - dL^2}{dL^2} = \mathbf{N} \cdot \mathbf{E} \mathbf{N}. \quad (2.19)$$

Introducing the unit vector \mathbf{n} in the direction of $d\mathbf{x}$, a similar expression can be derived using the *Almansi strain tensor*:

$$\frac{1}{2} \frac{dl^2 - dL^2}{dL^2} = \mathbf{n} \cdot \mathbf{e} \mathbf{n}. \quad (2.20)$$

Let us consider an infinitesimal volume element in the material configuration with edges parallel to the Cartesian axes given by $d\mathbf{X}_1 = \mathbf{E}_1 dX_1$, $d\mathbf{X}_2 = \mathbf{E}_2 dX_2$ and $d\mathbf{X}_3 = \mathbf{E}_3 dX_3$, where \mathbf{E}_1 , \mathbf{E}_2 and \mathbf{E}_3 are the orthogonal unit vectors (Figure 2.4).

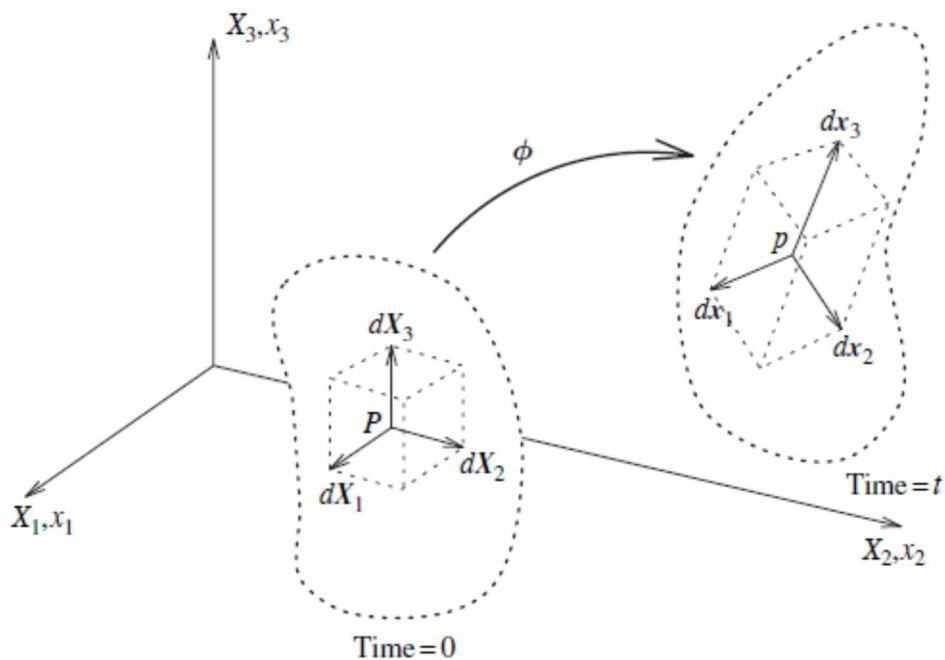


Figure 2.4 Volume change (Bonet and Wood 2008)

The elementary material volume dV defined by these three vectors is given as

$$dV = dX_1 dX_2 dX_3. \quad (2.21)$$

In order to obtain the corresponding deformed volume, dv , in the spatial configuration, using equations (2.6) and (2.7), we can write as follows:

$$dx_1 = \mathbf{F}d\mathbf{X}_1 = \frac{\partial \phi}{\partial X_1} dX_1 \quad (2.22)$$

$$dx_2 = \mathbf{F}d\mathbf{X}_2 = \frac{\partial \phi}{\partial X_2} dX_2 \quad (2.23)$$

$$dx_3 = \mathbf{F}d\mathbf{X}_3 = \frac{\partial \phi}{\partial X_3} dX_3. \quad (2.24)$$

The triple product of these vectors gives the deformed volume as:

$$dv = d\mathbf{x}_1 \cdot (d\mathbf{x}_2 \times d\mathbf{x}_3) = \frac{\partial \phi}{\partial X_1} \left(\frac{\partial \phi}{\partial X_2} \times \frac{\partial \phi}{\partial X_3} \right) dX_1 dX_2 dX_3. \quad (2.25)$$

the above triple product is the determinant of \mathbf{F} that gives the volume change in terms of the Jacobian J as

$$dv = JdV; \quad J = \det \mathbf{F}. \quad (2.26)$$

Finally, the element of mass can be related to the volume element in terms of the initial and current densities as:

$$dm = \rho_0 dV = \rho dv. \quad (2.27)$$

Hence, the conservation of mass or continuity equation can be expressed as

$$\rho_0 = \rho J. \quad (2.28)$$

2.1.3 Velocity and velocity gradient

Many nonlinear processes are time-dependent, consequently it is necessary to consider the velocity of various quantities. However, even if the process is not rate-dependent, it is nevertheless convenient to establish the equilibrium equations in terms of virtual velocities and associated virtual time-dependent quantities. For this purpose we consider the usual motion of the body given by Equation (2.1) as

$$\mathbf{x} = \phi(\mathbf{X}, t) \quad (2.29)$$

from which the velocity of a particle is defined as the time derivative of ϕ as:

$$\mathbf{v}(\mathbf{X}, t) = \frac{\partial \phi(\mathbf{X}, t)}{\partial t} \quad (2.30)$$

a spatial vector despite the fact that the equation has been expressed in terms of the material coordinates of the particle \mathbf{X} . In fact, by inverting equation (2.30) the velocity can be more consistently expressed as a function of the spatial position \mathbf{x} and time as

$$\mathbf{v}(\mathbf{x}, t) = \mathbf{v}(\phi^{-1}(\mathbf{x}, t), t). \quad (2.31)$$

Velocity was expressed in Equation (2.31) as a function of the spatial coordinates as $\mathbf{v}(\mathbf{x}, t)$. The derivative of this expression with respect to the spatial coordinates defines the *velocity gradient tensor* \mathbf{l} as

$$\mathbf{l} = \frac{\partial \mathbf{v}(\mathbf{x}, t)}{\partial \mathbf{x}} = \nabla \mathbf{v}. \quad (2.32)$$

This is clearly a spatial tensor, which gives the relative velocity of a particle currently at point q with respect to a particle currently at p as $d\mathbf{v} = \mathbf{l}d\mathbf{x}$.

The tensor \mathbf{l} enables the time derivative of the deformation gradient to be more usefully written as:

$$\dot{\mathbf{F}} = \frac{\partial \mathbf{v}}{\partial \mathbf{X}} = \frac{\partial \mathbf{v}}{\partial \mathbf{x}} \frac{\partial \phi}{\partial \mathbf{X}} = \mathbf{l}\mathbf{F}. \quad (2.33)$$

From which:

$$\mathbf{l} = \dot{\mathbf{F}}\mathbf{F}^{-1}. \quad (2.34)$$

2.1.4 Deformation rate

Consider again the initial elemental vectors $d\mathbf{X}_1$ and $d\mathbf{X}_2$ and their corresponding pushed forward spatial counterparts dx_1 and dx_2 given as (Figure 2.5)

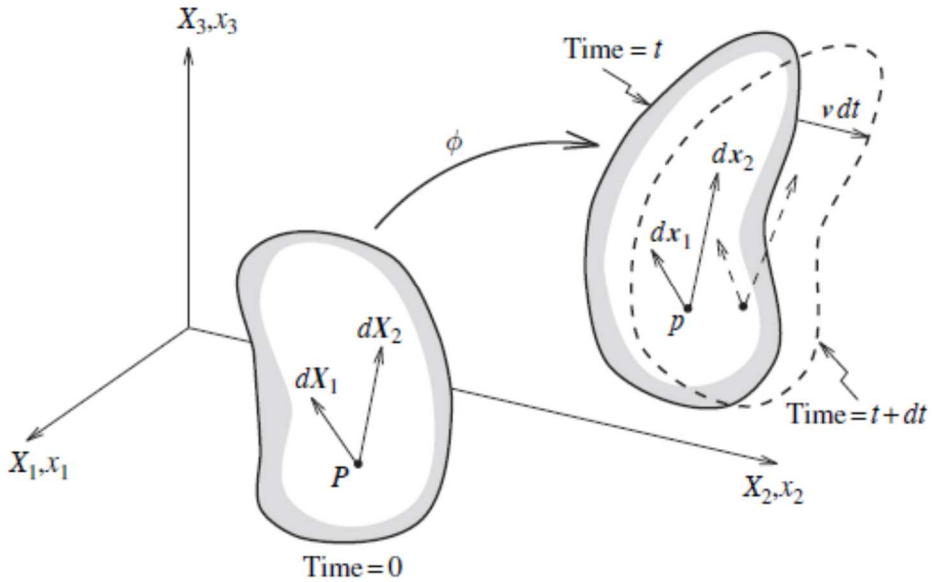


Figure 2.5 Rate of deformation (Bonet and Wood 2008)

$$dx_1 = FdX_1; \quad dx_2 = FdX_2. \quad (2.35)$$

In the previous paragraphs, strain was defined and measured as the change in the scalar product of two arbitrary vectors. Similarly, strain rate can now be defined as the rate of change of the scalar product of any pair of vectors. For the purpose of measuring this rate of change, the current scalar product could be expressed in terms of the material vectors $d\mathbf{X}_1$ and $d\mathbf{X}_2$ (which are not functions of time) and the time-dependent right *Cauchy–Green tensor* \mathbf{B} as

$$dx_1 \cdot dx_2 = d\mathbf{X}_1 \cdot \mathbf{B}d\mathbf{X}_2. \quad (2.36)$$

Differentiating this expression with respect to time and recalling the relationship between the Lagrangian strain tensor \mathbf{E} and the right Cauchy–Green tensor as $2\mathbf{E} = (\mathbf{B} - \mathbf{I})$ we give the current rate of change of the scalar product in terms of the initial elemental vectors as

$$\frac{d}{dt}(d\mathbf{x}_1 \cdot d\mathbf{x}_2) = d\mathbf{X}_1 \cdot \dot{\mathbf{B}}d\mathbf{X}_2 = 2d\mathbf{X}_1 \cdot \dot{\mathbf{E}}d\mathbf{X}_2, \quad (2.37)$$

where $\dot{\mathbf{E}}$, known as the *material strain rate tensor*, is the derivative with respect to time and can be obtained as follows:

$$\dot{\mathbf{E}} = \frac{1}{2}\dot{\mathbf{B}} = \frac{1}{2}(\dot{\mathbf{F}}^T \mathbf{F} + \mathbf{F}^T \dot{\mathbf{F}}). \quad (2.38)$$

The material strain rate tensor, $\dot{\mathbf{E}}$, gives the current rate of change of the scalar product in terms of the initial elemental vectors. Alternatively, it is possible to express the same rate of change in terms of the current spatial vectors. For this purpose, Equations (2.36) can be inverted as:

$$d\mathbf{X}_1 = \mathbf{F}^{-1}d\mathbf{x}_1; \quad d\mathbf{X}_2 = \mathbf{F}^{-1}d\mathbf{x}_2. \quad (2.39)$$

Introducing these expressions into equation (2.37), it gives the rate of change of the scalar product in terms of $d\mathbf{x}_1$ and $d\mathbf{x}_2$ as

$$\frac{1}{2} \frac{d}{dt}(d\mathbf{x}_1 \cdot d\mathbf{x}_2) = d\mathbf{x}_1 (\mathbf{F}^{-T} \dot{\mathbf{E}} \mathbf{F}^{-1}) d\mathbf{x}_2. \quad (2.40)$$

The tensor in the expression on the right-hand side is simply the pushed forward spatial counterpart of $\dot{\mathbf{E}}$ and it is known as the *rate of deformation tensor* \mathbf{d} given as:

$$\mathbf{d} = \mathbf{F}^{-T} \dot{\mathbf{E}} \mathbf{F}^{-1}. \quad (2.41)$$

We can also express the tensor \mathbf{d} as the symmetric part of \mathbf{l} as:

$$\mathbf{d} = \frac{1}{2}(\mathbf{l} + \mathbf{l}^T) . \quad (2.42)$$

2.1.5 Stress representation

In this paragraph we will introduce the stress and equilibrium concepts for a deformable body undergoing a finite motion. Stress is defined first in the current configuration in the standard way as force per unit area. This leads to the well-known Cauchy stress tensor as used in linear analysis. Then we will then derive the differential equations enforcing translational and rotational equilibrium and the equivalent principle of virtual work.

In contrast to linear small displacement analysis, stress quantities that refer back to the initial body configuration can also be defined. This will be achieved using work conjugacy concepts that will lead to the Piola–Kirchhoff stress tensors and alternative equilibrium equations.

2.1.5.1 *Cauchy stress tensor*

Consider a general deformable body at its current position as shown in Figure 2.6. In order to develop the concept of stress it is necessary to study the action of the forces applied by one region R_1 of the body on the remaining part R_2 of the body with that one is in contact.

For this purpose consider the element of area Δa normal to \mathbf{n} in the neighborhood of spatial point p shown in Figure 2.6. If the resultant force on this area is $\Delta \mathbf{p}$, the traction vector \mathbf{t} corresponding to the normal \mathbf{n} at p is defined as

$$\mathbf{t}(\mathbf{n}) = \lim_{\Delta a \rightarrow 0} \frac{\Delta \mathbf{p}}{\Delta a} , \quad (2.43)$$

where the relationship between \mathbf{t} and \mathbf{n} must be such that it satisfies Newton’s third law of action and reaction.

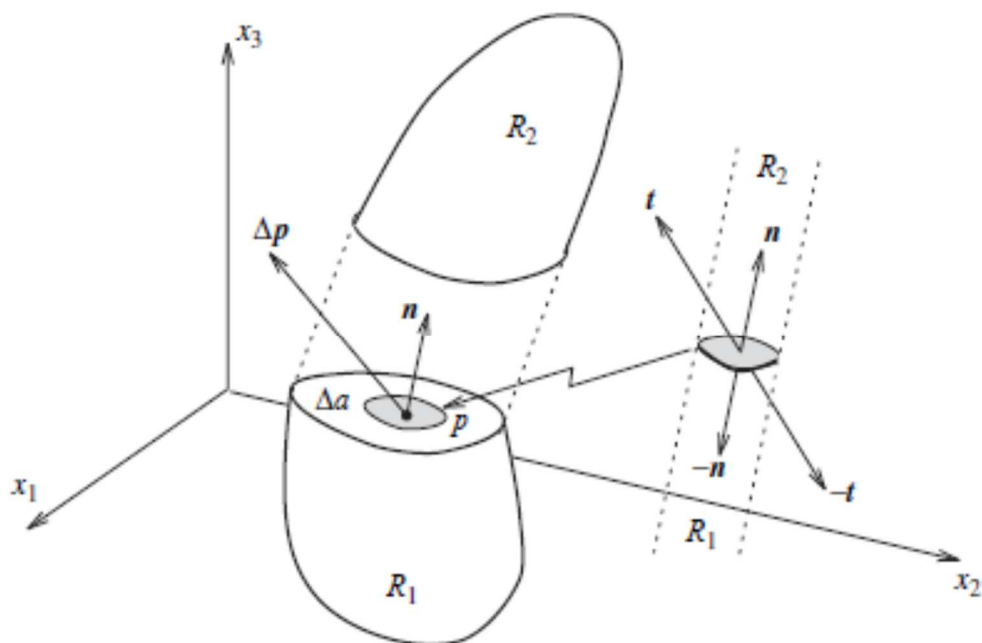


Figure 2.6 Traction vector (Bonet and Wood 2008)

To develop the idea of a stress tensor, let the three traction vectors associated with the three Cartesian directions e_1 , e_2 , and e_3 be expressed in a component form. These leads to the classical definition of the *Cauchy stress tensor* $\boldsymbol{\sigma}$ as:

$$\mathbf{t}(n) = \boldsymbol{\sigma} n. \quad (2.44)$$

2.1.5.2 The Kirchhoff stress tensor

The internal virtual work made by the stresses is expressed as:

$$\delta W_{\text{int}} = \int_v \boldsymbol{\sigma} : \delta \mathbf{d} dv. \quad (2.45)$$

This internal virtual work can be expressed in terms of the Kirchhoff stress tensor $\boldsymbol{\tau}$, using the relationship $dv = JdV$ as:

$$\delta W_{\text{int}} = \int_{\mathcal{v}} \boldsymbol{\tau} : \delta \mathbf{d} dV \quad (2.46)$$

$$\boldsymbol{\tau} = J \boldsymbol{\sigma} . \quad (2.47)$$

This equation reveals that the Kirchhoff stress tensor is work conjugate to the rate of deformation tensor with respect to the initial volume.

2.1.5.3 *The First Piola–Kirchhoff stress tensor*

The crude transformation resulted in the internal virtual work given above is not entirely satisfactory because it still relies on the spatial quantities $\boldsymbol{\tau}$ and \mathbf{d} . To alleviate this lack of consistency, note that the symmetry of $\boldsymbol{\sigma}$ together with equation (2.34) for l in terms of $\dot{\mathbf{F}}$ and the properties of the trace gives

$$\delta W_{\text{int}} = \int_{\mathcal{v}} J \boldsymbol{\sigma} : \delta l dV = \int_{\mathcal{v}} J \boldsymbol{\sigma} : (\delta \dot{\mathbf{F}} \mathbf{F}) dV . \quad (2.48)$$

We observe from this equality that the stress tensor work conjugate to the rate of the deformation gradient $\dot{\mathbf{F}}$ is the so-called *First Piola–Kirchhoff* stress tensor given as

$$\mathbf{P} = J \boldsymbol{\sigma} \mathbf{F}^{-T} . \quad (2.49)$$

To understand the physical meaning of the Cauchy stresses and thence the first Piola–Kirchhoff stress tensor consider an element of force $d\mathbf{p}$ acting on an element of area $d\mathbf{a} = \mathbf{n} da$. In the spatial configuration can be written as

$$d\mathbf{p} = \mathbf{t} da = \boldsymbol{\sigma} da . \quad (2.50)$$

The Cauchy stresses give the current force per unit deformed area, which is the familiar description of stress. The quantity $d\mathbf{p}$ can be rewritten in terms of the non deformed area corresponding to give an expression involving the first Piola–Kirchhoff stresses as

$$d\mathbf{p} = J\boldsymbol{\sigma}\mathbf{F}^{-T}d\mathbf{A} = \mathbf{P}d\mathbf{A} \quad (2.51)$$

This equation reveals that \mathbf{P} , like \mathbf{F} , is a two-point tensor that relates an area vector in the initial configuration to the corresponding force vector in the current configuration. Consequently, the first Piola–Kirchhoff stresses can be loosely interpreted as the current force per unit of non deformed area.

2.1.5.4 *The Second Piola–Kirchhoff stress tensor*

The first Piola–Kirchhoff tensor \mathbf{P} is an unsymmetric two-point tensor and as such is not completely related to the material configuration. It is possible to contrive a totally material symmetric stress tensor, known as the second Piola–Kirchhoff stress $\boldsymbol{\Sigma}_{II}$, by pulling back the spatial element of force $d\mathbf{p}$ from equation (2.51) to give a material force vector $d\mathbf{P}$ as

$$d\mathbf{P} = \mathbf{F}^{-1}d\mathbf{p} . \quad (2.52)$$

Substituting from equation (2.52) then $d\mathbf{p}$ gives the transformed

$$d\mathbf{P} = \boldsymbol{\Sigma}_{II}d\mathbf{A} \quad (2.53)$$

and

$$\boldsymbol{\Sigma}_{II} = J\mathbf{F}^{-1}\boldsymbol{\sigma}\mathbf{F}^{-T} . \quad (2.54)$$

2.2 ELASTOMER: an hyperelastic material

A material is elastic if its response function can be derived from the elastic energy accumulated during a training process. This is a potential scalar that depends on the state of the material and equals the deformation work. The elasticity of a generic material is generally manifested by small deformations, while some materials retain elastic behavior even for large deformations, but in this case the behavior is strongly nonlinear. These materials are called hyperelastic, and it is impossible to apply Hooke's law to describe their behavior. Such materials, among which elastomers are found, are described by going to determine an appropriate shape for the elastic potential function.

Elastomers belong to the class of hyperelastic materials, and are very often used in the industrial field. These materials exhibit elastic behavior but a strongly nonlinear stress-strain curve. The constitutive law of this materials is complex to determine, so there are numerous studies and models proposed to study such behavior. Therefore, it is necessary to define a constitutive law that also applies to large deformations and displacements (Rubin 2009). It is possible to express the deformation work through the Green Lagrange deformation tensor. The work of deformation, however, must be expressed through the second tensor of Piola-Kirchhoff, since this must prove to be an energetically-coupled effort measure with the Green-Lagrange tensor. Piola-Kirchhoff's tensor is linked to the Cauchy tensor, which represents the undeformed section, so the current configuration is considered through the expression:

$$\Sigma_{II} = JF^{-1}\boldsymbol{\sigma}F^{-T}, \quad (2.55)$$

where F is the deformation gradient, J is its determinant and $\boldsymbol{\sigma}$ is the Cauchy stress tensor. J represents the relationship between the volume of the material in the deformed configuration and the original configuration, and can be expressed by:

$$J = \frac{dv}{dV} . \quad (2.56)$$

The deformation work in the unit volume, for an increment of deformation $d\mathbf{E}$ will be:

$$\frac{dL_D}{dV} = l_D = \boldsymbol{\Sigma}_{II} : d\mathbf{E} , \quad (2.57)$$

where the scalar product is represented by the “:” that correspond to multiplying each other the identical terms of the two tensor $\boldsymbol{\Sigma}_{II}$ and \mathbf{E} . Assuming that the material has an elastic behavior it means that the work done during a process by the state \mathbf{E}_a to \mathbf{E}_b , is equal to the variation of elastic potential $\omega(\mathbf{E})$:

$$\Delta l_D = \Delta\omega(\mathbf{E}) = \int_{E_a}^{E_b} \boldsymbol{\Sigma}_{II} : d\mathbf{E} = \int_{E_a}^{E_b} d\omega(\mathbf{E}) . \quad (2.58)$$

It is implicitly assumed that the components of the second tensor of Piola-Kirchhoff can be obtained by deriving the elastic potential:

$$\boldsymbol{\Sigma}_{II} = \frac{\partial\omega(\mathbf{E})}{\mathbf{E}} . \quad (2.59)$$

In the linear case if the elastic potential was a quadratic form of deformations, then it can be represented by a generic function. Under the hypothesis of isotropic material, it is also possible to express the potential as a function of the deformation tensor invariants since the value of the latter is not dependent on the reference system used to describe the deformation state. For convenience, having hypothesized the isotropy of the material, the potential is expressed as a sum of two components, the

first referring to the deviation deformation, the second to the volumetric deformation. The advantage introduced by the decomposition of these two terms is related to the fact that the elastomeric materials have almost incompressible behavior, therefore the contribution offered by the potential component due to volumetric deformations will be quantitatively and qualitatively different from the contribution of the potential component of deviation deformations. In order to operate this breakdown, one can express the potential in function of the first two invariants of the left tensor of Cauchy-Green, \mathbf{B} , and its determinant J , where \mathbf{B} is:

$$\mathbf{B} = \mathbf{F}^T \mathbf{F} . \quad (2.60)$$

The two invariants are:

$$I_{B1} = \text{tr}(\mathbf{B}) = \mathbf{I} : \mathbf{B} \quad (2.61)$$

$$I_{B2} = \frac{1}{2} \left(I_{B2}^2 - \text{tr}(\mathbf{B} : \mathbf{B}) \right) . \quad (2.62)$$

In this case, therefore, the invariants will refer to the only deviatoric component of the state of deformation. Consider, therefore, a process of infinitesimal deformation with an infinitesimal gradient of displacement. The latter can be related to the infinitesimal increase of the deformation gradient, such as:

$$d\mathbf{L} = \frac{\partial \mathbf{u}}{\partial \mathbf{X}} \quad (2.63)$$

$$d\mathbf{F} = \frac{\partial \mathbf{u}}{\partial \mathbf{X}} + \mathbf{F} = d\mathbf{L} + \mathbf{F} . \quad (2.64)$$

where the infinitesimal increment of deformation is obtained from the symmetrical part of \mathbf{L} (which derives in respect of time represents the deformation velocity tensor) :

$$d\mathbf{D} = \frac{1}{2}(d\mathbf{L} + d\mathbf{L}^T). \quad (2.65)$$

The infinitesimal increments of volumetric and deviating deformation will be

$$d\mathcal{E}^{vol} = tr(\mathbf{D}) = \mathbf{I} : \mathbf{D} \quad (2.66)$$

$$d\mathbf{e} = d\mathbf{D} - \frac{1}{3}d\mathcal{E}^{vol} \mathbf{I} . \quad (2.67)$$

But in the process considered, the increase of J will be related only to the increase in volumetric deformation. So:

$$dJ = Jd\mathcal{E}^{vol} . \quad (2.68)$$

From these we observe how the increase of the two invariants depends only on the increase of deviation deformation:

$$dI_{B1} = 2\mathbf{B} : d\mathbf{e} \quad (2.69)$$

$$dI_{B2} = 2(I_{B1}\mathbf{B} - \mathbf{B} \cdot \mathbf{B}) : d\mathbf{e} . \quad (2.70)$$

So if we express the elastic potential in function of the two invariants and the determinant J , it is possible to separate the two volumetric and deviatoric components of the deformation. Therefore:

$$\omega = \omega(I_{B1}, I_{B2}, J) \Rightarrow d\omega = \frac{\partial \omega}{\partial I_{B1}} dI_{B1} + \frac{\partial \omega}{\partial I_{B2}} dI_{B2} + \frac{\partial \omega}{\partial J} dJ \quad (2.71)$$

$$d\omega = 2 \left[\left(\frac{\partial \omega}{\partial I_{B1}} + I_{B2} \frac{\partial \omega}{\partial I_{B2}} \right) \mathbf{B} - \frac{\partial \omega}{\partial I_{B2}} \mathbf{B} \cdot \mathbf{B} \right] : d\mathbf{e} + J \frac{\partial \omega}{\partial J} d\mathcal{E}^{vol} , \quad (2.72)$$

where $d\omega$ represents the increase of elastic potential expressed by the infinitesimal deformation increments obtained by the deformation velocity tensor. In this way, it is possible to obtain the expressions of energetically conjugated stress to the tensor dD which are nothing more than the components of the tensor of Cauchy's stress. In fact, for an infinitesimal deformation process, the deformation work, referring to the volume in the initial and deformed configuration, is expressed by using the isotropic hypothesis, thus separating the deviation component from the volumetric:

$$dL_D = \int_V (s : de - pd\varepsilon^{vol}) dv \Rightarrow \int_V J (s : de - pd\varepsilon^{vol}) dV \quad (2.73)$$

where s represents the deviation component of the Cauchy tensor and is the hydrostatic component, positive if it is in compression, energetically conjugated with volumetric deformation. To transform the integral referring to the deformed volume in that executed in the original volume is used $J = dv/dV$. But $dL_D = d\omega$ so it is possible to derive the components of the Cauchy stress, known as the deformation gradient and the expression of the potential, through the equations previously described (2.68), (2.71), (2.72) and (2.73)

$$s = \frac{2}{J} \left[\left(\frac{\partial \omega}{\partial I_{B1}} + I_{B2} \frac{\partial \omega}{\partial I_{B2}} \right) \right] \mathbf{B} - \frac{\partial \omega}{\partial I_{B2}} \mathbf{B} \cdot \mathbf{B} \quad (2.74)$$

$$p = -\frac{\partial \omega}{\partial J} . \quad (2.75)$$

Once known the Cauchy's stress, the other stress measurements can be obtained from deformation gradients. However, it is possible to directly relate the potential with other deformation measures and to obtain, the corresponding conjugate stress measures. In particular, for calibrating hyperelastic laws, it is useful to relate the potential to the main elongation ratios: $\lambda_1, \lambda_2, \lambda_3$. These relationships define, on the main axis of

deformation, all non-nulliform components of the deformation gradient, which result:

$$\mathbf{F} = \begin{bmatrix} \lambda_1 & 0 & 0 \\ 0 & \lambda_2 & 0 \\ 0 & 0 & \lambda_3 \end{bmatrix} = \begin{bmatrix} \frac{\partial u}{\partial X} + 1 & 0 & 0 \\ 0 & \frac{\partial v}{\partial Y} + 1 & 0 \\ 0 & 0 & \frac{\partial w}{\partial Z} + 1 \end{bmatrix} \quad (2.76)$$

$$\det \mathbf{F} = \lambda_1 \lambda_2 \lambda_3 = J . \quad (2.77)$$

The Green-Lagrange tensor, will be:

$$\mathbf{E}_\alpha = \frac{1}{2}(\lambda_\alpha^2 - 1); \quad \alpha = 1, 2, 3 . \quad (2.78)$$

Introducing nominal deformation:

$$\tilde{\epsilon}_\alpha = (\lambda - 1) . \quad (2.79)$$

From the energetically point of view:

$$dL_D = \int_V \Sigma_n : dF dV . \quad (2.80)$$

In this case it is possible to obtain the constitutive law in terms of nominal stress-nominal strain and evaluate the potential in relation to the main elongation ratios. Then, following laboratory tests, one can evaluate $\lambda_1, \lambda_2, \lambda_3$, known the main deformation directions, from which invariants depend, such as:

$$I_{B1} = \lambda_{B1}^2 + \lambda_{B2}^2 + \lambda_{B3}^2 \quad (2.81)$$

$$I_{B2} = \lambda_{B1}^{-2} + \lambda_{B2}^{-2} + \lambda_{B3}^{-2} . \quad (2.82)$$

Subsequently the potential is derived according to the principal elongation ratios and the nominal stress is obtained. Thus, it is possible to model the constitutive law of the hyperelastic material through experimental tests, by evaluating the elastic potential and calibrating it according to the parameters obtained from the tests.

2.2.1 Shape of the elastic potential

The constitutive law of the hyperelastic material is calibrated with a series of experimental tests after defining the shape of the elastic potential, function of a set of parameters. It is possible to refer to various forms of elastic potential that will be described below.

2.2.1.1 *Polinomial shape*

If we consider principal unit elongation ratios, the invariant of the left tensor of Cauchy-Green will have a value of 3, so there is no deformation. It follows that the deformation tensor determinant, J , will be equal to 1. These aspects are considered in order to define the potential so as to annul it for null deformations. It is possible to identify a polynomial form of elastic potential, function of invariants, I_{B1} , I_{B2} and J , as defined below:

$$\omega = \sum_{i+j=1}^N C_{ij} (I_{B1} - 3)^i (I_{B2} - 3)^j + \sum_{i=1}^N \frac{1}{D_i} (J - 1)^{2i} . \quad (2.83)$$

If invariants I_{B1} and I_{B2} are both considered in the polynomial form, only rarely approximations with order $N > 2$ are used. The first order coefficients define a linear function in the deviator deformation invariants which are function of the squares of the main deviation deformation values according to equations (2.81) and (2.82). Considering that the stress components are the derivatives of potential, so the response found by the

first order coefficients is linear and corresponds to the initial coefficient of stiffness of the material

$$G_0 = 2(C_{10} + C_{01}). \quad (2.84)$$

Coefficients D_i introduce, instead, the dependence of potential on volumetric deformation. The first order coefficient results in a quadratic contribution in J that corresponds to a linear correspondence between pressure and volumetric deformation. The initial *bulk modulus* of the material is thus defined by the first order coefficient according to the relation

$$K_0 = \frac{2}{D_i}. \quad (2.85)$$

For low values of D_i , then high values of K_0 , the material is defined incompressible, and it is possible to evaluate, also, the *Poisson ratio* related to the previous value, as we describe in the following table:

K_0 / G_0	Poisson ratio
10	0.452
20	0.457
50	0.490
100	0.495
1000	0.4995
10000	0.49996

Table 2.1 Rubber mechanical properties

2.2.1.2 Money-Rivlin model

This model is based on the particularization of the elastic potential expressed in polynomial form in the equation (2.83), for $N=1$

$$\omega = C_{10} (I_{B1} - 3) + C_{10} (I_{B2} - 3) + \frac{1}{D_1} (J - 1)^2. \quad (2.86)$$

In the case of elastomeric materials, this model cannot represent the change of slope that the material exhibits beyond an elongation ratio threshold. This elongation ratio is known as *locking stretch*.

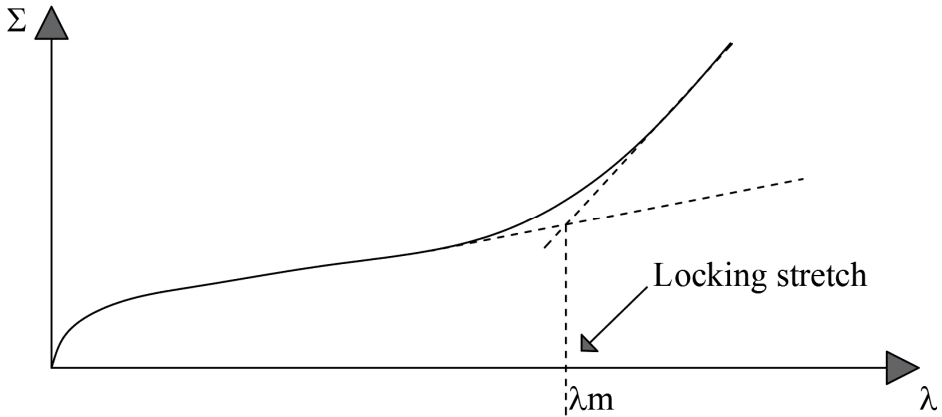


Figure 2.7 Constitutive law with locking stretch

2.2.1.3 Reduced polynomial shape

Thus, polynomial forms of simplified elastic potential are defined, with respect to which the dependence form of the second invariant of the deviation deformations is eliminated. Among the various reduced polynomial forms the most used is the *neo-hookian form*

$$\omega = \sum_{i+j=1}^N C_{i0} (I_{B1} - 3)^i + \sum_{i=1}^N \frac{1}{D_i} (J - 1)^{2i} \quad (2.87)$$

From the comparison of these models with experimental evidence of elastomeric materials, it is possible to say that these are well interpolated by models that provide great dependence on the second invariant. At the same time, if the second invariant improves the calibration in relation to the experimental tests, it has been observed that introducing them it has little results in predicting the behavior of the material.

2.2.1.4 *Ogden model*

This model expresses the elastic potential in function of the principal normalized elongation ratios.

$$\omega = \sum_{i=1}^N \frac{2\mu}{\alpha_i^2} (\bar{\lambda}_1^{\alpha_i} + \bar{\lambda}_2^{\alpha_i} + \bar{\lambda}_3^{\alpha_i} - 3) + \sum_{i=1}^N \frac{1}{D_1} (J - 1)^{2i}, \quad (2.88)$$

where the principal normalized elongation ratios are defined as:

$$\bar{\lambda}_i = \frac{1}{\sqrt[3]{J}} \lambda_i \Rightarrow \bar{\lambda}_1 \bar{\lambda}_2 \bar{\lambda}_3 = 1. \quad (2.89)$$

Observing equation (2.89) it can be seen that the volumetric deformation is null and that therefore there is a purely deviatory deformation state.

2.2.1.5 *Arruda-Boyce model*

This model is derived from an idealization of the molecular structure of an elastomer. It is considered a representative volume model of elastomeric material constituted by a cube that has inside it 8 elastic elements converging in the center of the element, as shown in the Figure 2.8.

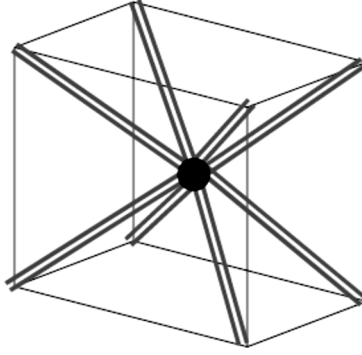


Figure 2.8 Schematic Arruda-Boyce model

The shape of the elastic potential is:

$$\omega = \mu \sum_{i=1}^N \frac{C_i}{\lambda_m^{2i-2}} (I_{B1}^i - 3^i) + \frac{1}{D} \left(\frac{J^2 - 1}{2} - \ln J \right), \quad (2.90)$$

where the coefficients C_i are known, and the values are obtained by applying a statistical model to the distribution of elastic properties of the eight internal elements to the representative volume. In particular, the coefficients C_i are obtained by the serial expansion of a mathematical function and have the following expression:

$$C_1 = \frac{1}{2}; C_2 = \frac{1}{20}; C_3 = \frac{11}{1050}; C_4 = \frac{19}{7000}; C_5 = \frac{519}{673750}; \quad (2.91)$$

Therefore, the parameters to be calibrated will be μ , D , and λ_m , where the latter represents the *locking stretch*.

2.2.2 Hyperelastic material models in Finite Element analysis

To calibrate the parameter discussed in the previous paragraphs some experimental test are used. In this section the objective of the testing described is to define and to satisfy the input requirements of mathematical material models that exist in structural, non-linear finite element analysis software. The testing of elastomers for the purpose of defining material models is often misunderstood. The appropriate experiments are not yet clearly defined by national or international standards organizations. This difficulty derives from the complex mathematical models that are required to define the nonlinear and the nearly incompressible attributes of elastomers.

In general, stress and strain data sets developed by stretching the elastomer in several modes of deformation are required and “fitted” to sufficiently define the variables in the material models. A typical set of 3 stress strain curves, appropriate for input into fitting routines, are shown in Figure 2.9. Appropriate experimental loading sequences and realistic strain levels are needed to capture the elastomer behavior that applies in the analysis

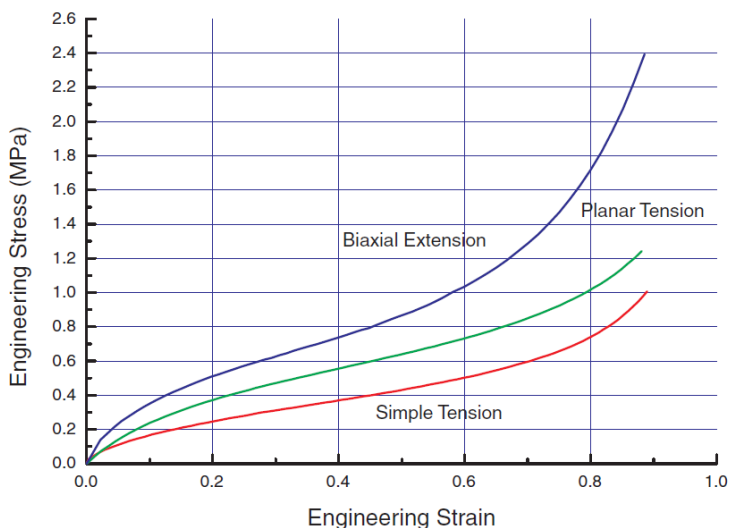


Figure 2.9 A typical final data set for input into a curve fitter (Miller 1999)

The modes of each deformation put the material into a particular state of strain. One objective of testing is to achieve “pure” states of strain such that the stress strain curve represents the elastomer behavior only in the desired state. For incompressible elastomers, the basic strain states are simple tension, pure shear and simple compression. For experimental reasons discussed further on, compression is replaced by equal biaxial extension. For slightly compressible situations or situations where an elastomer is highly constrained, a volumetric compression test may be needed to determine the bulk behavior.

2.2.2.1 Simple tension strain state

Simple tension experiments are very popular for elastomers. There are several standards for the testing of elastomers in tension. However, the experimental requirements for analysis are somewhat different than most standardized test methods. The most significant requirement is that in order to achieve a state of pure tensile strain, the specimen must be much longer in the direction of stretching than in the width and thickness dimensions. The objective is to create an experiment where there is no lateral constraint to specimen thinning. One can perform finite element analysis on the specimen geometry to determine the specimen length to width ratio (Figure 2.10). The results of this analysis will show that the specimen needs to be at least 10 times longer than the width or thickness.

The standard used as a reference for this type of test is UNI 6065 (UNI 6065, 1981). Tensile test allows to determine the tension-information binding and is realized by a dynamometer appropriately equipped according to the type of specimen.

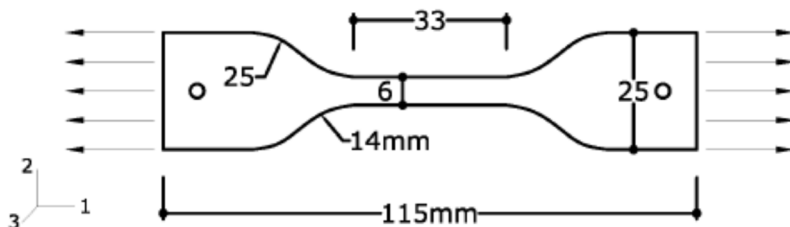


Figure 2.10 Dumbbell specimen with 2mm thickness

The Dumbbell test (Figure 2.10) is described in the standard and can be presented in four different sizes. It is necessary to measure the elongation of the sample in the useful trait, for example by means of extensometers, as such elongation is not directly proportional to the displacement of the test machine movable cross due to the deformability of the other parts of the specimen. The traction test characteristic points are as follows (Figure 2.12):

- Ca05: effort corresponding to a deformation of 50% (MPa)
- Ca1: Effort corresponding to a deformation equal to 100% (MPa)
- Ca3: effort corresponding to a deformation of 300% (MPa)
- CR: breaking force (MPa)
- AR: breaking deformation (%).

Young's modulus is not generally determined because, in correspondence of the initial trajectory of the traction curve, there may have slope variations that make its calculation uncertain. Furthermore the Young's modulus varies from point to point and therefore, more than one value, it would be necessary to determine the link between the Young's modulus and, for example, deformation. Many times the secant modules are calculated between two characteristic deformation levels. A typical tensile test problem for elastomeric materials is the determination of the effective section. In the case of Dumbbell specimens the thickness of the specimen is measured in three different points of the useful trait, than it is possible to calculate the mean value, and multiplies by the width of the specimen, whose variation is also measured.

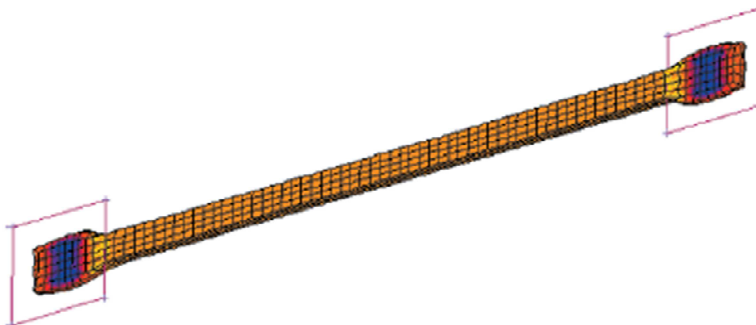


Figure 2.11 Analysis of a tension specimen (Miller 1999)

One can perform finite element analysis on the specimen geometry to determine the specimen length to width ratio (Figure 2.11). The results of this analysis will show that the specimen needs to be at least 10 times longer than the width or thickness. The length in this case refers to the specimen length between the instrument clamps. Specimen clamps create an indeterminate state of stress and strain in the region surrounding the clamp in the process of gripping. Therefore, the specimen straining must be measured on the specimen, but away from the clamp, where a pure tension strain state is occurring. A non-contacting strain measuring device such as a video extensometer or laser extensometer is required to achieve this (Figure 2.12).

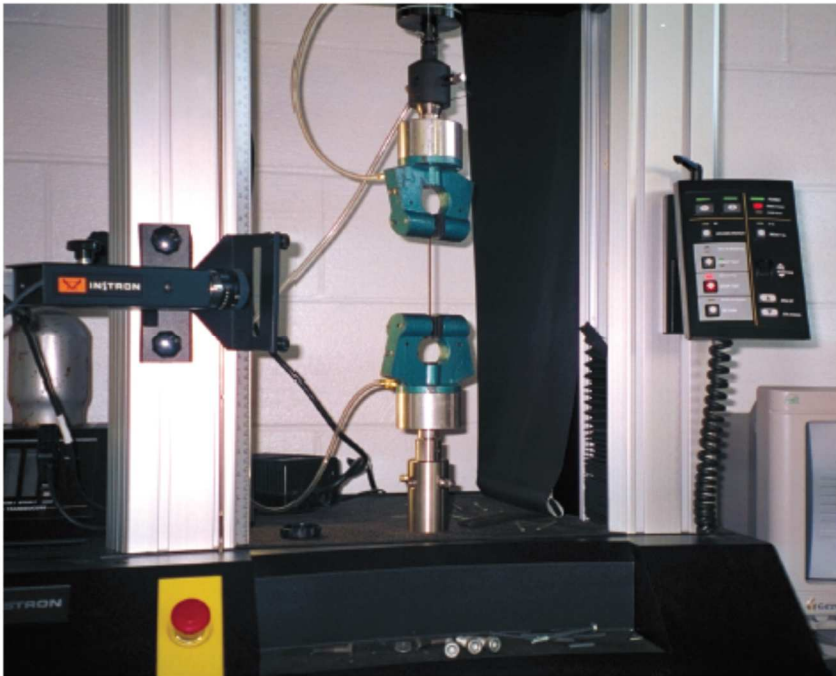


Figure 2.12 A tension experiment using video extensometer (Miller 1999)

2.2.2.2 *Pure shear strain state*

The pure shear experiment used for analysis is not what most of us would expect. The experiment appears at first glance to be nothing more than a very wide tensile test. However, because the material is nearly incompressible, a state of pure shear exists in the specimen at a 45 degree angle to the stretching direction ⁷. The most significant aspect of the specimen is that it is much shorter in the direction of stretching than the width. The objective is to create an experiment where the specimen is perfectly constrained in the lateral direction such that all specimen thinning occurs in the thickness direction. Finite element analysis of the specimen geometry will show that the specimen must be at least 10 times wider than the length in the stretching direction. This experiment is very sensitive to this ratio. A non-contacting strain measuring device must be used to measure strain away from the clamp edges where the pure strain state is occurring (Figure 2.13).

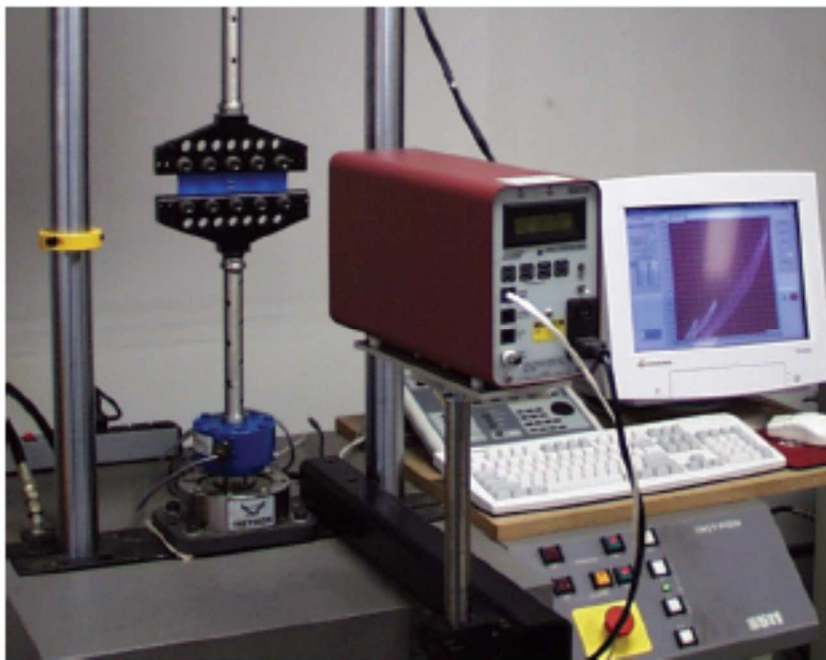


Figure 2.13 A pure shear experiment using a laser extensometer

2.2.2.3 *Simple compression strain state*

The compression experiment is also a popular test for elastomers. When testing for analysis, pure states of strain are desired and this is especially difficult to achieve experimentally in compression. Because there is friction between the test specimen and the instrument platens, the specimen is not completely free to expand laterally during compression. Even very small of friction coefficient levels such as 0.1 between the specimen and the platen can cause substantial shearing strains that alter the stress response to straining (Figure 2.14). Often, the maximum shear strain exceeds the maximum compression strain. Because the actual friction is not known, the data cannot be corrected.



Figure 2.14 A lubricated compression specimen showing lateral constraining from friction at the surface

2.2.2.4 *Equal biaxial strain state*

For incompressible or nearly incompressible materials, equal biaxial extension of a specimen creates a state of strain equivalent to pure compression. Although the actual experiment is more complex than the simple compression experiment, a pure state of strain can be achieved which will result in a more accurate material model. The equal biaxial strain state may be achieved by radial stretching a circular disc. Finite element analysis of the specimen is required to determine the appropriate geometry of the clamping points (Figure 2.15). Once again, a non-contacting strain measuring device must be used such that strain is measured away from the clamp edges (Figure 2.16).

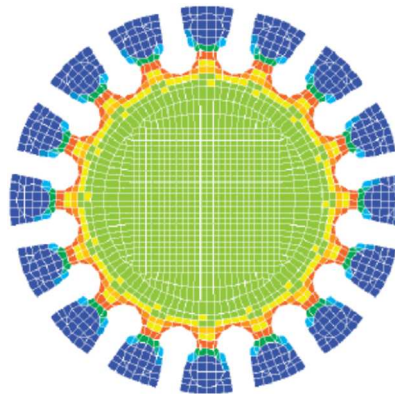


Figure 2.15 Analysis of a biaxial specimen



Figure 2.16 A biaxial extension experiment

2.2.2.5 Volumetric compression

Volumetric compression is an experiment where the compressibility of the material is examined. In this experiment, a cylindrical specimen is constrained in a fixture and compressed (Figure 2.17). The actual displacement during compression is very small and great care must be taken to measure only the specimen compliance and not the stiffness of the instrument itself. The initial slope of the resulting stress-strain function is the bulk modulus. This value is typically 2-3 orders of magnitude greater than the shear modulus for elastomers.



Figure 2.17 Volumetric compression fixture with specimen

2.2.2.6 Creating a consistent data set

Although the experiments are performed separately and the strain states are different, data from all of the individual experiments is used as a set. This means that the specimens used for each of the experiments must be of the same material. This may seem obvious but if the specimens are specially molded to accommodate the differing instrument clamps for different experiments, it is possible that the material processing parameters may

cause material variations from test to test. While it is reasonable to assume that variation exists in the production environment and that we can never really get the exact material properties every time, it is not acceptable to have this same variation within the data set. The data represents a “snapshot” in time. If even slight variation exists between experiments, a physically impossible material model may be developed in the analysis software. The best way to avoid this problem is to cut specimens for simple tension, pure shear and equal biaxial extension from the same slab of material. The loading conditions, strain levels and straining rates should also be developed considering the inter-relationship between tests.

The structural properties of elastomers change significantly during the first several times that the material experiences straining. This behavior is commonly referred to as the Mullin’s effect. If an elastomer is loaded to a particular strain level followed by complete unloading to zero stress several times, the change in structural properties from cycle to cycle as measured by the stress strain function will diminish. When the stress strain function no longer changes significantly, the material may be considered to be stable for strain levels below that particular strain maximum.

If the elastomer is then taken to a new higher strain maximum, the structural properties will again change significantly. This behavior is documented throughout the literature. One example of this behavior is shown in Figure 2.18 where a filled natural rubber is strained to 40% strain for 10 repetitions followed by straining to 100% for 10 repetitions. Another example is shown in Figure 2.19, Figure 2.20 and Figure 2.21, where a thermoplastic elastomer is strained to 20% strain for 10 repetitions followed by straining to 50% for 10 repetitions.

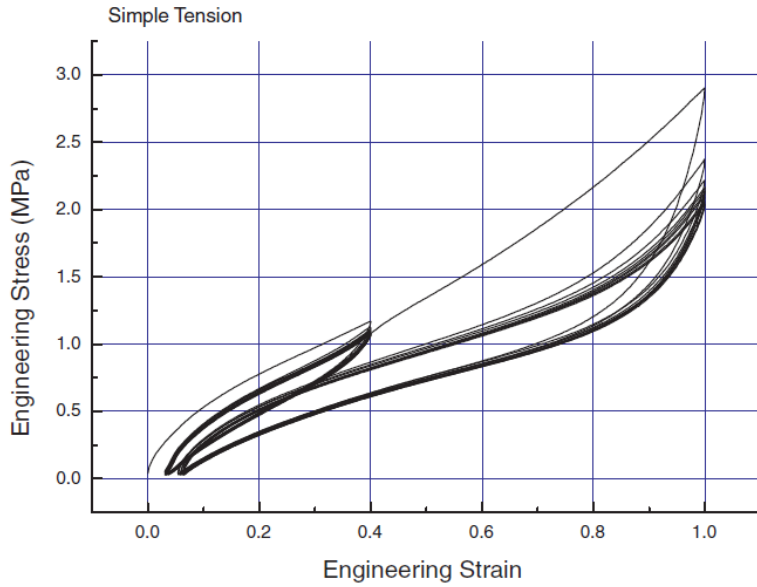


Figure 2.18 Cyclic loading of filled natural rubber (Miller 1999)

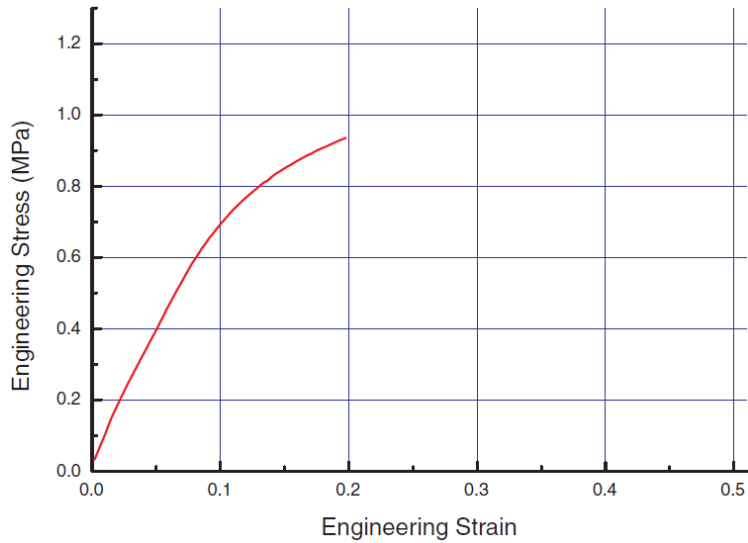


Figure 2.19 1st loading of a thermoplastic elastomer (Miller 1999)

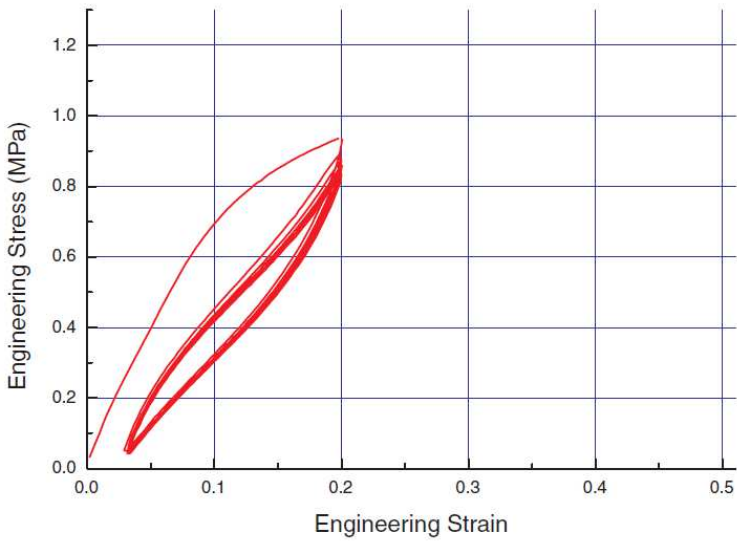


Figure 2.20 Multiple strain cycles of a thermoplastic elastomer (Miller 1999)

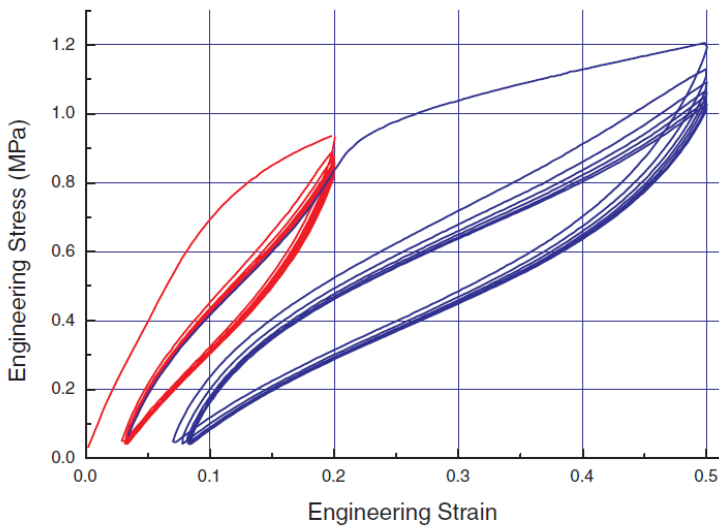


Figure 2.21 Multiple strain cycles of a thermoplastic elastomer at two maximum strain levels (Miller 1999)

2.2.2.7 *Elastomer characterization*

For the rubber taken as reference, UNI 60 Sha, two sets of tests are available, on different mix samples,. The first series has been characterized from the following tests: one-sided compression, one-sided traction, shear, compressibility. The second series is composed by: a one-sided tensile test, one for shear, one of biaxial traction and one of compressibility. The substantial difference between the two sets of tests is that the second one has been brought to levels of major deformations. Also, for the second set, the test of biaxial traction yields more reliable results because it is less affected edge effects (Figure 2.25).

Through static tests, the hyperelastic behavior of the material, that is, how the elastic modulus increases with the increase of deformation, gives more rigidity to the material.

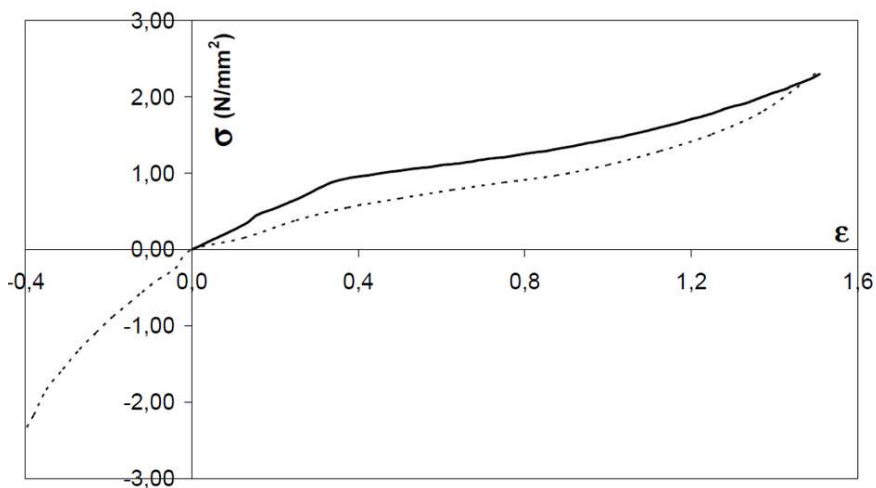


Figure 2.22 Uniaxial test on elastomer: first series with dashed line, second series with continuous line (Cuomo 2007)

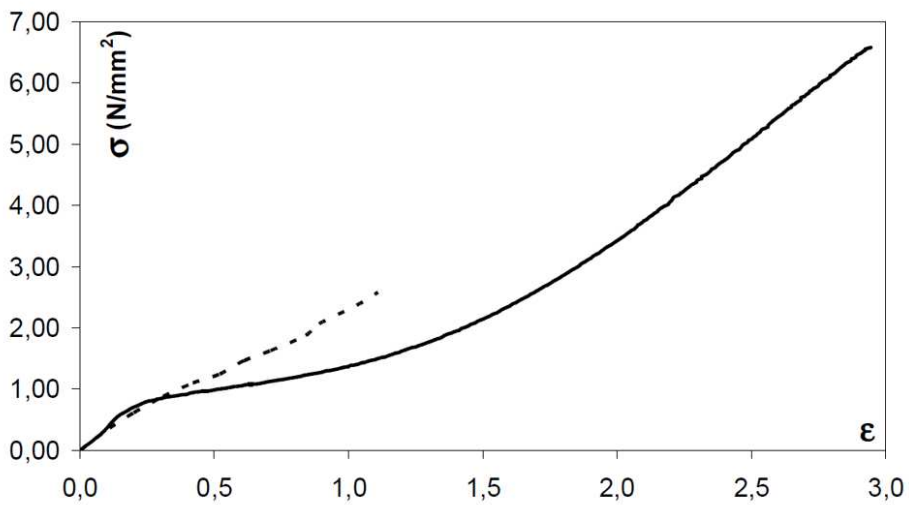


Figure 2.23 Planar test on elastomer: first series with dashed line, second series with continuous line (Cuomo 2007)

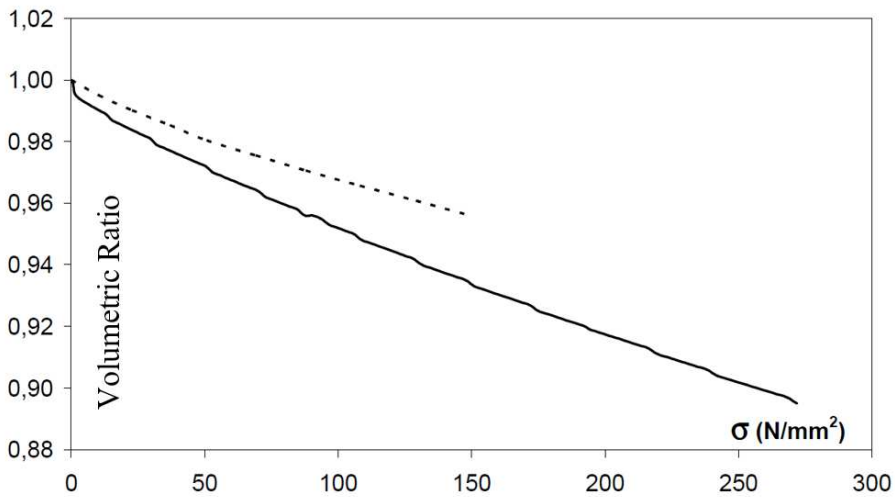


Figure 2.24 Volumetric test on elastomer: first series with dashed line, second series with continuous line (Cuomo 2007)

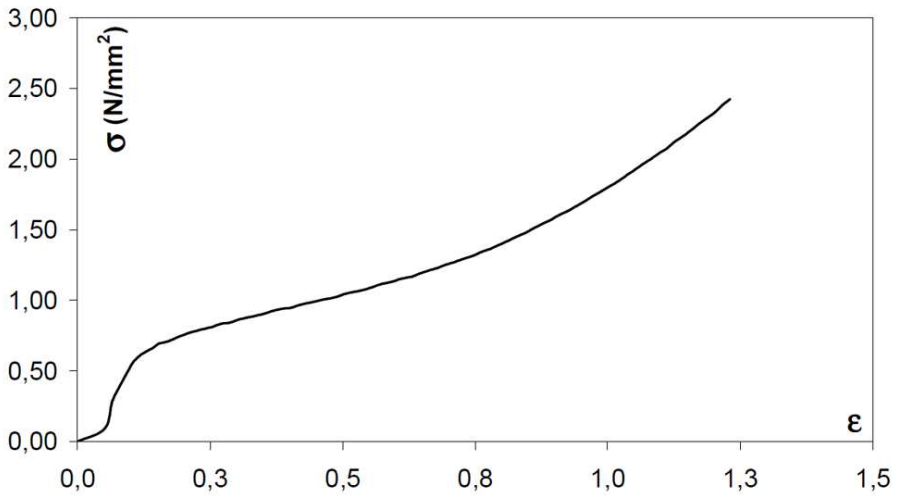


Figure 2.25 Biaxial test on elastomer: second series with continuous line (Cuomo 2007)

The results of the previous test, in particular the second series, has been implemented in the Finite Element Software ABAQUS CAE. Through this software is possible to find the coefficients of the previous described Potential Shape, once the experimental test are given. In the following Figure 2.26 - Figure 2.29 the various potential shape and the test data are shown to evaluate which is the better shape to represent the behavior of the elastomer chosen as reference.

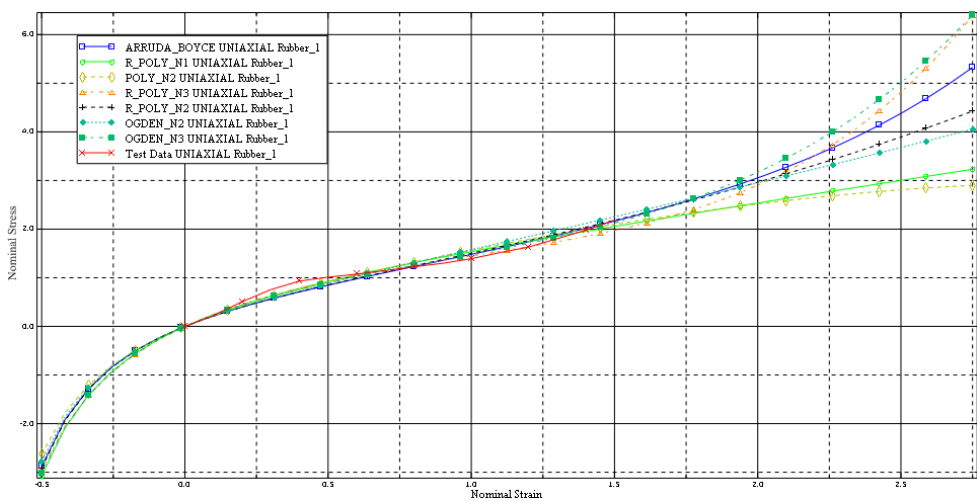


Figure 2.26 Uniaxial test curves from ABAQUS

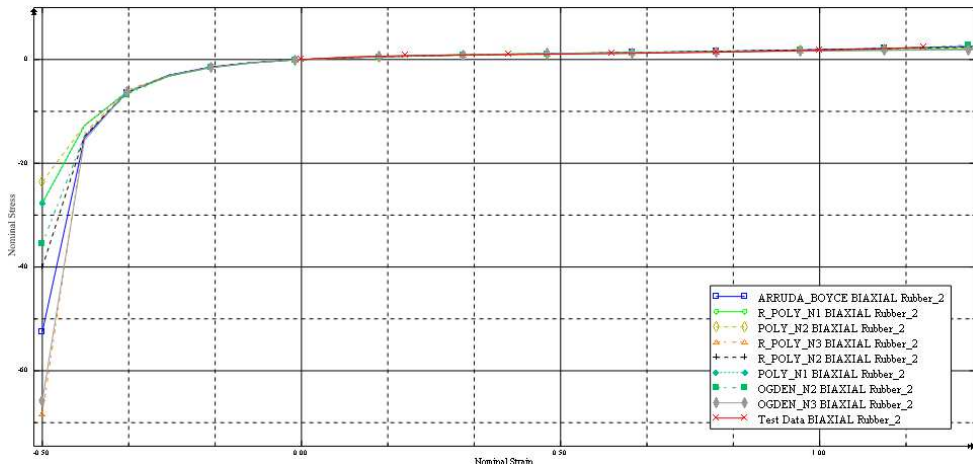


Figure 2.27 Biaxial test curves from ABAQUS

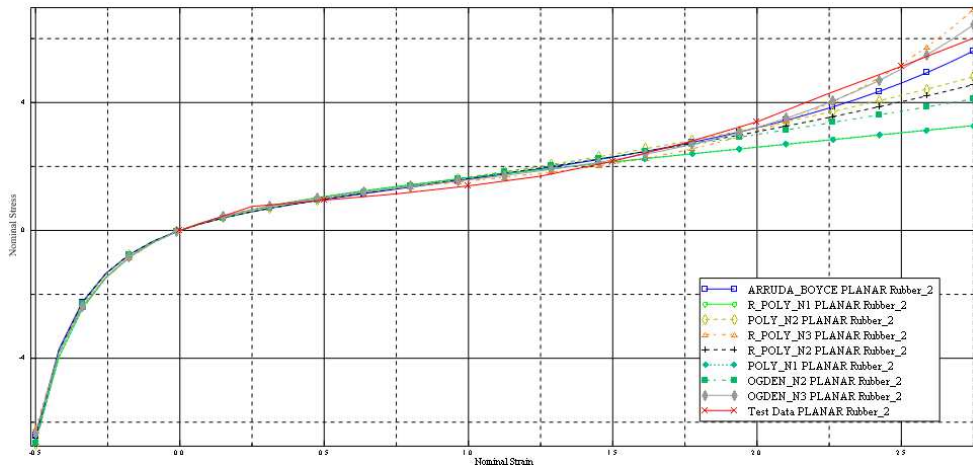


Figure 2.28 Planar test curves from ABAQUS

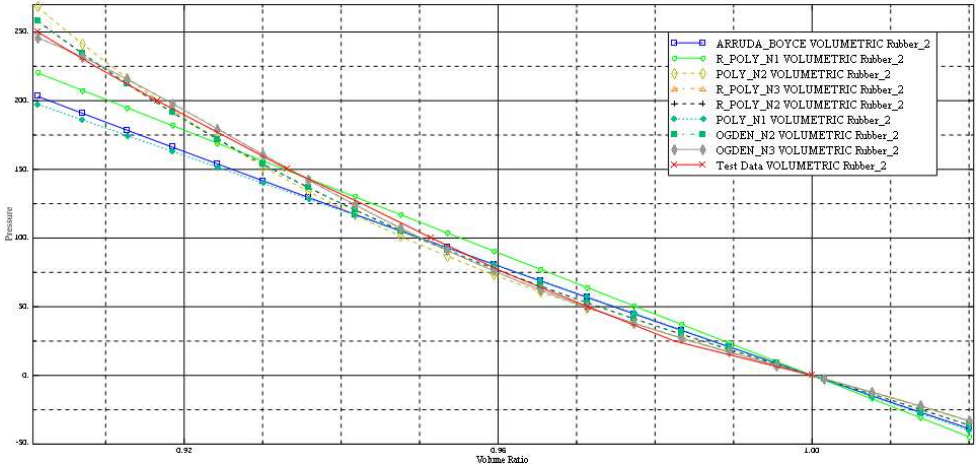


Figure 2.29 Volumetric test curves from ABAQUS

2.3 PTFE: a fluoropolymer with thermo-mechanical behavior

Fluoropolymers are a class of polymers defined by the presence of carbon (C) and fluorine (F), that have many unique mechanical and chemical properties. For example, fluoropolymers have a lower friction coefficient than almost any other solid material, and the chemical resistance and thermomechanical stability of fluoropolymers are better than most other polymeric materials. The era of fluoropolymers started in 1938 when R. Plucket of DuPont invented polytetrafluoroethylene (PTFE) (Ebnesajjad 2000). This material, which is based on the monomer $[(-CF_2 - CF_2-)_n]$, is the fluoropolymer with the highest chemical inertness and broadest range of temperature use, but due to its very high melt viscosity it is not melt-processable, and therefore difficult to use in some manufacturing applications.

Fluoropolymers, as well as other thermoplastics, exhibit a complicated non-linear response when subjected to external loads. At small deformations, the material response is linear viscoelastic. At larger strains, the material undergoes distributed yielding, unrecoverable deformation, viscoplastic flow, and finally, gradual material stiffening at large deformations until ultimate failure occurs. It is also known that the material response is strongly dependent on strain-rate and temperature: higher deformation rates and lower temperatures increase the stiffness of the material.

Below are reported the PTFE mechanical characteristics in terms of stress and strain also in relation to the temperature.

Traction Behavior

The stress-strain curves at the temperature variation (Figure 2.30) show how the sagging occurs for large deformations and that the material response is strongly influenced by the temperature range at which it works.

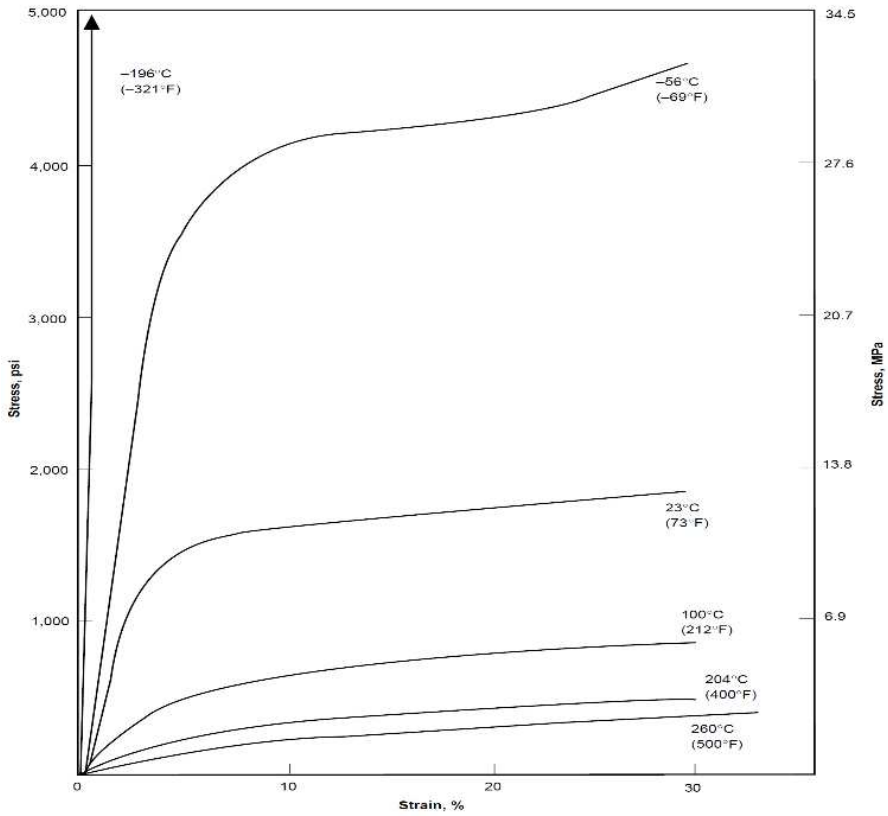


Figure 2.30 Stress-strain curve for different temperature (DuPont-Fluoroproducts 1996)

Temperature, °C	Teflon [®] PTFE Yield Strength, MPa
-251	131
-196	110
-129	79.3
-73	53.1
-56	26.2
0	12.4
23	9
70	5.5
121	3.4

Table 2.2 Yield values for different temperature (DuPont-Fluoroproducts 1996)

Likewise, elastic response begins to deviate from low-deformity linearity. Table 2.2 summarizes the value of the PTFE yield strength as a function of the temperature. Figure 2.31 shows the curves showing maximum tensile strength.

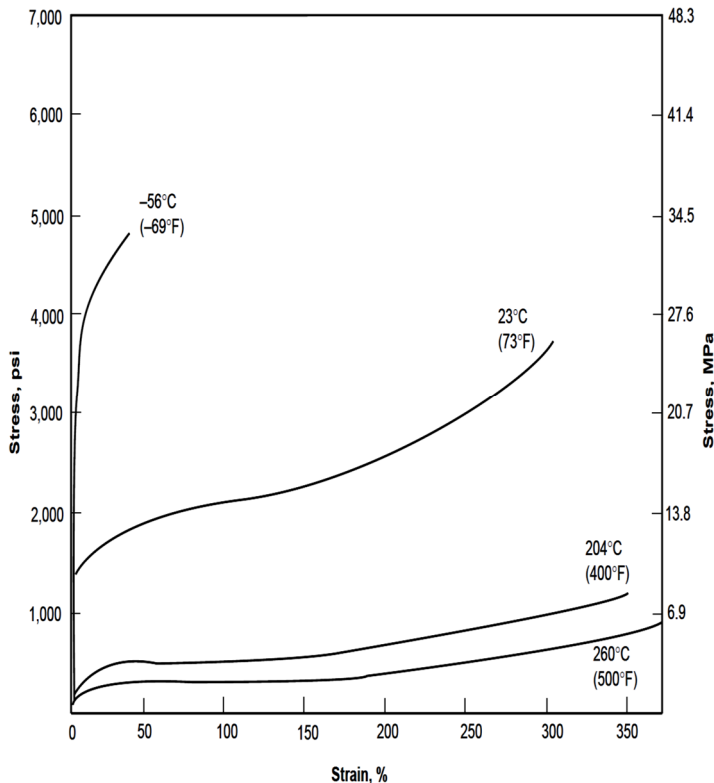


Figure 2.31 Tensile stress-strain curves (DuPont-Fluoroproducts 1996)

Figure 2.32 shows how variable deformation depends on temperature for fixed stress values. The percentage of deformation selected for design should take into account the highest temperature at which the part will be subjected.

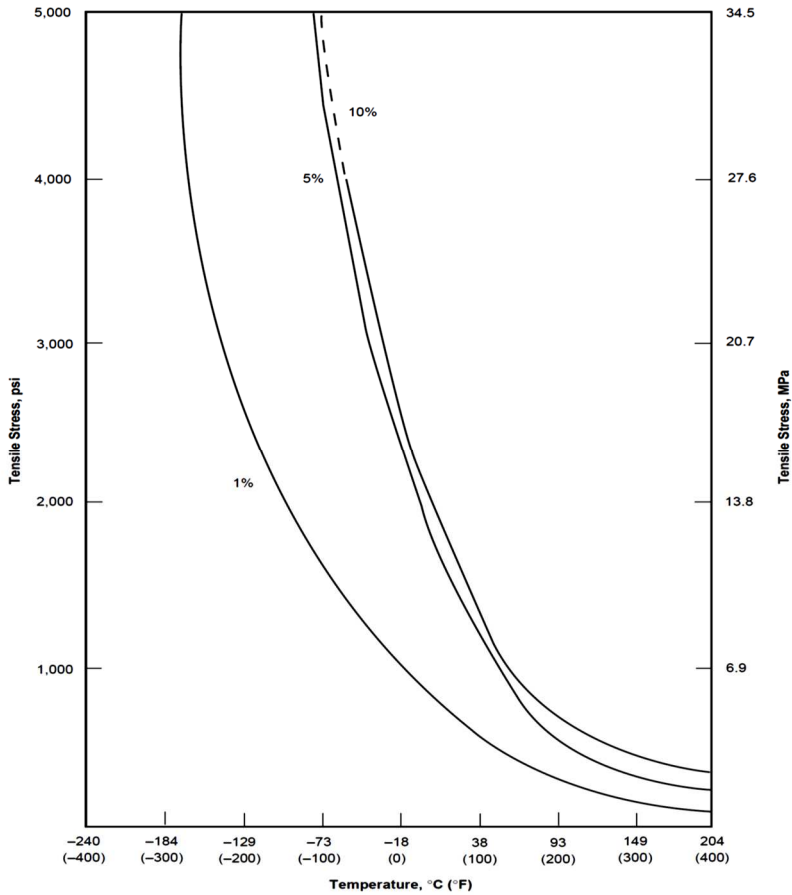


Figure 2.32 Variation of tensile stress with temperature (DuPont-Fluoroproducts 1996)

Compression behavior

The following figures shows three compression curves for three different temperature values (Figure 2.33). For low deformation values, stress-deformation curves are similar to traction curves (Figure 2.34). While increasing the deformation value the curves differ. Stress points for compression and traction are manifested for similar stress values.

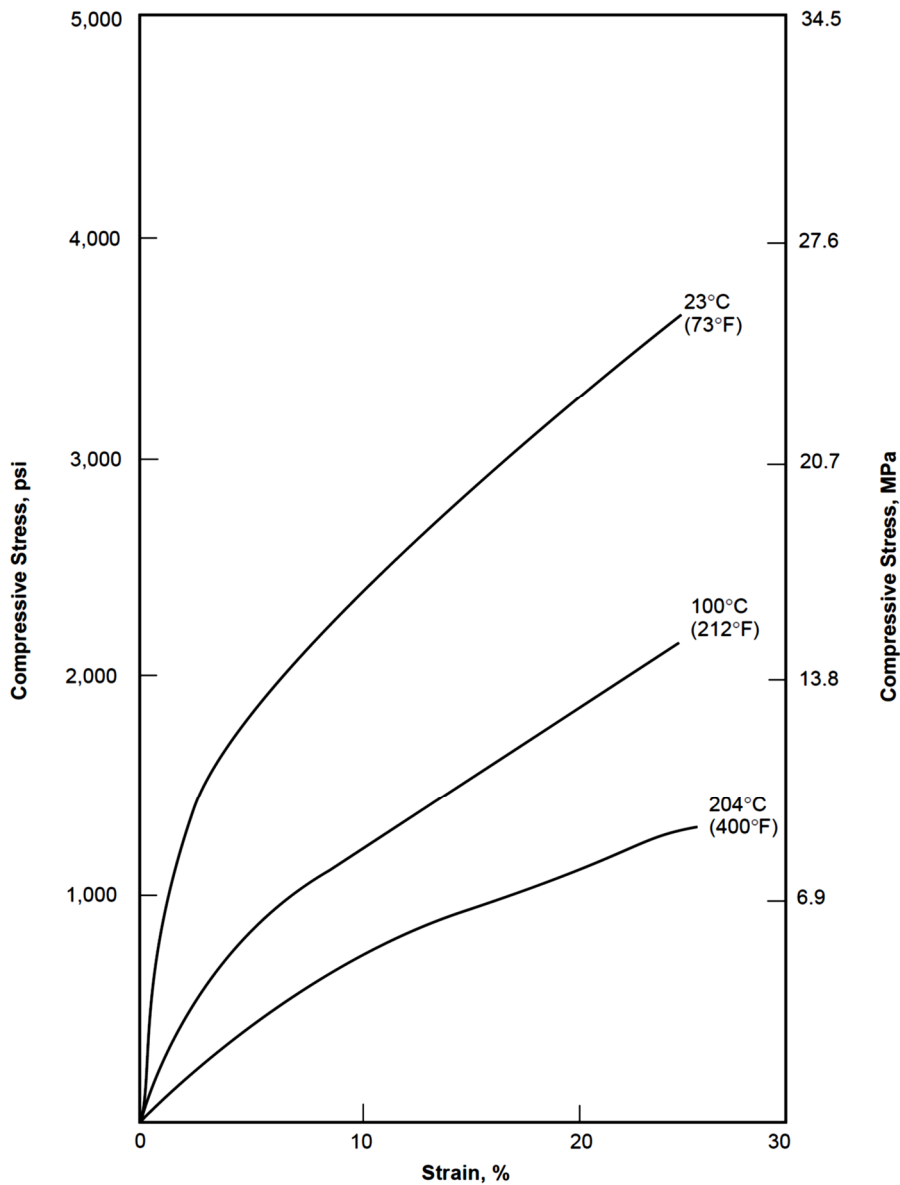


Figure 2.33 Variation of compression stress-strain curves with temperature (DuPont-Fluoroproducts 1996)

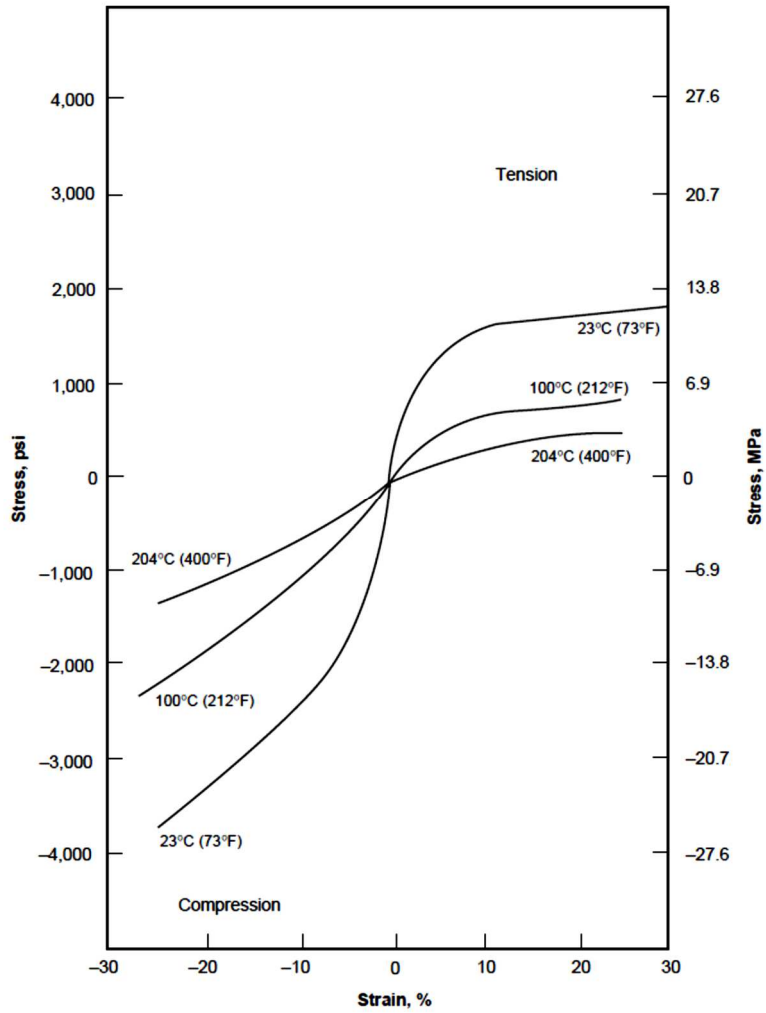


Figure 2.34 Tensile and Compression behavior (DuPont-Fluoroproducts 1996)

Shear behavior

Figure 2.35 is a representation of the shear stress at the variation of deformation.

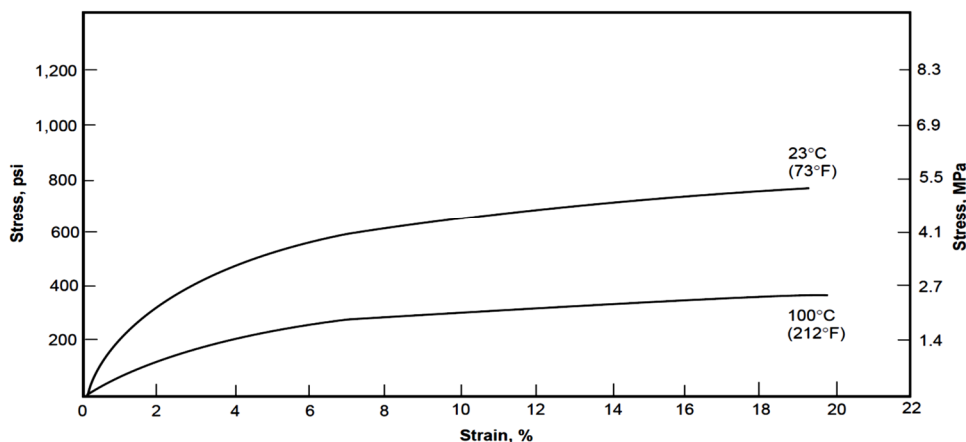


Figure 2.35 Stress-strain curves for shear (DuPont-Fluoroproducts 1996)

The PTFE Poisson module is 0.46 to 23 °C (73 ° F) and approaches a limit value of 0.50 with increasing temperature.

As for the elastic module, although the classic concept that implies linear proportionality between tension and strain is not strictly applicable to most plastic materials, the term is widely used with reference to PTFE. For most plastic materials, this ratio will not be constant but will depend on both the time when the tension is applied, either by the resulting deformation or viscous deformation. To understand the mechanical properties, it is important to study the viscous deformation and the study of the phenomenon of recovery. A special device for the study of PTFE compression viscous deformation has been developed. Figure 2.36 illustrates the general scheme of this tool. With this equipment the stress-strain time relationship at a constant temperature may be obtained by observing either the strain-time relationship at a constant stress (creep) (Figure 2.37).

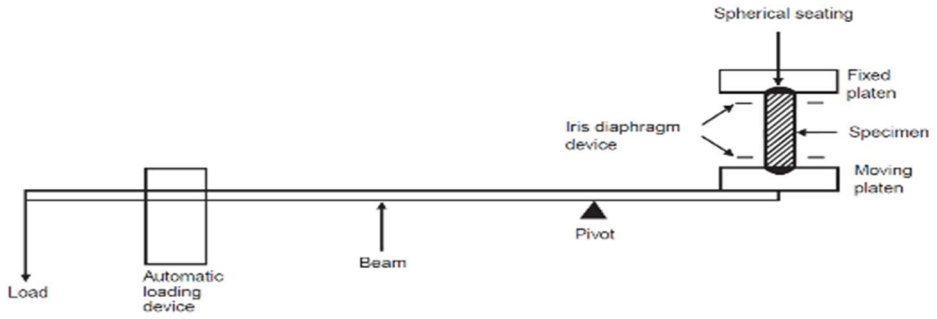


Figure 2.36 Basic creep testing equipment (Physical properties of Fluon unfilled and filled PTFE 2007)

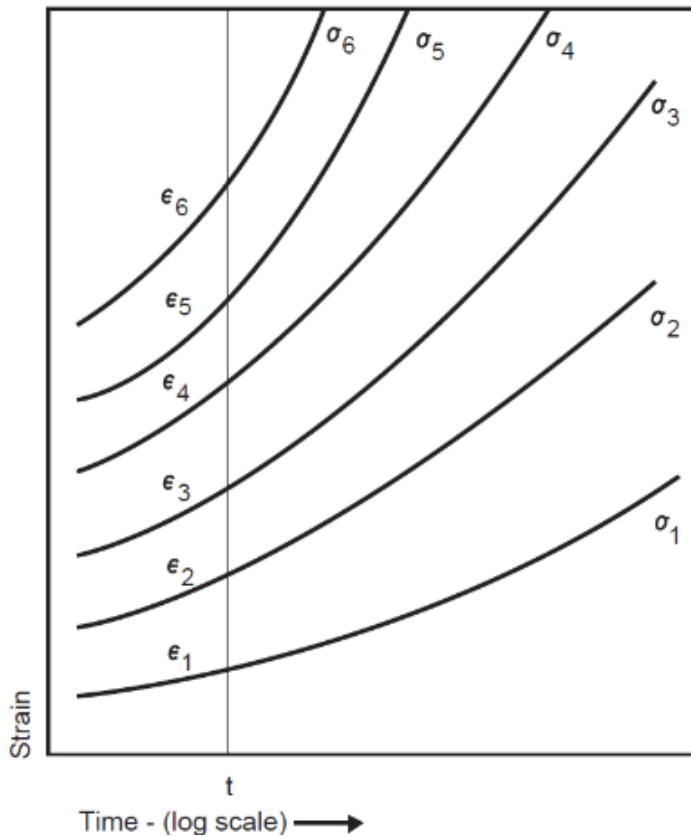


Figure 2.37 Compressive creep (Physical properties of Fluon unfilled and filled PTFE 2007)

Figure 2.38 shows the effect of the load application time in terms of PTFE stress-deformation, the non-linearity of the curves, even at quite low strains, shows how the apparent modulus decreases with increasing strain.

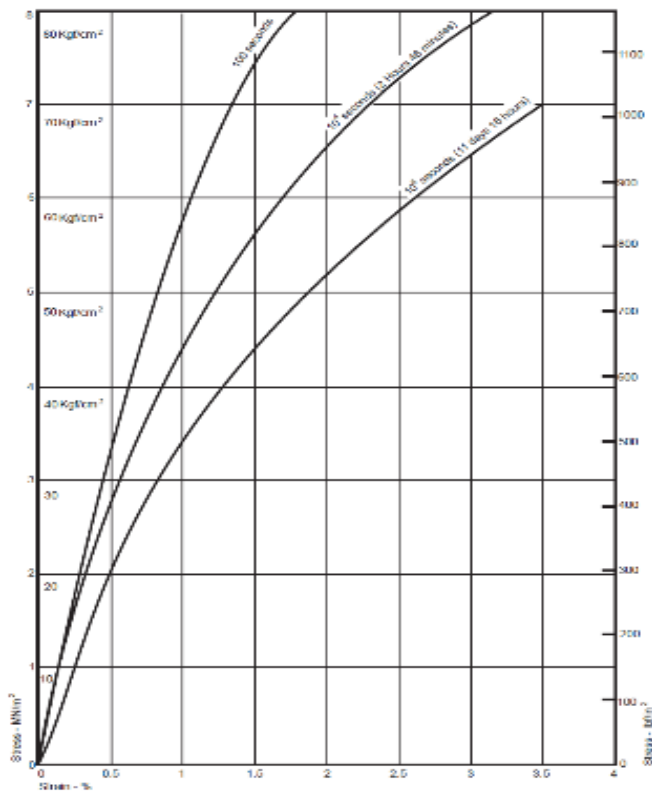


Figure 2.38 Isochronous stress-strain relationship in compression, at 25°C (Physical properties of Fluon unfilled and filled PTFE 2007)

Figure 2.39 shows the effects of four different stress levels on the rate of recovery of strain after removal of the applied compressive load. It can be seen that the higher the stress the slower is the recovery.

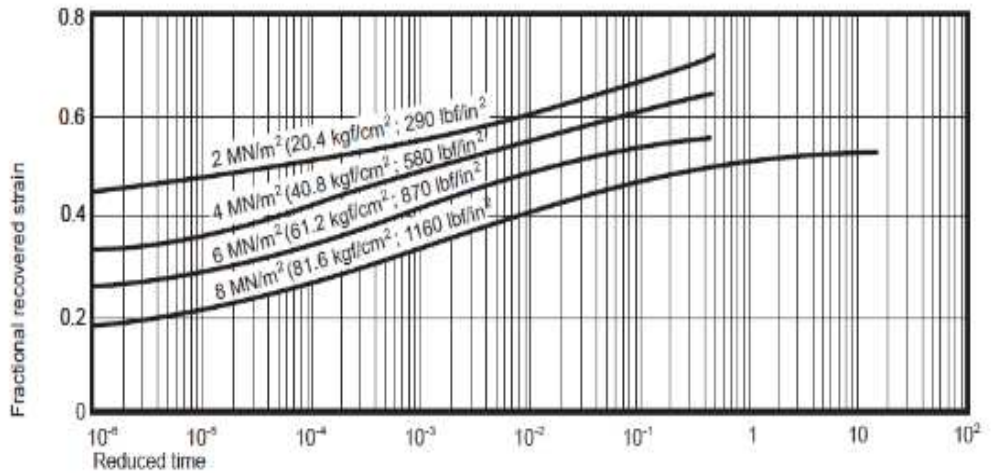


Figure 2.39 Recovery for creep in compression, at 25°C (Physical properties of Fluon unfilled and filled PTFE 2007)

2.3.1 Experimental test for characterization of compressive mechanical behavior

Since the mechanical response of fluoropolymers is highly non-linear the difficult is to find a suitable material model that can capture the observed experimental response. There are a number of different candidate material models that are documented in the literature for predicting the behavior of general thermoplastics (Arruda and Boyce 1995, Bergstrom et al. 2003, Ho and Krempl 2002, Lion 1997).

Development of advanced constitutive models for polymers is an active area of research that is continuously evolving and improving (Bergstrom and Hilbert 2005). Up until the last few years, there were no constitutive models specifically developed for fluoropolymers, and the most useful models were either classical isotropic plasticity, linear viscoelasticity models, or general models for thermoplastics (Arruda and Boyce 1995, Bergstrom and Boyce 2000). For these reasons and also because the behavior of this material is strictly influenced by the shape of the part, in this work has been preferred to print a disk of PTFE and evaluate the stress- strain curve in compression from an experimental test. This

curve, in the following, will be used for the fine element analysis of the proposed models.

A disk of PTFE, of about 50 mm of diameter and 8 mm of thickness, has been printed with virgin PTFE, the material was supplied by HEROFLON. The printing process expected an heat treatment and this process is usually repeated several times and is described below.

Preforming:

- ✓ the dust temperature must be between 20 and 25 °C, before loading into the mold and during preforming
- ✓ Preforming pressure: 45 MPa
- ✓ Initial compaction speed: 50 mm/min, descending at 20 mm/min when the pressure start to rise
- ✓ Lay off at the max pressure: 1.5 min
- ✓ Release time of pressure very slowly to avoid breaks
- ✓ Release time of stress before the sintering at the temperature of 20-25°C: 6 hours.

Steps of the heat treatment (sintering cycle) see Figure 2.40:

- ✓ Form 25 to 370°C in 2h30min
- ✓ At 370°C for 30min
- ✓ From 370 to 25°C in 2 hours

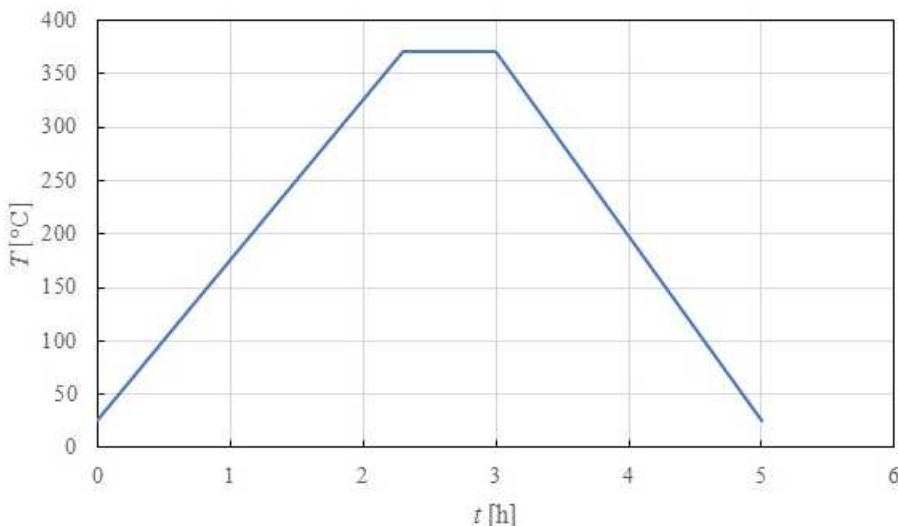


Figure 2.40 Heat treatment



Figure 2.41 The PTFE virgin dust into the mold



Figure 2.42 The molding equipment



Figure 2.43 The printing process: preforming pressure



Figure 2.44 Equipment for the heat treatment



Figure 2.45 Printed disk of virgin PTFE

In the following figures are reported the equipment for the compression tests (Figure 2.46) of the disk and the disk after the test. The test has been conducted at the velocity of 1.3 mm/s.



Figure 2.46 Compression test machine

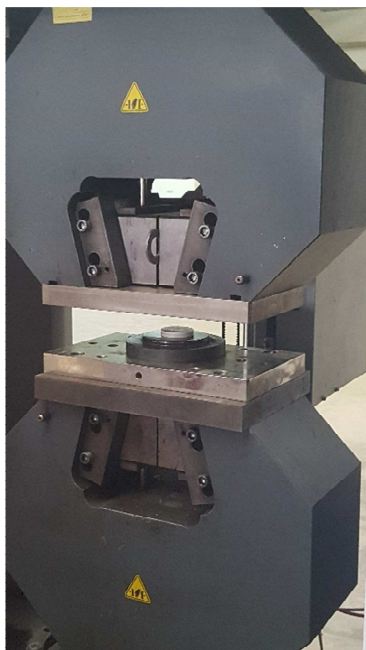


Figure 2.47 Compression testing machine

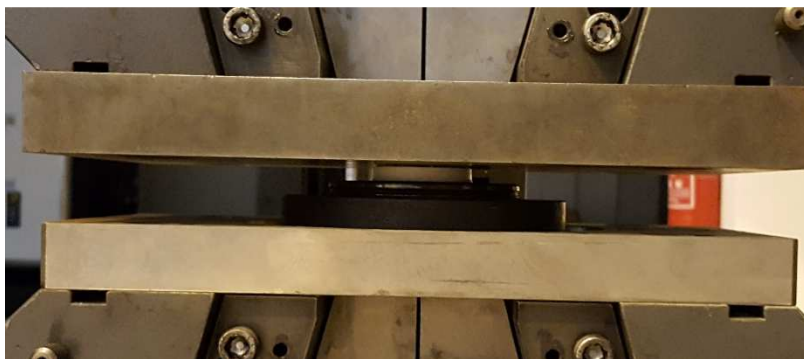


Figure 2.48 Disk of virgin PTFE during the test



Figure 2.49 Disk of vergin PTFE after the compression test

As shown in Figure 2.49, the dimensions of the disk are changed: after the test is possible to observe that the diameter has increased and, obviously, the thickness is reduced.

The results of the tests in terms of stress-strain curve are reported in Figure 2.50, and have been used to calibrate the constitutive model for PTFE in the software ABAQUS CAE.

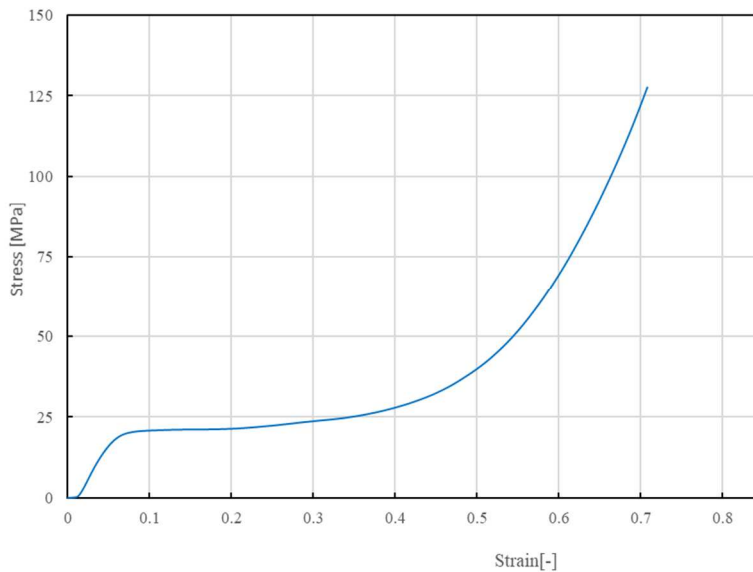


Figure 2.50 Stress-strain experimental curve in compression for the vergin PTFE

2.3.2 Friction sliding

In order to better understand the functioning of sliding devices, it is necessary to study the basic mechanism of this phenomenon. This requires a complete understanding of how friction between interfaces originates, this also to better interpret the results presented in this thesis. This section presents a physical interpretation of the friction phenomenon that develops in particular between a stainless steel interface and the other of PTFE, some of the most important aspects of prototype will be highlighted.

Friction is the resistance to motion, which exists when a solid object is moved tangentially with respect to the surface of another that it touches. This dissertation aims at explaining the “*sliding solid friction*”, which is friction caused by sliding movements between solid bodies.

The friction force F , at the interface, will be described by the classic *Coulomb friction law*:

$$F = \mu N , \quad (2.92)$$

where μ is the friction coefficient and N is the normal load acting in the interface. In accordance with the simplified theory of Coulomb for sliding bodies, the friction force is directly proportional to the applied normal load and is opposed to the direction of the motion. By means of Equation (2.92) it is possible to define the static or breakaway coefficient of friction as the ration, which is different with respect to the sliding coefficient of friction that occurs during the motion between two sliding surfaces.

The dynamic friction coefficient is considered independent from the actual contact area and sliding velocity. However, experimental experience demonstrates that this simplified theory can not be applied to all isolation systems (e.g. Friction Pendulum).

2.3.2.1 Basic mechanism of friction

To better understand the basic mechanisms of friction it is important to describe the microscopic events that cause friction. For this reason, here is reported an overview of the microscopic aspects of friction, this is limited to the events that may provide physical insight into the frictional behavior of sliding bearings (Bowden and Tabor 1950, 1964, 1973). Various mechanisms of friction have been proposed in the past years. The origin and magnitude of the frictional force is given from the “adhesion theory”, that considers the intimate atomic bonds that interact when two solid materials are placed in contact (Figure 2.51).

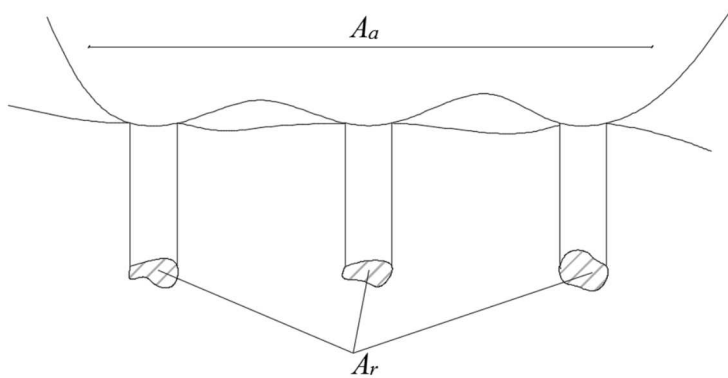


Figure 2.51 Schematic illustration of an interface, showing the apparent and real areas of contact

Some regions on their surface will be very close together in some regions called “junctions” and the sum of the areas of all the junctions constitutes the *real area of contact*, A_r . The total interfacial area consists of the contact area and also of those regions denoted as the *apparent area of contact*, A_a . When the two surfaces are pressed together by a load, a sliding is induced and the frictional force is given by the following equation:

$$F = sA_r, \quad (2.93)$$

where s is the shear strength of the junctions.

In spite of a discrete number of frictional phenomena are explained by the postulate mentioned above, friction mechanism presents some criticisms and limitations and still now it is generally recognized that the adhesion does not provide a clearly separate contribution of friction. Although, the main resistance to sliding arises from the need to shear of adherent surface atoms, there are a number of other important factors to be taken into account, such as:

- Roughness component: this component arises from the need, during the sliding of rough surfaces, to lift one surface over the roughness of the others. If we take into account the asperity θ , a contribution of the friction will be produced. However, if we consider a plane surface, during the motion there may be negative as well as positive values of θ . Summing up for all the contacts, the roughness friction contribution tends to zero and the remain contribution is about 0.05 to the overall friction coefficient.



Figure 2.52 Schematic illustration of the roughness of sliding surface. Positive and negative θ coexist

- Plowing component: when a hard surface has a sharp asperity and it slides over a soft surface, it will tend to dig into the softer surface and produce a plastic deformation. The energy of deformation represented by the groove must be supplied by the friction force, which will have the plowing contribution. By a simple calculation with a circular cone, asperity digs into a softer surface, as schematically illustrated in Figure 2.53.

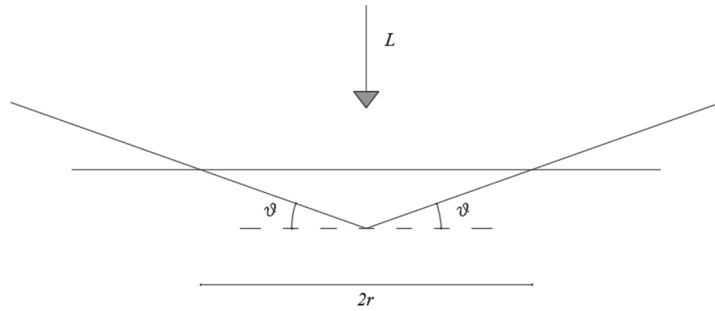


Figure 2.53 Schematic illustration of a cone pressed into a flat surface. The asperity moving horizontally creates a groove which is swept out of A_p

During sliding, the penetrated area A_p is given by:

$$A_p = \frac{1}{2} 2r \cdot r \tan \theta = r^2 \tan \theta. \quad (2.94)$$

The frictional force will be:

$$F = \pi r^2 s + r^2 \tan \theta p, \quad (2.95)$$

where:

$$p = \frac{L}{\pi r^2} \quad (2.96)$$

represents the pressure in the junction.

- Body effects: wear debris and contaminants at the sliding interface contribute with an additional term to the friction force. The contribution is due to plastic deformation as agglomerates of debris and contaminants roll between the surfaces or as they indent these surfaces.
- Viscoelastic Effect: polymers, such as PTFE, exhibit viscoelastic behavior. As asperities of a harder material slides over a viscoelastic material, some energy is dissipated, due to viscoelastic deformation, contributing thus an additional component to the friction.

It is believed that all these mechanisms contribute in the generation of friction in various degrees depending on the particular situation.

However, we will recognize that adhesion and mechanical deformation (elastic, plastic or viscoelastic) are collectively responsible for friction. Moreover, we will recognize that the real area of contact is of paramount importance in the qualitative description of friction at the macroscopic scale.

2.3.2.2 Static and sliding friction

The static (or breakaway) friction is the maximum force, which exists to start a macroscopic motion in a solid. The breakaway frictional force decreases, when we compare to the sliding frictional force, when macroscopic motion occurs. It is noticed from experimental results that the static friction is higher than the sliding friction force. Figure 2.54 illustrates a schematic test of a friction pendulum device, in which the low friction material that interfaces the stainless steel concave surface is an unlubricated polymer composite with about 400 compressive yield strength.

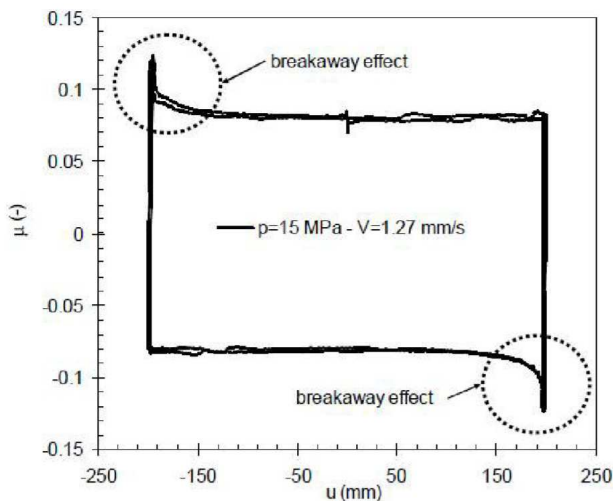


Figure 2.54 Typical friction force-sliding loop of polymer-stainless steel interface without the contribution of restoring stiffness W/R (pressure=15 MPa, peak velocity=1.27 mm/sec) (Trovato 2013)

The interface was at constant average pressure of 15 MPa. A cycle of sinusoidal motion with a pick velocity of 1.27 (mm/sec) was imposed. The difference between the static and sliding values of the coefficient of friction is relevant.

The stick slip

The stick slip phenomenon is a common experience in the sliding on one body over another under the effect of a continue force, and sometimes at constant or close to constant velocity. In displacement controlled testing of a sliding bearing (i.e., motion is imposed by an actuator and measurement of the friction force is made), stick-slip behavior is manifested as fluctuation in the recorded friction force versus time. Conversely, in a force controlled test the behavior is manifested as motion with stops. Stick-slip may be an intrinsic property of the sliding interface or more often is the result of inertia effects and the flexibility in the testing arrangement, although the phenomenon may be aggravated by the frictional behavior of the interface.

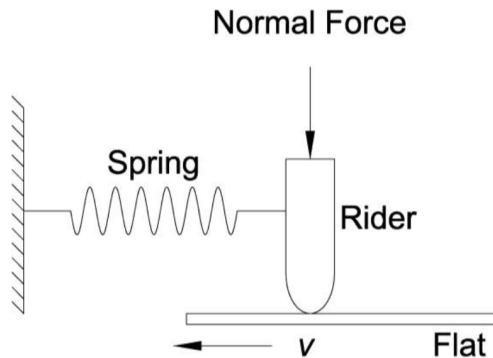


Figure 2.55 Schematic representation of a friction apparatus.

The stick slip phenomenon could be explained considering the sliding situation represented in Figure 2.55, in which a rider is fixed to a support by means of a spring and posed on a surface in motion under a constant velocity. It is supposed that the velocity is low so that the rider keeps up with the movement of the flat and the damping is consequently negligible.

Supposing a friction force displacement plot as shown in Figure 2.56 (a) if we start the run the rider will move over the flat maintaining a constant velocity. This phase is steady until the point is reached. At this point the frictional force drops abruptly and the rider tries to adjust its position following the force-displacement function of the spring. The discrepancy created between the straight line of slope and the friction force is highlighted with a dashed area. This portion has the dimension of energy, and it represents excess energy in the system, which becomes potential energy for the movement of the rider. Then the body slips until it reaches the point where all the kinetic energy has been used. The spring force at this point is below the friction force, so that the rider will stick to the flat and it will be dragged along by it until the point, where the friction force is large again to initiate relative motion.

In Figure 2.56 (b) it is plotted the friction force as a function of time. The path denoted an irregular stick slip that occurs really frequently with the sliding of clean metals, and the sliding of metals covered with a partially worn away solid film lubricant.

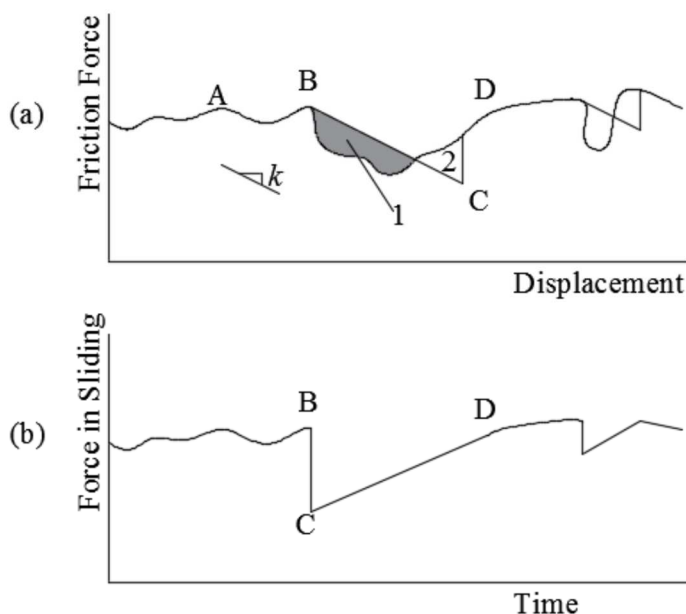


Figure 2.56 (a) A schematic hypothetical force displacement plot. (b) Friction record corresponding to the force displacement plot

In the first case the stick slip is basically due to the coalescence of the area contacts junctions in a larger junction, creating a severe fluctuation of the frictional force. In the second case the fluctuation arises because the rider proceeds alternately areas covered by the film and regions, in which the film is absent or worn.

2.3.2.3 PTFE- polished stainless steel sliding

PTFE is a synthetic fluoropolymer of tetrafluoroethylene (well known as the brand name Teflon by DuPont Co.), this material, or other PTFE based materials, has many applications and is one of the most used materials for contact interface in sliding isolators. The friction for this type of interface is basically due to the adhesion and, in the case of PTFE surfaces, the sliding occurs only at the interface, unlike other polymer.

Shear resistance is given, at first approximation, by a linear function of the actual pressure, which is the pressure on the real contact area (Tabor 1981).

$$\sigma = \sigma_0 + \alpha p_r . \quad (2.97)$$

The coefficient of friction is given by:

$$\mu = \frac{F}{N} = \frac{(\sigma_0 + \alpha p_r) A_r}{p_r A_r} = \frac{\sigma_0}{p_r} + \alpha . \quad (2.98)$$

Figure 2.57 shows the reduction of the coefficient of friction with the increase of normal load. PTFE is a viscoelastic material and is therefore subject to creep phenomenon. Experiments conducted by many groups shown increases both in the real contact surface and in the static friction force relative to the loading time. Other tests on sliding devices with PTFE interface were conducted by various authors to take account of the long-term load effect (Campbell et al. 1987, Mokha et al. 1990).

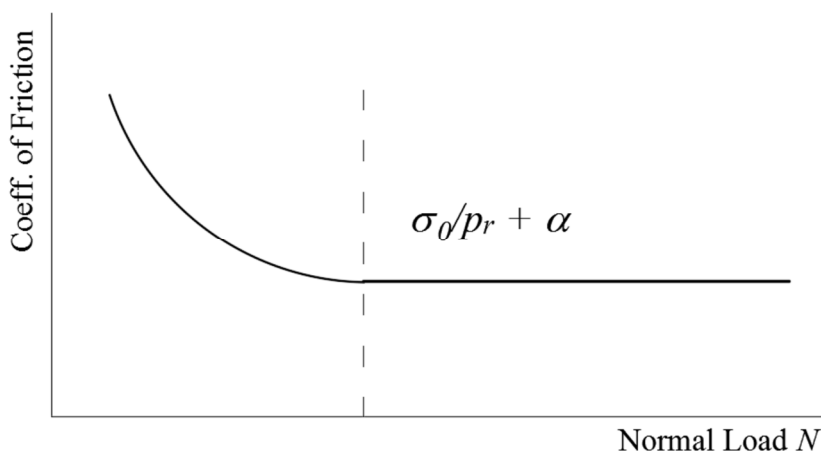


Figure 2.57 Schematic variation of real area of contact, Pressure and coefficient of sliding friction.

The results of these studies can be briefly summarized in the following points:

- static friction results show fluctuations that can not be related to static load. Rather, it has been observed that static friction is greater in the first test carried out on a new sample regardless of load, but is lower in any subsequent test, regardless of load;
- the PTFE time deformation is completed in a very short time, probably in the order of a few minutes or hours, resulting in a constant contact area.

As discussed above, experimental results on the dependence of low friction velocity on normal load suggest that the true contact area is approximately equal to the apparent area of device. An explanation for this phenomenon can be given by studying the PTFE deformation rate in confined compression conditions, where, in very short time, the true contact area is approximately equal to the apparent area of the device.

2.3.3 Theory of frictional heating

Due to the mechanical work done to overcome the friction forces involved during the motion, the sliding motion which occurs in polymer-stainless steel surfaces is coupled with a frictional heating. Applying the frictional heating concept it is important to understand which parameters are involved during the sliding motion, such as bulk, contact, and flash temperature (temperature rise).

The bulk temperature is defined as the average temperature of the body prior to frictional heating, the bulk temperature, T_b , remains constant in the body at some distance from the location of frictional energy dissipation. Upon frictional heating, the surface temperature ascends from this bulk temperature to a contact temperature, T_c , at each point comprising the real area of contact. This temperature increase is commonly referred to as the flash temperature, T_f . Therefore:

$$T_f = T_b - T_c. \quad (2.99)$$

When two surfaces engage in sliding over a given contact area, the thermal energy generated per unit time, q , is assumed to be distributed such that part of the heat, namely $q_1 = \gamma_1 q$, penetrates the first body, as the remainder, $q_2 = \gamma_2 q$, enters in the second body. The coefficients γ_1 and γ_2 are known as *heat partition factors*.

As a function of the thermal properties, bulk temperatures, and relative speeds of the respective components, expressions for γ_i have been developed recognizing that:

$$\gamma_1 + \gamma_2 = 1 \quad (2.100)$$

and that the contact temperature at each point on the interface is identical for both surfaces. Typically, only the maximum or mean surface temperatures within a given contact area are equated to ease the analysis.

Another important quantity is the *thermal conduction*, which describes the phenomenon by which heat is transported or transferred from

high to low temperature regions. The property that characterizes the ability of a material to transfer heat is the thermal conductivity

$$q = -k \left(\frac{\partial T}{\partial n} \right), \quad (2.101)$$

where q denotes the heat flux, or heat flow, per unit time per unit area, k is the thermal conductivity, T is the temperature and n is the normal of the surface of the body. The units for q and k are W/m^2 and $W/(m^\circ C)$ respectively. It should be noted that the above equation is valid for only steady-state heat flow, that is, for situations in which the heat flux does not change over time. In Table 2.3 are reported the value of k for stainless steel and PTFE.

	Thermal conductivity $W/(m^\circ C)$	Thermal diffusivity mm^2/s
Unfilled PTFE	0.24	0.010×10^{-5}
18%Cr, 8% Ni Steel	16.3	0.444×10^{-5}
15%Cr, 10% Ni Steel	19	0.526×10^{-5}

Table 2.3 Thermal properties of PTFE and stainless steel

The specific heat is the amount of heat per unit mass required to raise the temperature by one degree Celsius. The relationship between heat and temperature is usually expressed in the form shown below where c is the *specific heat*, and its units are $J/(kg^\circ C)$. The relationship is not applicable if a phase change is encountered, because the heat added or removed during a phase change does not change the temperature but the physical state of the molecules, by increasing their kinetic energy

$$q = c_p m \Delta T, \quad (2.102)$$

where m is the mass of the body.

Dividing the thermal conductivity by density ρ and specific heat capacity at constant pressure, we gives the *thermal diffusivity* D

$$D = \frac{k}{\rho c_p} . \quad (2.103)$$

It has the SI unit of m^2/s , in Table 2.4 the values of thermal diffusivity for various metal are reported:

Material	Thermal diffusivity m^2/s	Thermal diffusivity mm^2/s
Silver, pure (99.9%)	1.6563×10^{-4}	165.63
Gold	1.27×10^{-4}	127
Copper at 25°C	115×10^{-6}	255
Aluminium	8.418×10^{-5}	84.18
Steel, 1% Carbon	1.172×10^{-5}	11.72
Stainless Steel 304A	4.2×10^{-6}	4.2
Stainless Steel 310 at 25°C	3.352×10^{-6}	3.352
Iron	2.3×10^{-5}	23

Table 2.4 Thermal diffusivity of various metals.

It is also possible to define the *Péclet number*, P_e , that is a dimensionless number defined as:

$$P_e = \frac{\rho c_p v_c u_c}{k} = \frac{v_c u_c}{D} , \quad (2.104)$$

where v_c is the velocity and u_c is a characteristic length. It represents the thermal energy transported by the movement or convection of the medium to the thermal energy conducted away from the region where the frictional energy is being dissipated.

To evaluate the temperature rise at the sliding interface the Carslaw and Jaeger Theory (1959) has been typically used. These authors analyzed the problem of a semi-infinite solid subjected by a constant heat flux q (Figure 2.58).

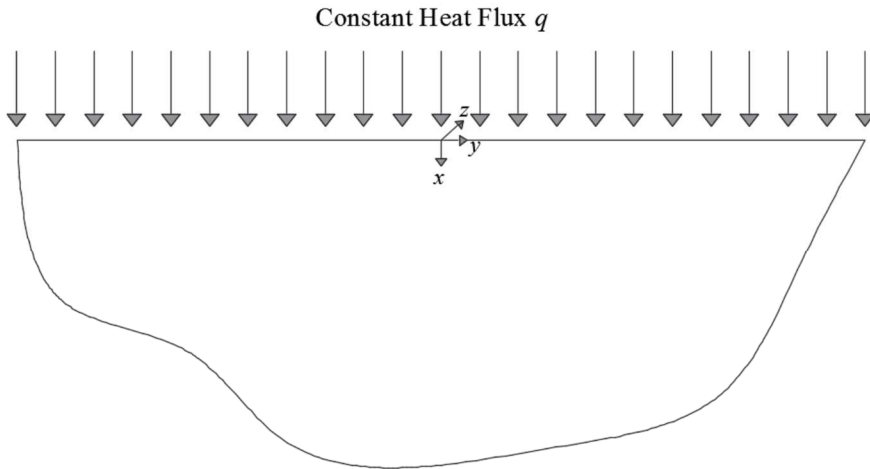


Figure 2.58 Semi-infinite solid with constant heat flux at the surface (Carslaw and Jager 1959)

The sliding contact may be considered as two solid bodies, of which one or even both move at uniform speed past heat source, which represents the sliding contact surface. This source has a heat flux distribution, q , with an average value of q_{av} . A schematic illustration of the problem is given in Figure 2.59. The maximum contact temperature, T , will occur at the surface of either body and it could be evaluated with equation (2.99). The temperature rise with respect to the bulk temperature will occur at the surface of both bodies and it is evaluated as,

$$T_s = F \frac{\gamma q_{av}}{b} \sqrt{t}, \quad (2.105)$$

where:

- t represents the time during which any points on the surface is exposed to heat

- $b = \sqrt{c_p \rho k}$ is a thermal contact coefficient
- F is dependent on the form of the heat flux distribution, q .

For example, for a square heat source with uniform distribution, we obtain $q = q_{av}$ and $F = 2/\pi^{1/2}$, which is a close approximation for a semielliptical distribution while γq represents the portion of heat entering to the body for which the heat partition factor is referred. With different notation, and considering reasonable that the portion has $q_1 = 0$ and $q_2 = q$ the equation (2.105) could be written as

$$T_s = \frac{2q}{k} \left(\frac{Dt}{\pi} \right)^{1/2}. \quad (2.106)$$

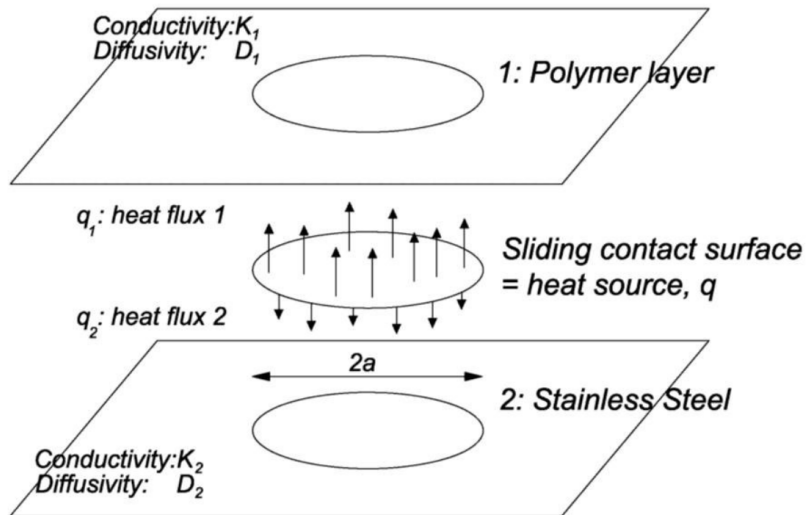


Figure 2.59 Schematic illustration of the sliding contact surface problem (Carslaw and Jager 1959)

In applying equations (2.105) and (2.106) it must be pointed out that the solution is valid for a half-space with heat flux over the entire free surface (see Figure 2.59), whereas the study case has a finite plan dimensions and depth. The approximation $q = \text{const}$ is not, in general, true because the heat flux generated by friction is dependent on the variation of

time and space, of the friction forces, and of the normal load distribution. Furthermore the effects of radiation and convection are not considered because the problem is limited for short time intervals. For longer time these factors could play an important role, and eventually a steady condition may be reached.

2.4 STEEL: an elastoplastic material

2.4.1 Material main features

The term *steel* identifies particular iron-carbon alloys characterized by well defined percentage quantities of the components. In particular, the iron-carbon alloys are distinguished, on the basis of the amount of carbon (C), in:

- ✓ *cast iron*, if the carbon content is more than 1.7%;
- ✓ *steel*, when the carbon content is lower.

The steels for buildings for civil and industrial use have a carbon content indicatively between 0.1% and 0.25%. Carbon elevates the characteristics of resistance, but reduces the ductility and weldability of the material; for this reason, construction steels must necessarily be characterized by a low carbon content. In addition to iron and carbon, in construction steels there are also modest quantities of other elements, some of which are already present in the raw material and not completely eliminated in subsequent processing and part instead specifically added to give it certain physical and mechanical characteristics.

The steel material is characterized by a constitutive stress-strain law with symmetric tensile and compressive behavior. It is usually determined by means of the tensile test on suitably pieces obtained from the steel profiles.

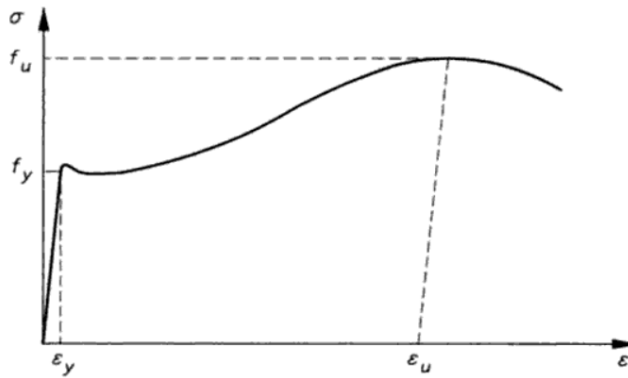


Figure 2.60 – Typical steel constitutive law for structural use

In Figure 2.60, for a construction steel, the typical constitutive law is shown due to a monoaxial stress state. In particular from Figure 2.60, it is possible to define the following phases:

- a first stretch that is almost straight (*elastic phase*) in which the material has practically linear elastic behavior until the yield stress f_y is reached. The deformation corresponding to f_y is indicated with ε_y . In this first section the slope identifies the modulus of elasticity of the material (Young's modulus E);
- a *plastic phase* characterized, in the $\sigma - \varepsilon$ reference system, by an extremely reduced or even zero slope;
- a last stretch (*hardening phase*), in which the slope is noticeably lower than the elastic phase, characterized in any case by an increasing tension until the specimen is broken corresponding to the value f_u .

Usually the steel constitutive law is schematized with linear strokes, as shown in the Figure 2.61, and in the design calculations a *perfect elasto-plastic* model is used, the slope and the increase in resistance of the hardening branch are neglected, limiting the capacity to achieve yield stress. The yield stress is the most significant design parameter, usually determined by a laboratory traction test.

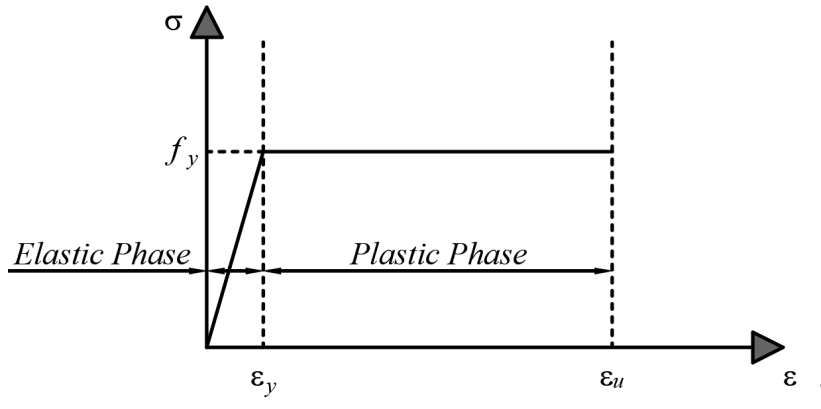


Figure 2.61 – Schematic steel constitutive law

The value of the parameter used in the following analysis are chosen following the EN 10025-2 code, and they are:

Characteristic of Steel			
Density	ρ	kg / m^3	7850
Elastic Modulus	E	MPa	210000
Poisson ratio	ν	-	0.3
Yield Stress (S355)	f_y	MPa	355

Table 2.5 Mechanical characteristic of steel

Chapter 3

FINITE ELEMENT MODELING OF EXISTING DEVICES

3.1 Finite Element Model (FEM) of HDRB device

In this section we describe the finite elements modeling of an HDRB device, carried out using ADINA calculation code (ADINA 2011), and we examine the types of models, materials and loads that can be adopted. For the numerical modeling of the elastomeric device, it is necessary to address the following issues:

1. choice of finished item type;
2. choice of the constitutive law of the material;
3. study of load conditions and contour conditions;
4. discretization of the device;
5. choice of type of analysis.

If we consider points 1 and 4, it must be emphasized that the choice of the order of the element and the type of discretization are subordinated to solution quality and to the computational burden. In fact, to use elements of superior order and more refined mesh enhance the solution quality, but inevitably it raises the computational burden expressed as the time taken by the computer to carry it out the analysis. In general, for the various models, we used a discretization with thickening near the outer edges so as to get, for these zones, more accurate results. Regarding the type of

analysis, a static analysis is performed introducing geometric non-linear conditions of the model from the moment that the problem lies in the field of large displacements and large ones deformations. Concerning the choice of the finite element type for the condition of vertical load, since, together with the geometry of the device, it satisfies the condition of axial symmetry, it is possible to adopt a model axisymmetric. In this model, CAX8 elements can be used for steel plates and CAX8H for rubber layers. For the horizontal load condition, it is not possible to use the axisymmetric model, and the three-dimensional model has become necessary (however suitable for the simulation of vertical loading conditions), in which C3D8 elements for steel plates will be used C3D8H for rubber layers. Depending from this choice of elements you can to overcome the theoretical-numerical difficulties presenting analysis the elements finished with incompressible or almost incompressible materials. For the mechanical behavior of the elastomeric material, the code has several hyperelasticity formulations well known in the literature, or different expressions of the deformation energy density function U , the deformation energy potential used to model the material elastomeric are all those listed and described in §2.2.1. The computation code, with the data of the experimental tests performed on the rubber, provides the characterization of the elastomeric material (i.e. for the definition of the coefficients characteristic of each single hyperelastic model); it determines automatically the values of the coefficients characteristic of the hyperelastic model considered by means of a dedicated algorithm. In this case for the elastomer constitutive law we have choose an hyperelastic Mooney Rivlin model of third order (characterized by 9 coefficients).As far as what concerns the steel plates, it has already been stated in §2.4 and in this case we used a bilinear plastic model.

To model the dissipation and hysteresis phenomena, the elastomeric material was equipped with constants suitable to define the viscoelasticity effects according to the Holzapfel formulation of ADINA. This formulation uses a generalized Maxwell model with α parallel chains of spring-damper, each one characterized by a stiffness E^α and a damping-viscosity factor η^α .

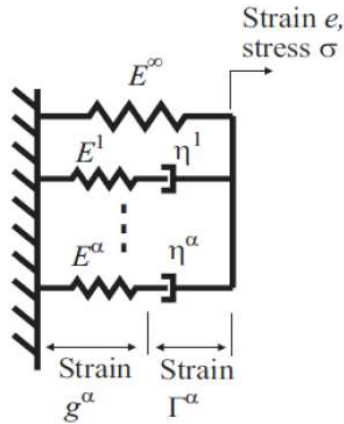


Figure 3.1 Maxwell model for elastomer viscoelasticity used in ADINA

The relaxation modulus of this model is given by:

$$E(t) = E^\infty \left[1 + \sum_{\alpha} \beta^\alpha \exp\left(-\frac{t}{\tau^\alpha}\right) \right] \quad (3.1)$$

Equation (3.1) represents a Prony series where:

$\beta^\alpha = \frac{E^\alpha}{E^\infty}$ is the ratio between the Young modulus of the single chain and the Young modulus at infinite time;

$\tau^\alpha = \frac{\eta^\alpha}{E^\alpha}$ is the late time.

The two parameter of the series should be calibrated on the experimental data.

The model is loaded vertically and horizontally. The horizontal load is applied in the form of lateral displacement for successive steps in a manner so that we can analyze the behavior of devices at different levels of deformation imposed. As for the constraints, they have imposed the conditions in which the isolation device is usually working, preventing the lower metal plate from moving and allowing it to superior to move freely, while keeping it parallel to the lower one. For these reasons, the base nodes of the lower metal plate have been all the knots belonging to the top plate were bound have the same vertical displacements. In the case of a three-dimensional model, it was possible to make the half-way modeling, thus obtaining a considerable one reduction of the total number of degrees of

freedom. In fact, both in horizontal vertical load condition, the half device model verifies the particular conditions of symmetry with respect to the diameter plane, parallel to the direction of the horizontal displacement imposed. In this model, at all points on the symmetric plane will be prevented from moving in the direction orthogonal to the plane of symmetry and rotations around the axis of parallel reference to the plane of symmetry. The fundamental goal of calibration is to reproduce numerically experimental results available for a HDRB 300mm diameter isolator, made with the materials of which the characterization is available.

Geometrical characteristics of HDRB			
External diameter	D	mm	300
Gross Area	A	mm ²	70686
Steel plate diameter	D'	mm	295
Steel plate area	A'	mm ²	68349
n° of rubber inner layers	n		15
Thickness of rubber layers	t	mm	4.8
Thickness of inner steel plate	t_s	mm	2
Thickness of lower steel plate	t_{s1}	mm	25
Thickness of upper steel plate	t_{s2}	mm	25
Total isolator thickness	h	mm	150
Total rubber thickness	t_r	mm	72

Table 3.1 Geometrical characteristics of the HDRB experimentally tested (Cuomo 2007)

Mechanical characteristics of Elastomer			
Elastic Shear Modulus	G	MPa	0.8
Bulk Modulus	K	MPa	2000
Stiffness	k	kN/m	785

Table 3.2 Mechanical characteristics of the HDRB experimentally tested (Cuomo 2007)

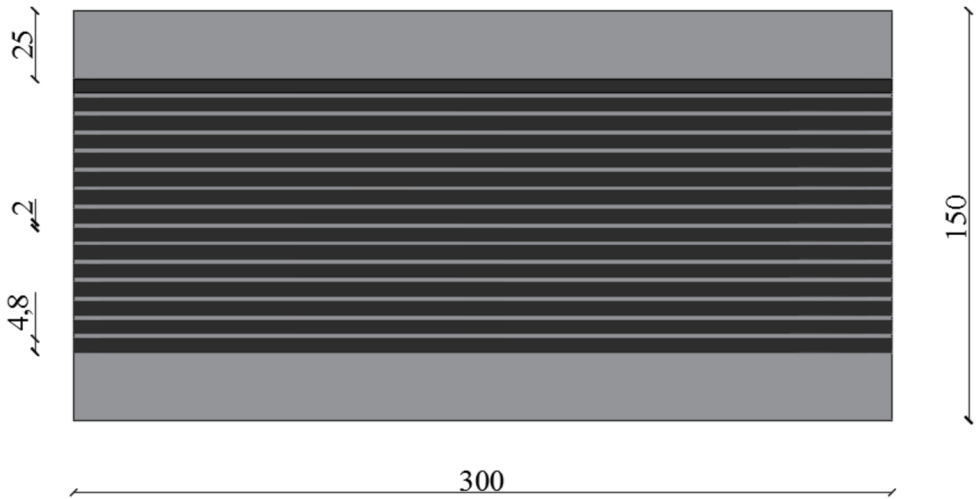


Figure 3.2 HDRB experimentally tested (model)

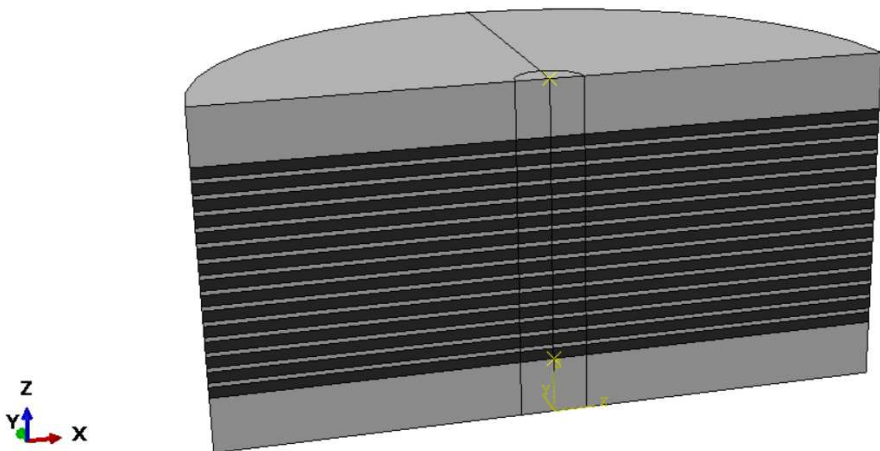


Figure 3.3 Model of the HDRB

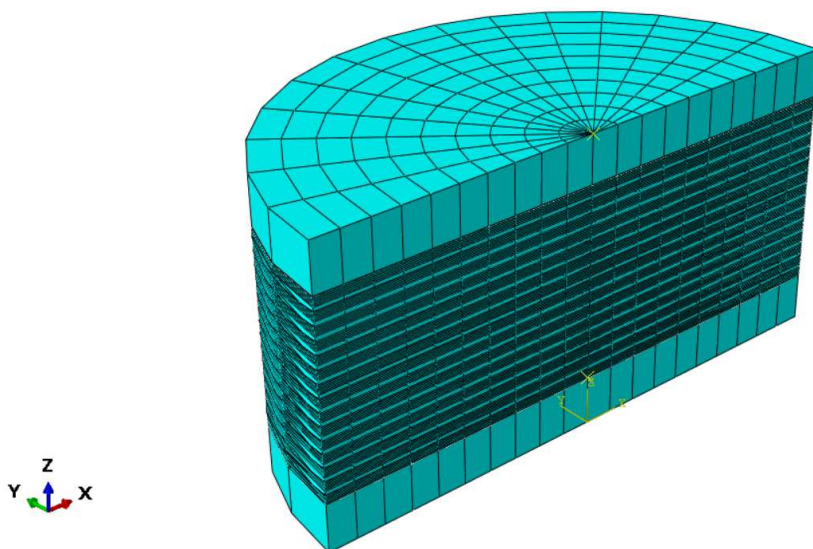


Figure 3.4 Mesh of the HDRB

Two load conditions have been examined:

1. Vertical pressure $p_m = 22.5\text{MPa}$ without shear load. The load was applied with 3 cycles, where the second one has a load level minor of the total one (about 60%).
2. Vertical pressure $p_m = 22.5\text{MPa}$ and a shear load corresponding to a tangential strain of the isolation device of $\gamma_{\max} = 180\%$, that, considering the dimensions of the isolator, corresponds to a horizontal displacement of 135 mm. Only one cycle has been simulated.

In Figure 3.5 and Figure 3.6 are reported respectively the load displacement curve and the deformed shape for the load case 1.

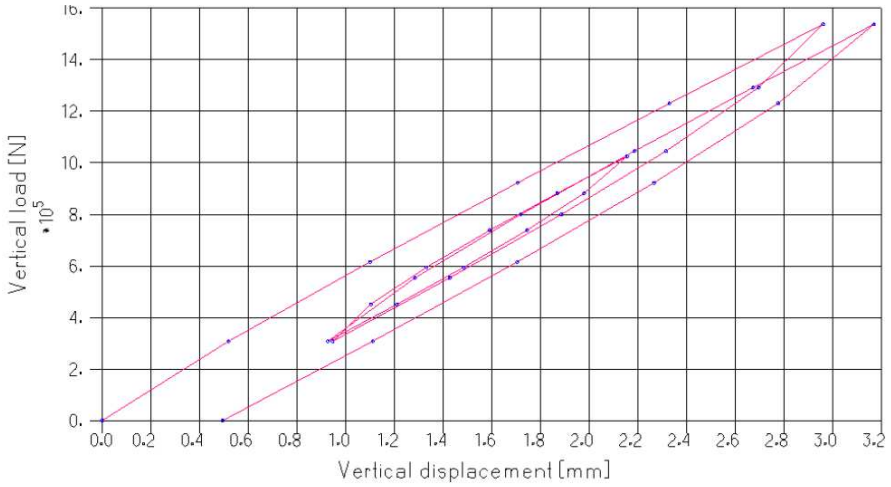


Figure 3.5 Load displacement curve for elastomer seismic isolator (case 1- $p_m=22.5$ MPa)

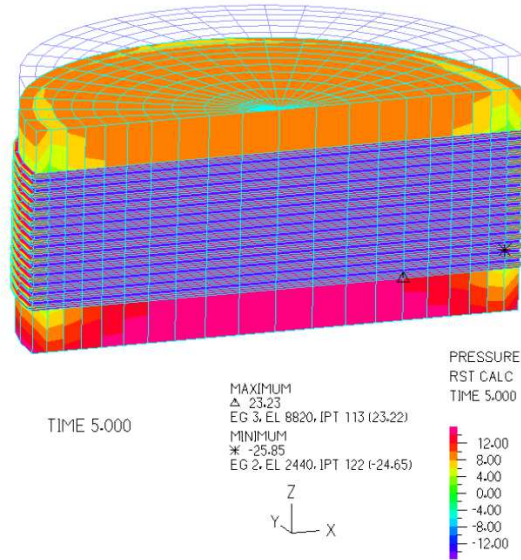


Figure 3.6 Deformed shape for the load case 1

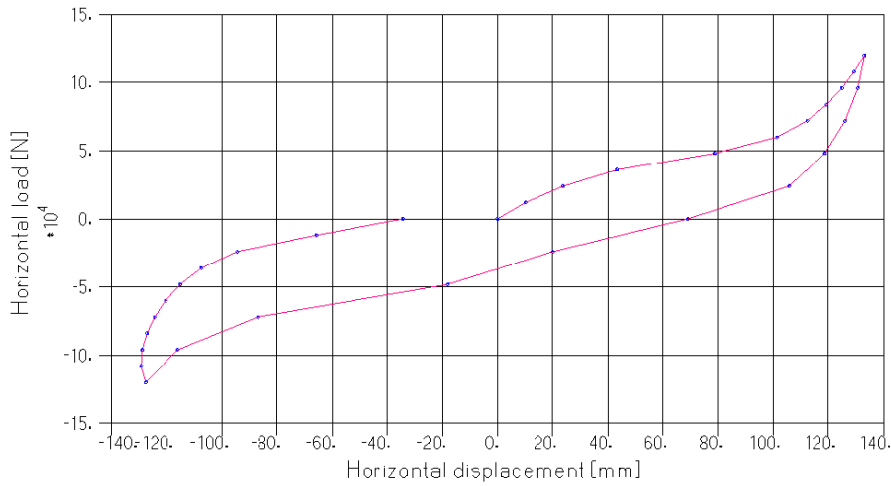


Figure 3.7 Load displacement curve for elastomer seismic isolator (case 2- $p_m=22.5$ MPa and $\gamma=180\%$)

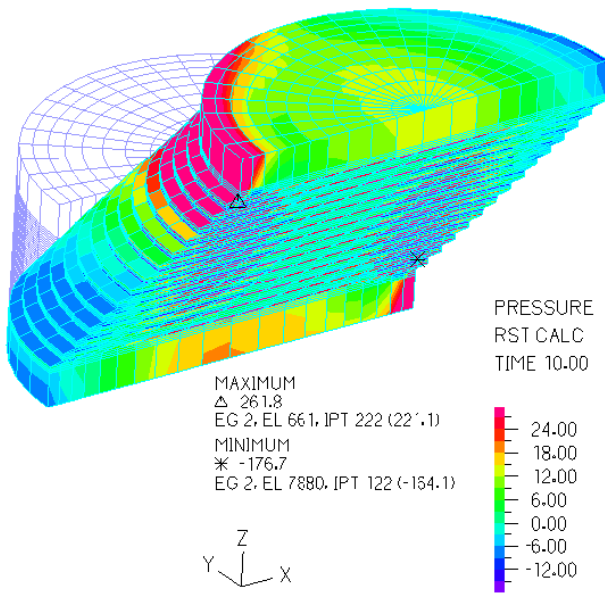


Figure 3.8 Deformed shape for the load case2

By inserting the viscoelasticity parameters, the dissipation of the isolator was succeeded. In Figure 3.9 and Figure 3.10 are reported the comparison between the results obtained from the FEM model and the experimental value described in (Cuomo 2007), we note a good agreement of the two curves.

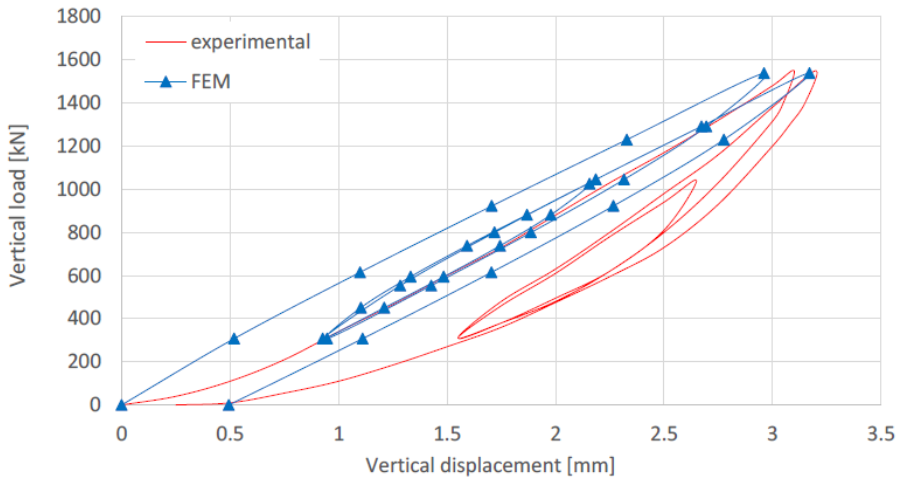


Figure 3.9 Simple compression test (comparison FEM model and experimental results (Cuomo 2007))

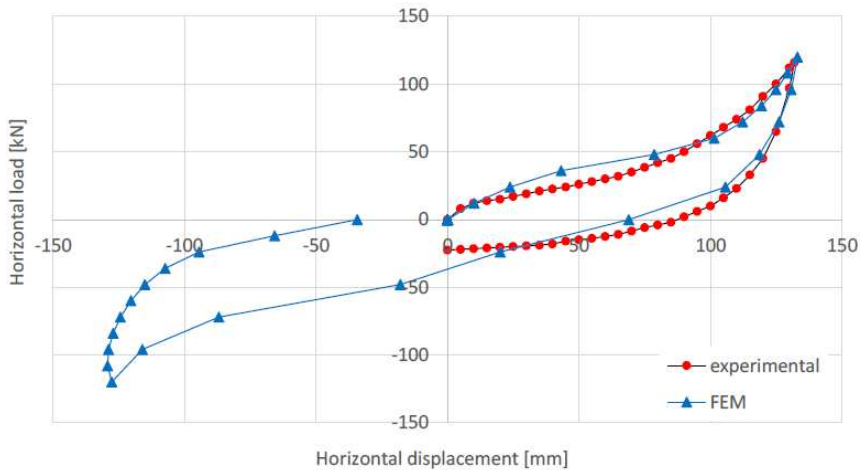


Figure 3.10 Combined compression and shear test (comparison FEM model and experimental results (Cuomo 2007))

3.2 Finite Element Model of Friction Pendulum devices

Friction Pendulum (FP) sliding bearings are widely used devices for seismic protection of bridges (Nestovito and Occhiuzzi 2016, Eröz and DesRoches 2008), buildings (Castaldo et al. 2015) and industrial facilities. The increasing popularity of the FP system can be ascribed to some attractive features as compared to other isolators (e.g. elastomeric bearings) having similar characteristics. The displacement capability of FP isolators is quite large, being limited only by the in-plane geometric dimensions of the device. Furthermore, the quite compact shape and the considerably thickness lower than the elastomeric devices having comparable load and displacement capacity make the FP particularly suitable for retrofit applications in existing structures. The self-centering action, induced by the pendulum operating principle, theoretically guarantees zero residual displacements after the seismic event, while the energy dissipation is controlled by the tribological properties of the sliding interfaces.

Nevertheless, the aforementioned advantages are generally accompanied by a rather complex mechanical behavior observed experimentally, especially when the device is tested under multi-directional paths like in a real earthquake scenario (Constantinou and Mokha 1990, Lomiento et al. 2013, Furinghetti et al. 2014, Mosqueda et al. 2004). Material science and technology have made significant progress to manufacture high-performance materials with enhanced durability, mechanical and physical characteristics under the range of contact pressures, sliding velocities and temperatures typically arising in seismic service conditions (Lissia et al. 2012, Mokha et al. 1990, Tsai et al. 2016). In spite of this, friction degradation and wear in thermoplastic materials adopted in the FP sliding interface cannot be avoided altogether. As a result, the friction coefficient is not constant as postulated by the simplified Coulomb model, but it evolves during an earthquake as it is strongly affected by the operating conditions.

A friction model that neglects the temperature rise would lead to underestimate the displacements expected during seismic events and to

overestimate the dissipative capacity of the isolator accordingly to Kumar et al. (2015) and Quaglini et al. (2014).

The same outcome is achieved by ignoring the bi-directional interaction and considering a uni-directional idealization, as if the two components of a bidirectional input (earthquake) were uncoupled (Lomiento et al. 2013, Furinghetti et al. 2014, Mosqueda et al. 2004). During experiments, it is extremely difficult to measure the temperature at the sliding surface while the slider is in motion, so numerical models could be a useful complement to testing protocols in order to gain a physical insight of the frictional heating and quantify the friction degradation for test conditions other than those prescribed by prototype tests.

The aim of this paragraph is to investigate the thermo-mechanical behavior of the FP via a numerical approach, following De Domenico et al. (2018). A Thermo-Mechanical Coupled (TMC) three-dimensional finite element model is set up in which the generation of frictional heat is reproduced via a moving heat source with local intensity dependent from the instantaneous friction coefficient, the relative velocity and the contact pressure at the sliding surface. The friction coefficient at the sliding interface is adjusted node-by-node, via a customized subroutine implemented into the FE-code the updated friction value is used to compute the heat flux at the next time step in a recursive way.

A simplified phenomenological model proposed in (Lomiento et al. 2013) is here recalled to check the consistency of the results from the developed TMC FE model. The phenomenological model is able to represent the variation of the frictional characteristics by means of a combined function of axial load, sliding velocity and temperature rise through a macroscale cycling variable. Attention is focused on the distinctive behavior observed in FP bearings, when subjected to multi-directional excitations like in a real earthquake scenario. First, we validate the developed model against experimental data concerning cloverleaf bi-directional tests. Also monodirectional tests with the single cloverleaf components are analyzed, so as to highlight the salient differences in comparison with the bi-directional counterpart. The analysis of the kinematics of the device and the assessment of the contact force distribution between the sliding surfaces highlighting some interesting features about the pendulum mechanism and the directionality of the

horizontal resisting force. Then, a wide-ranging parametric study is carried out in order to investigate the thermo-mechanical response of the FP under a few bidirectional orbits. The examined orbits involve different in-plane paths and sliding velocities ranging from 60 mm/s to 320 mm/s in an attempt to cover a broad variety of situations that may be encountered in practice.

3.2.1 Mechanical behavior

In its single concave configuration, cf. Figure 3.11a), the FP bearing is composed of:

- ✓ a primary, lower sliding surface made of polished stainless steel and having a concave profile with curvature radius R , which determines the natural period of vibration and allows the horizontal movement according to the pendulum operating principle;
- ✓ an upper steel plate featuring a secondary concave sliding surface via an internal semi-spherical articulation of radius r , the latter permitting the rotation and assuring the kinematic compatibility of the overall motion;
- ✓ between these two opposed surfaces a lentil-shaped articulated steel slider is placed, whose upper and lower external surfaces are both convex-shaped, so as to match the two concave profiles described above.

These two external surfaces of the slider are coated with a pad of material having specific frictional properties, typically high-bearing-capacity polymer composites like polytetrafluoroethylene (PTFE, Teflon[®]), PTFE-based composites with fillers or other enhanced variants of thermoplastic, self-lubricating polymers such as ultra-high-molecular-weight polyethylene (UHMWPE).

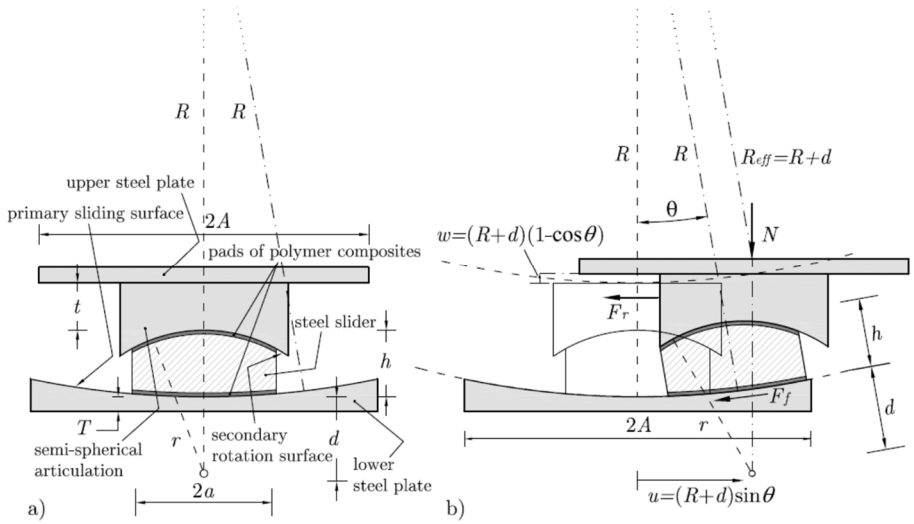


Figure 3.11 Section through a FP bearing: a) constituting elements and materials; b) kinematic analysis (De Domenico et al. 2018)

The coefficient of friction plays a key role in dissipating seismic energy and limiting accelerations and displacements induced in the isolated structure.

A special attention should be taken to the technological design and manufacturing aspects, not only of the primary sliding surface, but also of the secondary rotation surface. Indeed, also the latter surface affects, to some extent, the overall energy dissipated by the device.

The easy way to describe the mechanical behavior of FP bearings is based on the assumption of constant value of vertical load and constant value of the coefficient of sliding friction (Coulomb simplified theory). The FP system incorporates in a single device both the re-centering action, which is due to the curvature of the sliding surface, and the energy dissipation by friction. Consequently, combining the restoring force and the frictional force yields the following rigid-plastic hysteretic model for the total horizontal force (Zayas et al. 1987). The expression of the restoring force is:

$$F = F_r + F_f = \frac{N}{R_{eff} \cos \theta} u + \mu N \operatorname{sgn}(\dot{u}) \quad (3.2)$$

where:

- μ is the friction coefficient;
- the subscript r and f denote respectively the restoring and frictional contribution to the total horizontal force F ;
- $R_{eff} = R + d$ is the effective radius of the pendulum that accounts for the dimensions of the slider (Fenz and Constantinou 2006, Lomiento et al. 2013);
- N is the vertical load acting on the FP;
- θ is the rotation angle associated with the horizontal (radial in 3D) displacement u , identifying the position of the slider;
- \dot{u} , represents the sliding velocity;
- $\text{sgn}(\cdot)$ is the signum of the function so that $F = \pm\mu N$ depending on whether \dot{u} is positive or negative, respectively.

The nonlinear behavior of the device is thus converted into an equivalent linear one, as if a simpler spring-damper system could reflect the FP hysteretic behavior.

The equivalent linearized behavior is characterized by the effective stiffness and the effective damping (the adjective effective denotes the linearized counterpart of an intrinsically nonlinear variable) expressed respectively as (Zayas et al. 1987),

$$K_{eff} = \frac{N_d}{R_{eff} \cos \theta} + \mu \frac{N_d}{u_d}, \quad \zeta_{eff} = \frac{2\mu R_{eff} \cos \theta}{\pi(\mu R_{eff} \cos \theta + u_d)} \quad (3.3)$$

where N_d and u_d are the *design* vertical load and displacement, respectively.

The linear visco-elastic idealization, in the expressions of K_{eff} and ζ_{eff} , implicitly assumes that the frictional properties remain constant throughout the seismic event, whereas experimental evidence highlights the variability of the friction coefficient during an earthquake.

In principle, the lining material coating the upper and lower surface of the slider should be selected such that guarantees stable frictional

behavior under a range of contact pressures, sliding velocities and temperatures typically arising in seismic service conditions. Unfortunately, as we have seen in Chapter 2, friction degradation and wear in thermoplastic materials are rather complex phenomena that are actually affected by the operating conditions, and the friction contribution entering in (3.2) should be expressed more appropriately by a combined function of axial load (or contact pressure), sliding velocity and temperature rise at the sliding surface

$$F_f = \mu N, \quad \text{with } \mu = \mu(N, v, T) \quad (3.4)$$

The heating phenomena occurring at the sliding surfaces produce a significant friction degradation, so a friction model that neglects this reduction would lead to unconservative estimation in terms of displacements and dissipation capacity of the isolator.

It is well known that earthquake excitations are generally multidirectional, while K_{eff} and ζ_{eff} parameters arise from a simple unidirectional idealization of the FP behavior, as if the device motion were uncoupled in two orthogonal directions. Experimental investigations (Lomiento et al. 2013, Furinghetti et al. 2014, Mosqueda et al. 2004) have demonstrated that there exists significant coupling between the orthogonal components of the FP response (bi-directional interaction). Indeed, for bi-directional motion the displacement and forces across the isolator are expressed by vectors, $\mathbf{u} = [u_x, u_y]^T$ and $\mathbf{F} = [F_x, F_y]^T$, and the force-displacement relationship becomes:

$$\begin{bmatrix} F_x \\ F_y \end{bmatrix} = \begin{bmatrix} F_{rx} \\ F_{ry} \end{bmatrix} + \begin{bmatrix} F_{fx} \\ F_{fy} \end{bmatrix} = \frac{N}{R_{eff}} \begin{bmatrix} u_x \\ u_y \end{bmatrix} + \mu N \frac{1}{\|\dot{\mathbf{u}}\|} \begin{bmatrix} \dot{u}_x \\ \dot{u}_y \end{bmatrix} \quad (3.5)$$

where $\|\dot{\mathbf{u}}\| = \sqrt{\dot{u}_x^2 + \dot{u}_y^2}$ is the magnitude of the instantaneous velocity.

In Figure 3.12 is sketched the in-plane motion of the slider along with the force components entering in equation (3.5).

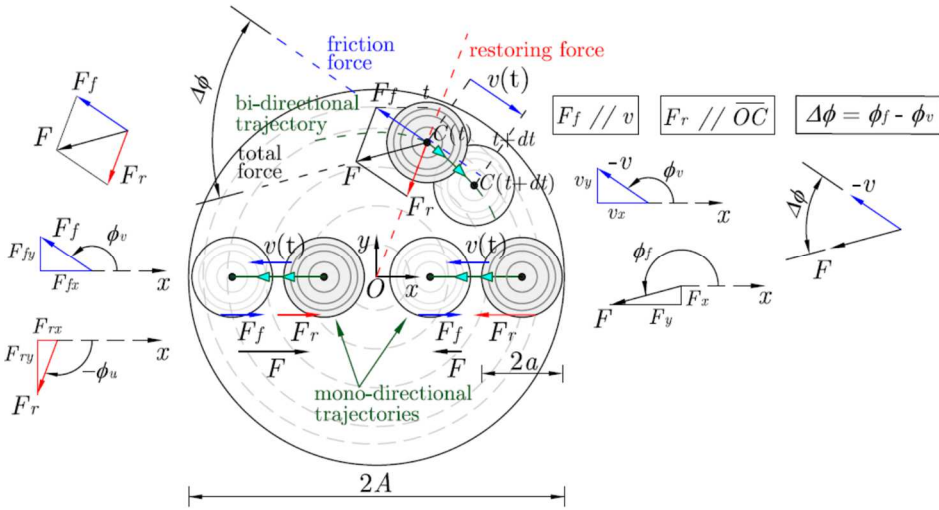


Figure 3.12 Sketch at two time-instants of in-plane motion of the slider with the resulting forces highlighted (De Domenico et al. 2018)

At any instant of time, the slider interface undergoes a displacement increment in the direction specified by the angle ϕ_v with respect to the x -axis, with $\phi_v = \arctan(\dot{u}_y / \dot{u}_x)$. The frictional force opposes the sliding motion and therefore its direction is defined by the same angle ϕ_v , whereas the line of action of the restoring (re-centering) force is radial, i.e., it is parallel to the vector \overline{OC} at any time instant, being O the center of the isolator and C the center of the lower interface of the slider.

For a reference axis system with origin at the center of the isolator as that shown in Figure 3.12, the direction OC can be represented by the angle $\phi_u = \arctan(u_y / u_x)$. Finally, the direction of the total force is identified by the angle $\phi_f = \arctan(F_y / F_x)$. From Figure 3.12, it emerges that an angular shift exists between the direction of the velocity vector and that of the force vector, namely $\Delta\phi = \phi_f - \phi_v$. Indeed, the restoring force component gives rise to deviations of the total resisting force with respect to the active seismic force, directed along the traveled trajectory (or instantaneous velocity). Notice that these deviations would be zero under uni-directional excitations, because in this case the restoring force and the friction force

would be parallel, with either the same sign or one pointing toward the other, as shown in the mono-directional trajectories depicted in Figure 3.12.

The same result would be obtained under general multi-directional excitations but at (not concave) sliding surface, because in this case the restoring force would cancel out as $R_{eff} \rightarrow \infty$ in equation (3.5). Moreover, by comparing equation (3.5) with equation (3.2), it is found that neglecting the orthogonal coupling in bi-directional excitations leads to an underestimation of displacements and an overestimation of forces (and dissipation of energy), thus implying that the design of the overlying isolated structure would be carried out in a nonconservative (unsafe) manner (Eröz and DesRoches 2008).

3.2.2 Macroscale phenomenological model

The sliding velocity affects the friction coefficient as a result of the viscous nature of the PTFE-type composite used for the liner. According to experimental observations, the coefficient of friction increases with increasing sliding velocity up to a constant value reached at a specific velocity threshold (approximately 130 mm/s in Constantinou et al. 1990, a bit lower namely about 25 mm/s in Mosqueda et al. 2004). Therefore, an exponential function describing the relationship between μ and the sliding velocity seems to be suitable for common applications (Chang et al. 1990). A widely recognized expression, incorporated in a few software codes like SAP 2000 (Computers and Structures 2013), is that proposed by Constantinou et al. 1990:

$$\mu = \mu_{\max} - (\mu_{\max} - \mu_{\min}) \exp(-\alpha |\dot{u}|) \quad (3.6)$$

where:

- μ_{\max} and μ_{\min} are the coefficients of friction at large and very low sliding velocity, respectively;
- α is a constant (for given bearing pressure) determining the shape of the relationship.

Similar exponential relationships to equation (3.6) have been developed by researchers to describe the dependence of μ upon contact pressure (Lomiento et al. 2013, Kumar et al. 2015), as well as upon heating of the sliding interface (Kumar et al. 2015, Quaglini et al. 2014) or, equivalently, some related parameter quantifying the energy dissipated over the repetition of cycles (Lomiento et al. 2013, Furinghetti et al. 2014). Overall, the variability of the friction coefficient can therefore be expressed as a combined function of these three effects.

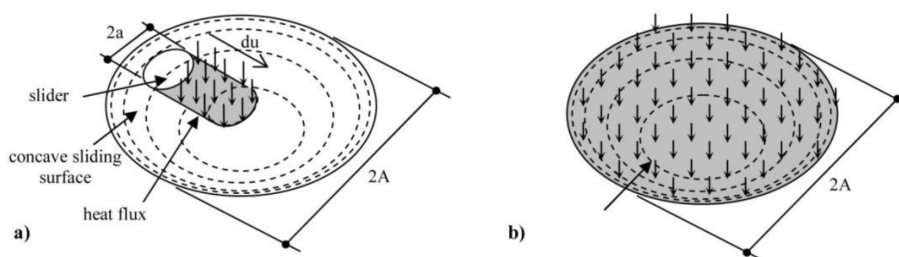


Figure 3.13 Heat flux generated during the time interval dt : a) actual; b) equivalent uniformly distributed (Lomiento et al. 2013)

A simple but effective phenomenological model describing all those effects has been presented in (Lomiento et al. 2013), and resumed in De Domenico et al. 2018, validated against a wide class of experimental data. In this model, the influence of axial load, sliding velocity and repetition of cycles on the friction coefficient are identified and isolated from each other, so that the combined effect can be expressed as the product of three independent contributions:

$$\mu(N, v, c) = f_N(N) \cdot f_v(v) \cdot f_c(c) \quad (3.7)$$

where:

- $f_N(N)$, $f_v(v)$ and $f_c(c)$ are functions describing the load, velocity and cycling effects;
- N is the compressive vertical load;
- v is the sliding velocity;
- c is a *macroscale* cycling variable identifying the temperature effects over the sliding surface.

The term *macroscale* here adopted refers to the fact that the heating phenomena are not accounted for in a local sense by assessment of the temperature profile in the contact areas, but in an average sense with regard to the overall effects on the friction degradation. The cycling variable c has been introduced based on the observation of the heat flux across the sliding interface. According to the simple sketch of Figure 3.13, the temperature rising is related to the heat flux (power dissipated per unit area) generated by the frictional forces and distributed over the contact surface between the slider and the concave sliding surface:

$$q = \frac{\mu N |v|}{\pi a^2} \quad (3.8)$$

where a is the radius of the contact surface.

The heat flux depends on the relative velocity and the contact force, thus varying in position and intensity during the sliding motion. In Figure 3.13, during the time interval dt the slider undergoes a displacement increment du and the resulting heat flux increment over the traveled gray surface $2a \cdot du$ may be considered as an equivalent heat flux uniformly distributed over the entire concave sliding surface (Figure 3.13b)

$$d\bar{q} = \frac{\mu N |v|}{\pi a^2} \cdot \frac{2a \cdot du}{\pi A^2} = \frac{2\mu N v^2 dt}{\alpha \pi^2 A^2} \quad (3.9)$$

For short duration motion, the temperature rise on the surface is directly related to the cumulative heat flux acting on the surface from the beginning of the sliding motion. The uniformly distributed heat flux developed during the time interval $(t - t_0)$ can be cumulated as follows:

$$\bar{q}(t) = \frac{2}{\alpha \pi^2 A^2} \int_{t_0}^t \mu N v^2 dt \quad (3.10)$$

The macroscale cycling variable $c(t)$, introduced before, is derived from equation (3.10) by elimination of the μ term and it has dimensions of a heat flux:

$$c(t) = \frac{2}{a\pi^2 A^2} \int_{t_0}^t N v^2 dt . \quad (3.11)$$

In equation (3.11) this cycling variable proved to be an effective tool to describe the friction degradation due heating phenomena, although the simplifying assumption of a uniformly distributed heat flux at the sliding interface disregards the existence of higher heat fluxes in areas subjected by more frequent and faster sliding activity.

In Lomiento et al. (2013) a more refined approach is presented, based on the spatial discretization of $c(t)$ to capture an heterogeneous heat flux but the achieved results appeared not significantly altered as compared to that ones of the above simplified model.

Once the cycling variable is defined, the combined model of friction introduced in equation (3.7) can be written out as (Lomiento et al. 2013):

$$\mu(N, v, c) = f_N(N) \cdot f_v(v) \cdot f_c(c) = [\mu_{s0} e^{-N/N_{ref}}] \cdot [\gamma + (1-\gamma)e^{-|v|/v_{ref}}] \cdot [e^{-(c/c_{ref})\beta}] \quad (3.12)$$

where:

μ_{s0} represents the theoretical slow-motion coefficient of friction under no vertical load;

N_{ref} is a load reference value (associated to a 63% friction reduction due to load effects);

γ is the ratio between the fast-motion and the slow-motion coefficient of friction;

v_{ref} is a reference velocity that characterizes the variation rate (associated to a 63% variation of the slow-motion friction coefficient due to velocity increment);

c_{ref} is a reference heat flux that controls the degradation rate of the friction coefficient with the cycling variable: smaller c_{ref} means faster degradation, $c = c_{ref}$ is associated to a 63% friction reduction due to cycling effects;

β is the exponential rate of the friction degradation.

The above experimental parameters should be identified by fitting experimental data from laboratory tests. Finally, we notice that the three independent effects are regulated via three exponential-like functions, according to other analytical models developed in the relevant literature.

3.2.3 Thermo Mechanical Coupled FE model

In this paragraph, a Thermo Mechanical Coupled (TMC) finite element model is set up in order to capture the variability of the friction coefficient from point to point with the local sliding velocity and temperature value. A real full-scale (single concave) FP is addressed here, that was tested at the Caltrans SRMD laboratory at the UCSD (Lomiento et al. 2013). With reference to the symbols defined in the sketch of Figure 3.11, the analyzed FP is characterized by the geometric dimensions reported in Table 3.3.

Dimensions	Length mm
A	435
a	180
R	2235
r	375
T	40
t	120
h	160
d	215

Table 3.3 Geometrical data of the analyzed FP (after Lomiento et al.2013)

The analyzed FP has been modeled through the FE code ADINA (ADINA 2011), employing 3D-solid (hexahedral) elements equipped with 20 nodes for element (i.e. quadratic shape functions are adopted throughout to describe better the kinematics and the contact conditions of the model). The number of FEs has been chosen after a preliminary mesh sensitivity study to assure an accurate FE solution. The total number of FEs and the final mesh is illustrated in Figure 3.14 a) and is composed of 8820 elements and corresponding 42325 nodes, each node having three degrees of freedom (DOFs), namely the three translations with respect to the Cartesian axis system shown in the figure. Note that the upper steel plate rigidly connected to the semi-spherical articulation (cf. Figure 3.11) is not included in the FE model as it does not affect the results. Large displacement formulation is assumed; additionally, the (very small) deformability of the plate components has been accounted for by including the elastic properties of the steel components as reported in Table 3.4 and Table 3.5 along with those of the PTFE pads. Typical thermal parameters of stainless steel and PTFE pads are assumed in order to properly simulate the thermal solution and to solve the TMC problem accordingly. The coefficients of thermal dilatation have been set equal to $1.2 \times 10^{-5} \text{ } ^\circ\text{C}^{-1}$ and $1.6 \times 10^{-4} \text{ } ^\circ\text{C}^{-1}$ for steel and PTFE, respectively.

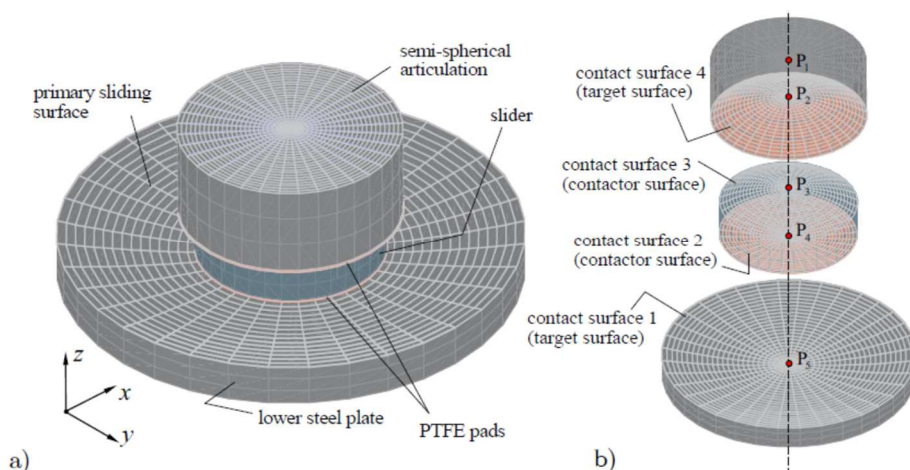


Figure 3.14 FE-model of the FP: a) isometric view; b) exploded drawing with contact surface labels

Mechanical Parameters			
	Elastic Modulus E (MPa)	Poisson's ratio ν -	Density ρ (ton/mm ³)
Steel	$2.0 \cdot 10^5$	0.3	$7.8 \cdot 10^{-9}$
PTFE	$1.5 \cdot 10^3$	0.46	$2.2 \cdot 10^{-8}$

Table 3.4 Mechanical parameters of the materials

Thermal Parameters		
	Conductivity k mW/mm°C	Specific heat C mJ/ton°C
Steel	17	$5 \cdot 10^8$
PTFE	0.25	$12 \cdot 10^9$

Table 3.5 Thermal parameters of the materials

Contact conditions between interfaces have been implemented through the constraint function method (ADINA 2011). For each contact pair that may come into contact during the solution, so-called target and contactor surfaces are defined as reported in Figure 3.14b): at each time instant, the constraint equations are imposed such that the nodes belonging to the contactor surface cannot penetrate the corresponding nodes lying on the target surface (the prevented motion is that along the direction specified by the normal vector to the target surface). The frictional contact heat generation rate at a contactor node G is computed as (ADINA 2011):

$$q_G^{I,J} = \tau \cdot \dot{U} \quad (3.13)$$

where:

τ is the frictional contact force;

\dot{U} is the relative velocity between the contacting bodies I and J at the point of contact.

The heat rate going to the contactor body $f_c q_G^{I,J}$ and to the target body $f_t q_G^{I,J}$ are tuned by two separation parameters f_c and f_t that can account for possible losses, with $0 \leq f_c \leq 1$, $0 \leq f_t \leq 1$ and $0 \leq f_c + f_t \leq 1$.

Owing to the low thermal conductivity of the PTFE pads as compared to that of steel, almost the whole frictional heat generated at each interface enters the surface of the steel part, therefore, a separation factor of 0:99, corresponding to the steel surface, has been assumed in line with other analytical studies (Quaglini et al. 2014). A uniform environmental temperature of $T_0 = 20^\circ\text{C}$ has been set for the entire FE-model at the beginning of the TMC analysis. Conductivity heat transmission is regulated by the thermal parameters reported in Table 3.5, whereas thermal radiation and convection from the sliding surfaces are small and have been neglected, owing to the short time intervals considered. With regard to the mechanical conditions, the FP is fixed on the lower face of the lower steel plate, and the loading condition is applied by means of a constant vertical load (in the z -direction) in conjunction with a history of horizontal displacements applied to the x - and y -directions. Proper constraints are introduced to keep the top surface of the semi-spherical articulation parallel to the bottom surface of the steel sliding plate.

The dependence of the friction coefficient upon axial load, sliding velocity and temperature rise at the sliding interfaces is accounted for in the TMC finite element model. To this aim, in De Domenico et al. 2017, a new customized Fortran subroutine governing the friction coefficient has been implemented in the FE code. This TMC subroutine generates a variability of μ (from node to node) according to the following expression, that is derived from equation (3.12) of the above phenomenological model

$$\mu(N, v, c) = f_N(N) \cdot f_v(v) \cdot f_c(c) = [\mu_{s0} e^{-N/N_{ref}}] \cdot [\gamma + (1 - \gamma) e^{-|v|/v_{ref}}] \cdot [e^{-\psi(T-T_0)^\delta}] \quad (3.14)$$

where ψ and δ are two parameters defining the function $f_T(T)$, describing the friction reduction due to temperature effects. Note that the temperature variable T has been introduced in order to replace the macroscale cycling variable c entering equation (3.12) with a local (nodal) variable quantifying the frictional heating at each point of the sliding surface. In so doing, the higher heat fluxes in the areas interested by more frequent sliding activity give rise to smaller friction coefficients, so that a

spatially varying friction coefficient is obtained over the sliding surface. In conclusion, the thermal solution affects the structural solution (since μ depends on the local temperature) and, in turn, the structural solution affects the thermal solution (since heat generation is produced by contact friction at the sliding interface). The coupled thermo-mechanical problem is therefore based on a system of partial differential equations that are solved in the FE model (ADINA 2011), with the above boundary conditions formulated in terms of temperatures, heat fluxes, displacements and loads.

In order to validate the TMC FE-model, experimental data are here considered. Bi-directional tests following a cloverleaf path were performed at the Caltrans SRMD laboratory at the UCSD (Lomiento et al. 2013), which is equipped with a 6 DOFs shake table specifically designed for full scale testing of isolators and energy dissipators. Monodirectional excitations, consisting in the single cloverleaf longitudinal and lateral components, were also examined to make a comparison between the bi-directional and mono-directional response of the FP. The duration of the experimental tests was approximately 30 s, which corresponds to peak velocities equal to 90 mm/s and 45 mm/s in the longitudinal and lateral direction, respectively. In the FE model, the time is discretized in 200 equally spaced time steps. The cloverleaf displacement pattern is depicted in Figure 3.15 together with the individual longitudinal (along the x -axis) and lateral (along the y -axis) components.

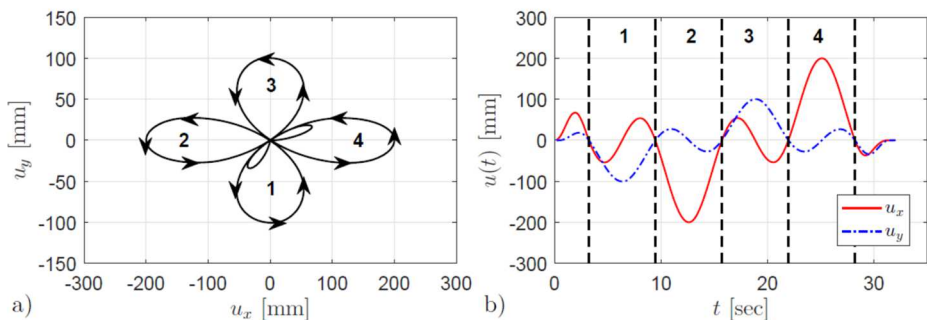


Figure 3.15 Cloverleaf test: a) in-plane trajectory; b) longitudinal (u_x) and lateral (u_y) components of motion (De Domenico et al. 2018)

As shown in Figure 3.15, to avoid the impulse effects due to high accelerations induced at the beginning and at the end of the tests, a starting and an ending branch of limited amplitude were also applied to the FP during the experimental campaign (Lomiento et al. 2013) and simulated in the numerical model accordingly. In the experimental test, the FP was first subjected to a vertical load equal to 6525 kN (corresponding to a contact pressure approximately 30MPa), which was applied by raising the shake table underneath the device, then a bidirectional motion was imposed according to the cloverleaf path described above.

Before comparing numerical and experimental results, we point out some interesting features about the pendulum mechanism under planar, bidirectional motion and the directionality of the horizontal resisting force, based on the remarks introduced in §3.2.1. To this aim, for the sake of simplicity a constant friction coefficient is first assumed ($\mu=0.06$) as the goal is to highlight geometric aspects rather than focusing on the mechanical response of the FP. Due to the rotation of the slider occurring concurrently with the translation induced by the semi-spherical articulation, the displacement of the centre of contact surface 2, i.e., the point P_4 on the lower face of the slider in Figure 3.14, is lower than the displacement imposed on the top of the isolator, point P_1 . The relevant trajectories computed for the bidirectional cloverleaf test are compared in Figure 3.16: more specifically, the maximum displacement of the point P_4 is approximately 10% lower than that of the point P_1 . By closely analyzing the trajectories we note that, if the vertical component of motion is neglected, most of the energy introduced into the system is expended to make the slider translate up to the maximum values u_{x4} and u_{y4} , however a small remaining part is spent to guarantee that such translation is compatible with the curvature of the above semi-spherical articulation having radius r .

To this aim, a relative displacement occurs between contact surface 3 (belonging to the slider) and contact surface 4 (of the semi-spherical articulation), with the former moving relative to the latter in a direction opposed to the overall isolator translation.

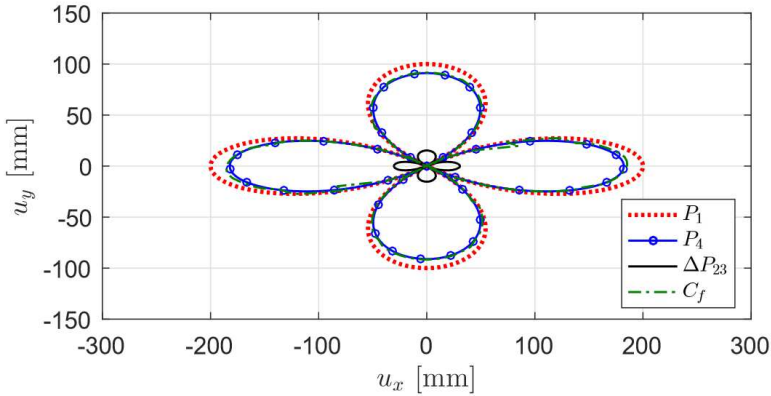


Figure 3.16 Comparative analysis of the trajectories traveled by the FP during the cloverleaf test (De Domenico et al. 2018)

This relative displacement can be quantified by computing the relative displacement ΔP_{23} between points P_2 and P_3 . The relative displacement ΔP_{23} generates contact force transmission between the two sliding surfaces, thus dissipating further energy.

As a result, the energy introduced into the system is dissipated via a two-fold mechanism, consisting in the slider translation along the primary sliding surface and the slider rotation along the secondary surface. Therefore, in the manufacturing process it is important to pay attention to the lubrication and tribological properties of both the sliding interfaces.

In Figure 3.16 it is reported the trajectory of the centroid C_f of the total contact force F , whose x - and y -components are given in equation (3.5). The coordinates of such point C_f at each time instant are computed, based on the distribution of the nodal forces f_i , so that:

$$x_{C_f} = \frac{\sum_i f_{yi} x_i}{\sum_i f_{yi}} = \frac{S_y}{F_y} \quad y_{C_f} = \frac{\sum_i f_{xi} y_i}{\sum_i f_{xi}} = \frac{S_x}{F_x} \quad (3.15)$$

whose vector plot at a generic time step is represented in Figure 3.17. The C_f trajectory slightly deviates from that one of the slider (point P_4), with differences mainly observed near the points of motion reversal.

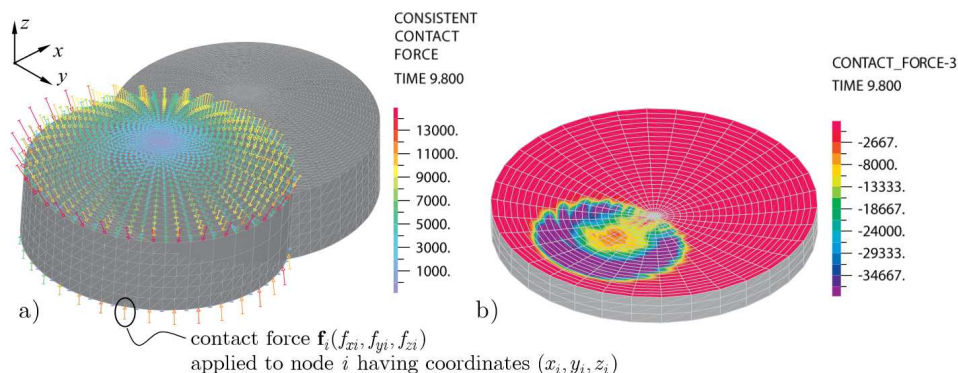


Figure 3.17 Contact force distribution: a) vector plot of the f_i forces; b) band plot of f_{zi} on the sliding surface

It is worth noting that if the sliding surface were flat (not concave), a uniform distribution of the contact forces would be found and the centroid C_f would coincide with the centre of the slider P_4 throughout the system motion. In addition to the trajectory of C_f it is possible to evaluate the angle formed by the total force vector with respect to the x -axis, $\phi_f = \arctan_2(F_y, F_x)$ and to compare it to the angle $\phi_v = \arctan_2(v_y, v_x)$ formed by the velocity vector (tangent to the traveled cloverleaf trajectory at each time instant), where \arctan_2 is the two-arguments arctangent function taking into account which quadrant the solution is inside. In this way, we can identify and quantify the angular shift $\Delta\phi = \phi_v - \phi_f$ formed by the force and velocity vectors, which has already been discussed in § 3.2.1 and depicted in Figure 3.12. The relevant results are illustrated in Figure 3.18 the velocity vector is parallel to the force vector (i.e., $\Delta\phi=0$) only when the slider centre (point P_4 in Figure 3.14) is going through the centroid of the primary sliding surface, point P_5 , a situation that is identified by the condition $u_x = u_y = 0$ and reported in dashed black line in Figure 3.18 a) and b).

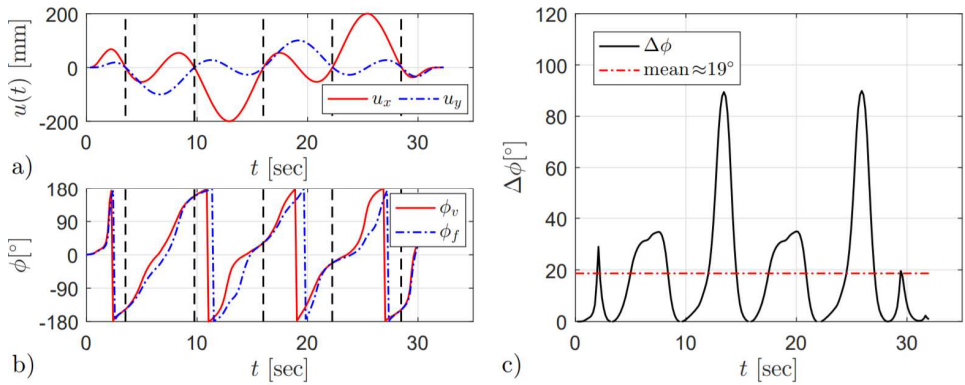


Figure 3.18 Angular shift $\Delta\varphi$ between the force vector and velocity for bidirectional cloverleaf test

In all the other kinematic configurations, the restoring force F_r , characterized by a radial recentering direction, generates deviations of the total resisting force opposed to the active seismic force (the latter being parallel to the trajectory traveled during the isolator motion). On the other hand, the friction force keeps the same direction as the velocity vector throughout the duration of the test. As a result, the maximum angular shift occurs concurrently with the maximum radial displacement as illustrated by analyzing Figure 3.18 a) and b) simultaneously, with $\Delta\varphi$ even higher than 90° and a mean value over the entire duration of the test equal to 19° , cf. Figure 3.18 c). This value is consistent with the experimental findings, in which an angular shift $\Delta\varphi \approx 14^\circ$ was detected (Lomiento et al. 2013). Once again, we emphasize that these deviations would cancel out in a unidirectional loading condition as well as under general bidirectional excitations but flat (not concave) sliding surface. Furthermore, by inspection of the time histories reported in Figure 3.18 b) we note that the angle of the velocity vector φ_v anticipates that of the force vector φ_f , which is physically reasonable: the velocity is the cause that produces the reactive force, i.e., the direction of the force vector arises as a consequence of the trajectory traveled during the test. Since for higher contact pressures the friction coefficient reduces, the restoring force, which is responsible for the angular shift, contributes to a larger extent to the overall resisting force,

therefore it is expected that the $\Delta\phi$ value is dependent on the vertical load acting on the FP.

μ_{s0}	N_{ref} [kN]	γ	v_{ref} [mm / s]	c_{ref} [kN/ m s]	β	ψ	δ
0.103	12300	1.40	10	12000	0.7	0.09	0.8

Table 3.6 Numerical parameters defining the analytical model and the TMC FE subroutine

The validation of the prediction models (namely the analytical model given in equation (3.12) and the TMC FE-model whose friction coefficient is governed by equation (3.14)) is carried out by comparison with the corresponding experimental results. The numerical parameters adopted for the phenomenological model and the TMC FE-model are collected in Table 3.6. Force-displacement loops predicted by the numerical models are presented in Figure 3.19 and compared with the experimental data.

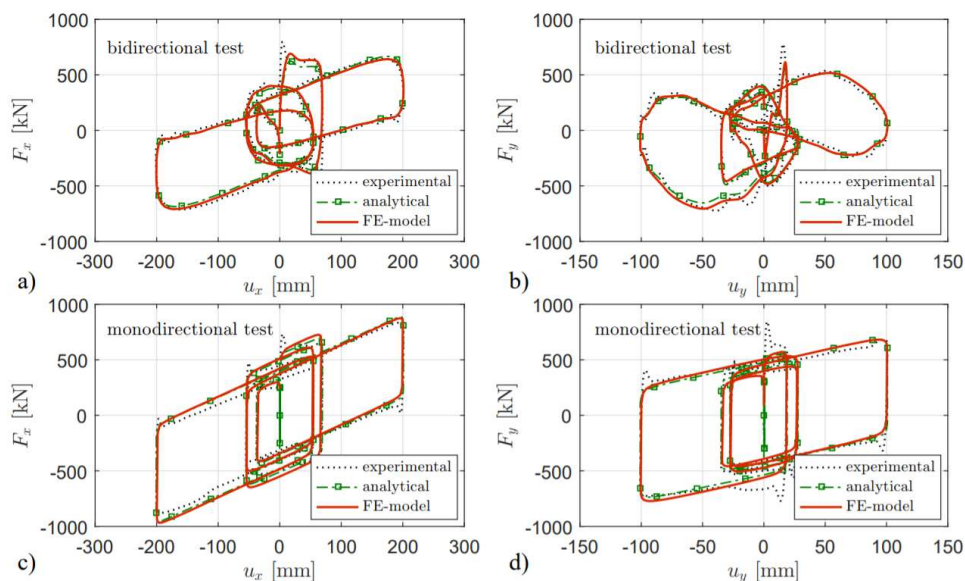


Figure 3.19 Force-displacement loops for cloverleaf test: a) and b) bidirectional; c) and d) monodirectional

It can be seen that a very good agreement between experimental evidence and numerical results is achieved for both the analytical and the FE-model. The TMC FE-model seems to be slightly more accurate in the prediction of the experimental data from the bidirectional test, however the

simple analytical model discussed in § 3.2.2 shows a reasonably good predictive performance despite its relatively simple formulation. In Figure 3.19 we note that the hysteretic loops get narrower with repetition of cycles due to the friction degradation that monotonically increases over the course of the test.

The friction degradation with time can be highlighted by isolating the μ value from equation (3.2) for the monodirectional tests and from equation (3.5), with regard to the bidirectional test. The corresponding plots are depicted in Figure 3.20. In both the analytical and the TMC solutions, the reduction of the friction coefficient can be quantified by computing the energy dissipated during the hysteretic loops in both bidirectional and monodirectional loading conditions.

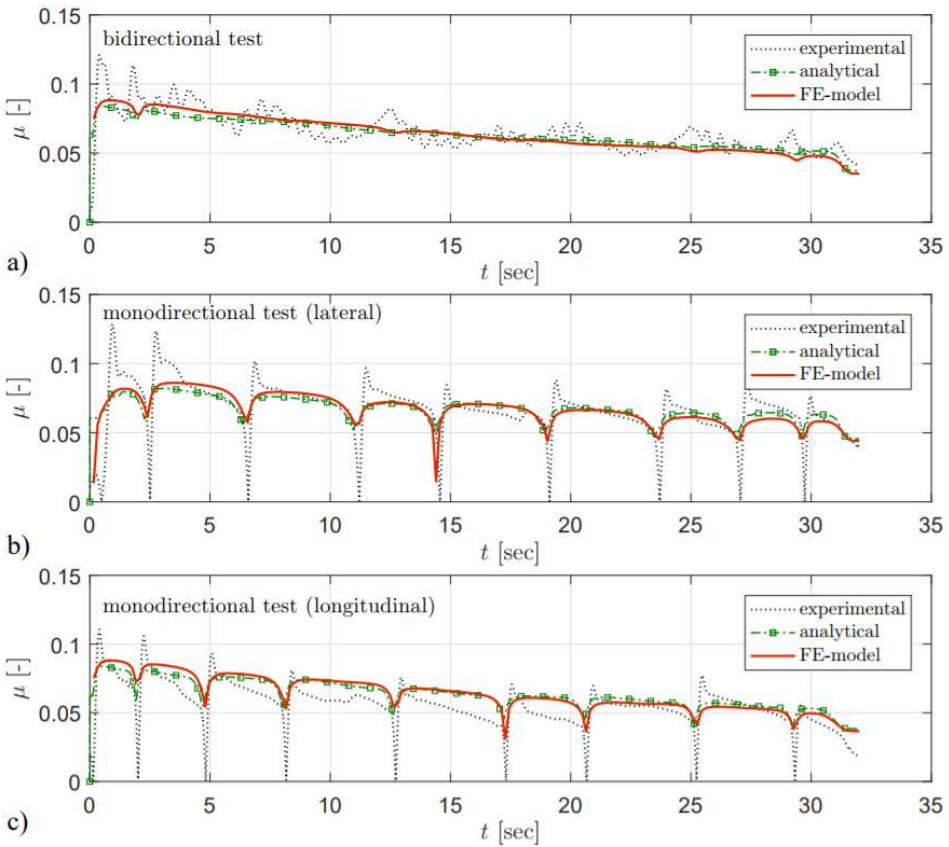


Figure 3.20 Plot of the friction coefficient versus time: a) bidirectional test; b) and c): monodirectional tests

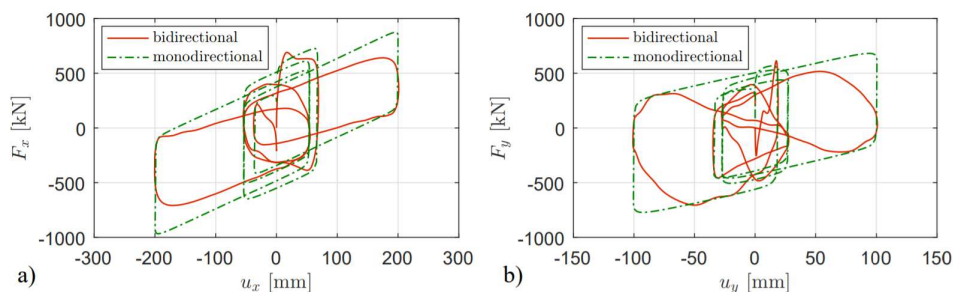


Figure 3.21 Force displacement loops from the TMC-FE model: a) longitudinal; b) lateral

For the TMC FE-model, the energy dissipated in bi-directional conditions is reduced in comparison with the uni-directional case of 32% in the longitudinal direction (changing from 613 kN m to 413 kN m) and of 39% in the lateral direction (reducing from 332 kN m to 201 kN m).

These results are in agreement with the experimental findings (Lomiento et al. 2013), in which reduction of the dissipated energy of 23% and 41% are observed in the longitudinal and lateral direction, respectively. The difference in the longitudinal direction is consistent to the slight overestimation of the friction coefficient predicted by the TMC FE-model in the monodirectional longitudinal test over the time interval from $t = 10$ sec to $t = 20$ sec, as illustrated in Figure 3.21.

According to the above results, the displacement components under bi-directional excitations may be significantly higher than the corresponding components in the monodirectional case. Neglecting the bi-directional interaction could lead to considerably overestimate the dissipative capacity of the isolator or, equivalently, underestimate the maximum displacements expected during seismic events.

It is interesting to analyze the thermal solution associated with the mechanical solution of the coupled thermo-mechanical problem. The temperature distribution is obtained at each solution time and at each node of the FE model. In Figure 3.22 and Figure 3.23 the contour plots of the temperature on the sliding plate (contact surface 1) and on the sliding PTFE pad (contact surface 2) are shown for ten time instants in order to capture the spatial distribution and the trend over the test duration. Different temperature values are obtained in the two contact surfaces as a result of the thermal conductivity of the PTFE that is significantly lower than that

of the steel part. The temperature rise on the sliding plate is not uniform since it is strongly affected by the contact pressure that increases from the centre of the pad towards the perimeter perpendicularly to the instantaneous direction of motion (see Figure 3.17). This distribution can be better identified by inspection of the temperature map of the corresponding monodirectional tests in the longitudinal (along the x -axis) and lateral (along the y -axis) directions, as illustrated in Figure 3.24 and Figure 3.25, respectively.

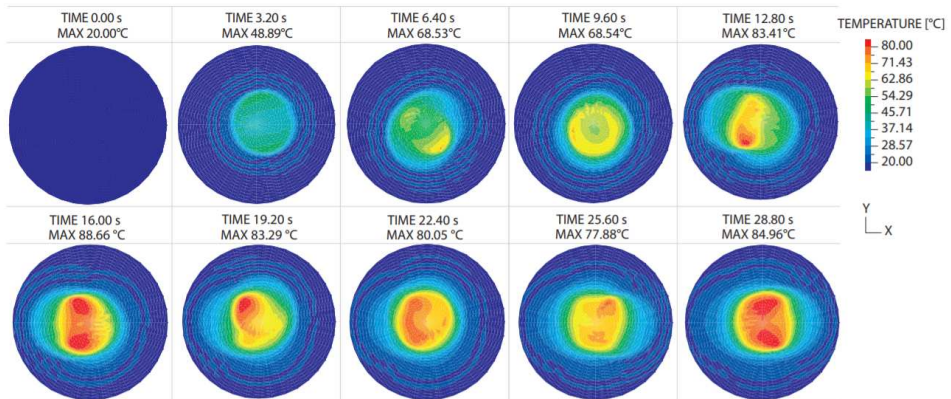


Figure 3.22 Temperature distribution on the sliding plate for bidirectional cloverleaf test

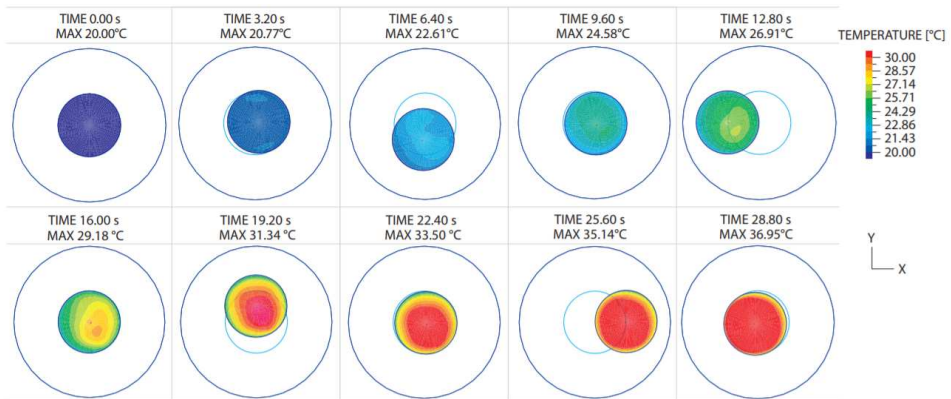


Figure 3.23 Temperature distribution on the sliding PTFE pad for bidirectional cloverleaf test

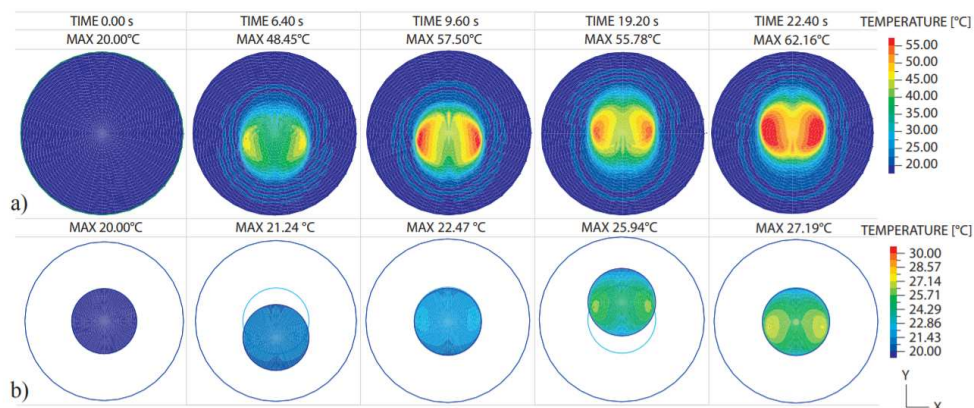


Figure 3.24 Temperature for monodirectional test (lateral) on: a) sliding plate; b) PTFE pad

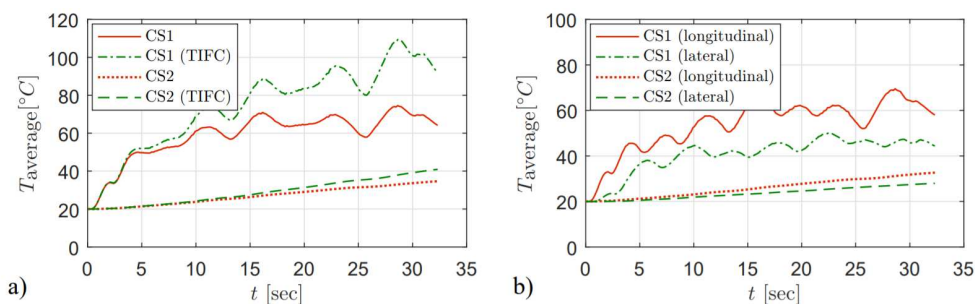


Figure 3.25 Average temperature histories during the test: a) bidirectional test; b) monodirectional test (CS stands for “contact surface”; TIFC stands for “Temperature-Independent Friction Coefficient”) (De Domenico et al. 2017)

Generally speaking, the highest temperature is expected in the area interested by more frequent sliding activity, which is therefore characterized by the lowest friction coefficient as a result of the TMC subroutine, equation (3.14). The temperature rise is usually of short duration and is therefore called “flash temperature” in the relevant literature (Blok 1963, Carslaw and Jaeger 1959, Constantinou 1999, Stachowiak and Batchelor 2005). This concept is clarified in Figure 3.25 in which the temperature histories for bidirectional and monodirectional tests are reported. More specifically, at each time instant we compute the average temperature on the contact surface 2 (i.e., on the sliding PTFE pad) and on the contact surface 1 (i.e. on the steel sliding plate). To compute the average temperature on the sliding plate, the average operator is restricted to the

actual, instantaneous footprint of the slider having radius a and not to the entire area of radius A in order to quantify the real temperature rise resulting from the sliding activity. This calculation is thus based on an evolutive area interested by the instantaneous sliding activity, which depends on the imposed displacements that affect the slider motion. With reference to the plots of Figure 3.26, temperature fluctuations are observed in contact surface 1 that reflect the variation of the sliding velocity during the cloverleaf test and the intrinsic short duration of the flash temperature.

On the other hand, the frictional heating gives rise to a temperature rise that propagates and expands so as to involve the entire PTFE-pad over the duration of the test. This is why the average temperature in the contact surface 2 appears to be almost monotonically increasing in Figure 3.25. Overall, the friction coefficient depends on the temperature at the sliding interface, being affected by the temperature on both the sliding PTFE-pad and the sliding plate. High flash temperatures developed at the sliding interface reduce the friction coefficient according to the TMC subroutine equation (3.14), thus producing a decrease in the frictional heating generated at the sliding interface. In turn, this gives rise to a limitation in a further temperature increase in accordance with the mechanism of “thermal control of friction” (Ettles 1986)..

To highlight this concept, in Figure 3.25a) we also report the temperature value that would be predicted for the bidirectional test by using a temperature-independent friction coefficient, i.e., by assuming $f_T(T) = 1$ in the TMC subroutine equation (3.14). Obviously, the latter assumption would not be able to capture the above mechanism and would overestimate the (average) temperature rise significantly, even more than 50% as compared to the temperature prediction obtained by the proposed temperature-dependent friction model.

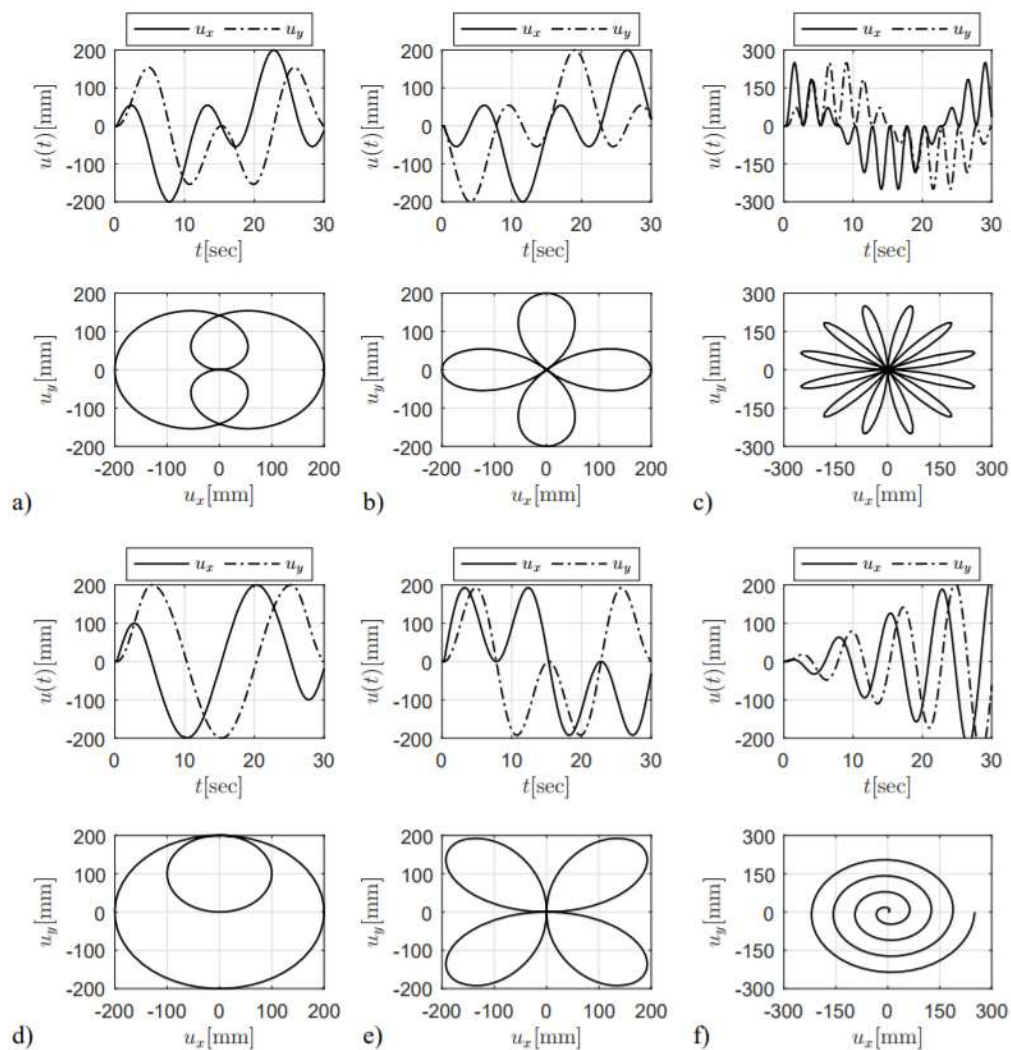


Figure 3.26 Bidirectional orbits analyzed in the parametric study: a) Durer's folium; b) straight cloverleaf; c) twelve-leaf clover; d) circular orbit; e) oblique cloverleaf; f) spiral orbit

Chapter 4

NEW ISOLATION DEVICES

Nowadays, many new materials and devices continue to be proposed for use in base isolation. Based on the extent of control to be achieved over the seismic response, the choice of the isolation system varies and thereupon its design is done to suit the requirements of use of the structure. Most commonly used seismic isolating systems can satisfy all the requirements while having their own characteristics. However, no one type device is perfect as each device has its own drawbacks. Therefore, there is always a continuous need to enhance the existing isolation systems or even to innovate others to get the most benefits of seismic isolation while avoiding any unwanted negative effects. The new isolation devices here proposed are one for the horizontal component of the seismic action and one for the vertical component; together they compose a tridimensional isolation device.

For the horizontal isolation device the idea is to create a horizontal seismic isolation device that can overcome the problems associated with the existing devices but at the same time take advantage of the technologies already known to implement the devices. The invention aims to exploit the friction dissipation mechanism, characteristic of the sliding device, using a flat (non-curved) sliding surface while the elastic part is attributed to an elastomer element, for this reasons is called Hybrid Friction Rubber Isolator. In detail, the device, as shown in Figure 4.1, will have a compact shape and will be comprised of a flat sliding square slider (6) that allows horizontal displacement, a central cylindrical element (7) in steel and a further square plate upper (1) steel. The element (7) and the element (1) are mechanically connected to each other by means of an additional steel plate (2). The device has a circular elastomeric crown (4), which is the elastic

part of the same, vulcanized above and below two steel plates (3). The latter are mechanically connected to the plate (1) and are connected to the plate (6) by means of a C-section (5) steel element. At the bottom of the element (7) a disk (8) is made of properly treated materials (generally polished stainless steel, fluoropolymers such as PTFE or high strength polymers) which exhibit low friction resistance but at the same time offer a high carrying capacity against vertical loads transmitted by the structure. This disk (8) may also be made of composite material by inserting a reinforcement within its thickness (see Chapter 6). The elastomer element (4) can also be reinforced with steel blades to increase its carrying capacity.

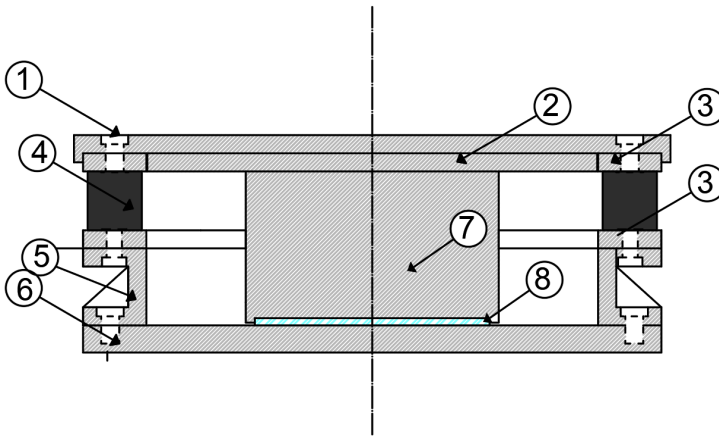


Figure 4.1 Schematic section of the Hybrid Friction Rubber Isolator

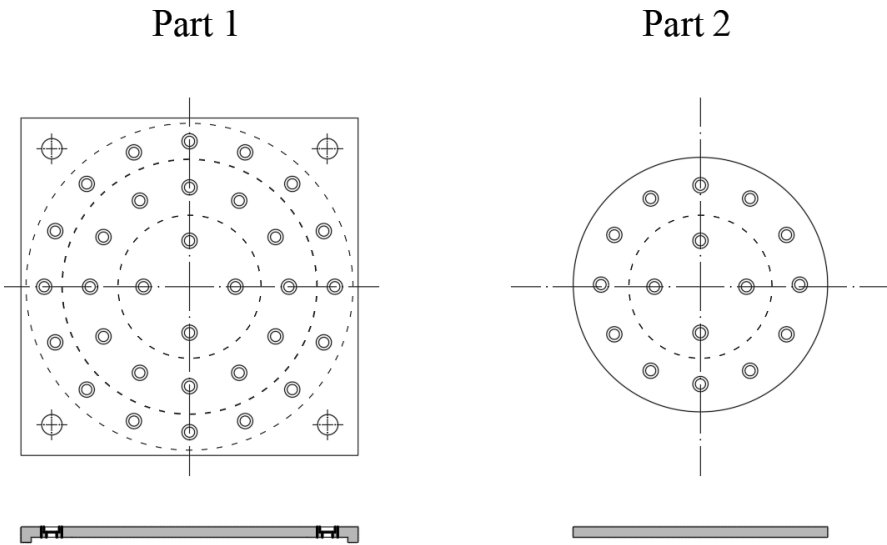


Figure 4.2 Part1 and 2 of the Hybrid Friction Rubber Isolator

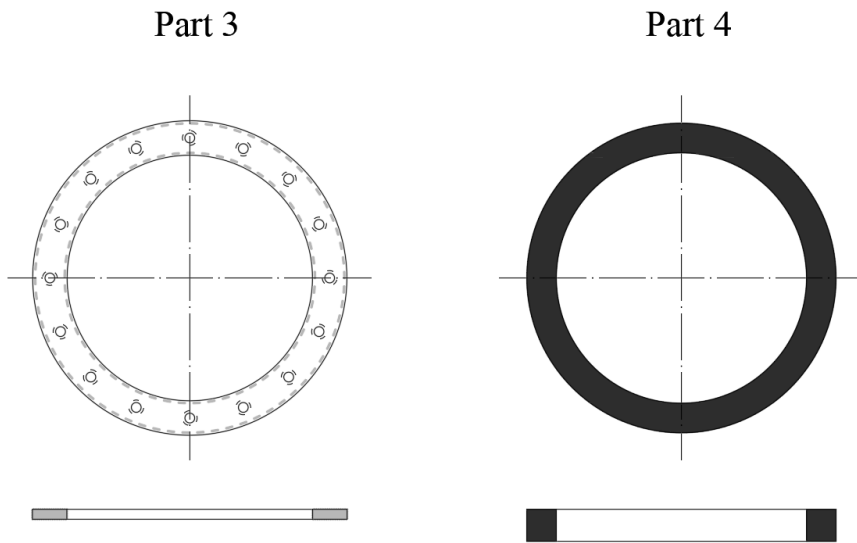
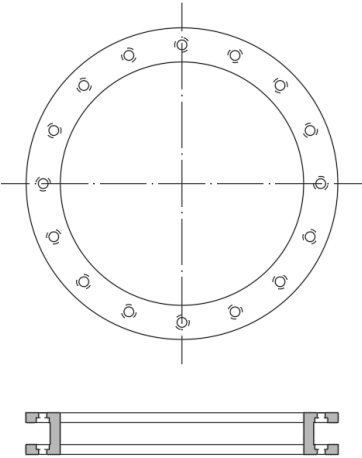


Figure 4.3 Part 3 and 4 of the Hybrid Friction Rubber Isolator

Part 5



Part 6

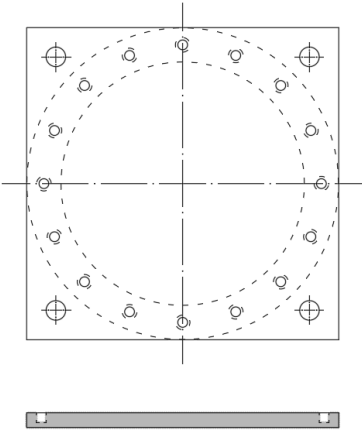
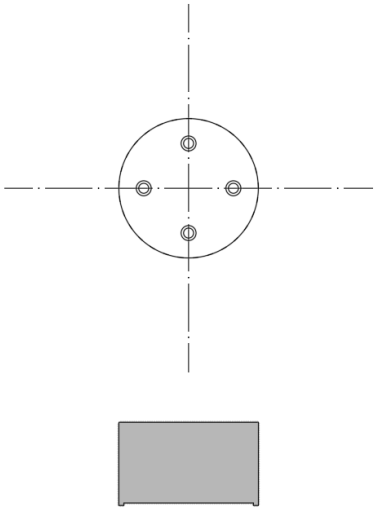


Figure 4.4 Part 5 and 6 of the Hybrid Friction Rubber Isolator

Part 7



Part 8

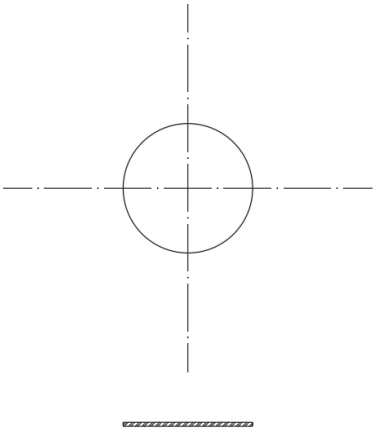


Figure 4.5 Part 7 and 8 of the Hybrid Friction Rubber Isolator

For the mitigation of the vertical component of the seismic action to date there are devices, generally consisting of springs or elastic elements (such as rubber or elastomers) in series or in parallel, characterized by a high vertical flexibility and therefore potentially capable of isolating relatively to vertical seismic action. Such devices have been widely used in the field of mechanical vibration isolation produced by machinery such as motors, current generators, chillers, UTA. The use of such devices in the field of structural civil engineering (buildings, bridges, nuclear power plants) for isolation from vertical seismic action did not have the same diffusion. This is presumably due to the lack of effective and valid technology, which is easy to implement and can be introduced into the construction market. The object of the invention is precisely a seismic protection device for civil engineering structures (buildings, bridges, tanks, nuclear power plants) in relation to vertical action. The geometric conformation of this device allows a vertical isolation by using some elementary mechanisms already used in the traditional horizontal isolation devices. In particular, the proposed device has the shape of a parallelepiped and is made up of two steel plates, constituting the base and top of the device, running on the jaws having a predetermined inclination, also made of steel. At the center of the device, inserted between the upper jaws and placed symmetrically with respect to the vertical and horizontal planes, there is a central element in reinforced elastomer (elastomer with alternating layers of thin steel blades). Under the vertical action due to the proper weight of the structure, the two plates approach and move into a static equilibrium configuration. In this configuration, the two steel plates transfer a compression load through the action of the jaws to the central elastomer element. The vertical load ratio, that is transferred to the elastomer, is determined by the inclination angle of the steel jaws: the vertical movement of the plates, approaching the action of the static loads of the structure, results in a horizontal movement of the jaws which, in reason of their angle of inclination, compress the elastomer between them.

Under further oscillatory action due to the vertical component of the earthquake, the two steel plates oscillate with respect to the static equilibrium configuration described above. Since the vertical component of the earthquake generates forces below the weight of the structure,

following the oscillation of the device, the elastomeric element will always be in an alternating compression state.

The surfaces placed on the interface between the plates and the jaws are covered with appropriately treated materials (generally polished stainless steel, fluoropolymers such as PTFE or high strength polymers), characterized by low friction resistance, but at the same time a 'High carrier capacity against the loads transmitted. The dissipation mechanism of the device is thus based on the friction between these surfaces, while its vertical stiffness is dependent on the elasticity of the central elastomeric element rather than by the inclination of the jaws. The design of this device can therefore be based on consolidated concepts used in the design of horizontal devices: shape factors, armature percentages, and choice of interface material to achieve a more stable friction coefficient.

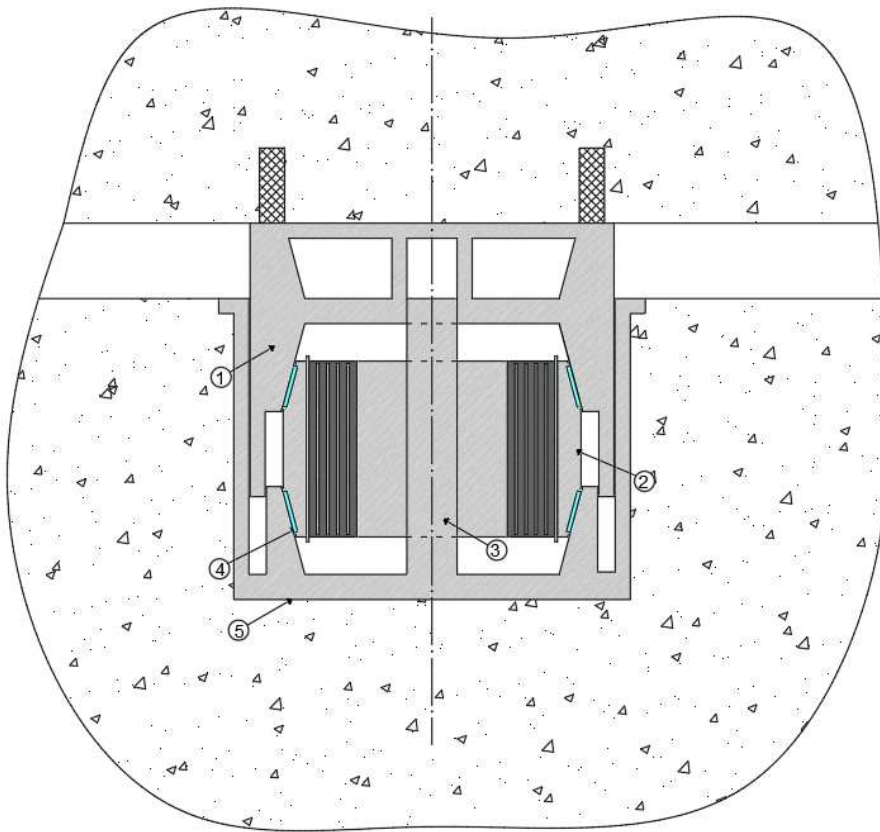
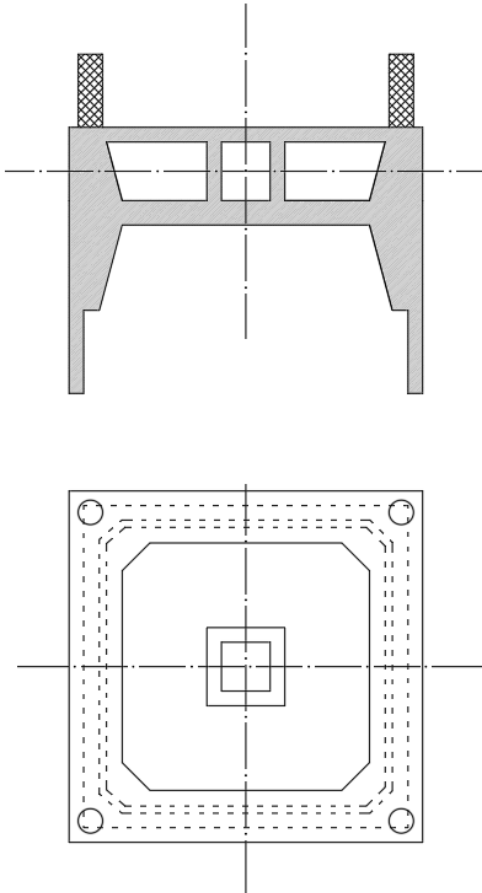


Figure 4.6 Schematic section of the Vertical Isolation Device

Part 1



Part 2

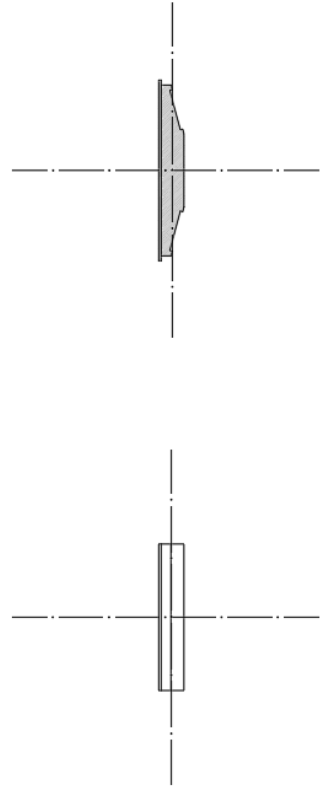
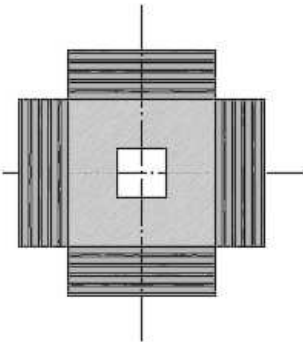
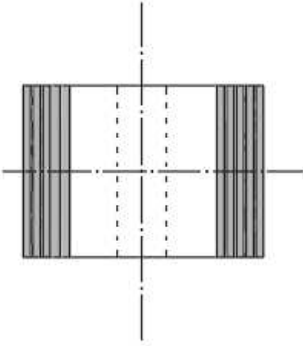


Figure 4.7 Part 1 and 2 of the Vertical Isolation Device

Part 3



Part 4

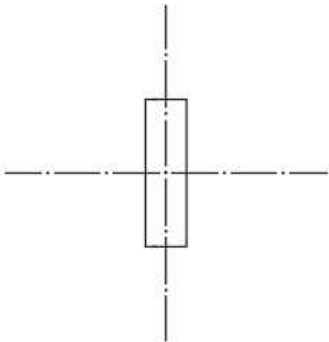
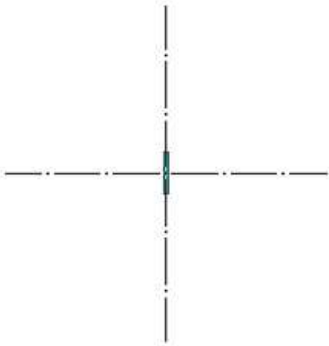


Figure 4.8 Part 3 and 4 of the Vertical Isolation Device

Part 5

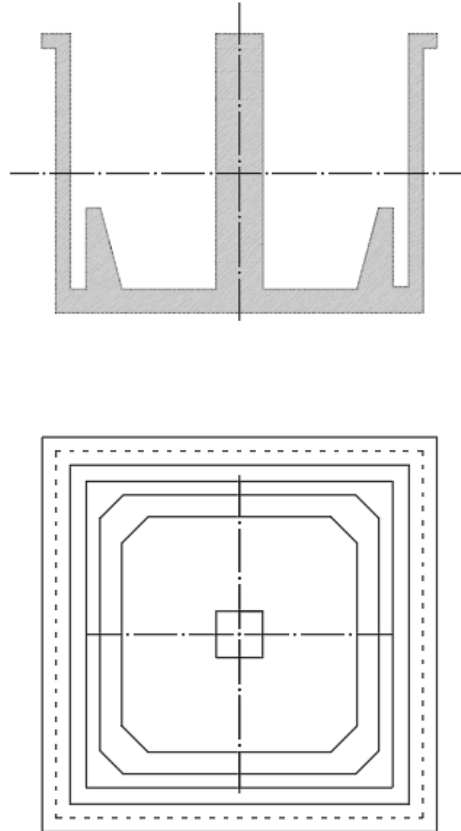


Figure 4.9 Part 5 of the Vertical Isolation Device

The vertical prototype will be provided with a retaining device, a sort of fuse, which will allow it to be activated only in case of seismic action and not for small oscillations due to slight variations in the static vertical load.

The two devices here proposed could be coupled to realize a tridimensional isolation device, as shown in Figure 4.10. The vertical device can be coupled also with one of the commercial horizontal devices already in use (see, for example, Figure 4.11).

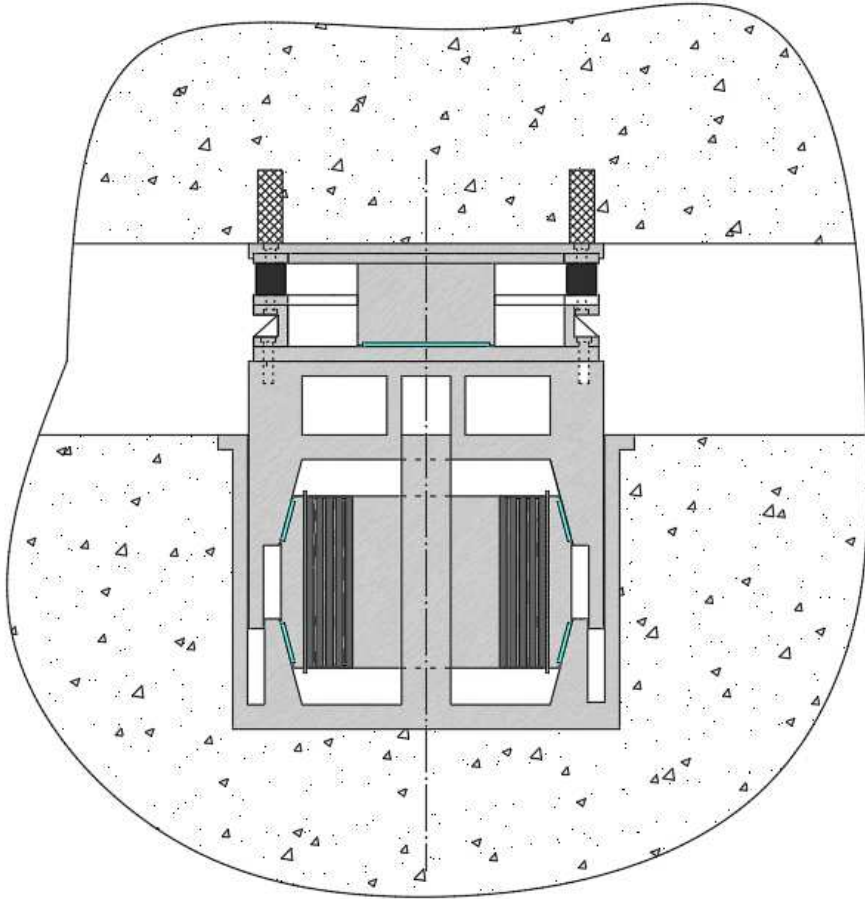


Figure 4.10 The tridimensional isolation device made by the two proposed devices

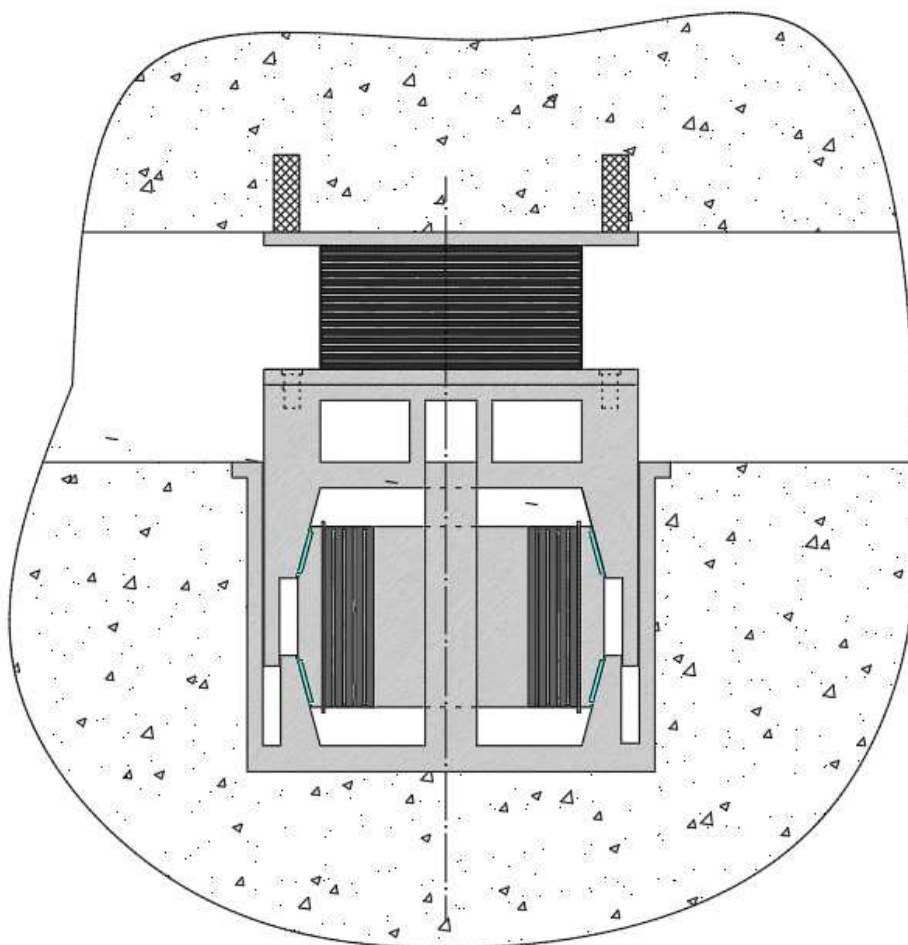


Figure 4.11 The tridimensional isolation device made by the vertical proposed device and a classic elastomeric isolation device

4.1 Design criteria

4.1.1 Behavior of rubber in pure shear

The most important mechanical property of an horizontal isolator is, of course, its horizontal stiffness, that is given by (Naeim and Kelly 1999):

$$K_H = \frac{GA}{t_r}, \quad (4.1)$$

where G is the shear modulus of the elastomer, A is the full cross-sectional area and t_r is the total thickness of the rubber. The maximum horizontal displacement D is related to the maximum shear strain γ by:

$$\gamma = \frac{D}{t_r}. \quad (4.2)$$

4.1.2 Behavior of multilayer rubber in compression

The vertical frequency for an isolated structure is, for the case of vertical isolator, the most important design criterion and is controlled by the vertical stiffness of the rubber part. It is given by the formula (Kelly and Konstantinidis 2011):

$$K_v = \frac{E_c A}{t_r} \quad (4.3)$$

where A is the loaded area, t_r is the total thickness of rubber, that is the sum of the thicknesses of the individual layers, and E_c is the instantaneous compression modulus of the rubber-steel composite under the specified

level of vertical load. The value of E_c , which is computed for a single rubber layer, is controlled by the shape factor S , defined as

$$S = \frac{\text{loaded area}}{\text{free-force area}} \quad (4.4)$$

which is a dimensionless measure of the aspect ratio of the single layer of the rubber. For example, for an infinite strip of width $2b$ and thickness t :

$$S = \frac{b}{t} \quad (4.5)$$

for a circular pad of radius R and thickness t :

$$S = \frac{R}{2t} \quad (4.6)$$

for a rectangular pad of side dimensions $2b$ and l and thickness t :

$$S = \frac{bl}{(l + 2b)t} \quad (4.7)$$

The analysis for the compression stiffness is an approximate one based on two sets of assumptions, the first one relating to the kinematics of the deformation and the second one to the stress state. For direct compression, the kinematic assumptions are as follows:

- i. points on a vertical line before deformation lie on a parabola after loading;
- ii. horizontal planes remain horizontal.

Consider an arbitrarily shaped pad of thickness t and locate, as shown in Figure 4.12(a), a rectangular Cartesian coordinate system (X, Y, Z) in the middle surface of the pad.

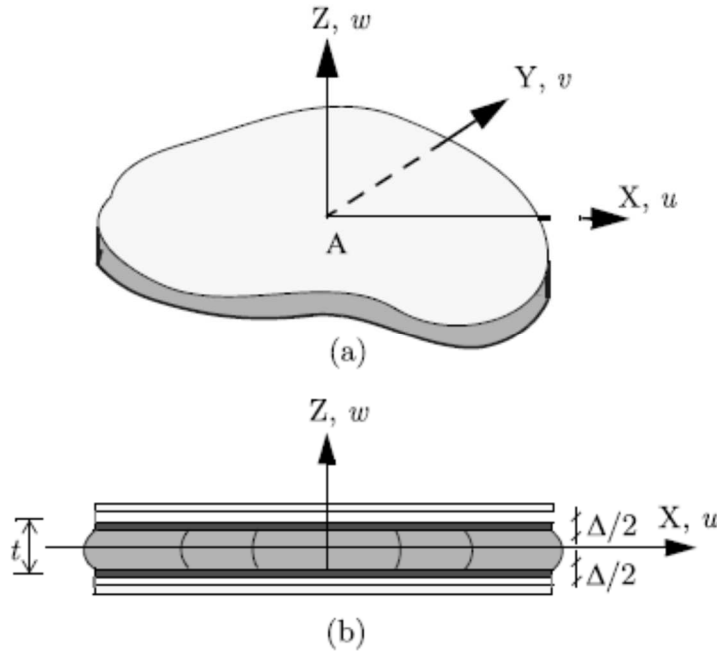


Figure 4.12 (a) Cartesian coordinate system on an arbitrarily shaped pad; (b) displacement fields of an arbitrarily shaped pad (Kelly and Konstantinidis 2011)

As shown in Figure 4.12 (b), under the kinematic assumptions described above, the displacements (u, v, w) in the coordinate directions are

$$\left\{ \begin{array}{l} u(x, y, z) = u_0(x, y) \left(1 - \frac{4z^2}{t^2} \right) \\ v(x, y, z) = v_0(x, y) \left(1 - \frac{4z^2}{t^2} \right) \\ w(x, y, z) = w(z) \end{array} \right. \quad (4.8)$$

This displacement field satisfies the constraint that the top and bottom surfaces of the pad are bonded to rigid layers. The assumption of

incompressibility produces a further constraint on the three components of strain, $\varepsilon_{xx} = \partial u / \partial x$, $\varepsilon_{yy} = \partial v / \partial y$, $\varepsilon_{zz} = \partial w / \partial z$, in the form

$$\varepsilon_{xx} + \varepsilon_{yy} + \varepsilon_{zz} = 0 \quad (4.9)$$

which leads to:

$$\left(\frac{\partial u_0}{\partial x} + \frac{\partial v_0}{\partial y} \right) \left(1 - \frac{4z^2}{t^2} \right) + \frac{dw}{dz} = 0 \quad (4.10)$$

from which:

$$\frac{\partial u_0}{\partial x} + \frac{\partial v_0}{\partial y} = - \frac{1}{1 - \frac{4z^2}{t^2}} \frac{dw}{dz} \quad (4.11)$$

we see that we have a function x e y , on the left-hand side and a function of z on the right, and since the equation is an identity that holds everywhere, both sides must equal a constant k . To determine k , we solve

$$\frac{dw}{dz} = -k \left(1 - \frac{4z^2}{t^2} \right) \quad (4.12)$$

to get:

$$w(z) = -k \left(z - \frac{4z^3}{3t^2} \right) + c, \quad (4.13)$$

where c is a constant of integration. Using the boundary $w(t/2) = -\Delta/2$ and $w(-t/2) = -\Delta/2$, we find that $c = 0$ and $k = 3\Delta/2t = 3\varepsilon_c/2$, where the compression strain ε_c is defined by:

$$\varepsilon_c = -\frac{w(t/2) - w(-t/2)}{t}, \quad (\varepsilon_c > 0). \quad (4.14)$$

Then we obtain the distribution of the displacement w through the thickness of the pad, if this is needed, and the integrated form of the compressibility constraint as

$$\frac{\partial u_0}{\partial x} + \frac{\partial v_0}{\partial y} = \frac{3\varepsilon_c}{2}. \quad (4.15)$$

The stress state is assumed to be dominated by the internal pressure, p , such that the normal stress components σ_{xx} , σ_{yy} , σ_{zz} , differ from $-p$ only by terms of order $(t^2/l^2)p$ (where l is a characteristic length in the $x-y$ plane),

$$\sigma_{xx} \approx \sigma_{yy} \approx \sigma_{zz} \approx -p \left(1 + O\left(\frac{t^2}{l^2}\right) \right). \quad (4.16)$$

The shear stress components, τ_{xz} and τ_{yz} , which are generated by the constraints at the top and bottom of the pad, are assumed to be of order $(t/l)p$; the in-plane shear stress, τ_{xy} , is assumed to be of order $(t^2/l^2)p$. The complete equations of equilibrium for the stresses are:

$$\begin{cases} \frac{\partial \sigma_{xx}}{\partial x} + \frac{\partial \tau_{xy}}{\partial y} + \frac{\partial \tau_{xz}}{\partial z} = 0 \\ \frac{\partial \tau_{xy}}{\partial x} + \frac{\partial \sigma_{yy}}{\partial y} + \frac{\partial \tau_{yz}}{\partial z} = 0. \\ \frac{\partial \tau_{xz}}{\partial x} + \frac{\partial \tau_{yz}}{\partial y} + \frac{\partial \sigma_{zz}}{\partial z} = 0 \end{cases} \quad (4.17)$$

If $\sigma_{xx} = \sigma_{yy} = -p$

$$\begin{cases} \frac{\partial \tau_{xz}}{\partial z} = \frac{\partial p}{\partial x} \\ \frac{\partial \tau_{yz}}{\partial z} = \frac{\partial p}{\partial y} \end{cases} \quad (4.18)$$

The third of the equations of equilibrium can be differentiated with respect to z , obtaining:

$$\frac{\partial^2 p}{\partial x^2} + \frac{\partial^2 p}{\partial y^2} = \nabla^2 p = \frac{\partial^2 \sigma_{zz}}{\partial z^2}. \quad (4.19)$$

Assuming that the material is linearly elastic, the shear stresses, τ_{xz} and τ_{yz} , are related to the shear strains, γ_{yz} and γ_{xz} , by $\tau_{xz} = G\gamma_{xz}$ and $\tau_{yz} = G\gamma_{yz}$, being G the shear modulus of the rubber; since $\gamma_{xz} = \partial u / \partial z + \partial w / \partial x$ and $\gamma_{yz} = \partial v / \partial z + \partial w / \partial y$

$$\tau_{xz} = -\frac{8G}{t^2} z u_0; \tau_{yz} = -\frac{8G}{t^2} z v_0; \quad (4.20)$$

From the equilibrium equations, therefore,

$$\frac{\partial p}{\partial x} = -\frac{8G}{t^2} u_0, \frac{\partial p}{\partial y} = -\frac{8G}{t^2} v_0 \quad (4.21)$$

which, when inverted give u_0 and v_0 . Inserir (4.21) into the incompressibility condition, gives

$$\frac{t^2}{8G} \left(\frac{\partial^2 p}{\partial x^2} + \frac{\partial^2 p}{\partial y^2} \right) = -\frac{3\epsilon_c}{2} \quad (4.22)$$

that is possible to reduce in the form:

$$\frac{\partial^2 p}{\partial x^2} + \frac{\partial^2 p}{\partial y^2} = \nabla^2 p = -\frac{12G\epsilon_c}{t^2} \quad (4.23)$$

The partial differential equation (4.23) has to be satisfied by $p(x, y)$ and by the area of the pad. The boundary condition $p=0$, on the edge of the pad, completes the system for $p(x, y)$.

With the substitution of equation (4.23), we have an equation for the distribution of σ_{zz} through the thickness of the pad in the form

$$\frac{\partial \sigma_{zz}}{\partial z^2} = \frac{12G\epsilon_c}{t^2}. \quad (4.24)$$

To use this in order to determine E_c , we solve for p and integrate over the area of the pad A to determine the resultant normal load, P . Then E_c is then given by

$$E_c = \frac{P}{A\epsilon_c} \quad (4.25)$$

This treatment does not consider the rubber compressibility; to include this aspect we can replace the constrain equation (4.9) with:

$$\epsilon_{xx} + \epsilon_{yy} + \epsilon_{zz} = -\frac{P}{K}, \quad (4.26)$$

where K is the bulck modulus. Integration through the thickness leads to

$$\nabla^2 p - \frac{12G}{Kt^2} p = -\frac{12G\epsilon_c}{t^2} \quad (4.27)$$

that we solved with the boundary condition, $p = 0$, on the edge of the pad.

To compute the effective stiffness, E_c , for a rectangular pad (Figure 4.13) with a large shape factor, we first solve equation (4.27) by using the rapidly convergent single series solution:

$$p(x, y) = \sum_{m=1}^{\infty} P_m(y) \sin\left(\frac{m\pi x}{2b}\right) \quad (4.28)$$

Here $P_m(y)$ is the Fourier coefficient and must satisfy the following condition:

$$\frac{d^2 P_m}{dy^2} - \beta_m^2 P_m = -\frac{12G\epsilon_c}{t^2} a_m. \quad (4.29)$$

where $a_m = 4/m\pi$ for odd m and zero otherwise, while $\beta_m^2 = (m\pi/2b)^2 + 12G/Kt^2$. After solving for P_m , the pressure distribution takes the final form

$$p(x, y) = \frac{12G\epsilon_c}{t^2} \sum_{m=1}^{\infty} \frac{a_m}{\beta_m^2} \left(1 - \frac{\cosh(\beta_m y)}{\cosh\left(\frac{\beta_m l}{2}\right)} \right) \sin\left(\frac{m\pi x}{2b}\right) \quad (4.30)$$

Integrating over the domain:

$$p = \int_{-l/2}^{l/2} \int_0^{2b} p(x, y) dx dy = \frac{12G\epsilon_c}{t^2} \sum_{m=odd} \frac{ba^2}{\beta_m^2} \left(1 - \frac{2}{\beta_m} \tanh\left(\frac{\beta_m l}{2}\right) \right), \quad (4.31)$$

and using $S = lb/[t(l+2b)]$ and $E_c = P/(A\varepsilon_c)$, we obtain:

$$E_c = \frac{384}{\pi^4} GS^2(1+\rho)^2 \sum_{m=odd}^{\infty} \frac{1}{m^4 \zeta_m^2} \left(1 - \frac{2\rho}{m\pi\zeta_m} \tanh\left(\frac{m\pi\zeta_m}{2\rho}\right) \right), \quad (4.32)$$

where $\rho = 2b/l$ is the aspect ratio of the pad, and

$$\zeta_m = \sqrt{1 + \frac{48GS^2(1+\rho)^2}{K(m\pi)^2}}. \quad (4.33)$$

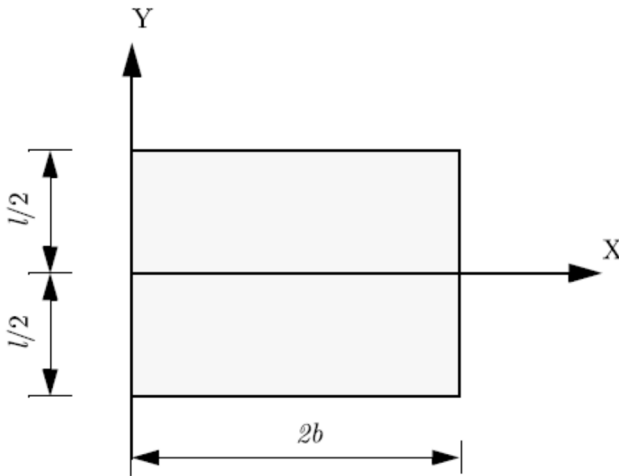


Figure 4.13 Coordinates system for a rectangular pad with side lengths l and $2b$ (Kelly and Konstantinidis 2011)

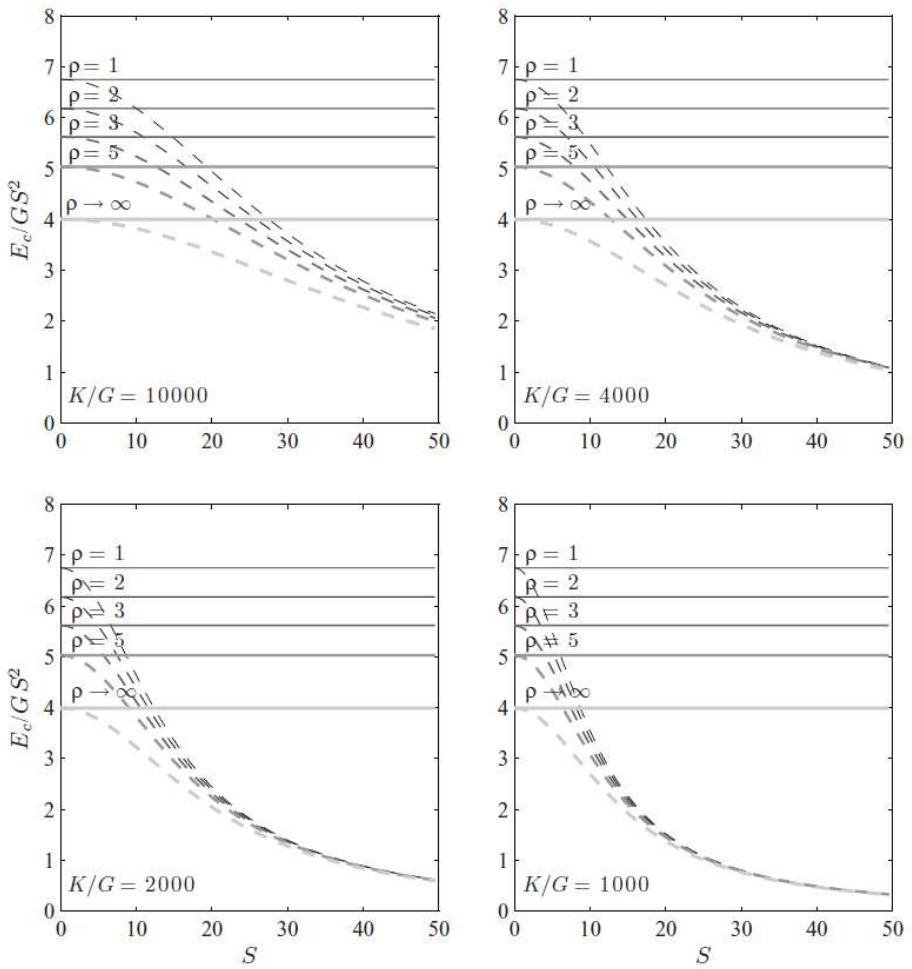


Figure 4.14 Effect of bulk compressibility on E_c for rectangular pads with different length-to-width ratios, ρ (Kelly and Konstantinidis 2011)

4.1.3 Kinematics of VID

The idea behind the design of the VID prototype in question is to give to the device a low vertical stiffness, able to dissipate energy thanks to the presence of sliding surfaces, characterized by a coefficient of friction μ , which are designed inclined by a sufficiently large angle ϑ , in any case less than 90° , so as to associate to the vertical movement a horizontal movement of suitable jaws present inside the device, which produce, by sliding along these surfaces and approaching each other, a compression action on a central rubber element with elastic behavior. The prototype studied in the present work can be schematized as shown in Figure 4.15.

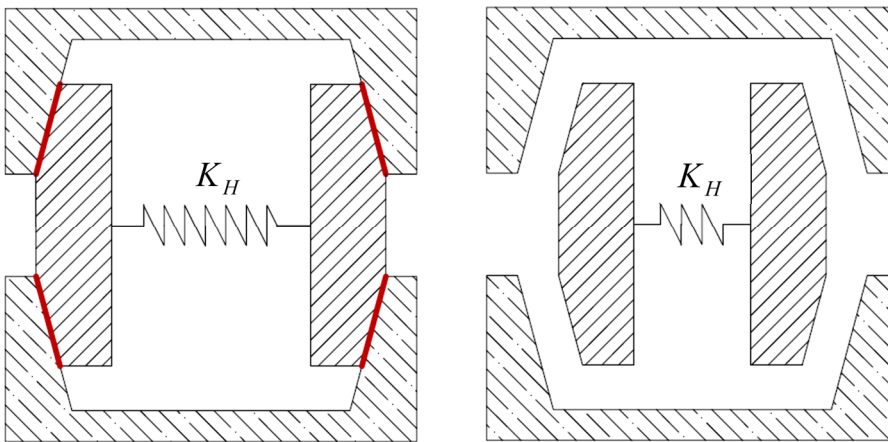


Figure 4.15 Schematic sketch of the VID

The kinematics of the latter can be studied going to evaluate the equilibrium of the forces characterizing the system in the descending and ascending phase relative to the body 1, i.e. the base, and the body 2, or the jaw. In fact with this study it is possible to have knowledge of the functioning of the prototype so as to better understand it.

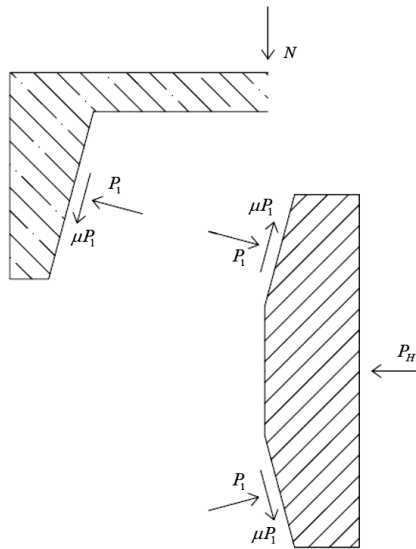


Figure 4.16 Equilibrium of the ascending phase

The equilibrium equations related to the first body, in the ascending phase will be:

$$\frac{N}{2} = P_1 \cos \vartheta - \mu P_1 \operatorname{sen} \vartheta \rightarrow \frac{N}{2} = P_1 (\cos \vartheta - \mu \operatorname{sen} \vartheta). \quad (4.34)$$

The equilibrium equations related to the second body in the ascending phase will be:

$$\frac{P_H}{2} = P_1 \operatorname{sen} \vartheta + \mu P_1 \cos \vartheta \rightarrow \frac{P_H}{2} = P_1 (\operatorname{sen} \vartheta + \mu \cos \vartheta). \quad (4.35)$$

Equaling the equations, we obtain:

$$\frac{N}{\cos \vartheta - \mu \operatorname{sen} \vartheta} = \frac{P_H}{\operatorname{sen} \vartheta + \mu \cos \vartheta} \quad (4.36)$$

$$N = \frac{\operatorname{ctg} \vartheta - \mu}{1 + \mu \operatorname{ctg} \vartheta} P_H, \quad (4.37)$$

where $P_H = K_R \Delta u = w \operatorname{ctg} \vartheta K_R$, when w is the base vertical displacement and Δu is the horizontal displacement, and $\Delta u = w \operatorname{ctg} \theta$:

$$N = \frac{\operatorname{ctg} \vartheta - \mu}{1 + \mu \operatorname{ctg} \vartheta} w \operatorname{ctg} \vartheta K_R \quad (4.38)$$

$$N = \frac{\operatorname{ctg} \vartheta - \mu}{\operatorname{tg} \vartheta + \mu} w K_R$$

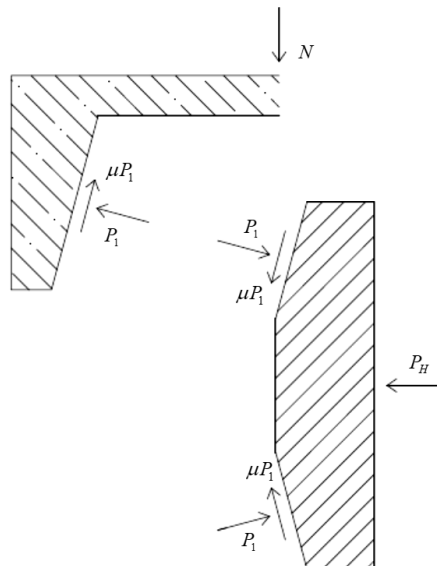


Figure 4.17 Equilibrium of the descending phase

The equilibrium equations related to the first body in the descending phase will be:

$$\frac{N}{2} = \mu P_1 \text{sen} \vartheta + P_1 \cos \vartheta \rightarrow P_1 = \frac{N}{2(\cos \vartheta + \mu \text{sen} \vartheta)}. \quad (4.39)$$

The equilibrium equations related to the second body in the descending phase will be:

$$\frac{P_H}{2} + \mu P_1 \cos \vartheta = P_1 \text{sen} \vartheta \rightarrow P_1 = \frac{P_H}{2(\text{sen} \vartheta - \mu \cos \vartheta)}. \quad (4.40)$$

from which:

$$\frac{N}{\cos \vartheta + \mu \text{sen} \vartheta} = \frac{P_H}{\text{sen} \vartheta - \mu \cos \vartheta} \quad (4.41)$$

$$P_H = \frac{\text{sen} \vartheta - \mu \cos \vartheta}{\cos \vartheta + \mu \text{sen} \vartheta} N \quad (4.42)$$

$$P_H = \frac{\text{tg} \vartheta - \mu}{1 - \mu \text{tg} \vartheta} N \quad (4.43)$$

$$N = \frac{1 - \mu \text{tg} \vartheta}{\text{tg} \vartheta - \mu} P_H$$

Remembering that $P_H = K_R \Delta u = wctg\vartheta K_R$:

$$N = \frac{1 - \mu tg\vartheta}{tg\vartheta - \mu} wctg\vartheta K_R \quad (4.44)$$

$$N = \frac{ctg\vartheta + \mu}{tg\vartheta - \mu} wK_R \quad (4.45)$$

Observing the schematization of the behavior of the device it is evident that the vertical stiffness is mainly influenced by the stiffness of the elastic element compressed by the two jaws. The phase of carding resizing for the subsequent study of the prototype is therefore aimed at determining, given a vertical stiffness of design, the stiffness characterizing the central element in rubber, being the two related.

For the determination of the stiffness, neglecting the friction, the descending phase of the device was studied, and the compression action was evaluated on an element of dimensions $l \times l \times h$.

In absence of friction, the equilibrium equation are:

$$\begin{cases} \frac{N}{2} = P_1 \cos \vartheta \rightarrow P_1 = \frac{N}{2 \cos \vartheta} \\ \frac{P_H}{2} = P_1 \text{sen} \vartheta \rightarrow P_1 = \frac{P_H}{2 \text{sen} \vartheta} \end{cases} \quad (4.46)$$

Then:

$$\frac{N}{\cos \vartheta} = \frac{P_H}{\text{sen} \vartheta} \rightarrow P_H = N \text{tg} \vartheta \quad (4.47)$$

Considering equation (4.47), is possible to find a relationship between K_v and K_R . Infact:

$$\left\{ \begin{array}{l} \sigma = \frac{N \operatorname{tg} \vartheta}{lh} \\ \varepsilon = \frac{N \operatorname{tg} \vartheta}{lhE} \end{array} \right. \rightarrow \Delta l = \varepsilon \cdot l = \frac{N \operatorname{tg} \vartheta}{Eh} \quad (4.48)$$

From which:

$$\left\{ \begin{array}{l} K_R = \frac{N \operatorname{tg} \vartheta}{\Delta l} = \frac{N \operatorname{tg} \vartheta}{N \operatorname{tg} \vartheta} Eh = Eh \\ K_v = \frac{N}{w} = \frac{N \operatorname{ctg} \vartheta}{\Delta l} = \frac{N \operatorname{ctg} \vartheta}{N \operatorname{tg} \vartheta} Eh = \frac{Eh}{\operatorname{tg}^2 \vartheta} \end{array} \right. \quad (4.49)$$

À p

Then:

$$K_R = K_v \operatorname{tg}^2 \vartheta \quad (4.50)$$

4.1.4 Analogies between horizontal and vertical spectra

For the design of the VID prototype, a comparison was made between the vertical and horizontal seismic action, exploiting the elastic response spectra in such a way as to carry out evaluations adhering to the philosophy that underlies the now clearing of the basic isolation for components of the horizontal seismic action, so as to perform a linear static analysis. In the case of use of base isolators, to improve the response of a generic structure in the presence of earthquake evaluated with respect to its horizontal components, the objective is to increase the period of the structure so as to

reduce the actions that weigh on it. In particular, in according to the Italian standar code, the linear static analysis method can be applied if the isolated construction satisfies some requirements including:

- the equivalent period of the isolated structure has a value included between $3 \cdot T_{bf}$ and 3.0 s, in which T_{bf} is the period of the superstructure assumed to be a fixed base, estimated with an approximate expression.

In order to understand how to design the prototype of a vertical isolator, it has therefore been observed, in terms of reducing the period of the structure, what are the effects of the introduction of a horizontal earthquake isolation system.

Assuming a period T_{bf} between T_B and T_C , in a reference site, the elastic response spectrum was evaluated.

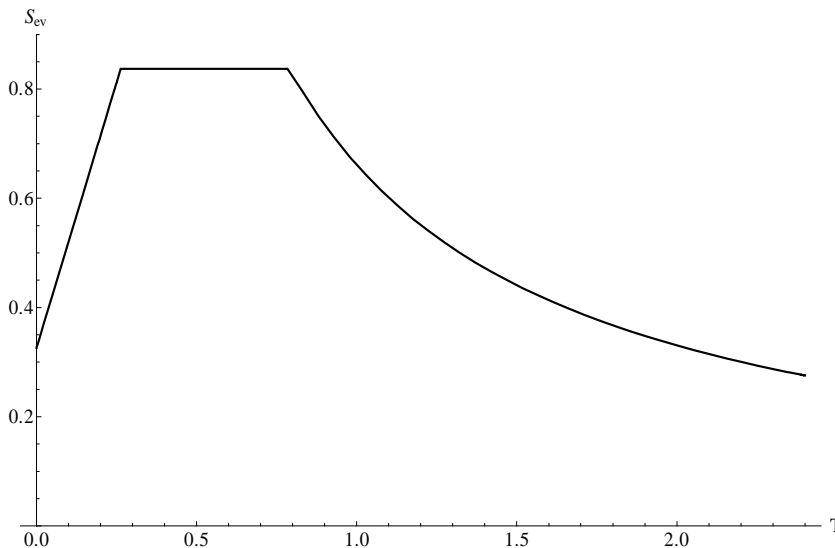


Figure 4.18 Elastic spectrum of the horizontal component

Considering $T_B < T_{bf} < T_C$, for example $0.263 < T_{bf} < 0.790$, we have fixed $T_{bf} = 0.5$ sec, and we have supposed to obtain $T_{is} = 2$ sec. Starting from this

point we have evaluated the pseudoaccelerations for the fixed and the isolated structure, obtaining:

$$\begin{cases} S_e(T_{bf}) = 0,836 \\ S_e(T_{is}) = 0,33 \end{cases} \quad (4.51)$$

From equation (4.51), we find that the horizontal pseudoacceleration is reduced of near 40% ($S_e(T_{is}) \cong 40\% S_e(T_{bf})$), in analogy we can evaluate the vale of the period of isolation for which the vertical pseudoacceleration in reduced of the same percentage.

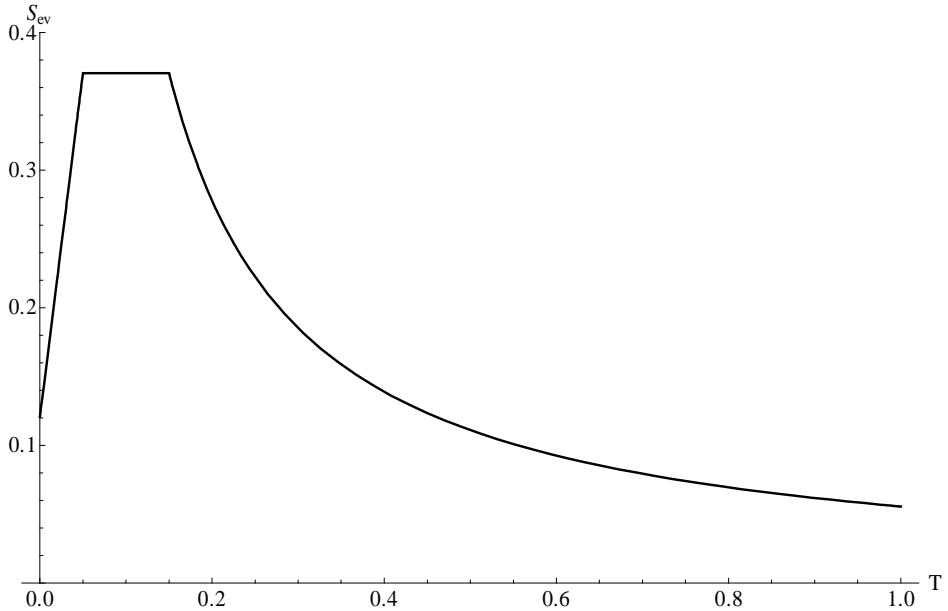


Figure 4.19 Elastic spectrum of the vertical component

Considering that $T_B < T_{bf} < T_C$ and for example $0.05 < T_{bf} < 0.15$, we have fixed $T_{bf} = 0.1 \text{ sec}$, we obtain:

$$\begin{cases} S_{ve}(T_{bf}) = 0,37 \\ S_{ve}(T_{is}) \cong S_{ve}(T_{bf}) \cdot \frac{40}{100} = 0,148 \end{cases}$$

$$S_{ve}(T_{is}) = 40\% S_{ve}(T_{bf}) \quad . \quad (4.52)$$

$$T_{is} = 0,4 \text{ sec}$$

These considerations can be extend also to the elastic spectrum of horizontal displacements, known that:

$$S_{De}(T) = S_e(T) \cdot \left(\frac{T}{2\pi} \right)^2 \quad (4.53)$$

For the latter case, in which we examin the horizontal component, we obtain:

$$\begin{cases} S_{De}(T_{bf}) = S_e(T_{bf}) \cdot \left(\frac{T_{bf}}{2\pi} \right)^2 = 5,18 \cdot 10^{-2} m \\ S_{De}(T_{is}) = S_e(T_{is}) \cdot \left(\frac{T_{is}}{2\pi} \right)^2 = 0,33m \end{cases} \quad . \quad (4.54)$$

$$S_{De}(T_{is}) = (6,39) S_{De}(T_{bf})$$

Similarly, for the elastic response spectrum of th evertical displacement, we have:

$$\left\{ \begin{array}{l} S_{Dve}(T_{bf}) = S_{ve}(T_{bf}) \cdot \left(\frac{T_{bf}}{2\pi} \right)^2 = 9.19 \cdot 10^{-4} m \\ S_{Dve}(T_{is}) = S_{ve}(T_{is}) \cdot \left(\frac{T_{is}}{2\pi} \right)^2 = 5.88 \cdot 10^{-3} m \end{array} \right. \quad (4.55)$$

$$S_{Dve}(T_{is}) = (6,39)S_{Dve}(T_{bf})$$

Therefore, in order that the vertical isolation system is effective, in analogy with what has been seen for the horizontal isolation system, it will result:

$$T_{is} \geq 0,4 \text{ sec} \quad (4.56)$$

4.1.5 Standard Code for the design

The European standard that covers the design of devices that are provided in structures, with the aim of modifying their response to the seismic action, is the ISO 15129. It specifies functional requirements and general design rules in the seismic situation, material characteristics, manufacturing and testing requirements, as well as acceptance, installation and maintenance criteria.

The anti-seismic devices and their connections to the structure will be designed and constructed in such a way that the following requirements are met, each with an adequate degree of reliability:

a) No failure requirement.

The anti-seismic devices and their connections to the structure will be designed and constructed to withstand the design seismic action defined in 2.1 of EN 1998-1, without local or global failure. In this way they retaining their functional integrity and a residual mechanical resistance, including, when applicable, a residual load bearing capacity, after the seismic event.

b) Damage limitation requirement.

The anti-seismic devices and their connections to the structure will be designed and constructed to withstand a seismic action having a larger probability of occurrence than the design seismic action, without the occurrence of damage and the associated limitations of use, the costs of that would be disproportionately high in comparison with the costs of the structure itself. The seismic action to be considered for the damage limitation requirement is defined in 2.1 of EN 1998-1.

According to EN 1998-1, sub-clause 10.3 (2) P, in the case of isolation systems, increased reliability will be required for the isolation devices and their connections to the structure.

Devices and their connections to the structure will be designed and constructed in such a way as to function according to the design requirements and tolerances throughout their projected service life, given the mechanical, physical, chemical, biological and environmental conditions expected. Devices and their connections to the structure will be designed, constructed and installed in such a way that their routine inspection and replacement are possible during the service life of the construction.

Seismic isolators will support the gravity load of a structure without excessive creep and resist non-seismic actions such as wind loadings and thermally induced displacements. They will provide by a low horizontal stiffness or other means the desired low horizontal natural frequency for the isolated structure. They will be able to accommodate the large horizontal displacements produced by seismic actions, whilst still safely supporting the gravity load of the structure and resisting the vertical forces produced by the seismic actions. They will provide a level of damping sufficient adequately to control the horizontal displacements produced by the seismic actions, unless supplementary devices are used to provide the damping.

The types of isolators covered by this clause are:

- a) elastomeric isolators, including those with a plug of lead or high damping polymeric material to enhance the damping;
- b) sliders, both curved and flat surface.

The devices designed in this thesis are both hybrid slider isolators with flat surface, where the restoring force is due to the elastomeric part.

For this kind of devices we have followed also the standard UNI EN 1337-2, in particular for sliding elements incorporating sliding surfaces with PTFE sheets. The PTFE sheets will be recessed into a backing plate, as shown in Figure 4.20.

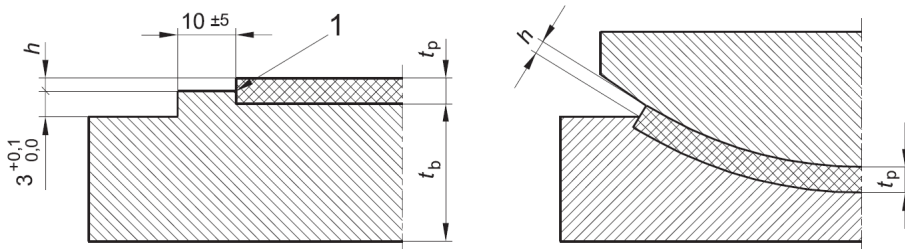


Figure 4.20 Details of PTFE recess and relief (UNI EN 1337-2)

For pressures due to characteristic permanent actions G_k exceeding 5 MPa a uniform pattern of dimples will be provided to retain the lubricant. The shape and arrangement of the dimples in the unloaded and unused condition is shown in Figure 4.21. The dimple pattern will be aligned with the main direction of sliding, as shown in Figure 4.21.

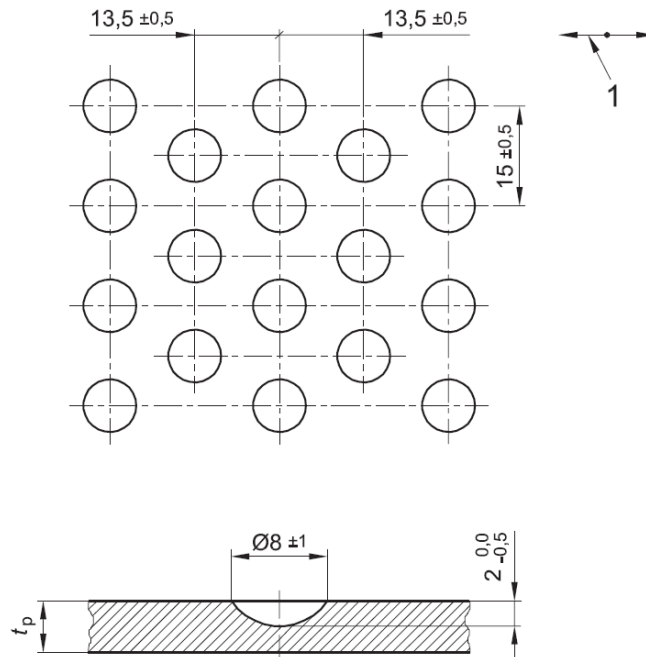


Figure 4.21 Pattern of dimples in recessed PTFE sheet (UNI EN 1337-2)

The thickness t_p of the PTFE sheets and the protrusion h , in the unloaded condition with corrosion protection, will meet the following conditions:

$$h = 1.75 + \frac{L}{1200} \text{ (mm) but not less than } 2.2\text{mm} \quad (4.57)$$
$$2.2h \leq t_p \leq 8.0 \text{ (mm)}.$$

The tolerance on the protrusion h is $\pm 0.2\text{mm}$ for L less than or equal to 1200mm and $\pm 0.3\text{mm}$, for L greater than 1200mm . The protrusion h will be verified at marked measuring points, where the corrosion protection coating will not exceed $300 \mu\text{m}$. There will be at least two measuring points, suitably located. Flat PTFE sheets will be circular or rectangular and may be sub-divided into a maximum of four identical parts.

Dimensioning sliding surfaces, all the internal forces and moments due to actions and frictional resistance will be considered. The design values of the action to be taken into account will be determined in accordance with the basic design criteria given in EN 1337-1. Separation of the sliding surfaces may lead to loss of lubricant, wear due to contamination and increased deformation due to lack of confinement of PTFE. As this could endanger long term fitness for use, the condition $\sigma_p = 0$, where σ_p is the PTFE normal pressure, is considered as serviceability limit state. It will be verified that $\sigma_p \geq 0$, under the characteristic combination of actions. In doing so, the sliding material will be assumed to be linear elastic and the backing plates will be deemed to be rigid.

Excessive pressure may cause loss of the sliding function and this may lead to structural failure or states close to structural failure. Therefore this condition is considered an ultimate limit state, and the following condition will be verified:

$$N_{sd} \leq \frac{f_k}{\gamma_m} \times A_r, \quad (4.58)$$

where:

N_{sd} is the design value of the axial force due to the design values of action;

f_k is the characteristic compressive strength given in Table 4.1;

γ_m is the partial safety factor of the material and the recommended value is $\gamma_m = 1.4$;

A_r is the reduced contact area of the sliding surface whose centroid is the point through which N_{sd} acts with the total eccentricity e , which is caused by both mechanical and geometrical effects.

Moreover, A_r will be calculated on the basis of the theory of plasticity assuming a rectangular stress block.

Material	Action	f_k [MPa]
PTFE for main bearings surfaces	Permanent and variable loads	90

Table 4.1 Characteristic compressive strength for PTFE (UNI EN 1337-2)

4.2 Finite Element model

The code used for modeling the devices under design is ABAQUS CAE v6.14 (Hibbit et al. 20023). ABAQUS CAE is a general purpose finite element analysis tool with a group of engineering simulation programs capable of modelling structures under different loading conditions. It can solve problems of relatively simple structural analysis to the most complicated linear to nonlinear analyses. In a nonlinear analysis ABAQUS CAE automatically chooses appropriate load increments and convergence tolerances and continually adjusts them during the analysis, to ensure that an accurate solution is obtained. The software consists of a widespread library of elements, wherein any type of geometry can be modelled. Apart from solving structural problems, it can also solve problems in other different areas like fracture mechanics, soil mechanics, static analysis, piezoelectric analysis, coupled thermal-electrical analyses, heat problems, and acoustics etc..

4.2.1 Geometric model

This section describes the modeling of the finite elements of the proposed prototype, carried out using the Abaqus v 6.14 computational code (Hibbitt et al. 2003), describing the model, materials, and loads to be adopted. In the Abaqus computing code, many finite elements are available, that can be used in modeling structures and structural elements. Each element is characterized by five aspects:

- Families belonging;
- Numbers of degrees of freedom;
- Numbers of nodes;
- Formulations;
- Integration types.

Each element is defined by a name that identifies the five aspects mentioned. The degrees of freedom of each element are computed in the nodes of the element itself. In three-dimensional problems, the degrees of freedom of a node are equal to 6 (the three movements and the three rotations). At each point within the element, the displacements are obtained by interpolating the nodal displacements. Generally, the interpolation order is determined by the number of nodes used in the element. Elements having nodes only arranged at their vertices, use a linear interpolation and are thus called linear or first order elements, whereas those having nodes also along the edges use quadratic interpolation and are therefore called quadratic or second order elements. Some element families have a standard formulation, while others have a hybrid formulation. It is in these families that we come to pick up the elements necessary to describe the behavior of rubber material with almost complete incompressibility. In fact, the kinematic constraint of non-compressibility makes the volumetric part of the tension field, hydrostatic pressure, decoupled from the field of displacement and consequently indeterminate. The field of tension remains so defined to less than a constant. Moreover, the existence of a singularity in equilibrium equations makes the problem difficult to solve. In the solution to the finite

elements this results in numeric problems and consequently incorrect assessments of the tension state.

Considering the almost incompressible material, the foregoing considerations are less obvious since in this case the condition of quasi-incompressibility is only a problem of the numerical model and not the mechanical one. The difficulties encountered are, therefore, exclusively of a numerical nature and concern malformations of the stiffness matrix, blocking phenomena, and the presence of incorrect results.

Over the past decades, a great interest in the study of the problem has allowed the development of methodologies that can handle the constraint in finite element formulations. An interesting alternative to mixed methods is the reduced integration technique. The method, which uses different quadratures to evaluate the deviation part and the volumetric part of the stiffness matrix, treats the problem of incompressibility with excellent results by avoiding the computational burden of introducing the new range of required variables in mixed formulations. We can also show the equivalence of the method to mixed methods. Abaqus uses numeric techniques to integrate various quantities into the volume of each element. For most elements it uses the Gaussian quadrature method, so that the response of material, to a finite number of integration points within the element, is evaluated. Particularly for modeling the device, the following types of elements are available:

Plane Elements with Plane deformation

Elements of this type are used when a plane deformation condition is expected for the rubber with deformation out of the zero plane. These elements are generally used to model isolator with behavior similar to the infinite strip. Four dimensional CPE4H quadrilateral elements (flat-to-hybrid formulation) can be used for modeling the rubber, while for steel plates we use CPE4 elements.

Axialsymmetric elements

Axialsymmetric elements are used for modeling continuous revolutionary solid under load conditions that verify the condition of radial symmetry. Axialsymmetric elements can be used to analyze the problem by discretizing a cross section. The volume of the material, associated with the

element, is that of a solid revolution. The value of the assigned forces or the reactions in the nodes are integrated over the entire circumference.

In the library of two-dimensional elements of this type, elements of the first and second order are available. In relation to those usable in the elaborations carried out we can mention:

- CAX4 axialsymmetric element with 4 nodes and bilinear interpolation functions ;
- CAX4H axialsymmetric hybrid element with 4 nodes and bilinear interpolation functions for the displacements and constant for the pressure;
- CAX8 axialsymmetric element with 8 nodes and biquadratic interpolation functions;
- CAX8H axialsymmetric hybrid element with 8 nodes and biquadratic interpolation functions for the displacements and linear for the pressure.

Tridimensional elements

The elements included in the calculation code are of first and second order. The first order elements are "brick elements" with eight nodes; interpolation functions are classic trilinear functions for isoparametric elements. The second order elements are twenty-node parallelepipeds, whose interpolation functions are classic triquadratic functions for isoparametric elements. The elements that can be used in the processing can be:

- C3D10 10-node tetrahedral element with biquadratic interpolation function;
- C3D8 brick element with 8 nodes with trilinear interpolation function;
- C3D8H brick hybrid element with 8 nodes with trilinear interpolation function for the displacements and constant for the pressure;
- C3D20 brick element with 20 nodes with triquadratic interpolation function;
- C3D20H brick element with 20 nodes with triquadratic interpolation function for the displacements and constant for the pressure.

The following problems are addressed in the numerical modeling of the device:

1. choice of finite element type;

2. choice of the constitutive law for all the materials of the devices;
3. study of the boundary conditions and of the loads;
4. choice of the mesh of the device;
5. choice of the analysis type.

We remember that using superior order elements and more discreet discretizations, certainly improves the quality of the solution, but inevitably raises the computational burden expressed as the time taken by the computer to complete the analyzes. In general, for the various models, a discretization was carried out near the outer edges so as to obtain more accurate results for these areas. Regarding the type of analysis, static analysis is conducted by introducing geometric non-linear conditions of the model since the problem is the field of large displacements and large deformations.

4.2.2 Finite element for the calibration of the model

Concerning the choice of the finished element type, the C3D4 elements for the steel plates and the cylindrical element will be used, while C3D8H for the rubber ring, and a C3D10 for the PTFE element. With this choice, of elements you can overcome the theoretical-numerical difficulties presenting the finite elements analysis of the incompressible or almost incompressible materials.

4.2.3 Constitutive law of the materials used

For the mechanical behavior of the elastomeric material, the computing code used, Abaqus v6.14, has various well-known literature in hyperelasticity, i.e. different expressions of the U-deformation energy density function. Forms of energy potential of deformations adopted to shape the elastomeric material are all those listed and described in §2.2.1.

For the characterization of the elastomeric material, i.e., for the definition of the coefficients characteristic of each single hyperelastic model, the data of the experimental tests carried out on the rubber are

provided to the calculation code. The computing code, by means of a dedicated algorithm, automatically determines the values of the characteristic coefficients of the hyperelastic model considered. As far as steel plates are concerned, it has already been mentioned in §2.4.

For this computational analysis, we chose to use a second-order Ogden function to describe elastomer behavior. The performance of the characteristics was derived from experimental data in the literature, while the choice of the type of functions was based on the comparison between the curves that best approximated the experimental data (see §2.2.2.7).

4.2.4 Modeling contact interaction surfaces

The contact condition between the surfaces has been implemented through the *contact interaction surface to surface* algorithm, defining for each interface a master surface and a slave surface. The slave surface nodes are bound not to exceed those of the target surface with respect to the direction located from the normal position to the master surface.

Contact interactions for contact pairs and general contact pairs are defined by specifying surface pairings and self-contact surfaces. General contact interactions typically are defined by specifying self-contact for the default surface, which allows an easy, yet powerful, definition of contact.

The general contact algorithm in Abaqus/standard:

- is specified as part of the model definition;
- allows very simple definitions of contact with very few restriction on the types of surfaces involved;
- uses sophisticated tracking algorithms to ensure that proper contact conditions are enforced efficiently;
- uses the finite-sliding, surface-to-surface contact;
- can be used to define interactions between bodies in mechanical, coupled temperature displacement, heat transfer simulations and other problems.

To every contact pair is assigned a contact formulation that must refer to an interaction property. There are different methods for defining the components of a mechanical contact property model.

When surfaces are in contact they usually transmit shear as well as normal forces across their interface. There is generally a relationship between these two force components, the relationship, known as the friction between the contacting bodies, is usually expressed in terms of the stresses at the interface of the bodies. The friction model used for the analysis here effectuated includes the classical isotropic Coulomb friction model, which in ABAQUS:

- in its general form allows the friction coefficient to be defined in terms of slip rate contact pressure, average surface temperature at the contact point, and field variables;
- provides the option to define a static and kinetic friction coefficient with a smooth transition zone defined by an exponential curve.

The friction between the surfaces was initially modeled by a constant coefficient μ , according to the simplified theory of Coulomb: drawing from the experimental data he assumed $\mu=0.05$.

As we have said in Chapter 2, the energy dissipated during the sliding motion of the FP is converted by friction into heat, thus inducing a temperature rise at the contact surfaces. Frictional heating produces a decrease in the hardness of the thin surface layer that generates friction degradation. In turn, the reduction of the friction coefficient leads to a substantial decrease in the heat being generated at the sliding interface. It can be concluded that friction degradation and temperature rise are two interconnected mechanisms that should be investigated via a *thermo-mechanical coupled* analysis.

Following the analysis done for the FP in §3.2.3, after a previous model in which is not taken into account the effect of temperature, a second model has been made with a TMC but a constant coefficient of friction. Then a third model has been made, in which the coefficient μ has the shape depicted in Figure 4.22.

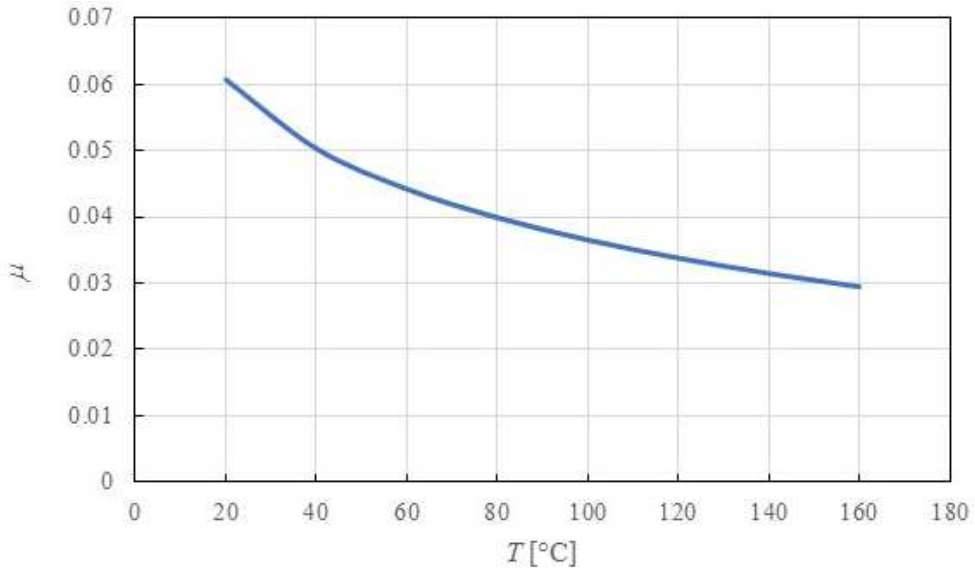


Figure 4.22 Degradation of the friction coefficient with temperature

4.2.5 Boundary conditions and loads

The models of both devices are loaded vertically and horizontally. The horizontal load is applied as lateral displacement for subsequent steps in such a way as to analyze the behavior of the devices at different deformation levels imposed. Regarding the constraints, the conditions in which the isolation device generally is working are determined, preventing the lower metal plate from moving and allowing the upper one to move freely parallel to the lower one. For these reasons, the base nodes of the lower metal plate have been stacked, while all nodes belonging to the top plate have been bound to have the same vertical displacements.

4.3 Hybrid Friction Rubber Isolator FE model

The number of FEs has been chosen after a preliminary mesh sensitivity study to assure an accurate FE solution. The total number of FEs and the final mesh is illustrated in Figure 4.24-Figure 4.27 and is composed of 35989 elements and corresponding 54531 nodes, each node having three degrees of freedom (DOFs), namely the three translations with respect to the Cartesian axis system shown in the Figure 4.24. Large displacement formulation is assumed; additionally, the (very small) deformability of the plate components has been accounted by including the elastic properties of the steel components as reported in Table 3.4, along with those of the PTFE pads. A three-dimensional finite element model is set up in which the generation of frictional heat is reproduced via a moving heat source with local intensity dependent from the instantaneous friction coefficient, the relative velocity and the contact pressure at the sliding surface. The friction coefficient at the sliding interface is adjusted node-by-node, via a customized subroutine implemented into the FE-code the updated friction value is used to compute the heat flux at the next time step in a recursive way.

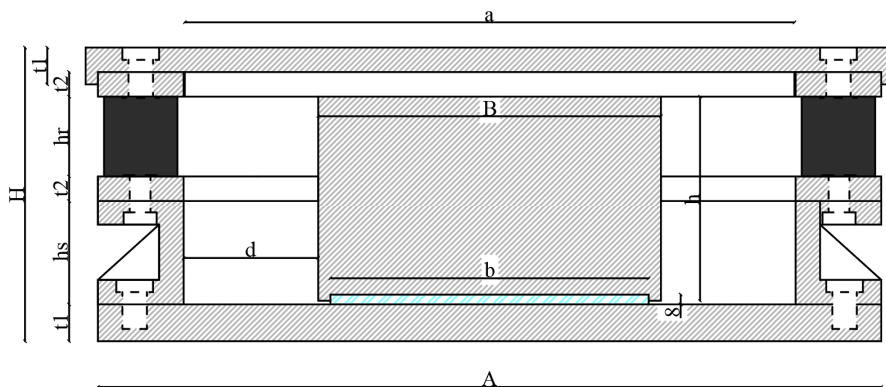


Figure 4.23 Schematic sketch of the HFRI with the representation of the dimensions

Typical thermal parameters of stainless steel and PTFE pads are assumed in order to properly simulate the thermal solution and solve the thermo-mechanical problem accordingly. The coefficients of thermal dilatation have been set equal to $1.2 \cdot 10^{-5} \text{ }^\circ\text{C}^{-1}$ and $16 \cdot 10^{-5} \text{ }^\circ\text{C}^{-1}$ for steel and PTFE, respectively.

Dimensions	Length mm
A	640
a	500
B	280
b	260
H	240
hr	65
hs	85
h	167
t ₁	30
t ₂	20
d	100

Table 4.2 Geometrical characteristic of the HRFI studied

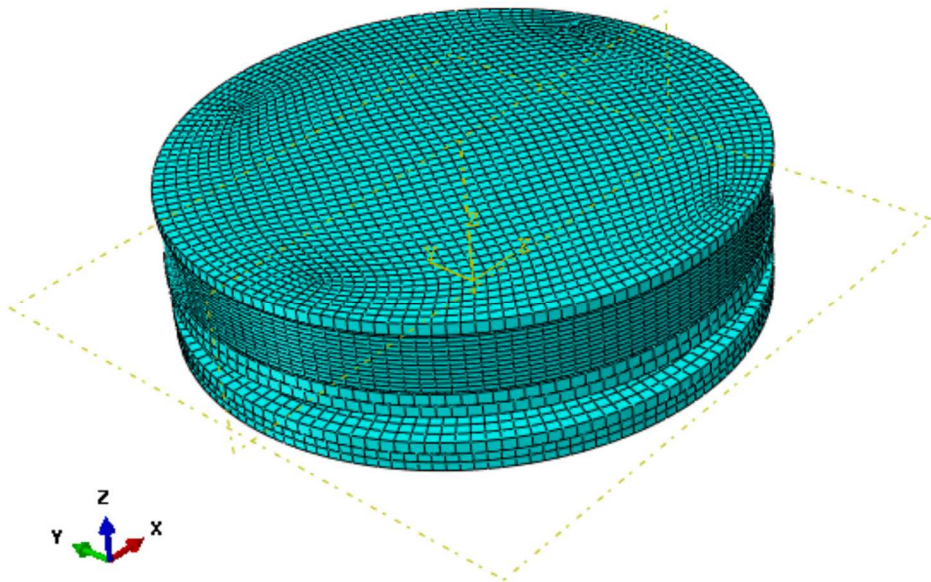


Figure 4.24 ABAQUS-3D model of the horizontal device

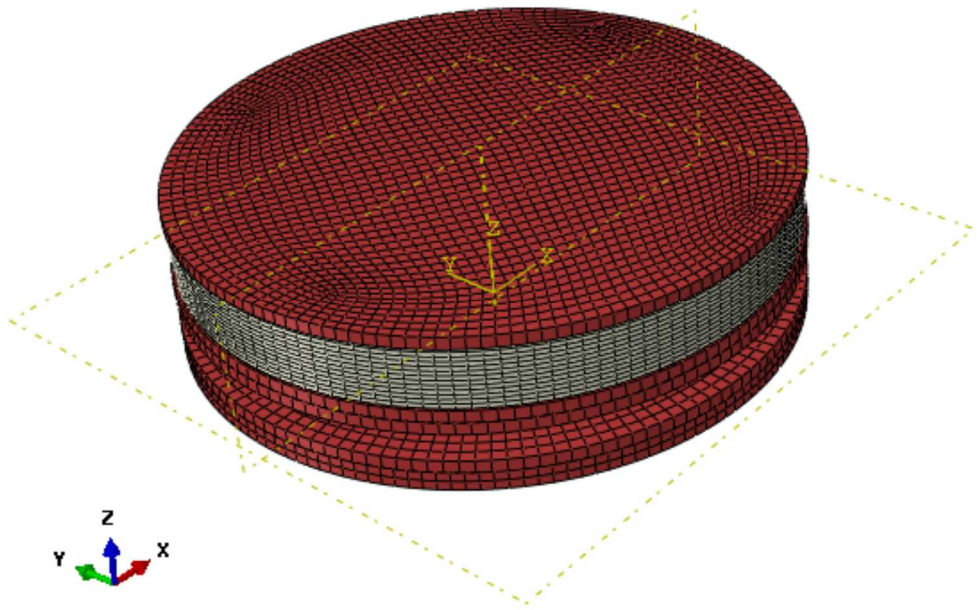


Figure 4.25 ABAQUS-3D model highlighting the different material with different colors

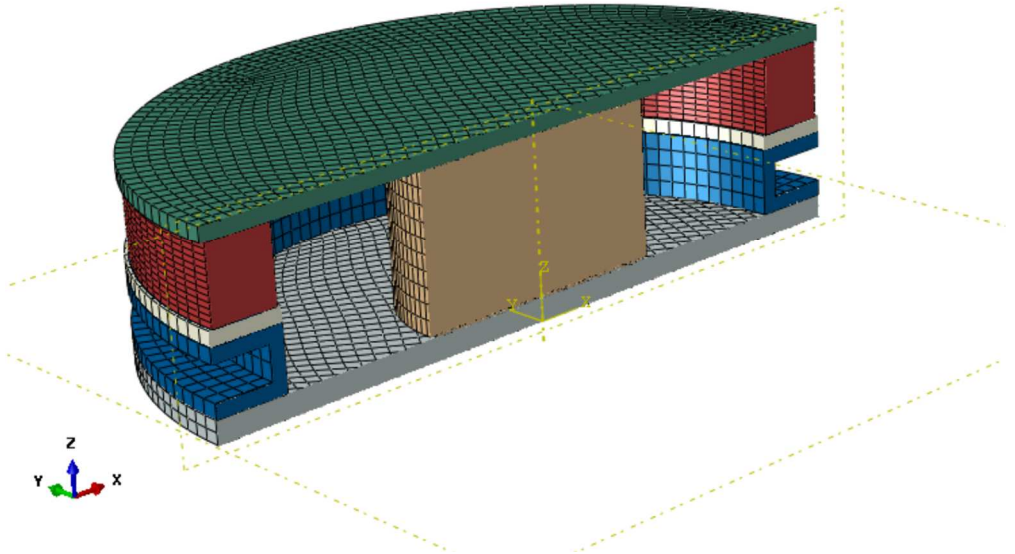


Figure 4.26 ABAQUS-3D Section model highlighting the different part with different colors

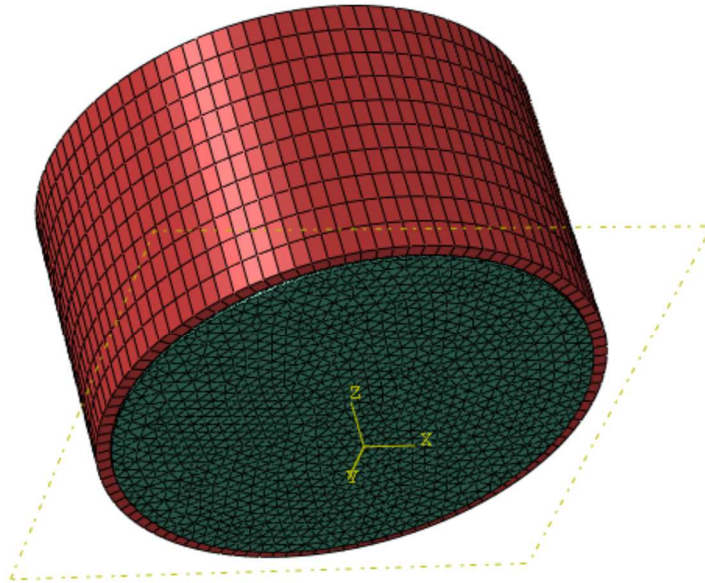


Figure 4.27 ABAQUS-3D model of the PTFE pad

Case 1.A

A first case has been made to study the behavior of the device under loading conditions. The geometrical properties are reported in Table 4.2, as we have said these are the characteristic of a medium device, that could be used in the case of ordinary civil structures. The model, after a first step in which only the vertical load is acting, is subjected to a cyclic displacement in the x-axis, represented in Figure 4.28. This kind of time history reproduces the real load to which the device is subjected during an experimental test. For the sake simplicity, in thi analisys the friction coefficient is assumed to be constant and equal to $\mu = 0.05$.

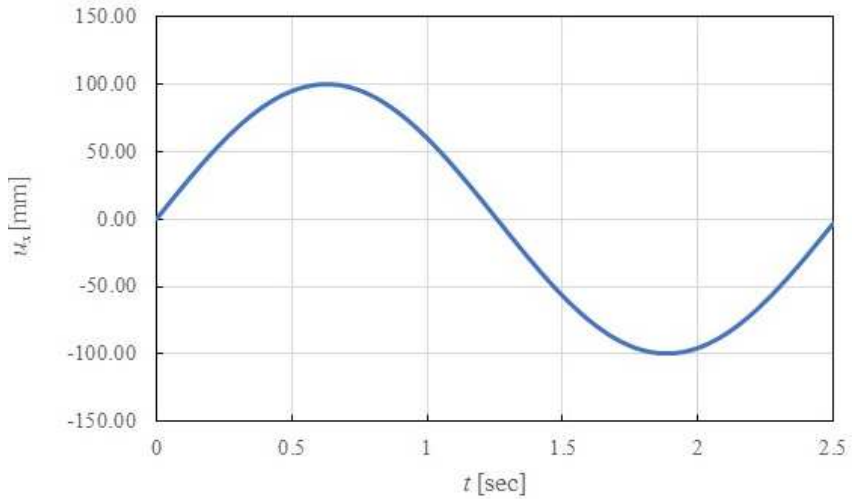


Figure 4.28 Time history of the horizontal displacement with $A=100$ mm, $v_p=250$ mm/sec

In Figure 4.29 it is shown the deformed shape at the final step, we can see that, as we expected, the elastomeric part is responsible of the restoring force. In Figure 4.30 is reported the tensional analysis of the device in terms of $\sigma_{33} \equiv \sigma_{zz}$, in which it is possible to see that everywhere the stress value is in the limit range of the materials involved. In Figure 4.31 is shown the stress state for the rubber part only, we note that the as suggested the rubber is all in a compression state.

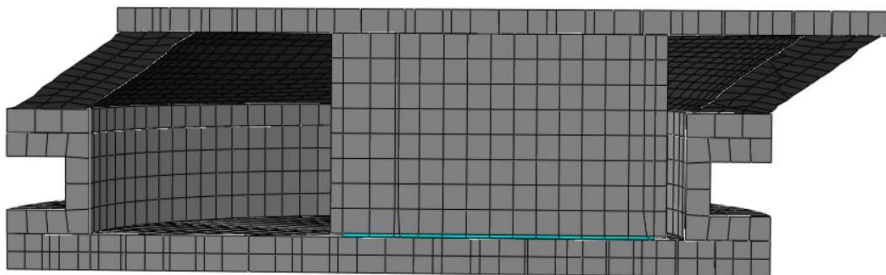


Figure 4.29 Deformed shape of HDRI at the final step

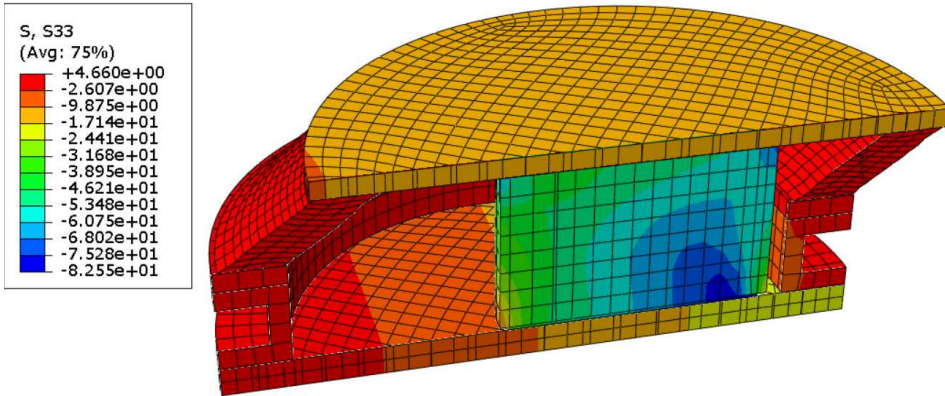


Figure 4.30 Stress distribution at the final step

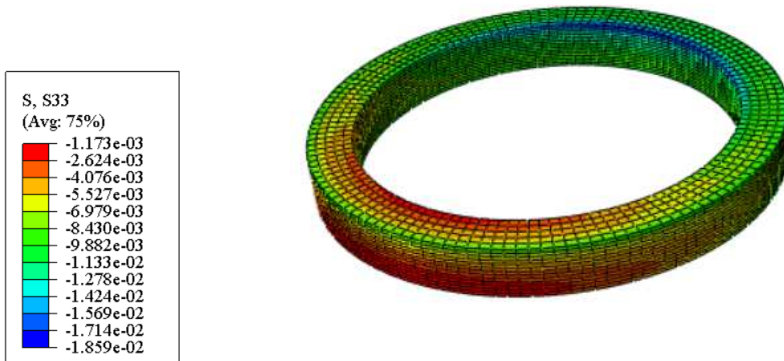


Figure 4.31 Stress distribution at the final step in the rubber part

Finally, for this first analysis, a force-displacement loop is depicted in Figure 4.32. The typical shape of a friction based dissipative mechanism is obtained. The effects of the hyperelasticity of the elastomer are visible in the non linear shape of the ascending and descending branches of the loop.

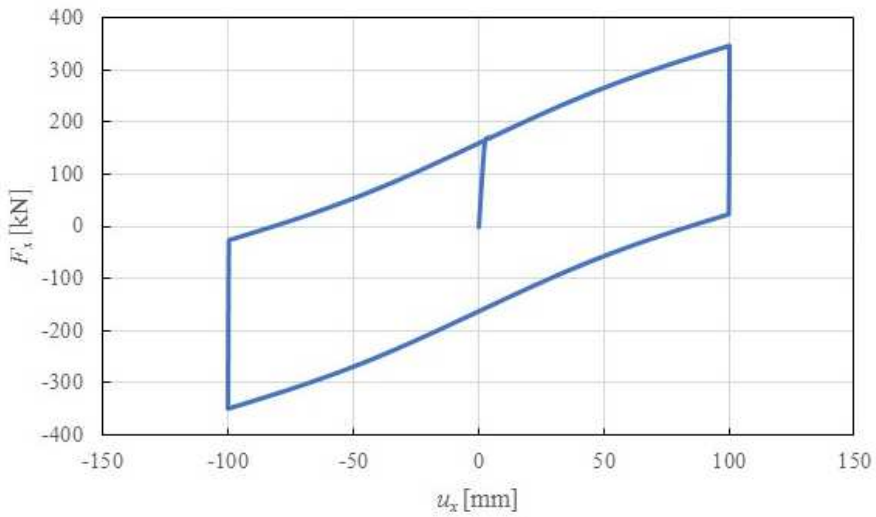


Figure 4.32 Force-displacement loop from the FE model

Case 1.B

In this case the model is the same of the previous one, in which a *thermo-mechanical coupled* analysis has been made where the friction coefficient is variable with the temperature T , following the shape depicted in Figure 4.22. The model, after a first vertical load, in the second step has been subjected to a cyclic displacement history, see Figure 4.33, to highlight the effect of the temperature on the device.

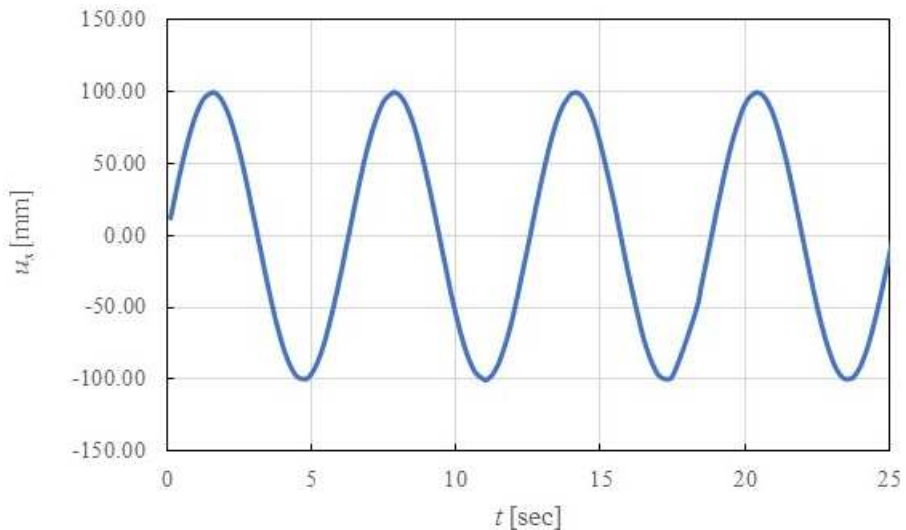


Figure 4.33 Time history of the horizontal displacement with $A=100$ mm, $v_p=100$ mm/sec

The force-displacement loops are depicted in Figure 4.34. Also in this case the typical shape of a friction based dissipative mechanism is obtained.

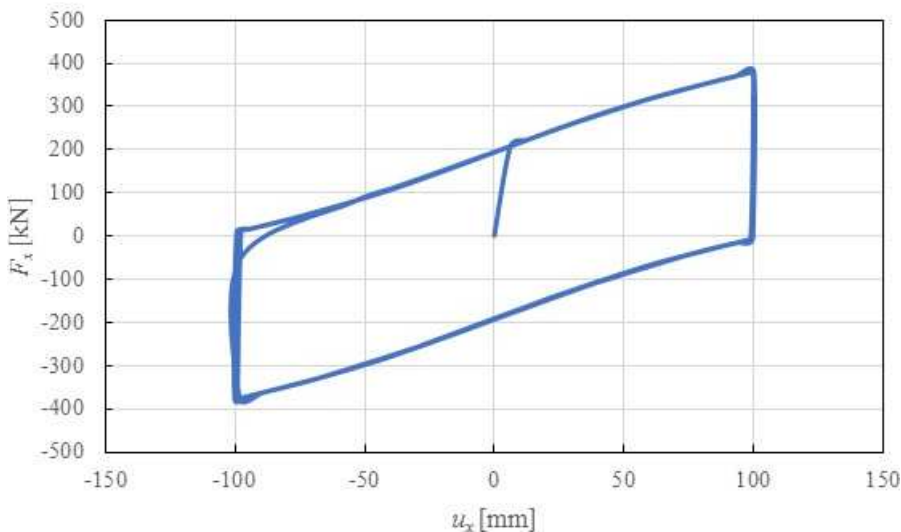
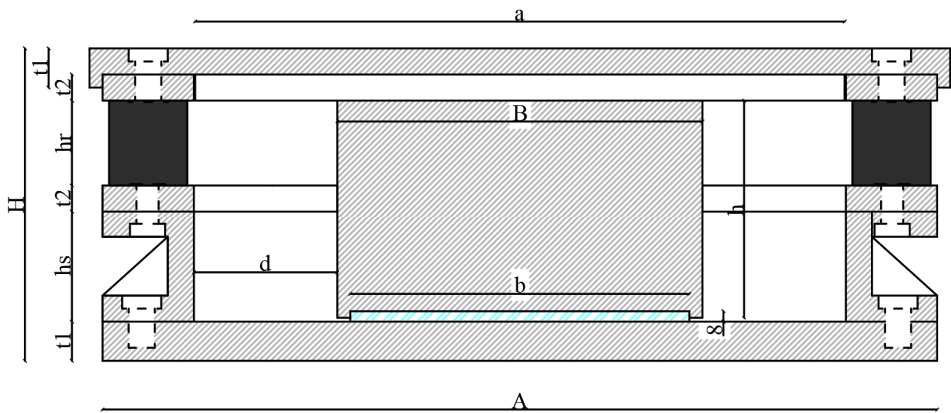


Figure 4.34 Force-displacement loop from the FE model

Case 2

To make a comparison, we have dimensioned another device similar to the Friction Pendulum described in §3.2 for which we have the result of the experimental bidirectional clover leaf test. For this reason, after the geometrical characterization (reported in Geometrical characteristic of the HRFI studied in case 2) the model 2 has been subjected to the same cloverleaf test (see Figure 4.35) in a thermo-mechanical coupled analysis where the friction coefficient is variable with the temperature T , following the shape depicted in Figure 4.22.



Dimension	Length mm
A	970
a	770
B	350
b	330
H	255
hr	100
hs	85
h	202
t ₁	30
t ₂	20
d	200

Table 4.3 Geometrical characteristic of the HRFI studied in case 2

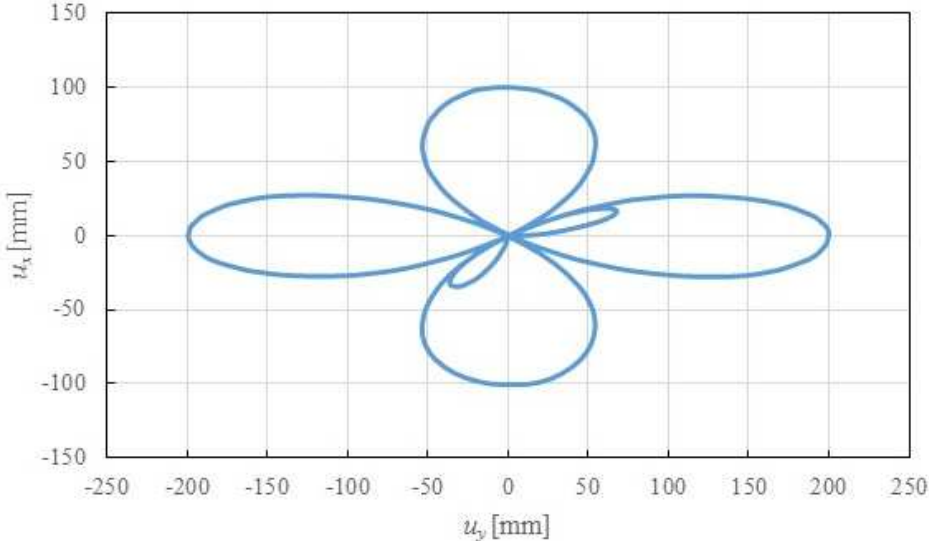


Figure 4.35 Trajectories of the clover leaf test

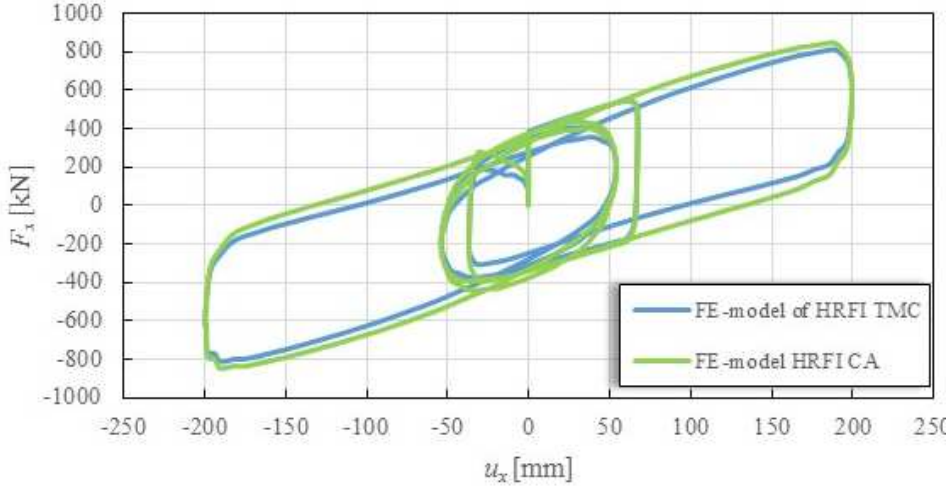


Figure 4.36 Force displacement loop for the clover leaf test in direction x: comparison between simple analysis and TMC analysis

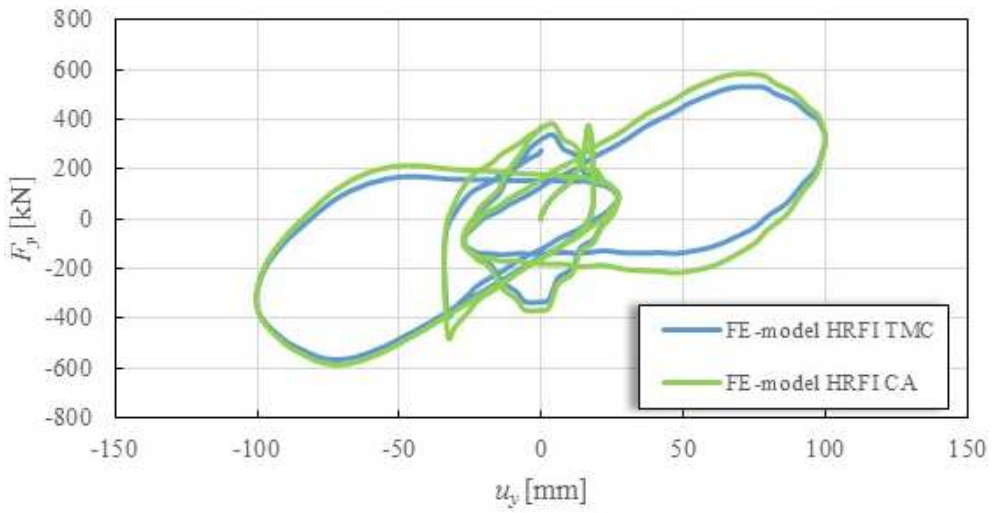


Figure 4.37 Force displacement loop for the clover leaf test in direction y: comparison between simple analysis and TMC analysis

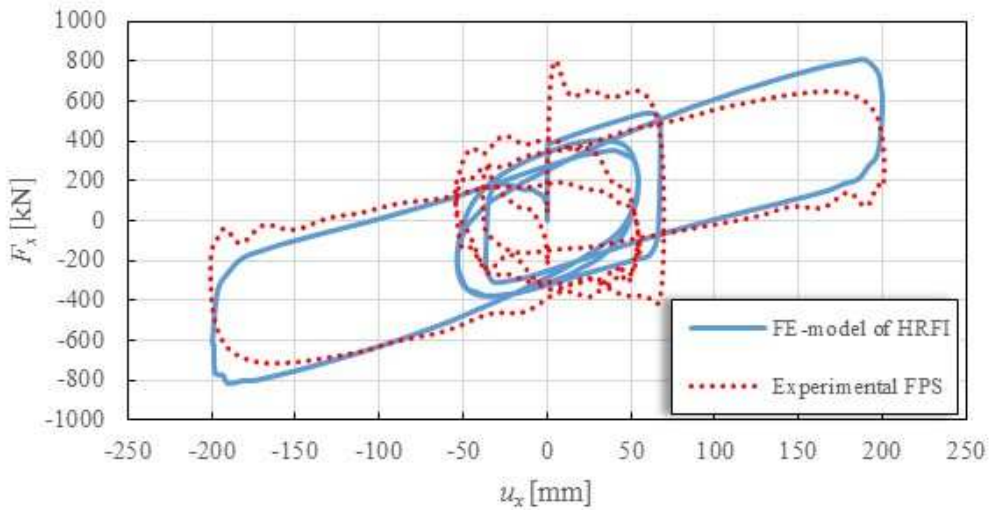


Figure 4.38 Force displacement loop for the clover leaf test in direction x: comparison between simple analysis and experimental test

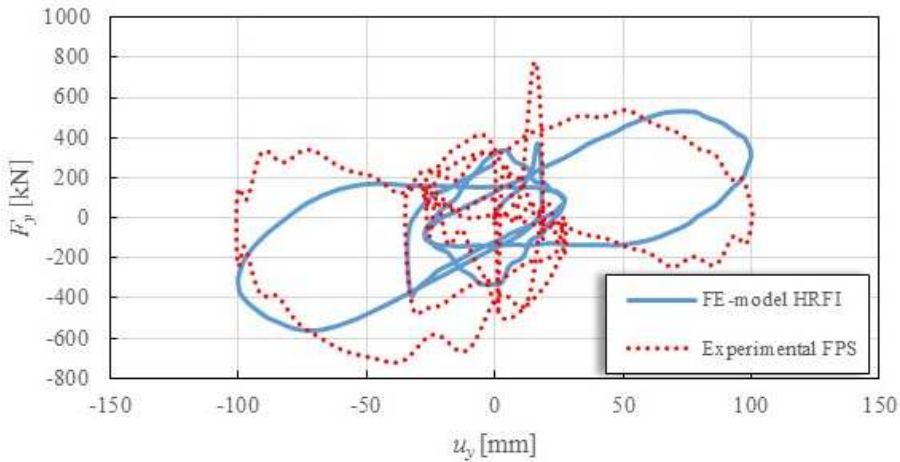


Figure 4.39 Force displacement loop for the clover leaf test in direction y: comparison between simple analysis and experimental test

In Figure 4.40 is reported the temperature distribution on the sliding PTFE pas for bidirectional cloverleaf test of the HRFI proposed. The results are in accord to that one of the FP analyzed in §3.2.3, shown in Figure 3.22.

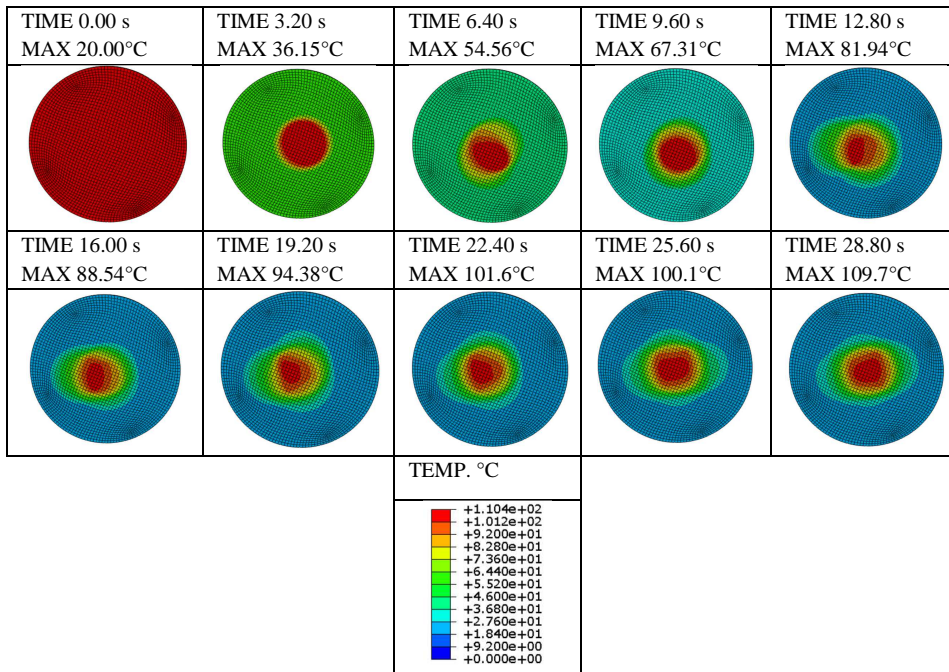


Figure 4.40 Temperature distribution on the sliding plate for bidirectional cloverleaf test of HRFI

The highest temperature is expected in the area interested by more frequent sliding activity. As we have already shown in § 3.2.3, the temperature rise is usually of short duration and is therefore called “flash temperature” in the relevant literature. This concept is clarified in Figure 4.41, in which the temperature histories for bidirectional and monodirectional tests are reported. More specifically, at each time instant we compute the average temperature on the contact surface. To compute the average temperature on the sliding plate, the average operator is restricted to the actual, instantaneous footprint of the slider. The frictional heating gives rise to a temperature rise that propagates and expands so as to involve the entire PTFE-pad over the duration of the test. This is why the average temperature in the contact surface appears to be almost monotonically increasing in Figure 4.41. Overall, the friction coefficient depends on the temperature at the sliding interface, being affected by the temperature on both the sliding PTFE-pad and the sliding plate.

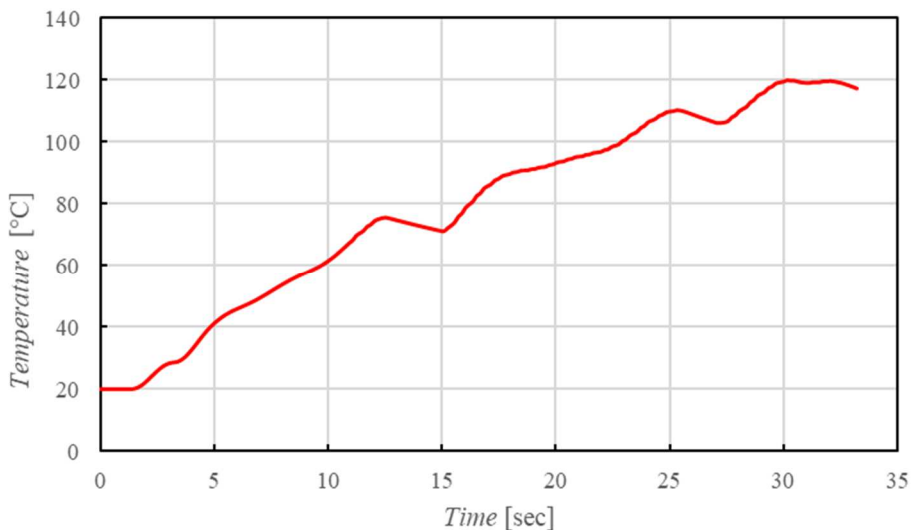


Figure 4.41 Average temperature histories during the bi-directional test

High flash temperatures developed at the sliding interface reduce the friction coefficient according to the TMC subroutine, thus producing a decrease in the frictional heating generated at the sliding interface. In turn, this gives rise to a limitation in a further temperature increase in accordance with the mechanism of “thermal control of friction” (Ettles 1986).

4.4 Vertical Isolation Device FE model

To realize the model we have chosen to design a vertical device of medium characteristics (see Table 4.4 and Figure 4.42 , with, for example, a vertical displacement of about 15mm. The number of FEs has been chosen after a preliminary mesh sensitivity study to assure an accurate FE solution. The total number of FEs and the final mesh is illustrated in Figure 4.43-Figure 4.45 and is composed of 144754 elements and corresponding 78434 nodes, each node having three degrees of freedom (DOFs), namely the three translations with respect to the Cartesian axis system shown in the Figure 4.43. Large displacement formulation is assumed as for the horizontal device.

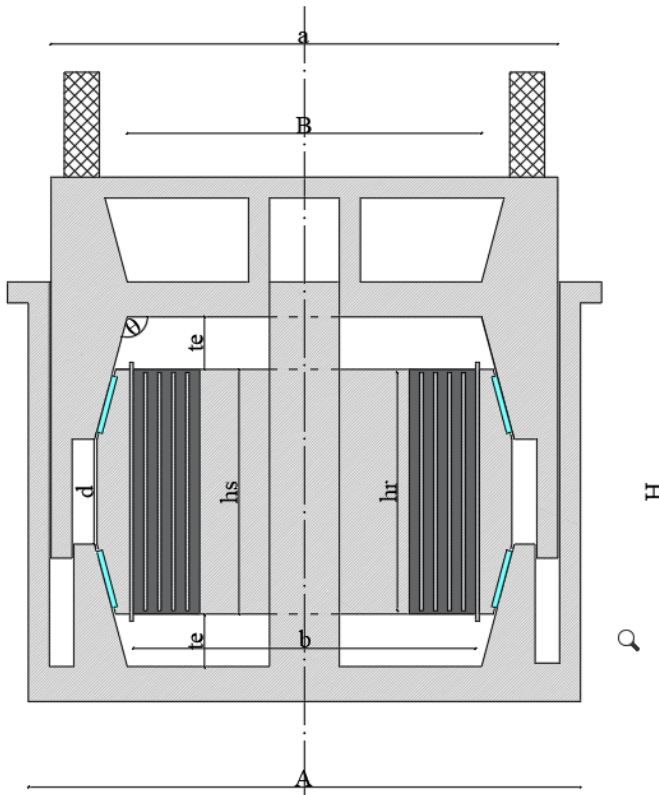


Figure 4.42 Schematic sketch of the VID with the representation of the dimensions

Dimensions	Length mm
A	790
a	725
B	506.92
b	490
H	600
hr	340
hs	350
h	167
θ	105°
te	75
d	150

Table 4.4 Geometrical characteristic of the VID studied

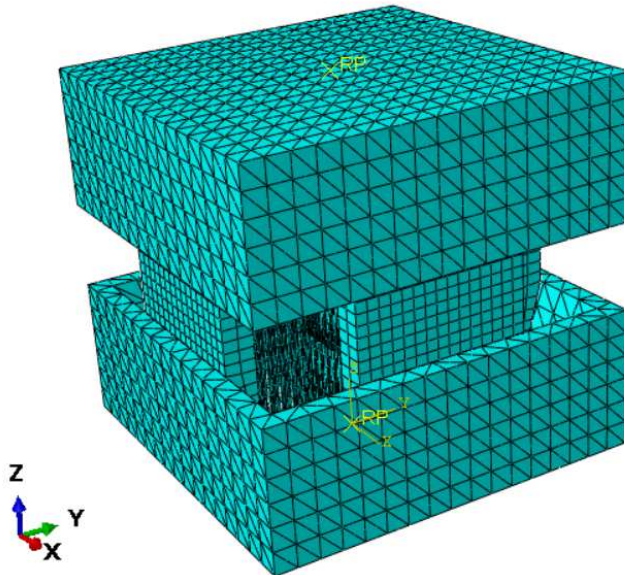


Figure 4.43 ABAQUS-3D model of the vertical device

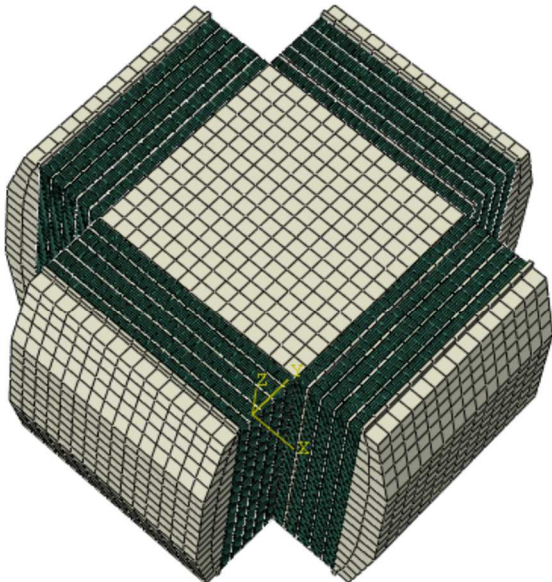


Figure 4.44 ABAQUS-3D model of the inner part of the vertical device

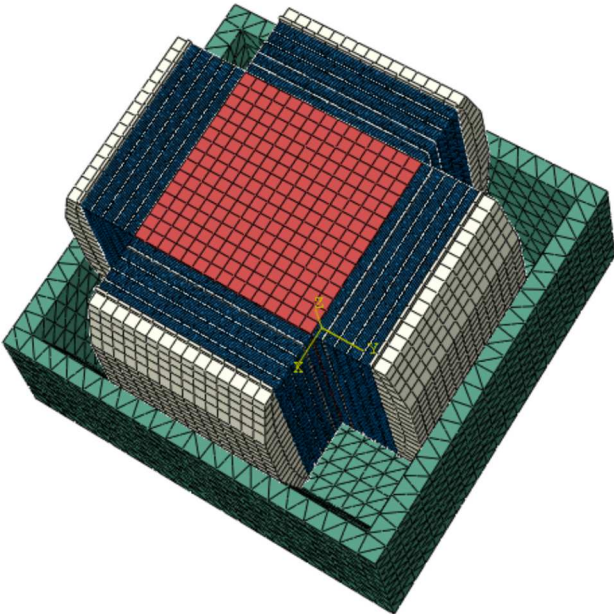


Figure 4.45 ABAQUS-3D model of the vertical device

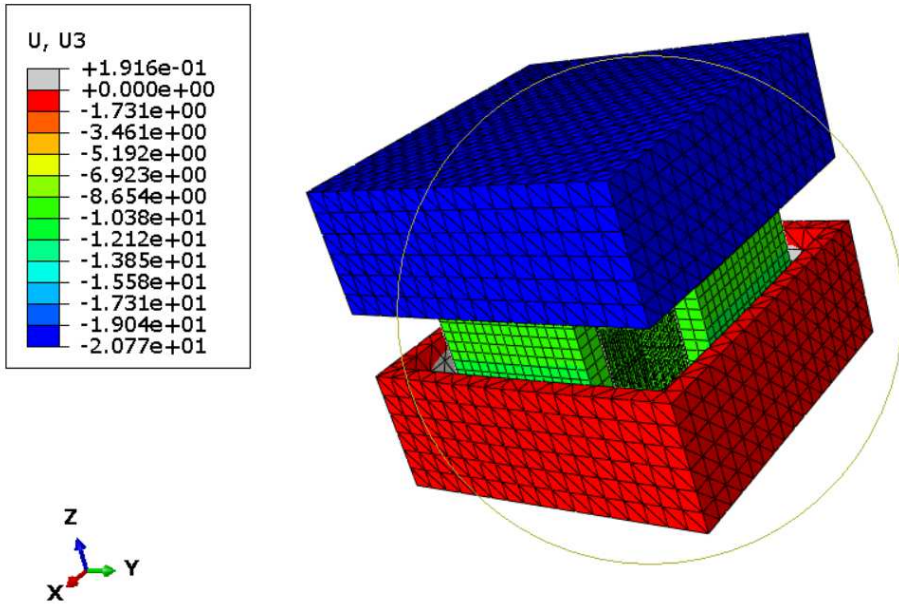


Figure 4.46 Deformed shape after ONE cycle

The model was subjected at first to the vertical static pressure due to the presence of the superstructure; then the model was subjected to a cyclic-displacement in the z-axisis.

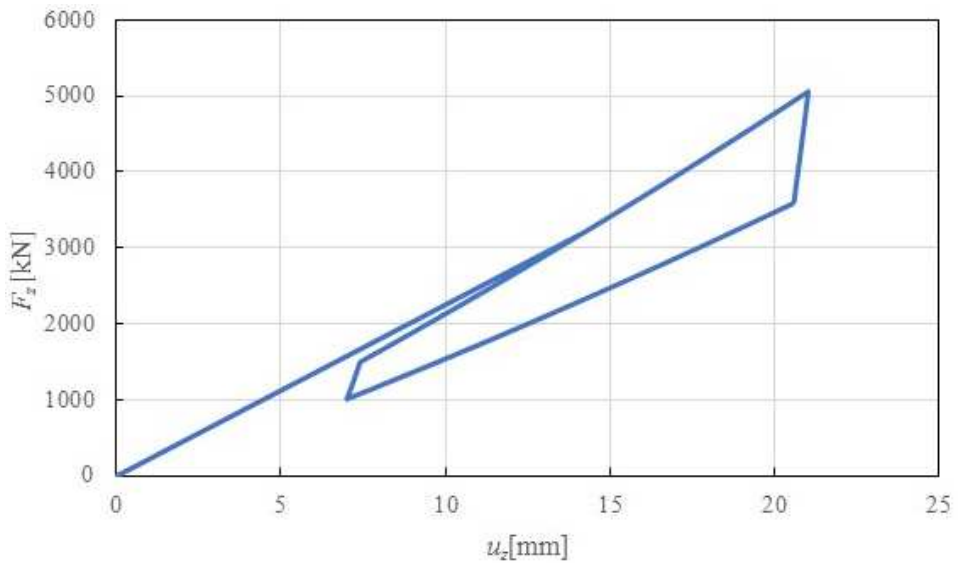


Figure 4.47 Force-displacement loop for the VID

As can be seen from Figure 4.47, after a first lowering due to the static load, the hysteresis cycle starts, as expected, with a slope that is different from the downward slope.

4.4.1 Numerical application on a steel tank

After the modeling and the study of the proposed vertical prototype, an application was carried out using SAP2000 16 software. Therefore, the behavior of data systems was observed in the presence or absence of the proposed isolation system, highlighting thus the effects and effectiveness of the latter. In the specific case, a metal structure was studied to reproduce the covering of a metallic tank for the storage of crude oil (see Figure 4.48).

The characteristics of the tank have been taken from the literature (Carlos and Héctor 2008) and is constituted by rings, with variable thickness t along of the height H and are reported in Table 4.5 and Table 4.6; on the basis of this information we proceeded to design a metal covering structure with steel supporting elements and aluminum closure. For this case we have design a VID with bigger dimensions, that can realize the stiffness needed to reach the isolation period.



Figure 4.48 Circular cylindrical steel storage tanks of 150 thousands barrels

With the help of SAP 2000 we have at first modeled the structure without the isolation system (Figure 4.49) and we have performed a dynamic analysis with time history, using a spectrocompatible accelerogram generated in accordance with what is stated in §4.2.2.

E_s	206000	Steel Young Modul (Mpa)
ν	0.3	Poisson ratio
γ_s	76910.4	Steel weight for volume unit N/m ³
ρ_s	7840	Steel density kg/m ³
γ_l	9810	Liquid weight for volume unit N/m ³
ρ_l	1000	Water density kg/m ³
γ	2206	Liquid compressibility in Mpa

Table 4.5 Mechanical characteristics of materials of circular cylindrical steel storage tanks

Dimensions	150000 barrels tank	Rigid ring (mm)
H (m)	14.63	1.2
h (m)	13.563	
R (m)	22.847	
t1 (mm)	25	12.7
t2 (mm)	22	
t3 (mm)	19	
t4 (mm)	16	
t5 (mm)	13	
t6 (mm)	10	

Table 4.6 Geometrical characteristics of the circular cylindrical steel storage tanks

The response was then evaluated in terms of displacements of the central point of the cover and the normal strength of a system beam.

The characteristic of this system are:

- Period of 0.184 sec
- Frequency of 5.46 Hz
- Mass of 729.85 kg

After this analysis we proceeded to insert vertical isolation device, modeled by NLLINK (Figure 4.50), such as to guarantee a symmetric period for the structure in order to reduce the rocking phenomenon. Therefore, in accordance with what was done for fixed structure, the response was evaluated in terms of displacements of the central point of the cover and the normal strenght of a system beam.

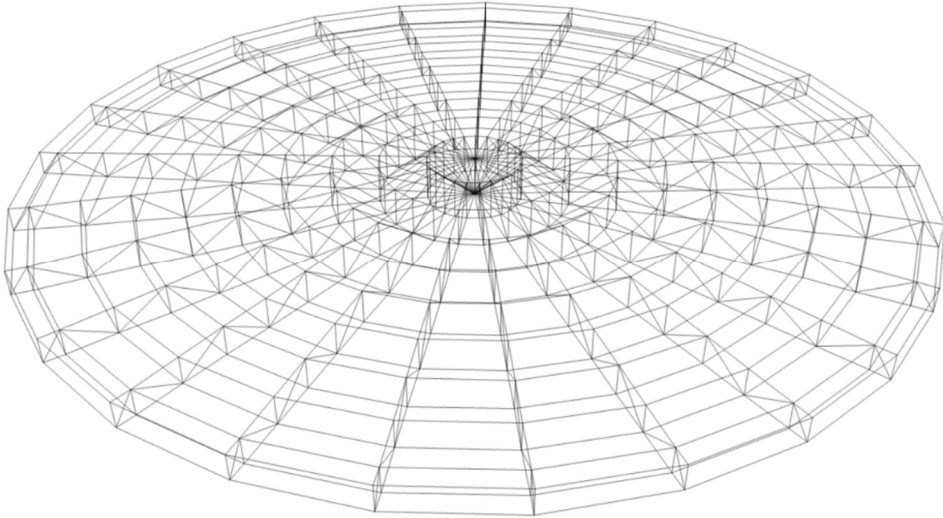


Figure 4.49 SAP model of the structures without the VID

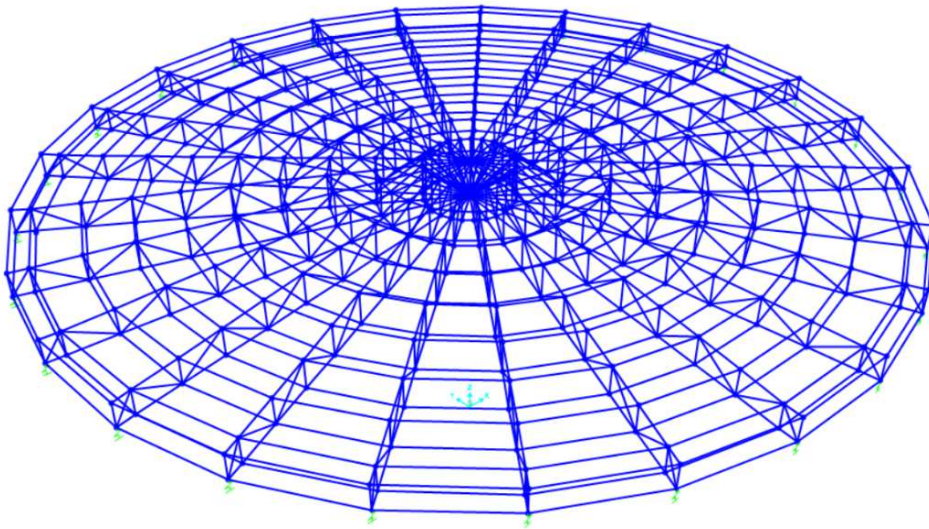


Figure 4.50 SAP model of the structures with the VID

From the comparison between the outputs of the fixed and the isolated structure (Figure 4.51, Figure 4.52) we observed as expected an increase in the response in terms of displacement, and at the same time a reduction in stresses.

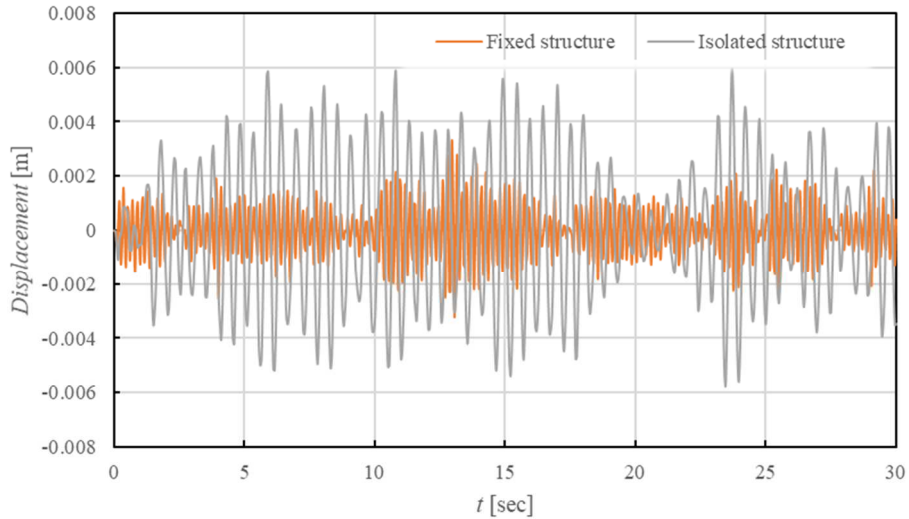


Figure 4.51 Displacement of the central point: fixed vs isolated structure

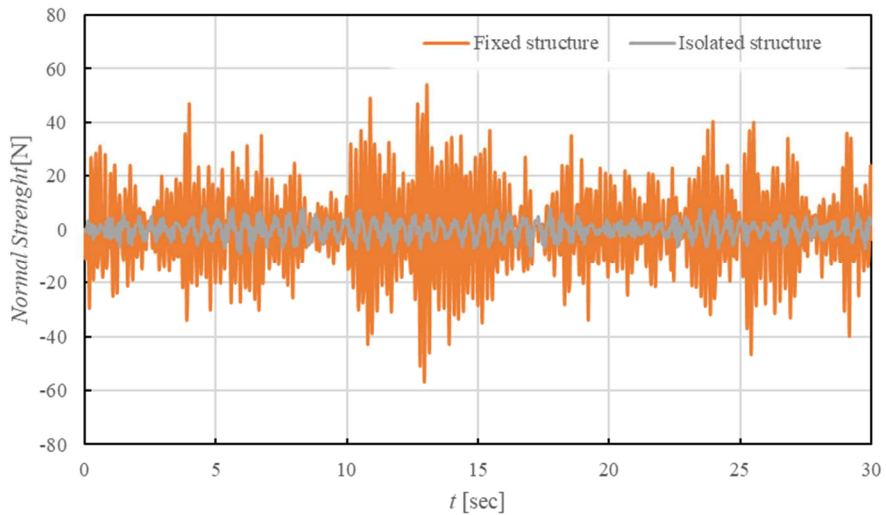


Figure 4.52 Normal strength of a beam: fixed vs isolated structure

4.5 Advantaged of the proposed isolation devices

4.5.1 HRFI

1. Uniform distribution of contact forces (compared to FP):
In pendulum devices, the center of gravity of the contact forces (including the callback and the attractive contribution) whose coordinates are calculated from the distribution of the nodal forces differs slightly from that followed by the slider, with the most significant differences in proximity of the reversal points of the bike. In the case of flat sliding surface there is a uniform distribution of the contact forces and therefore the center of gravity would always coincide with the slider geometric center.
2. Convenient distribution of overheating temperatures more uniformly avoids concentrated peaks (mechanical behavior of the friction coefficient more stable over time than FP).
3. Minor effects due to multi-directional motion due to flat sliding surface (compared to FP).
4. To avoid damaging uplifting phenomena for the superstructure (FP elevation, Lowering elastomeric): in the projected device there is no vertical displacement resulting from a horizontal displacement. In the case of FP, for its geometric shape, a horizontal displacement due to the earthquake always corresponds to a rise; while in the case of elastomeric devices, due to the properties of the elastomer which is subjected to vertical loading, at vertical displacement there are vertical depressions.
5. The vertical load is imputed to the central cylindrical steel element (compared to LRB and HDRB): this allows the elastomer element to remain unarmed with the intermediate steel plates and does not affect the mechanical characteristics of the cylindrical steel. Elastomer which are generally dependent on the vertical load.
6. The device has modular geometric shapes and simple repeatability (compared to FP).
7. Possibility to mount multiple units in series for smaller dimensions.

8. Mechanical recurrence, due solely to the elasticity of elastomer (compared to FP).
9. The elastic circular crown consists of a single core, economic advantages, in order to avoid the need for vulcanization processes with intermediate steel platelets which represent weakness areas (adhesion stress concentrations).
10. Economic savings in the production process of steel surfaces, flat rather than curved (compared to FP).
11. Reduced dimensions compared to similar performance devices (LRB - HDRB and FP) if the polymeric material is reinforced.
12. The device contemplating the use of low damping elastomer (purely frictional dissipation) avoids the triggering of scragging phenomena: the mechanical properties of high damping (HDRB) isolator vary considerably during the first deformation cycles, due to the phenomenon known as "scragging" for which, upon discharge, there is a partial recovery of the initial properties. In the case of low friction tires used in the new device this phenomenon does not occur
13. Tensile strength of the device for any lifting forces that can arise in very high (rocking vulnerable) structures (compared to FP).

4.5.2 VID

1. The proposed isolation mechanism is based on simple mechanical concepts, unlike alternative proposed systems that employ viscous damping, elastic components in steel (springs), magnetic levitation.
2. Materials (steel, elastomer and polymers) are already widely used for the construction of horizontal seismic isolation devices (elastomeric isolators and sliding isolators).
3. Simplicity, standardization and consequent economy of the production and marketing process as geometric elements are rather regular.
4. Possibility of extending the isolation technology, from vertical vibrations produced by industrial machinery, to the civil engineering sector, with buildings-related applications, bridges, tanks, nuclear power plants that involve far greater loads than the above-mentioned machinery.

Chapter 5

TUNED MASS DAMPER INERTER

The introduction of base isolation system results in a discontinuity in the vertical development of the building and, acting as a filter against the typical excitatory frequencies of the earthquake, decouples the motion of the superstructure from that of the ground, inducing in the same lesser stresses as well as a significant perception lower than seismic shocks for occupants. However, the earthquake-induced displacement demand is mainly absorbed by the isolation system itself, which should therefore be designed to support significant displacements (i.e. 30-50 cm). All this has an impact on the construction economy in the choice of isolation devices as well as project connections (e.g. pedestrian, carriage, water, sewage, electrical, gas pipelines) that will have to withstand such high travel. These drawbacks have motivated the development of alternative, so-called “hybrid” control strategies combining the conventional base isolation scheme with other active or passive control systems (Jang et al. 1991). The most common strategy explored by researchers is to connect the base isolation system to a tuned-mass-damper (TMD) (Den Hartog 1934, Taniguchi et al. 2008, Tsai 1995, Xiang and Nishitani 2014). This latter device behaves as a vibration absorber that is directly connected to the isolation system to effectively hold displacement demand at more acceptable levels. Nevertheless, the effectiveness of such a system in reducing displacements is strictly bound to the use of a significant mass of TMD, which obviously constitutes a practical limitation to the use of such a system.

In this chapter we will describe an innovative passive vibration control system to apply to civil structures based on the use of a device called the *inertor*. The inertor concept was first introduced by Smith in 2002 using the force-current analogy between mechanical and electrical

networks. In this context, the inerter is considered to represent the equivalent of the capacitor. As a result it has the property that the force generated is proportional to the relative acceleration between its end points (or nodes). The constant of proportionality, b , for the inerter is called *inertance* and is measured in kilograms. In fact, we define the ideal inerter to be a mechanical two-node(two-terminal), one-port device with the property that the equal and opposite force applied at the nodes is proportional to the relative acceleration between the nodes (see equation (5.1)).

$$F = b(\ddot{x}_2 - \ddot{x}_1) . \quad (5.1)$$

This system, consisting for example of a combination of rotating and gears, has been widely and effectively used in the automotive sector for the production of high performance suspension systems. It was widely known as “J-damper” (Chen et al. 2009) in Formula One Racing since it delivered significant performance gains in handling and grip. The main advantage of this device is that high levels of vibration isolation can be achieved by using small amounts of mass thanks to a particular mass amplification effect ('apparent' masses can be obtained up to 200-300 times the mass device physics). When the inerter is installed in series with spring and damper elements, a lower-mass and more effective alternative to the traditional tuned-mass-damper (TMD) is obtained, i.e., the tuned-inerter-damper (TID) wherein the device inertance plays the role of the TMD mass. By attaching a TID to the isolation floor, it is demonstrated that the displacement demand of base-isolated structures can be significantly reduced. The inerter is currently under study by the structural dynamics scientific community because of its interesting, appealing properties.

In the last few years, inerter-based devices have attracted the attention of researchers focused on vibration suppression of mechanical elements and structural systems (Lazar et al. 2014, Marian and Giaralis 2014, Pietrosanti et al. 2017, Brzeski et al. 2015, Garrido et al. 2013, Hu and Chen 2015).

Most of these studies focused on the determination of the optimal tuning parameters of the inerter-based device to reduce some primary response indicator, either by means of closed-form expressions based on a

simplified model idealization, or by solving the optimization problem via a numerical search method, or by analyzing and studying the frequency response functions. In line with the above discussion, this represents a novel hybrid control strategy in which the base isolation system is used to decouple the building from the ground motion, while the TMID guarantees that the displacement demand of the base isolation system remains limited to within a reasonably acceptable threshold. As compared to the previously discussed hybrid control strategy, combining the base isolation system with the TMD, the drawbacks regarding the effective mass amount of the TMD are avoided by the TID via the adjustment of the inerterce. In this way, the base isolation system displacement demand is reduced without causing unacceptably large displacements in the TID, which instead occurs if the TMD is connected to the isolation floor.

In the following paragraphs, we will introduce the equation of motion of a system with a TMDI and after a brief discussion on the optimal parameter that must be adopted for a numerical application on a 5-story building, we will design a fluid inerter device to apply in civil structure prone to earthquake and we will describe some quantities that must be taken into account in the design of a real inerter device.

5.1 Equation of motion of systems with TMDI

To better illustrate the fundamentals of the hybrid control strategy, a base-isolated SDOF is considered, in which a TID is attached to the isolation floor (De Domenico and Ricciardi 2017). This scheme may be meant as being representative of the shear-frame idealization of a one-story building equipped with the proposed hybrid control strategy, i.e., the base isolation system combined with the TID. Therefore, a 3DOF-system is analyzed for practical purposes, and the obtained results will be extended later to more realistic base-isolated multi-story buildings. The enhanced base isolation scheme equipped with TID is schematically shown in Figure 5.1.

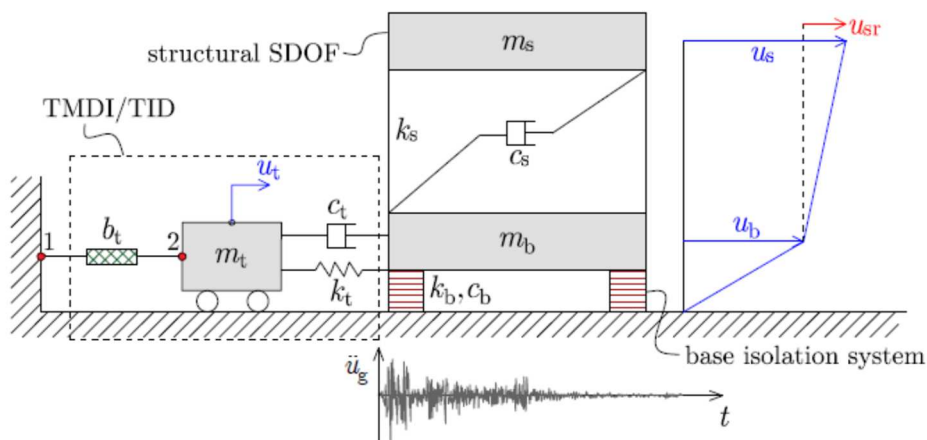


Figure 5.1 Sketch of a base-isolated one-story building with attached TID (De Domenico and Ricciardi 2017)

The base isolation system is here represented by a SDOF system (i.e., the displacement u_b relative to the ground) having mass m_b , stiffness k_b and equivalent viscous damping c_b . The base isolation system is interconnected to the superstructure, which in this simple sketch is a planar one-story building represented by a SDOF system whose main dynamic properties are the mass m_s , equivalent viscous damping c_s and stiffness k_s . In the hybrid control strategy proposed by De Domenico and Ricciardi 2017, a TMDI/TID subsystem is attached to the isolation floor in order to reduce the displacement demand of the base-isolated structure. This is basically a TMD (having mass m_t and connected to the base isolation system via a linear spring of stiffness k_t and a dashpot of viscous damping c_t) in which the inerter device, schematically represented by its inertance b_t (depicted as a hatched box in Figure 5.1) is placed between the TMD mass and the ground (points 1 and 2). The TMDI physical mass m_t is negligible as compared to the device inertance b_t , the TMDI can be dealt with as a TID.

The combined system is subject to the horizontal ground acceleration $\ddot{u}_g(t)$. In order to assess the performance of the hybrid control scheme with respect not only to the base isolation system but also to the superstructure

response, it is more convenient to write the equations of motion in terms of the relative displacement of the mass m_s with respect to the base isolation system $u_{sr} = u_s - u_b$ rather than to the displacement u_s (Figure 5.1). This will be very useful analyzing multi-degree-of-freedom (MDOF) systems. By application of the D'Alembert's principle, the governing equations of motion of the combined 3DOF-system can be readily written in matrix form as follows:

$$\mathbf{M}\ddot{\mathbf{u}}(t) + \mathbf{C}\dot{\mathbf{u}}(t) + \mathbf{K}\mathbf{u}(t) = -\boldsymbol{\tau}\ddot{u}_g(t), \quad (5.2)$$

where:

$$\mathbf{M} = \begin{bmatrix} 1 & 1 & 0 \\ 1 & 1 + \mu_b & 0 \\ 0 & 0 & \mu_t + \beta_t \end{bmatrix}; \quad \mathbf{C} = \begin{bmatrix} 2\zeta_s \omega_s & 0 & 0 \\ 0 & 2\zeta_b \omega_b \mu_b + 2\zeta_t \omega_t \mu_{et} & -2\zeta_t \omega_t \mu_{et} \\ 0 & -2\zeta_t \omega_t \mu_{et} & 2\zeta_t \omega_t \mu_{et} \end{bmatrix};$$

$$\mathbf{K} = \begin{bmatrix} \omega_s^2 & 0 & 0 \\ 0 & \omega_b^2 \mu_b + \omega_t^2 \mu_{et} & -\omega_t^2 \mu_{et} \\ 0 & -\omega_t^2 \mu_{et} & \omega_t^2 \mu_{et} \end{bmatrix}; \quad \boldsymbol{\tau} = \begin{bmatrix} 1 \\ 1 + \mu_b \\ \mu_t \end{bmatrix}; \quad \mathbf{u}(t) = \begin{bmatrix} u_{sr}(t) \\ u_b(t) \\ u_t(t) \end{bmatrix};$$
(5.3)

where this position has been introduced:

$$\omega_s = \sqrt{\frac{k_s}{m_s}}; \quad \zeta_s = \frac{c_s}{2m_s \omega_s}; \quad \omega_b = \sqrt{\frac{k_b}{m_b}}; \quad \zeta_b = \frac{c_b}{2m_b \omega_b};$$
(5.4)

$$\omega_t = \sqrt{\frac{k_t}{(m_t + \beta_t)}}; \quad \zeta_t = \frac{c_b}{2(m_t + \beta_t) \omega_t};$$

$$\mu_b = \frac{m_b}{m_s}; \quad \mu_t = \frac{m_t}{m_s}; \quad \beta_t = \frac{b_t}{m_s}; \quad \mu_{et} = \mu_t + \beta_t = \frac{m_t + b_t}{m_s} = \frac{m_{et}}{m_s}. \quad (5.5)$$

in which all the three equations have been divided by the superstructure mass m_s . In particular, expressions (5.4) define the (uncoupled) natural frequencies and damping ratios of the three subsystems, while equations (5.5) express the dimensionless mass ratios of the base isolation system and of the TMDI with respect to the superstructure mass. A new mass parameter has been introduced in the last expression, namely the effective mass of the TMDI m_{et} that incorporates both the physical mass m_t and the apparent mass b_t , related to the inertance. The dimensionless inertance β_t multiply the relative accelerations between points 1 and 2, which coincides with \ddot{u}_t . While the inertial forces in the TMDI are associated with the effective mass μ_{et} , the earthquake-induced accelerations on the right- side of equation (5.2) multiplies the physical mass μ_t only. Therefore, due to the peculiar format of Equation (5.2), increasing the inertance β_t it is more beneficial than increasing the TMD mass μ_t because it selectively raises the TMDI inertia properties without increasing the corresponding seismic force to which the device is subject.

The properties of the BIS have been fixed, in particular, medium-damped isolators have been considered, by assuming a BIS equivalent damping ratio $\zeta_b = 0.2$. We now want to approach the problem of designing the BIS from a different perspective. The elastic and damping properties of the TMDI system, k_t and c_t , may be meant as the effective stiffness and equivalent viscous damping ratio of an auxiliary set of isolators acting in parallel with the conventional isolators, the latter featured by corresponding k_b and c_b , as sketched in Figure 5.2. The only difference between these two groups of isolators is that the auxiliary isolators are equipped with an inerter device, which connects them to the ground. Therefore, this model idealization represents an enhanced BIS with a particular arrangement of conventional isolators, auxiliary isolators, and inerter.

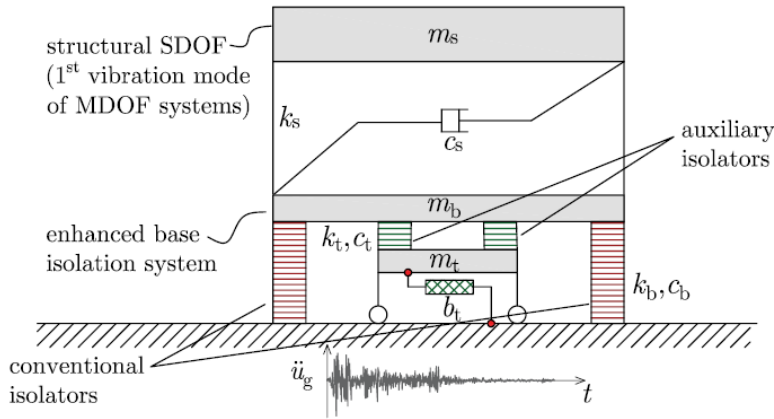


Figure 5.2 Schematic arrangement of the proposed enhanced base-isolation system.

It seems interesting to investigate how the effectiveness of this enhanced BIS is affected by the properties of the conventional isolators. To this aim, in Figure 5.3 A, B, we report the displacement variances of these two sets of isolators for five different damping ratios of the conventional BIS ζ_b (a value of $\mu_t = 0.01$ is assumed for all the curves).

In accordance with other literature findings related to TMD-based systems, the effectiveness of such inerter-based vibration control strategy increases when low-damping isolation bearings are addressed. For instance, adopting $\beta_t = 0.2$, the reduction of the BIS displacement variance is more than tripled passing from $\zeta_b = 0.3$ to $\zeta_b = 0.05$. Additionally, also, the auxiliary BIS, ie, the TMDI, is more effectively controlled for low-damping BIS because the range of displacement reduction widens when lowering the ζ_b and the attained σ_{ut}^2 value decreases accordingly, where σ_{ut}^2 is the displacement variance of the auxiliary TMDI. By inspection of the corresponding optimal parameters of the TMDI shown in Figure 5.3 C, D, it seems that the auxiliary BIS should be more flexible ($\omega_{opt} \approx 0.35\omega_b$) and should have more inherent damping ($\zeta_{opt} = 0.2-0.3$) than the conventional BIS to perform at its best.

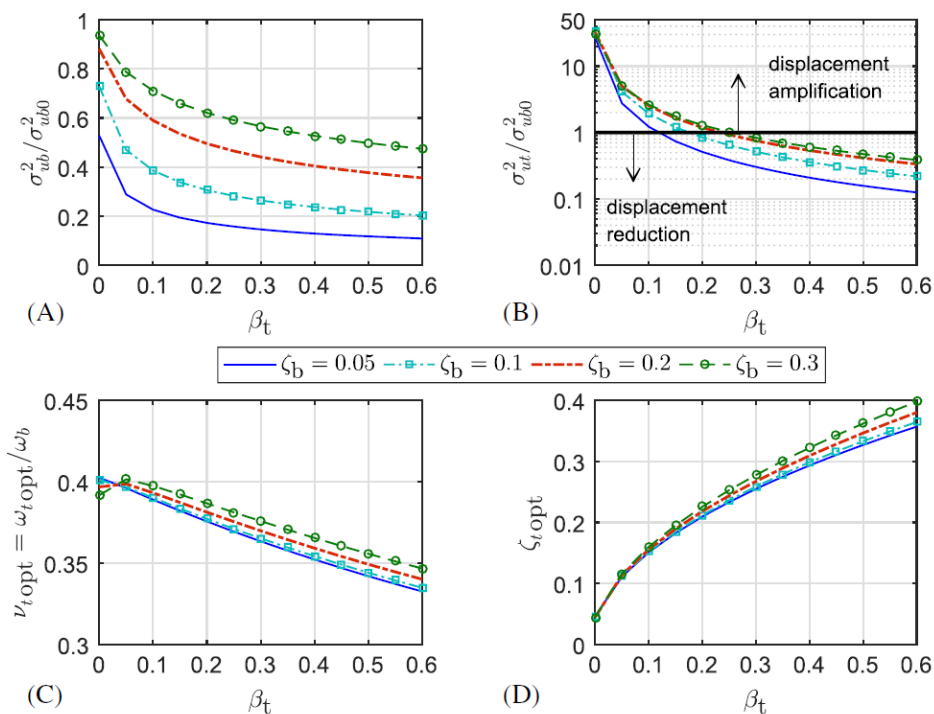


Figure 5.3 Enhanced base-isolation system (BIS) for different ζ_b values. A,B, normalized displacement variance of the conventional BIS and of the auxiliary BIS (TMDI). C,D, corresponding optimal TMDI parameters (De Domenico and Ricciardi 2018)

Based on these results, it may be stated that the optimal BIS consists in a combination of low-damping conventional isolators, eg, $\zeta_b \approx 0.1$, in parallel with medium-to-high damping flexible auxiliary isolators, e.g., $\zeta_i \approx 0.25$, the latter installed in conjunction with an inerter device having inertance ratio around $\beta_i = 0.4$.

5.1.1 Numerical application on a 5-story building

All the considerations done in § 5.1, can be extended to a MDOF system, so let us considered a planar 5-story building as sketched in Figure 5.4, in which the proposed enhanced BIS is implemented. Following a typical approach to this problem, a preliminary static condensation method has already been applied to the superstructure to eliminate the (zero-mass) rotational degrees of freedom (DOFs). As a result, the superstructure has 5 dynamic DOFs, represented by the displacements of the 5 story masses m_{sj} ($j = 1, \dots, 5$) relative to the BIS (cf again Figure 5.4), which are collected in the array $\mathbf{u}_{sr}^T(t) = [u_{sr1}(t), u_{sr2}(t), \dots, u_{sr5}(t)]^T$. The 5-story symmetric-plan base-isolated building we have analyzed through the equivalent planar frame depicted in Figure 5.4. Constant bay width L and column height H are assumed. With axial deformations in beams and columns neglected, the frame has 35 DOFs, with 5 dynamic DOFs represented by the displacements of the 5 stories relative to the BIS. The elastic modulus is $E = 206000 \text{ MN}/\text{m}^2$ (typical of a reinforced concrete frame), and the second moment of the cross-sectional area is computed according to the column and beam sections reported in Figure 5.4. The mass of the superstructure is lumped at the floor level, with $m_j = 60000 \text{ kg}$ denoting the mass for the first 4 floors ($j = 1, \dots, 4$) and $m_5 = 50000 \text{ kg}$ for the fifth floor.

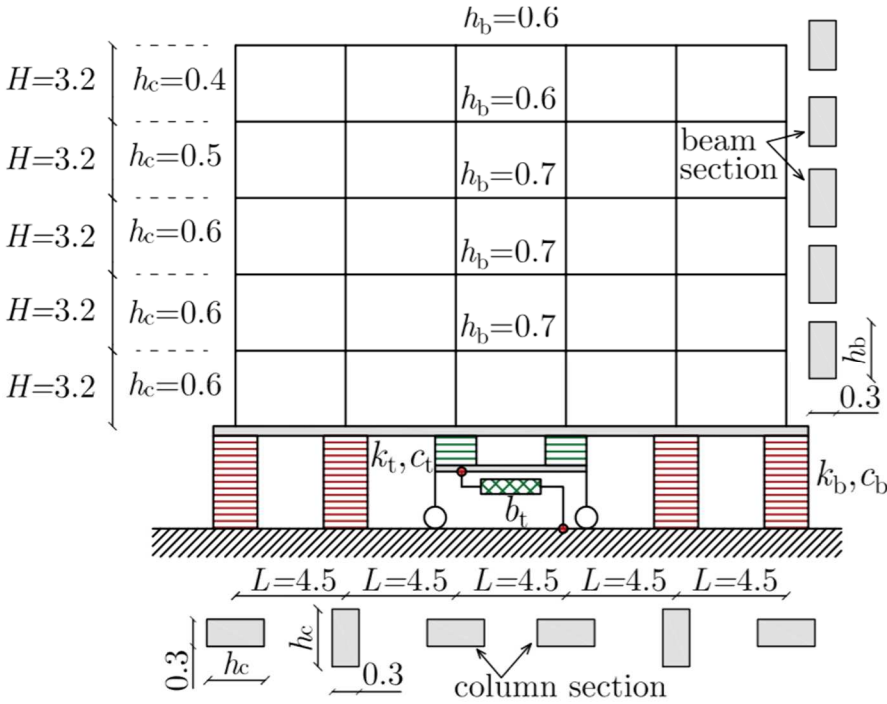


Figure 5.4 Multistory building with proposed enhanced base-isolation system.

The equations of motion expressed in equation (5.2) still hold, but now involving matrices having dimension $r \times r$ with $r = n + 2 = 5 + 2$, in particular:

$$\begin{aligned}
 \mathbf{M} &= \begin{bmatrix} \mathbf{M}_s & \mathbf{M}_s \boldsymbol{\tau}_s & \mathbf{0} \\ \boldsymbol{\tau}_s^T \mathbf{M}_s & m_{s \text{ tot}} + m_b & 0 \\ 0 & 0 & m_t + b_t \end{bmatrix}; \quad \mathbf{C} = \begin{bmatrix} \mathbf{C}_s & \mathbf{0} & \mathbf{0} \\ \mathbf{0}^T & c_b + c_t & -c_t \\ \mathbf{0}^T & -c_t & -c_t \end{bmatrix}; \\
 \mathbf{K} &= \begin{bmatrix} \mathbf{K}_s & \mathbf{0} & \mathbf{0} \\ \mathbf{0}^T & k_b + k_t & -k_t \\ \mathbf{0}^T & -k_t & k_t \end{bmatrix}; \quad \boldsymbol{\tau} = \begin{bmatrix} \mathbf{M}_s \boldsymbol{\tau}_s \\ m_{s \text{ tot}} + m_b \\ m_t \end{bmatrix}; \quad \mathbf{u}(t) = \begin{bmatrix} \mathbf{u}_{sr}(t) \\ u_b(t) \\ u_t(t) \end{bmatrix};
 \end{aligned}
 \tag{5.6}$$

where $m_{s \text{ tot}} = \sum_{i=1}^5 m_i$, \mathbf{M}_s , \mathbf{C}_s , \mathbf{K}_s are the n -dimensional matrices of mass, damping and stiffness of the superstructure as if it were on a fixed base, $\boldsymbol{\tau}_s$

is the 5×1 influence vector of the superstructure associated with the ground motion $\ddot{u}_g(t)$, and $\mathbf{0}$ is a 5×1 vector of zero terms.

Applying the classical modal analysis to the superstructure leads to the following natural periods and participating mass ratios:
 $T_{si}(s) = [0.501, 0.189, 0.112, 0.079, 0.056]$ and
 $\varepsilon_{si}(\%) = [81.77, 10.67, 3.96, 2.55, 1.04]$.

The enhanced BIS is a set of 6 isolators as shown in Figure 5.4, two of which (the so-called auxiliary isolators) are smaller in size (more flexible) and equipped with the inerter. The basement mass is assumed to be $m_b = 50000$ kg, so resulting in a mass ratio $\mu_b = 0.17241$. The damping coefficients of the superstructure are assumed to be stiffness proportional (“classically damped system”) with $\zeta_{si} = 0.02$ ($i = 1, \dots, 5$), while the conventional BIS is assumed to have an equivalent (effective) natural period $T_{eff} = 2$ sec and an equivalent viscous damping $\zeta_b = 0.1$ (i.e., low-damping isolation bearings are considered).

The input base acceleration \ddot{u}_g is represented by a “colored-noise” PSD function that is spectrum compatible with the Eurocode 8. According to the Monte Carlo method, a set of 100 artificial accelerograms (whose stationary duration is $T_s = 20$ s) consistent with the EC8 reference response spectrum, ground type A, and peak ground acceleration $a_g = 0.3g$, are generated by the superposition of harmonic waves with random phase from a parent spectrum-compatible PSD function, see Figure 5.5.

Two different passive vibration control systems are scrutinized and compared: (1) the proposed BIS with TMDI ($\mu_t = 0.01$ and $\beta_t = 0.4$); (2) the conventional BIS equipped with optimal conventional TMD ($\mu_t = 0.1$). The BIS without any additional secondary subsystem, i.e., the conventional base-isolation scheme, is also analyzed and considered as reference solution. The following optimal parameters are found:
 $\omega_{topt} = 2.7318$ (rad / s) and $\zeta_{topt} = 0.26$ for the TMDI,
 $\omega_{topt} = 2.8103$ (rad / s) and $\zeta_{topt} = 0.13$ for the conventional TMD, and
 $\omega_{topt} = 2.3027$ (rad / s) and $\zeta_{topt} = 0.23$ for the nonconventional TMD.

The results of 100 time history analyses (each relevant to a given accelerogram) are then averaged to obtain the mean rms values and the mean max values of the response indicators.

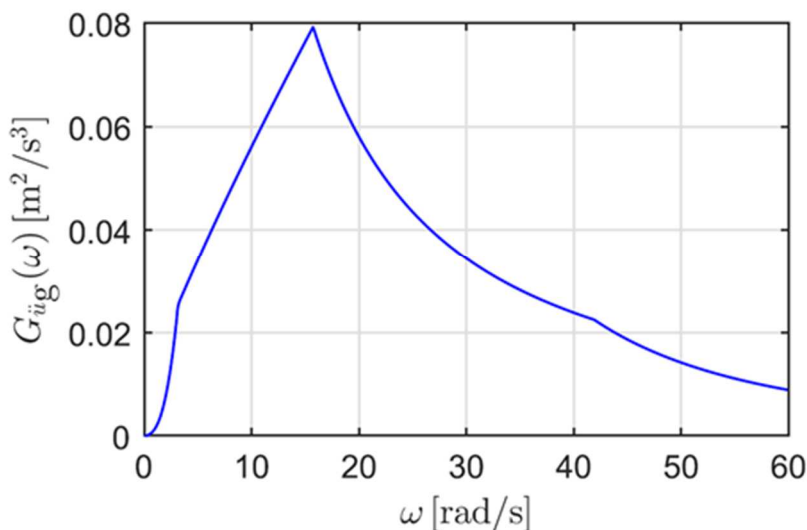


Figure 5.5 PSD function according to Eurocode 8 ground type A spectrum-compatible base acceleration.

A selection of (arbitrarily chosen) response indicators that are useful and of practical importance for design engineers are computed for the 3 systems (conventional BIS, BIS with conventional TMD, BIS with the proposed TID), including the last-floor displacement u_{s5} , and the TMDI/TMD displacement u_t .

By inspection of the results, the enhanced BIS equipped with optimally TMDI attains an excellent level of vibration reduction, not only in terms of displacement demand of the BIS (with reductions of more than 50%), but also regarding all the other response indicators. The value of inertance, related to the fixed value of μ_{et} and the optimal values founded, is of $b=116000$ kg. For the design of the proposed scheme, we will introduce 2 inerters with respectively 60000 kg of inertance.

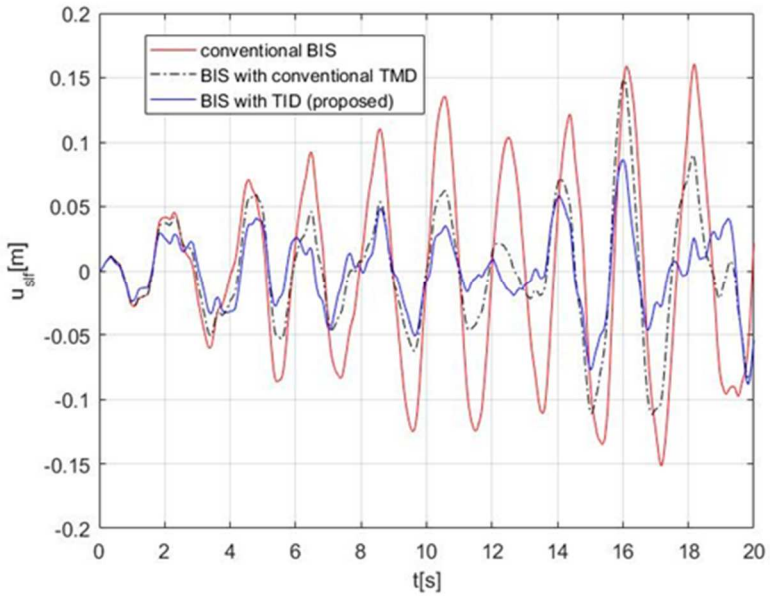


Figure 5.6 Time histories responses of the last floor displacements

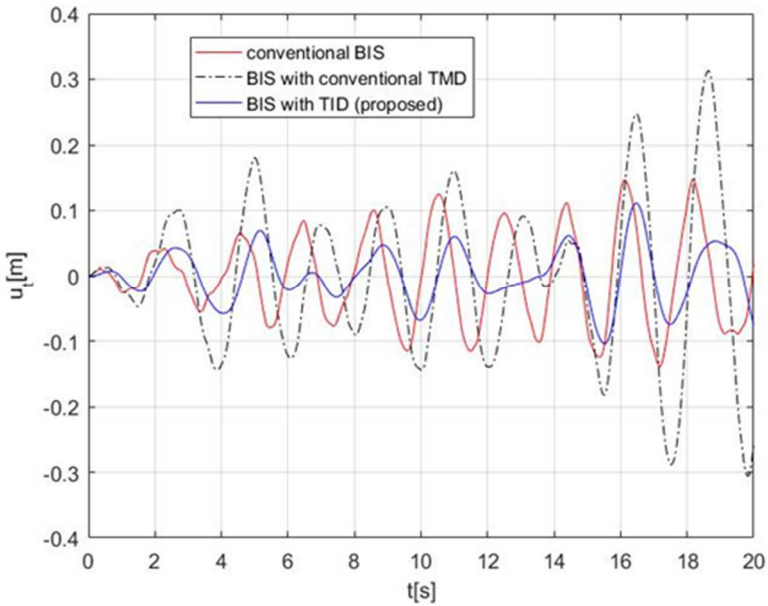


Figure 5.7 Time histories responses of the proposed TID displacements

5.2 Methods to realize of an inerter device

For the mechanical design of the inerter device is useful to know that such devices also need to satisfy certain practical conditions, which we list as follows (Smith 2002):

1. The device should be capable of having a small mass, independent of the required value of inertance.
2. There should be no need to attach any point of the physical device to the mechanical ground.
3. The device should have a finite linear travel which is specifiable, and the device should be subject to reasonable constraints on its overall dimension.
4. The device should function adequately in any spatial orientation and motion.

The second condition is necessary if the inerter is to be incorporated in a free-standing device which may not easily be connected to a fixed point in an inertial frame, e.g., a suspension strut which is connected between a vehicle body and wheel hub. We mention that conditions of the above type hold for the ordinary spring and damper. The aforementioned realizability conditions can indeed be satisfied by a mechanical device which is easy to construct. A simple approach is to take a plunger sliding in a cylinder which drives a flywheel through a rack, pinion, and gears (see Figure 5.8).

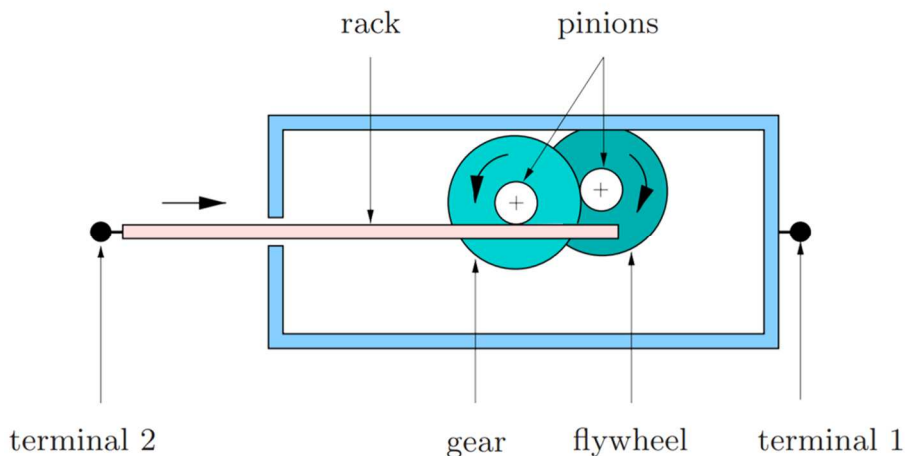


Figure 5.8 Schematic of a mechanical model of an inerter (Smith 2002)

In Mirza Hessabi and Mercan 2016, for example, is described a rack pinion inerter device (see Figure 5.9) with several gears to realize a bigger value of inertance. Infact, as the number of gears increases, also the inertance increases.

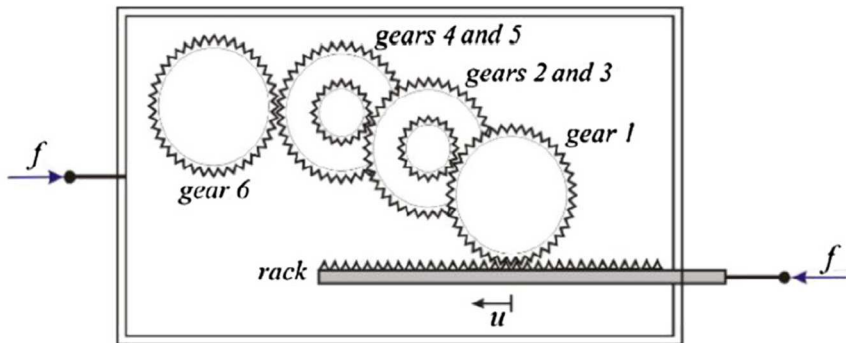


Figure 5.9 – Rack-Pinion inerter device with several gears (Mirza Hessabi and Mercan 2016)

For this scheme they realize an experimental set (Figure 5.10) for a small-scale prototype, with a mass of the gears of 98.11 gr, the value of the correspondent inertance is 29.87 kg, the amplification is about 304.5.

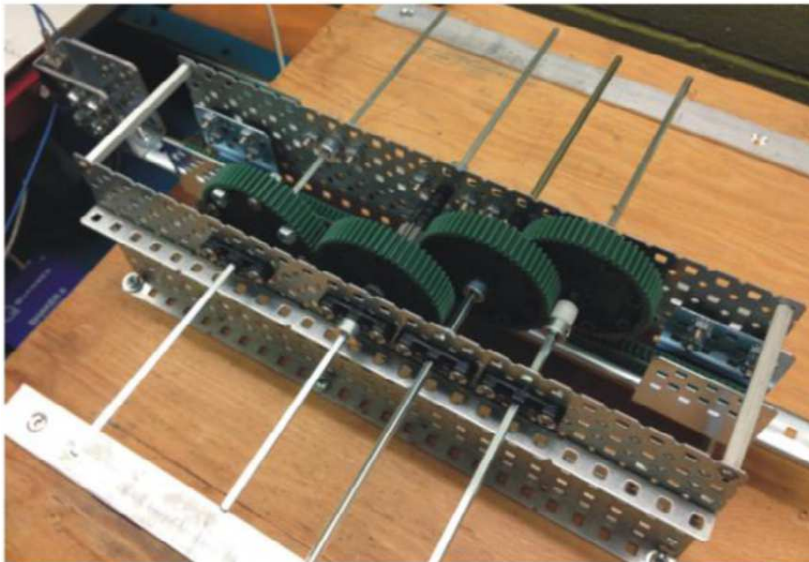


Figure 5.10 The small scale prototype gears (Mirza Hessabi and Mercan 2016)

In Figure 5.11, measured forces are plotted against the applied displacements. It has been shown before that the performance of inertial dampers can be affected by nonlinearities. As discussed by Smith and Wang in 2016, the experimental data match better with the theoretical predictions, when the effects of friction forces are considered.

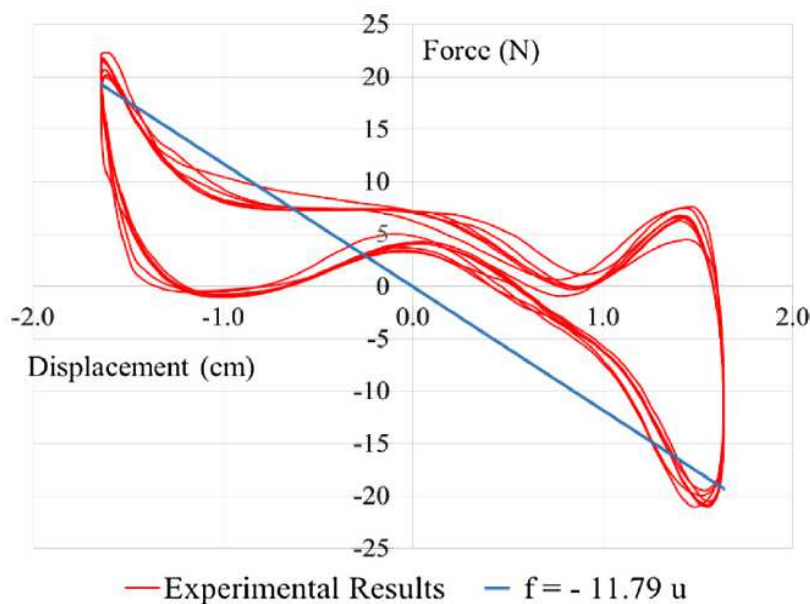


Figure 5.11 Measured force vs measured displacement for the prototype with $b = 29.87$ kg (Mirza Hessabi and Mercan 2016).

Other methods of construction are described in (Smith 2008), e.g. using hydraulics (Figure 5.14) or screw mechanisms. Figure 5.12 shows a schematic of a ball-screw inerter and an example of such a device is pictured in Figure 5.13. For such devices the value of the inertance b is easy to compute. In general, if the device gives rise to a flywheel rotation of α radians per meter of relative displacement between the terminals, then the inertance of the device is given by $b = J\alpha^2$, where J is the flywheel's moment of inertia.

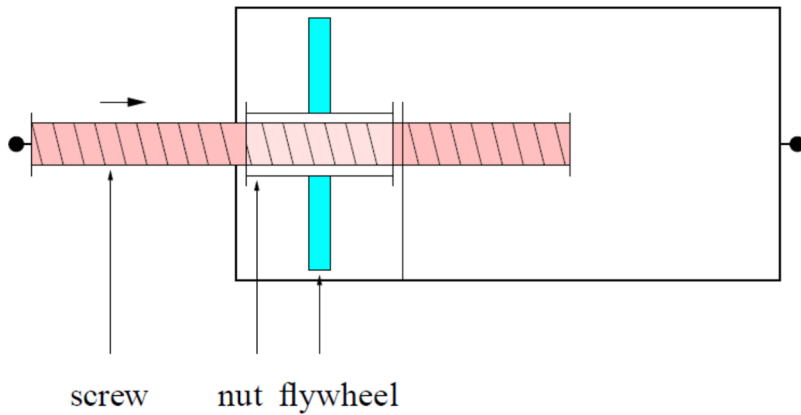


Figure 5.12 Schematic of a mechanical model of a ballscrew inerter (Smith 2008)

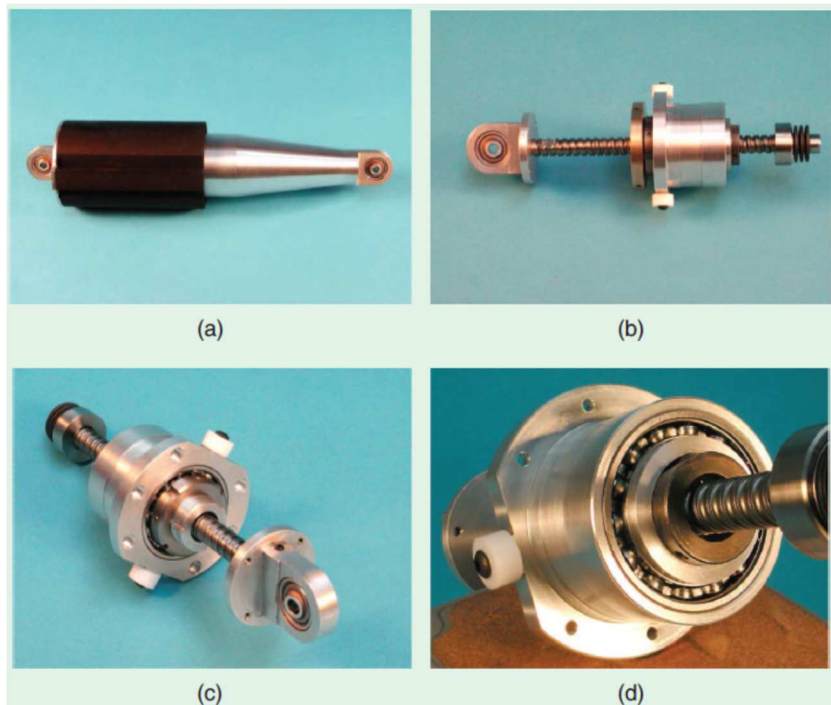


Figure 5.13 Ballscrew inerter made at Cambridge University Engineering Department; Mass < 1 kg, Inertance (adjustable) = 60–240 kg. (a) Complete with outer case, (b) ballscrew, nut and flywheel, (c) flywheel removed, (d) thrust bearing. (Smith 2002)

The idea of a hydraulic inerter were proposed in (Smith 2001), which suggested the use of a gear pump to convert the linear motions into rotational motions (Figure 5.14).

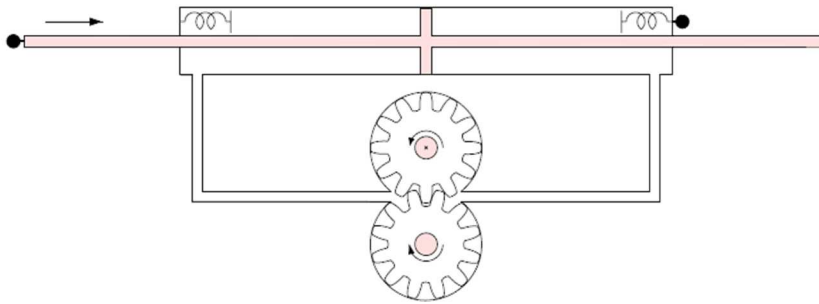


Figure 5.14 Schematic of a mechanical model of a hydraulic inerter (Smith 2008)

Then in Wang et al. 2010, is proposed an hydraulic inerter that is a closed hydraulic system that consists of a hydraulic motor, a hydraulic cylinder, and connection pipes, as shown in Figure 5.15. The working principle of the hydraulic inerter is similar to a hydropower generator, as shown in Figure 5.16.

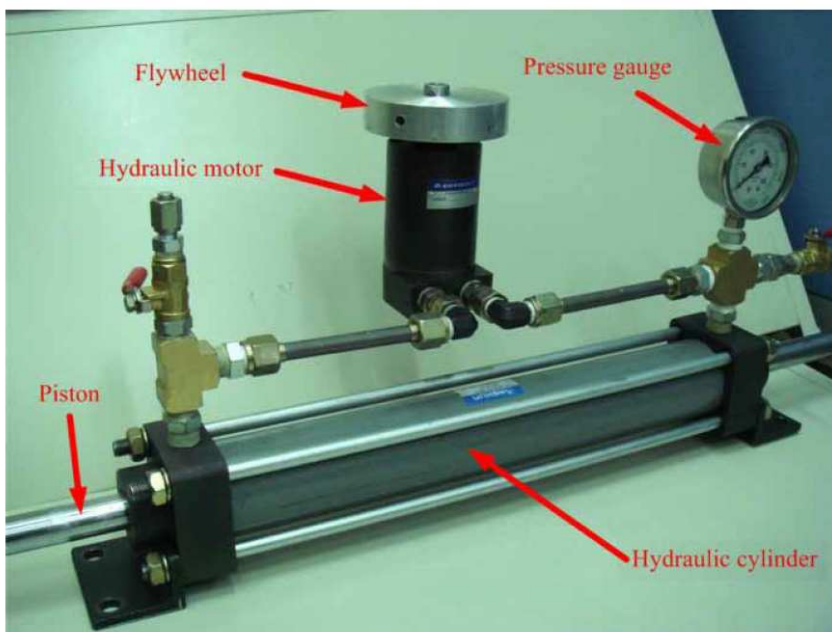


Figure 5.15 A prototype of the hydraulic inerter (Wang et al. 2010)

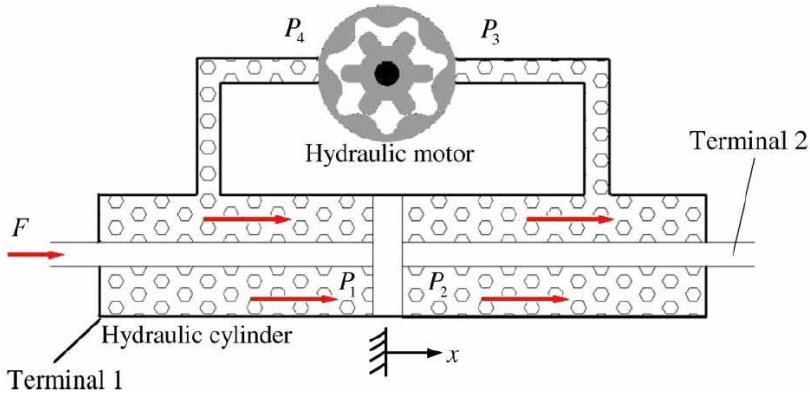


Figure 5.16 The working principle of an hydraulic inerter (Wang et al. 2010)

Two terminals of the hydraulic inerter are the hydraulic cylinder (terminal 1) and the piston (terminal 2). If F is the applied force and x is the relative displacement of the two terminals, when F is positive, then the piston moves rightwards relative to the cylinder and the pressure P_2 (P_3) is higher than the pressure P_1 (P_4). The hydraulic motor is operated by the pressure difference between P_3 and P_4 , and the fluid flows through the pipes. Similarly, when the applied force F is negative, the piston and the hydraulic motor move in the reverse direction.

In Swift et al. 2013, a fluid inerter device is then proposed (see Figure 5.17), in this case the cylinder body and the piston rod are the two device terminals, their relative motion driving fluid through the helical channel. The channel fluid velocity is scaled up from the piston velocity by the ratio of the areas of the channel and the piston.

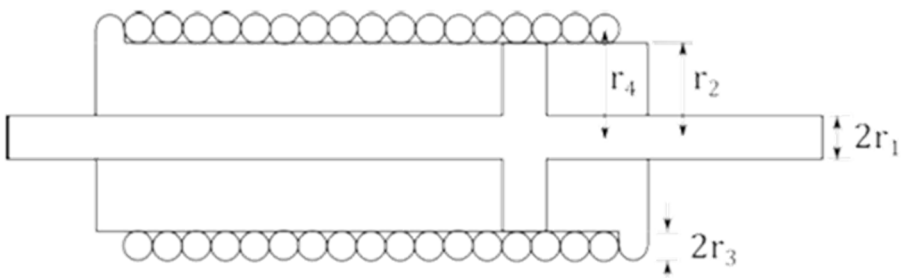


Figure 5.17 Schematic of a mechanical model of a fluid inerter (Swift et al. 2013)

In Smith and Wagg 2016, the design and testing of a novel type of fluid inerter system is presented, where the inertance can be varied. This variable inertance is achieved by having a fluid filled cylinder that induces flow in a helical pipe system (see Figure 5.18). The parameters of the helical pipe system can be adjusted to give different amounts of inertial force depending on the requirements.



Figure 5.18 Fluid inerter device designed and tested in Smith and Wagg (2016).

5.3 Design of a rack pinion inerter device

The device here proposed is a rack and pinion one, similar to the one described in Saito 2012 and Hessabi and Mercan 2016, in particular using a rack and assembly of gears, the relative translation of the terminals is transformed into a rotation of the gears. For these group of inertial dampers the equivalent mass of the device can be easily adjusted by changing the radius of the gears. In Figure 5.19 is shown a possible sketch of the inerter device, we propose a system the can be replicate in plane just to reach the

value of inertance that is needed by the hybrid system. In the studied case, for example, we need four repetitions in plane and this can be also reproduced in height.

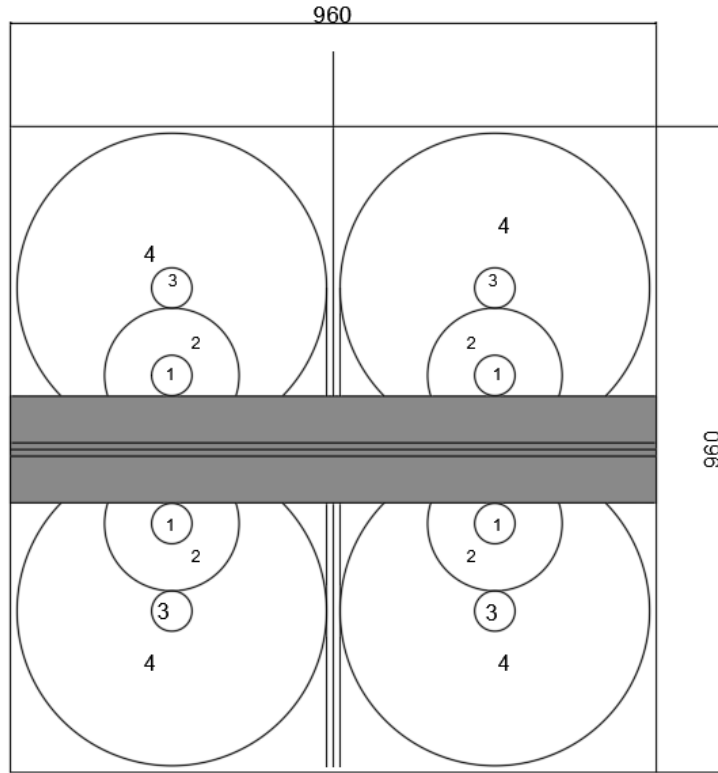


Figure 5.19 Schematic schetck of the inerter damper proposed

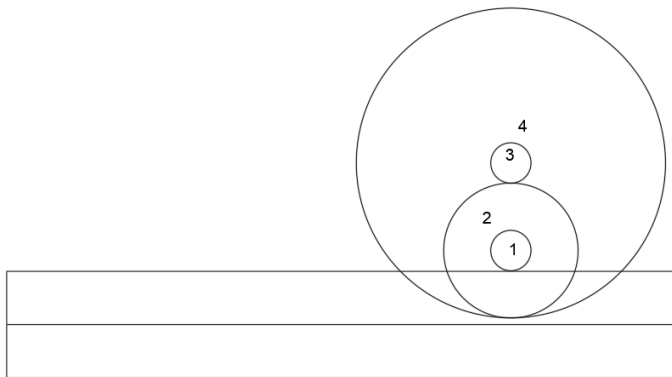


Figure 5.20 Part of the rack pinion inerter device

The device presents two axes of symmetry, so it is possible to study only a part of the initial system.

Gears in rotating system act similarly to levers in translating system. Figure 5.20 shows the device subjected to a tie varying relative axial force $f(t)$, it consists in two compound gears. The force acting on each of these gears is determined by considering the equilibrium between the gears in contact, considering also the rotational inertia of all the gears. By neglecting the mass of the rack, the equation of motion for each gears can be written as:

$$-J_3\ddot{\theta}_3 - J_4\ddot{\theta}_4 + f_{2-3}r_3 = 0 \quad (5.7)$$

$$J_1\ddot{\theta}_1 + J_2\ddot{\theta}_2 - \frac{f}{8}r_1 + f_{2-3}r_2 = 0, \quad (5.8)$$

where r_i and J_i denote the radius and mass moment of inertia of the i -th gear, respectively. In the equations of motion, an ideal efficiency is assumed and damping effects of gear friction or backlash are neglected. The geometric relationship between the arc lengths of the gears results in the following relations between the angular rotations of each of the gears and the first gear:

$$\begin{aligned} \ddot{\theta}_1 &= \ddot{\theta}_2 \\ \ddot{\theta}_3 &= \frac{r_2}{r_3} \ddot{\theta}_2 = \frac{r_2}{r_3} \ddot{\theta}_1 \\ \ddot{\theta}_4 &= \ddot{\theta}_3. \end{aligned} \quad (5.9)$$

After combining equations (5.7) and (5.8), the following relationship can be derived between $\ddot{\theta}_1$ and the tangential force in the first gear :

$$f = 4 \left[\frac{(J_1 + J_2)}{r_1^2} + \frac{(J_3 + J_4)r_2^2}{r_1^2 r_3^2} \right] r_1 \ddot{\theta}_1. \quad (5.10)$$

The gear ratios of the compound gears 1 and 2 are defined as $N_1 = r_2 / r_1$ and $N_2 = r_4 / r_3$, respectively. It can be shown that the number of teeth on a gear is proportional to the radius of its pitch circle. The transitional displacement of the rack, u , is related to the rotation of the first gear, $u = r_1\theta_1$, and the tangential force in the first gear is equal to $f/8$. By replacing the mass moment of inertia J_i with their respective expression $J_i = m_i r_i^2$, the force-acceleration relationship can be rearranged as follows:

$$f = 4[m_1 + (m_2 + m_3)N_1^2 + m_4N_1N_2]\ddot{u} \quad (5.11)$$

where m_i shows the mass of the i -th gear. Equation (5.11) can be summarized as

$$f = b\ddot{u} . \quad (5.12)$$

The parameter b in equation (5.12) is called the *equivalent mass* and for the considered device is equal to:

$$b = 4[m_1 + (m_2 + m_3)N_1^2 + m_4N_1N_2] . \quad (5.13)$$

It easy to see that the force generated in the devide is proportional to the relative translational acceleration, where b is the proporzionality constant. For the case of study we obtain:

r_1	30	mm	γ	7850	Kg/m^3	
r_2	60	mm	m	846.38	kg	
r_3	30	mm	b/m	38.24		
r_4	150	mm	u	120	mm	

Table 5.1 Mechanical and geometrical characteristic of the designed rack pinion inerter device

The theoretic mechanical model has been realized with SolidWorks software and is shown in



Figure 5.21 Theoretical mechanical model of a part of the proposed rack pinion inerter device

5.4 Design of a fluid inerter device

In this section we will introduce a new fluid inerter device to apply in civil structures. In this device the cylinder's body and the piston rod are the two device terminals, their relative motion drives fluid through an helical channel.

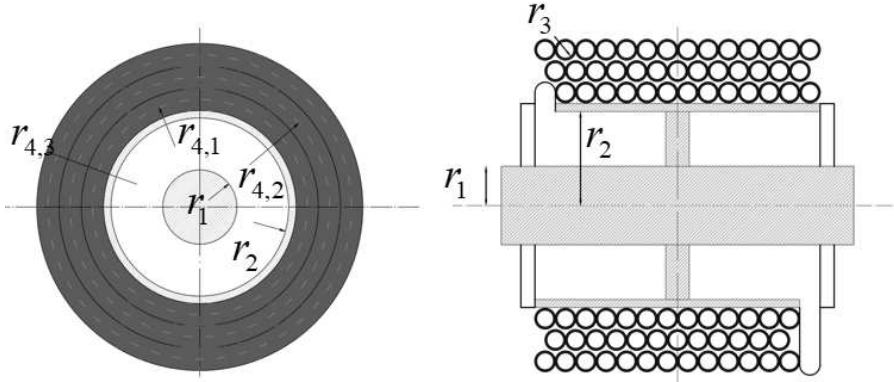


Figure 5.22 Cross and longitudinal sections of the proposed inerter device

The channel fluid velocity is scaled up from the piston velocity by the ratio of the areas of the channel and the piston. The inertance can be expressed as follows:

$$b = \frac{m}{1 + (h / 2\pi r_4)^2} \left(\frac{A_1}{A_2} \right)^2. \quad (5.14)$$

where

$m = \rho l A_2$ is the mass of the fluid in the helical channel;

$A_1 = \pi(r_2^2 - r_1^2)$ is the cross-sectional area of the piston;

$A_2 = \pi r_3^2$ is the cross-sectional area of the helical channel;

and $l = n\sqrt{h^2 + (2\pi r_4)^2}$ is the length of helical channel, n is the circle number of the helical channel.

From equation (5.14), we can see that the inertance can be increased by reducing the area of the channel or increasing the area of the piston, both of which increase the fluid velocity for a given rate of strut movement. Following the approach for the design proposed by Swifth et al. (Swifth et al. 2013), for the fluid we have chosen a Pro-RST Silkolene oil, which properties are function of temperature, in particular:

$$\rho = \rho_1 / (1 + \alpha_{hc}(T - T_1)) \quad (5.15)$$

where:

$\alpha_{hc} = 0.00090 \text{ K}^{-1}$ is the thermal expansion coefficient;

$\rho_1 = 816 \text{ kg/m}^3$ is the density at the temperature of $T_1 = 20^\circ\text{C}$.

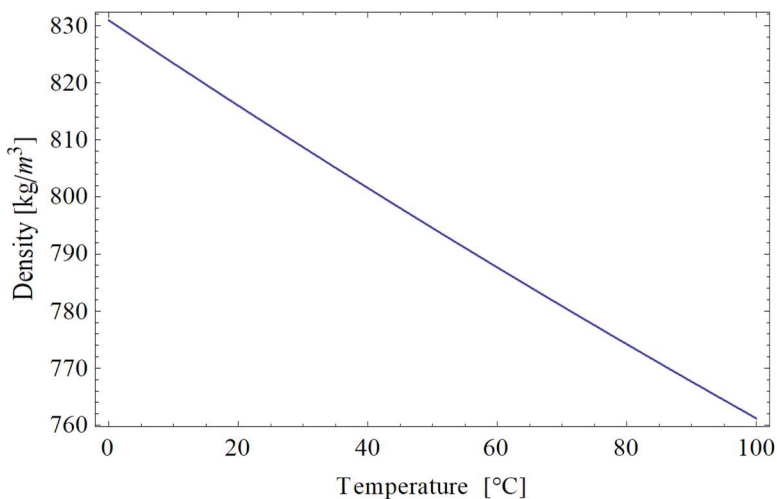


Figure 5.23 Pro-RST Silkolene oil density versus temperature (assuming a linear extrapolation).

Starting from the value of inertance that we want to realize, we have designed the fluid inerter, for a fixed temperature, and the dimensions are reported in Table 5.2.

T	26	$^{\circ}\text{C}$	r_1	50	mm
ρ	810	Kg/m^3	r_2	120	mm
μ	0.27	Pa s	r_3	13	mm
d	120	mm	$r_{4,1}$	145	mm
m	11.7	kg	$r_{4,2}$	175	mm
b/m	5135		$r_{4,3}$	205	mm

Table 5.2 Dimension of the proposed fluid inerter device

Despite the characteristics of the oil are variable with temperature, the value of the inertance is not very sensitive to this variation, as we can see from Figure 5.24.

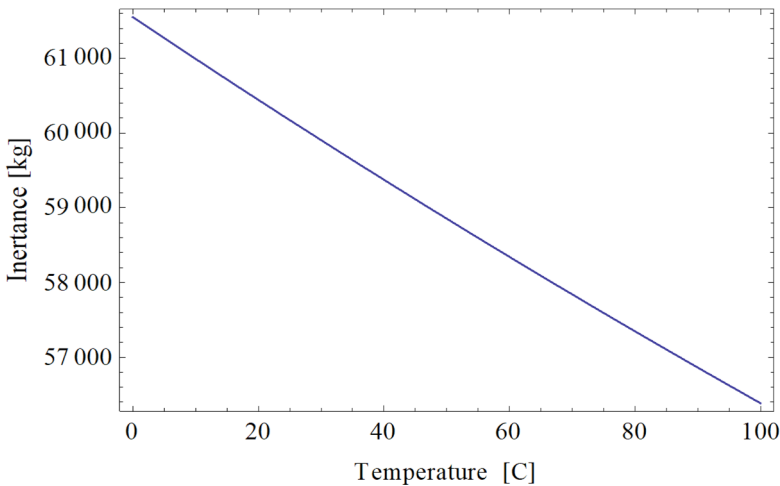


Figure 5.24 Inertance of the proposed device versus temperature

As we have illustrated before, this inerter device is for civil application, so the value of inertance are higher of the classical value used in vehicle suspension and for this reason it was necessary to insert 3 coil of helical tube, especially to keep the size of the device small (see Figure 5.25).

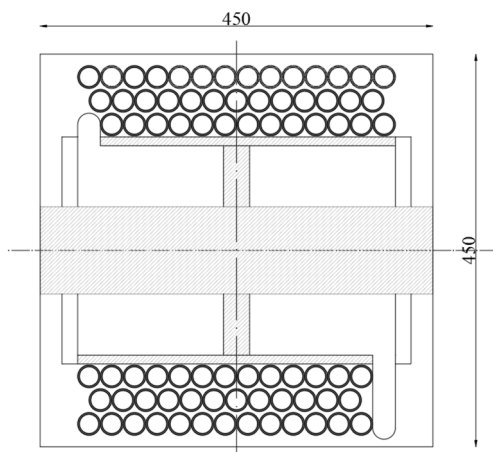


Figure 5.25 Plant of the proposed device

For the design of the helical channel, we have imposed to be in a turbulent motion of the fluid, so that the Reynolds number, given by equation (5.16), results equal to 2×10^5 , being

$$\text{Re} = \frac{\rho u D}{\mu}, \quad (5.16)$$

where u is the average flow velocity of fluid in the helical channel and μ is the viscosity of the fluid.

According to the volume conservation of flow for incompressible fluid, we can express the average flow velocity in terms of the displacement x of the piston as:

$$A_2 u = A_1 \dot{x}. \quad (5.17)$$

The fluid inerter is similar to rack and-pinion inerter or ball-screw inerter, because the fluid flowing in the helical channel can be taken as a “fluid flywheel” to provide the inertia force. Researches above are all concentrated on the ideal inerter, ignoring considering its nonlinearities. In Wang and Su 2008, the non linearities including friction, elastic effect,

backlash of a rack and pinion and ball-screw inerter were taken into consideration. In Glover et al. 2009, Swift et al. 2013, a new kind of inerter called fluid inerter was proposed and the inner force was investigated, but the effect of the nonlinear model on the suspension performance was not discussed. In the following we will consider the nonlinearity of the real fluid inerter.

When the force F is applied to the fluid inerter, both the friction caused by the motion of piston rod, hydraulic cylinder f and the damping force caused by the viscosity of the fluid f_c will block the motion of the piston. The dynamic equation is:

$$F(t) - f(t) - f_c(t) = b\ddot{x}(t). \quad (5.18)$$

The friction model can be described by the Column Friction Model as follows:

$$f(t) = f_0 \text{Sign}(\dot{x}(t)), \quad (5.19)$$

where f_0 is the amplitude of the friction, $\dot{x}(t)$ is the velocity of the piston, and $\text{Sign}(\dot{x}(t))$ is the signum function. The direction of friction f between the piston and hydraulic cylinder is related to the velocity of the piston and has the constant value. This makes a small contribution at low strut velocities, but negligible at working velocities in the range $0.1-1 \text{ m/s}$.

For an hydraulic device, the damping force caused by the viscosity of the fluid is the most important impact on the dynamic performance. According to the Hagen Poiseuille Law, the flow of the fluid in the helical channel Q and the pressure drop between the two terminals Δp have the relation as follows:

$$Q = \frac{\pi r_3^4}{8\mu l} \Delta p \quad (5.20)$$

The related pressure drop is:

$$\Delta p_{vis}(t) = \frac{8\mu l}{r_3^2} u(t) . \quad (5.21)$$

A fluid flow entering a new channel will also experience an energy loss at the inlet and outlet of the hydraulic cylinder; the empirical formula for the resulting pressure drop is given in (Massey 1997). The pressure drop across the inlet and the outlet is thus estimated to be

$$\begin{aligned} \Delta p_{in}(t) &= 0.5 \frac{\rho u^2(t)}{2} \\ \Delta p_{ou}(t) &= \frac{\rho u^2(t)}{2} . \end{aligned} \quad (5.22)$$

So, the parasitic damping force of the inerter can be gained as follows:

$$f_c(t) = (\Delta p_{vis}(t) + \Delta p_{in}(t) + \Delta p_{ou}(t)) A_1 = \frac{8\mu l}{r_3^2} \frac{A_1^2}{A_2} \dot{x}(t) + \frac{3\rho}{4} \frac{A_1^3}{A_2^2} \dot{x}^2(t) . \quad (5.23)$$

From equation (5.23), the damping force is related not only to the velocity but also to the square of the velocity of the piston.

The total force of the fluid inerter device can be gained as follows:

$$F(t) = f_0 \text{Sign}(\dot{x}(t)) + \frac{8\mu l}{r_3^2} \frac{A_1^2}{A_2} \dot{x}(t) + \frac{3\rho}{4} \frac{A_1^3}{A_2^2} \dot{x}^2(t) + b \ddot{x}(t) \quad (5.24)$$

In Figure 5.27 it is shown the response in terms of total force versus time, when the device is subjected to a sinusoidal displacement with amplitude of 120 mm and a frequency of 0.5 Hz.

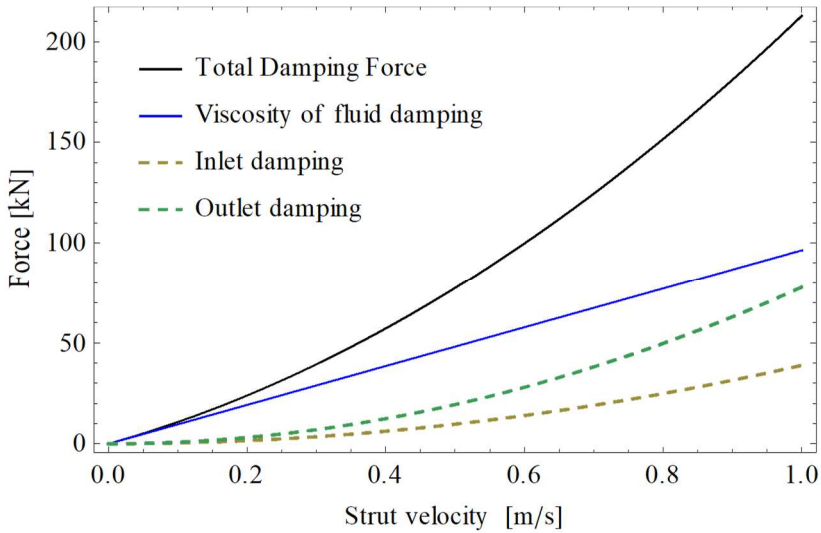


Figure 5.26 Parasitic damping force

In the same figure are also represented the single contributions to the total force. We note that the major contribution is related to the inertance, but also the contributions of the parasitic damping force, as the inlet and outlet and the viscosity part, are significant. The friction force has been neglected; infact the maximum value of the velocity for the case in exam is 0.37 m/s.

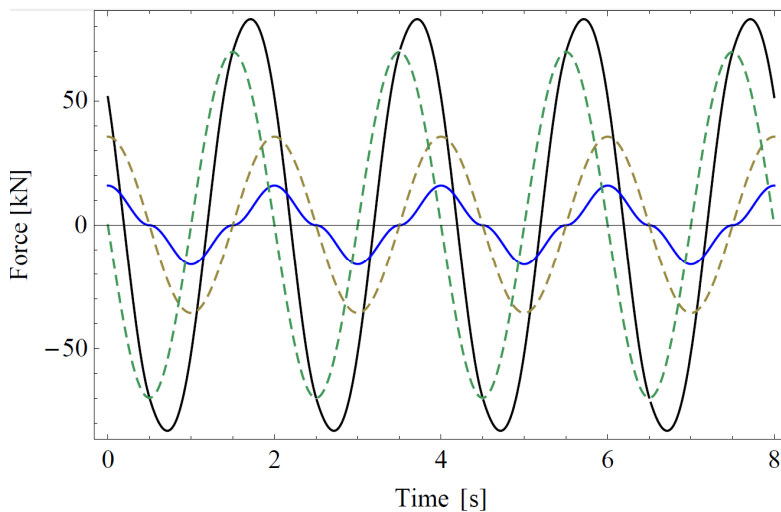


Figure 5.27 Total force of the proposed device (total force in black; inertance part in dashed green; viscosity of the fluid in blue; inlet and outlet part in dashed brown)

For the same parameters we have also represented the force displacement loop (see Figure 5.28).

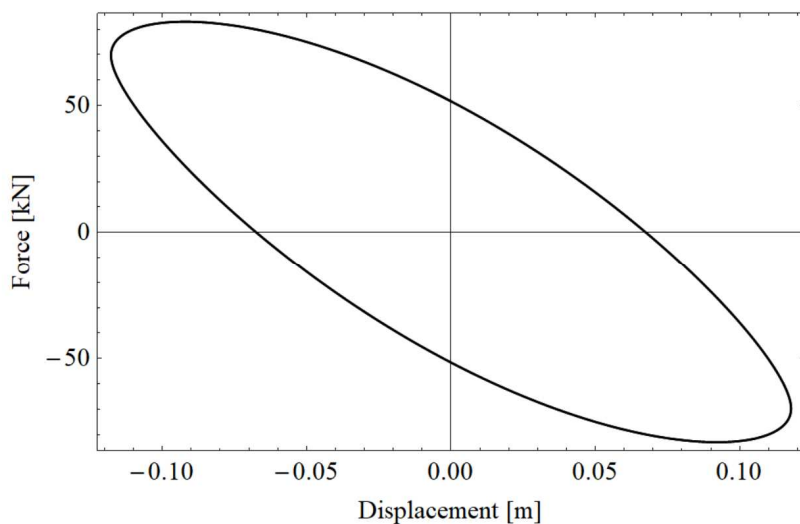


Figure 5.28 Force-displacement loop for the proposed device (frequency of 0.5 Hz; displacement of 120 mm)

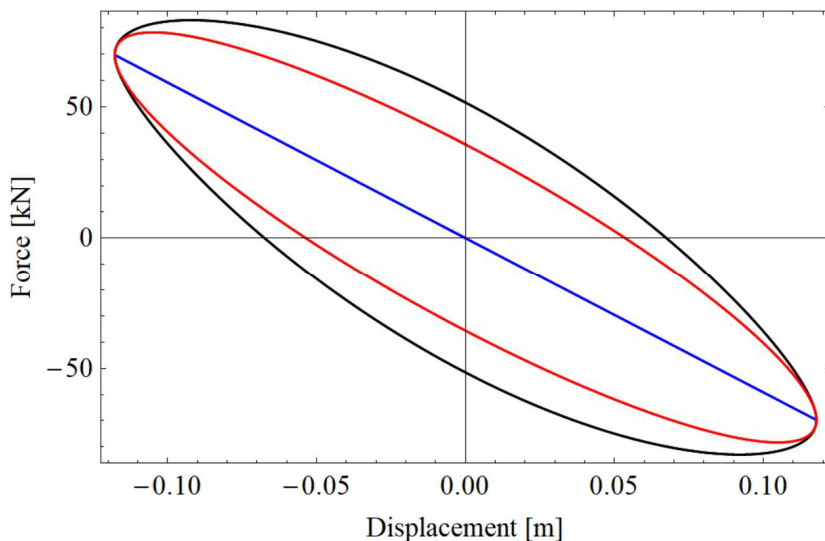


Figure 5.29 Force-displacement loops for the proposed device (frequency of 0.5 Hz; displacement of 120 mm): total inverter force (black line), inertia contribution plus linear part of the parasitic force (red line), inertia contribution to the total inverter force (blue line)

Just to make a comparison, in Figure 5.29 we have represented the force-displacement loop considering the total quadratic force (the black line in Figure 5.29), only the linear part of the force (the blue line in Figure 5.29), and only the contribution due to the inertance part (the red line in Figure 5.29).

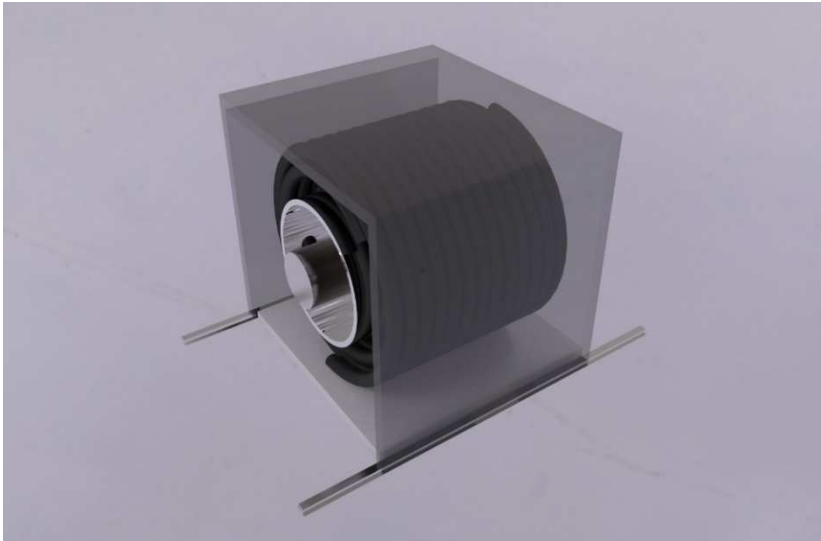


Figure 5.30 3D mechanical model of the proposed fluid inerter device from SolidWorks

The theoretical mechanical model has been realized with SolidWorks software and is shown in Figure 5.30. From the comparison between this device and the one described in §5.3, we can assert that the fluid inerter device produces a bigger amplification with a smaller quantity of mass, and so it is the better solution to realize an inerter device.

Chapter 6

FIBER REINFORCED PTFE

In this chapter we propose a new fiber reinforced material starting from a virgin PTFE, following the approach illustrated in (Riul et al. 2012). In Chapter 2, §2.3.1, we have illustrated the compression behavior of virgin PTFE, to do this we have realized a disk of 8mm of thickness and we have performed a compression test. For the use of PTFE in the proposed isolation device (Chapter 4) we need to have a material with very low friction, such as the virgin PTFE, and at the same time with a good resistance to the compression load. One solution should be to use filled PTFE, for this reason we have printed two disks, one filled with bronze and the other filled with glass fiber, and we have performed the compression tests. Although these two disks show an increase in compression strength, also the friction coefficient increases. The idea proposed here, following a research field developed in the last years (Gu et al. 2009), is to realize a disk of virgin PTFE reinforced with a glass fiber positioned in the free part of the disk, in order to increase the compressive strength without increasing the coefficient of friction which, therefore, remains equivalent to that of the virgin PTFE. For this material the main problem is the behavior at the interface; in fact, continuous fiber reinforced PTFE composites must be fabricated by sintering processing at high temperatures ($> 300\text{ }^{\circ}\text{C}$). Therefore, it is difficult to completely avoid the formation of porosity resulting from the thermal pyrolysis of some organic materials. Furthermore, because PTFE is highly chemically inert, it is difficult possible to achieve strong interfacial bonding between the PTFE matrix and the fiber in order to ensure load transmission. For these reasons we have chosen a glass fiber with a wide mesh (see Figure 6.7).

6.1 Manufacturing process and compression tests

The materials studied in this chapter were unreinforced virgin polypropylene (PTFE), PTFE filled with a glass fibre content of 30% by weight (30GL-NFF) and PTFE filled with bronze content of 40% (40BRR-NFF). The materials were supplied by HEROFLON. In this section we have studied and designed a new material: PTFE reinforced with one layer of glass fiber. To realize the three disks we have followed the procedure described in § 2.3.1, with an initial printing process and then an heat treatment. In Figure 6.1 and Figure 6.4 the two disks of filled PTFE are shown before the compression test (described in § 2.3.1).



Figure 6.1 Disk of PTFE filled with glass fiber



Figure 6.2 Disk of PTFE filled with glass fiber after the compression test

As we can see from Figure 6.2 and Figure 6.5, the deformed shape of the two filled disks is very different from the of the virgin PTFE (see Figure 2.49), the behavior shown is more plastic, infact from the stress strain curve

of the two disks (Figure 6.3 and Figure 6.6), we note an increase in strain and also an increase in strength.

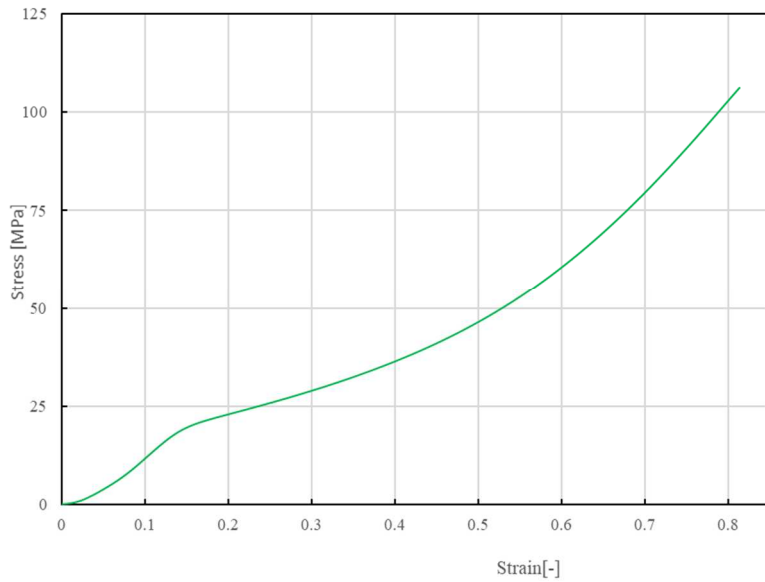


Figure 6.3 Stress-strain behavior of the disk of PTFE filled with glass fiber



Figure 6.4 Disk of PTFE filled with bronze



Figure 6.5 Disk of PTFE filled with bronze after the compression test

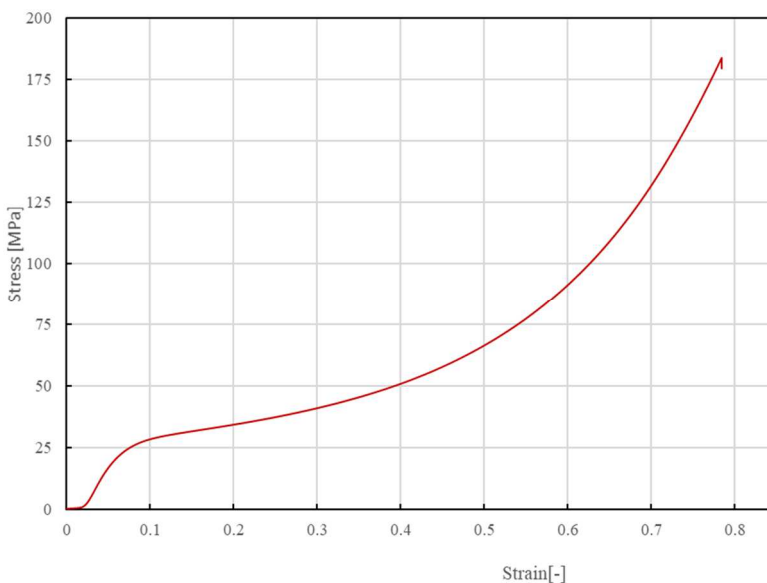


Figure 6.6 Stress-strain behavior of the disk of PTFE filled with bronze

After the test on this two disks, the attention has been focused on the new material. In Figure 6.7 and Figure 6.8, respectively, the glass fiber, used for the realization of the proposed new material disk, and the inclusion of this fiber glass inside the stamp are shown. The dust has been weighted in such a way to collocate the fiber at a height in the disk that will be in the free part inside the sliding device.

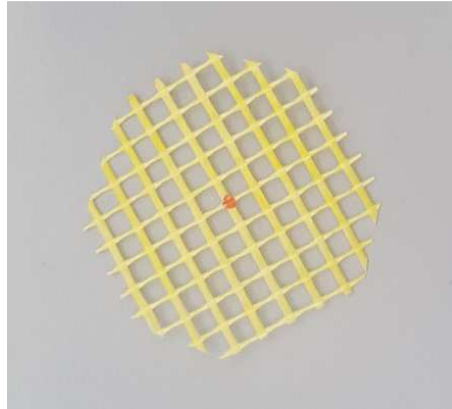


Figure 6.7 Glass fiber used for the proposed new material



Figure 6.8 The inclusion of the fiber inside the the stamp

In Figure 6.9 the deformed shape of the reinforced disk is reported. We note that is completely different from the of the vergin PTFE (see Figure 2.49) and, instead, the behavior is similar to the two filled disk.



Figure 6.9 Fiber reinforced PTFE after the compression test

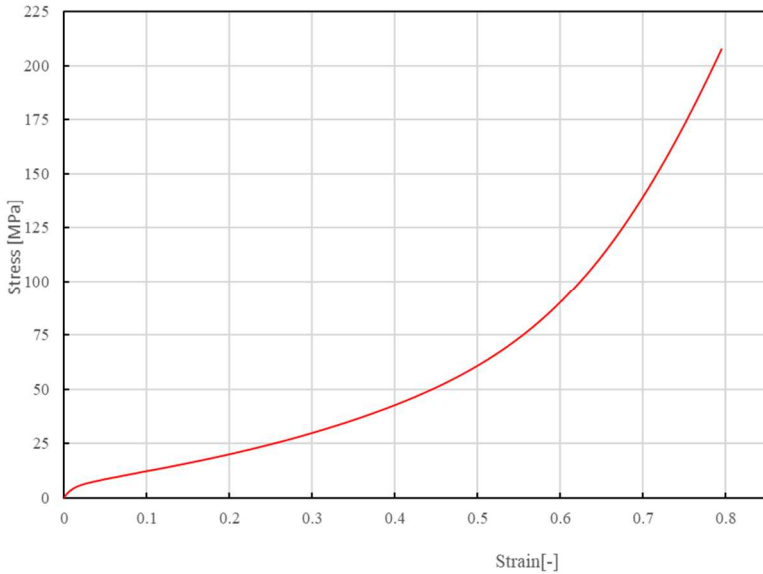


Figure 6.10 Stress-strain behavior of the disk of reinforced virgin PTFE

As we can see from the comparison of the two disks, virgin and reinforced virgin PTFE (Figure 6.11) after the compression test and from the two stress-strain curves (Figure 6.12), the behavior of the new proposed material is improved, the compression strength is increase of more the 60%, with an strain increase of only 15%.



Figure 6.11 Comparison between the two disks after the compression test (virgin PTFE on the left; reinforced PTFE on the right)

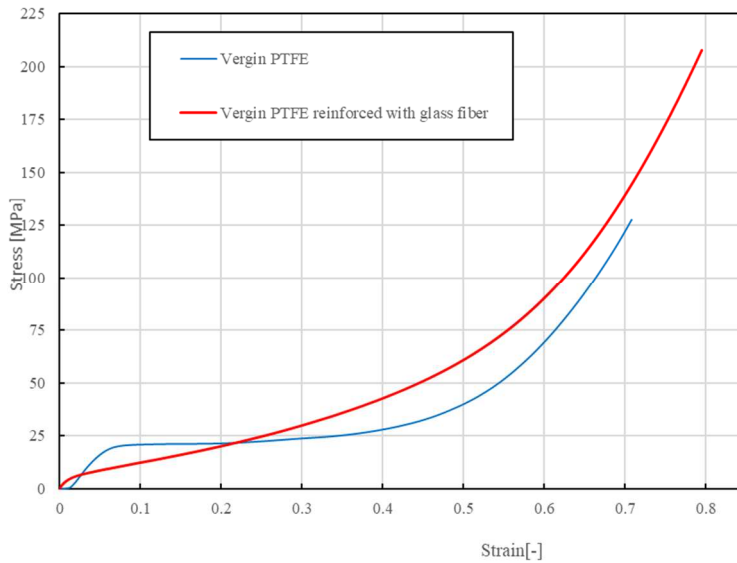


Figure 6.12 Comparison between the stress–strain curve of the two disks

For a complete representation, in Figure 6.13 the comparison between the all four disk realized in the experimental set is shown. The behavior of the new proposed material is similar to the two filled disks, in particular for large deformations and it reaches the maximum strength with respect to the other disks.

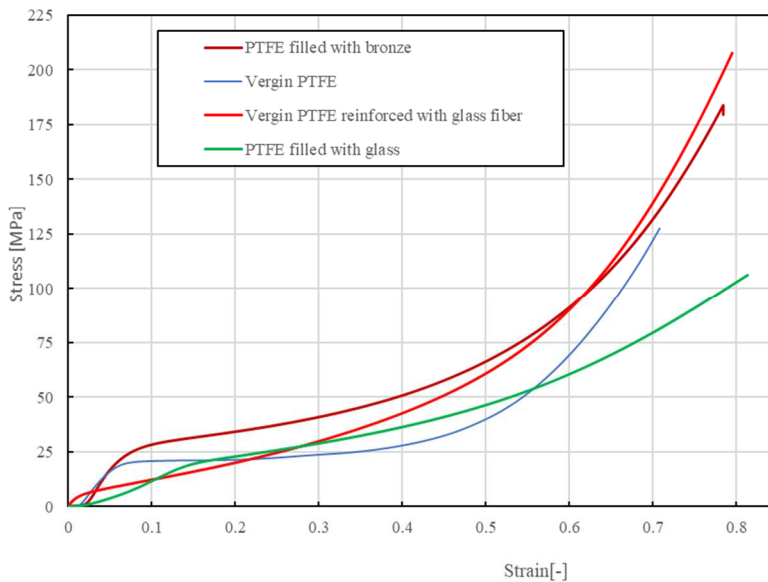


Figure 6.13 Comparison between the stress–strain curve of the four printed disks

6.2 Finite element model of the new proposed material

For a complete analysis of the new proposed material, we have modeled the reinforced virgin PTFE with the FE software Abaqus 6.14 (Hibbit et al. 2003) trying to simulate the compression test. To do this we have also modeled the two steel plates that confine the disk (see Figure 6.14 and Figure 6.15). In Figure 6.16 the mesh of the model is shown.

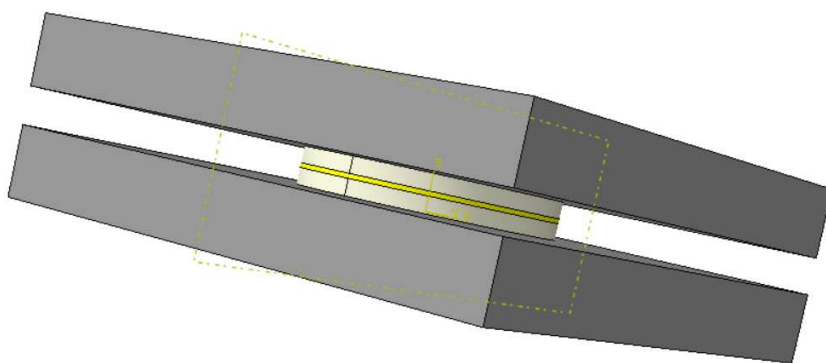


Figure 6.14 3D model of the reinforced disk realized with ABAQUS 6.14

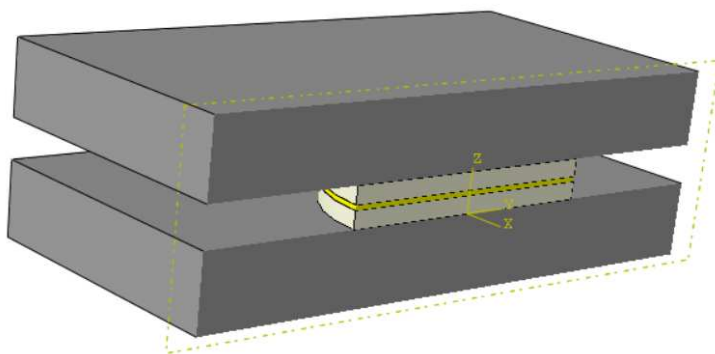


Figure 6.15 Section of the 3D model of the reinforced disk realized with ABAQUS 6.14

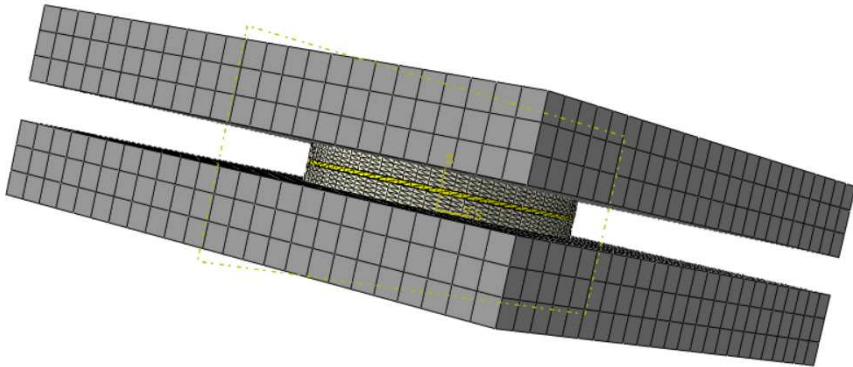


Figure 6.16 Mesh of the reinforced disk

In Figure 6.17 is represented the stress-strain curve obtained from the FE model. From the comparison with experimental test (Figure 6.18) we note that the results are in good agreement, especially in the shape of the curve. The difference between the two curves is, probably due to the behavior of the glass fiber, for which we have considered the standard mechanical characteristic instead to conduct the same characterization test.

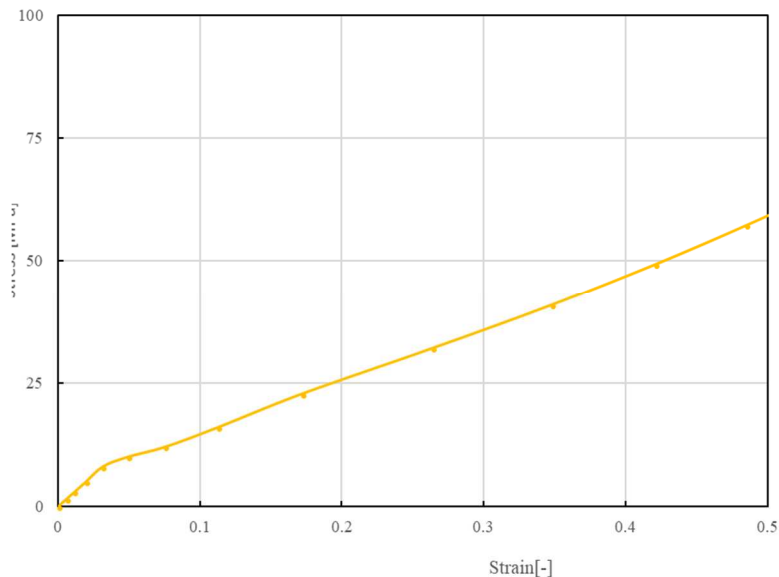


Figure 6.17 Stress-strain curve from the FE model

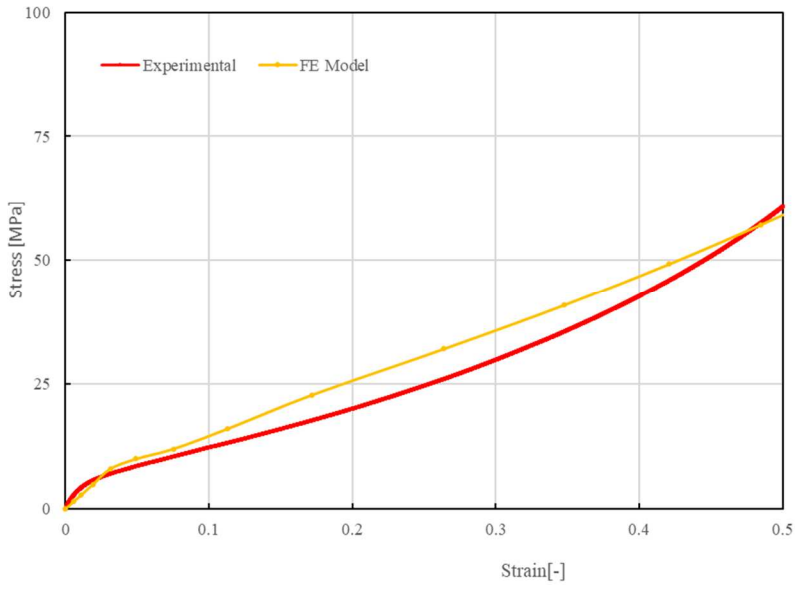


Figure 6.18 Comparison between experimental and FE model

CONCLUSIONS

Base isolation technique is one of the most widespread solutions for the mitigation of damage induced by seismic action on structures.

In this Ph.D. thesis we have proposed novel devices and strategies that could overcome the problems of existing isolation devices that are currently more widespread. We also will fill the technological vacuum currently present in the field of isolation, with respect to the vertical component of the seismic action.

The research work, after a careful and targeted bibliographic research (Chapter 1), was directed first to the study of the behavior of the materials that are used in the isolation devices, such as Steel, Elastomer and PTFE (Polytetrafluoroethylene) (Chapter 2). To better characterize the compression behavior of PTFE, laboratory specimens were made from the virgin product and with addition of reinforcements in the chemical composition, and they underwent compression tests. Subsequently in Chapter 3, we moved on to the modeling, by using Finite Elements of the existing devices, e.g. Elastomeric HDRB and Friction Pendulum. This step has been of fundamental importance to highlight all the problems, already known in the literature, related to the devices already present on the market. Once the study was completed on existing devices, in Chapter 4 we focus on the design of a new isolation device for the horizontal component of the seismic action, called HFRI (Hybrid Friction Rubber Isolator), and an isolation device for the vertical component, called VID (Vertical Isolation Device). After an initial design, obtained following the UNI standards in this regard, the finite element models were processed using the Abaqus CAE calculation code, with these models it was possible to study the hysteretic behavior of devices that are both based on a dissipation mechanism by friction between PTFE and lubricated steel. These models allowed also to study the stress state that develops in the devices. From these analysis, it has been found that both devices are feasible and valid for

use in the seismic protection of structures. In particular, the HRFI device is comparable, in terms of performance and size in plan, to a Friction Pendulum, while for what concerns the VID device, since it is completely innovative and there are no similar products on the market, it was not possible to compare it with any other product. As part of this research, in Chapter 5 a seismic isolation system was also studied which involves the insertion of a device called *Inerter* combined with a dissipator and an elastic element, thanks to which it is possible to significantly reduce the displacements of the isolated structure, manifesting a peculiar effect that exploits the concept of a mass-produced damper but uses small amounts of mass.

For a particular numerical application, two kinds of inerter device has been designed, a rack-pinion one and a fluid one, from which it is possible to demonstrate that the fluid inerter device is the one that better increases the mass. Finally, in order to improve the performance of the two designed isolation devices (HFRB and VID), in Chapter 6 a glass fiber reinforcement was studied for the PTFE part, and in particular experimental test on two filled printed PTFE disk and one reinforced PTFE have been carried out. To make a complete study, numerical simulation with FE software has been conducted in the reinforced part. Both the experimental tests and the FE simulation have demonstrated that the reinforcement improves the compressive behavior of the vergin PTFE. The research activity carried out during the three-year period led to the presentation of two patent applications for the devices studied, which are currently being processed.

REFERENCES

- ADINA R & D, Inc. (2011), Theory and Modeling Guide Volume I: ADINA. Report ARD 11-8. Watertown (MA,USA).
- Anderson T.L., (1989), “Seismic Isolation for the Losangeles Country Fire Command and Control Facility”, *Proc. ASCE Structures Congress* Vol. 1, San Francisco, CA.
- Arnold C., (2001) “Architectural considerations. The Seismic Design Handbook”, 2nd ed. F. Naeim, 275–326.
- Arruda E. and Boyce M., (1995), “Effects of strain rate, temperature and thermomechanical coupling on the finite strain deformation of glassy polymers”, *Mechanics of Materials*, **19**,193–212.
- Asai T., Araki, Y., Masui T. and Yoshida N., (2008),“Vertical Vibration Isolation Device using Constant Load Supporting Mechanism”, *Structures Congress*.
- Asher J.W. et al., (1995), “Seismic performance of the base isolated USC University hospital in the 1994 Northridge Earthquake”, *Seminar 1 on Isolation, Energy Dissipation and Control of Vibration of Structures*, Santiago, Chile.
- Bergström J.S., Rimnac C. and Kurtz S., (2003), “Prediction of multiaxial mechanical behavior for conventional and highly crosslinked UHMWPE using a hybrid constitutive model”, *Biomaterials*, **24**, 1365–1380.

- Bergström J.S. and Boyce M.C., (2000) “Large strain time-dependent behavior of filled elastomers” *Mechanics of Materials*, **32**, 620–644.
- Bergström J.S. and Hilbert Jr L.B., (2005) “A constitutive model for predicting the large deformation thermomechanical behavior of fluoropolymers”, *Mechanics of Materials* 2005, **37**, 899-913.
- Bıçakcı A. N. and Erkman M., (2006), “SolidWorks”, *İstanbul: Pusula Yayıncılık*.
- Bonet J. and Wood R. D., (2008), “Nonlinear Continuum Mechanics for Finite Element Analysis (Second Edition)”, *Cambridge University Press, Cambridge, UK*.
- Bowden F.P. and Tabor D., (1950), “The Friction and Lubrication of Solids: Part I”, *Oxford University Press, Oxford, UK*.
- Bowden F.P. and Tabor D., “Friction: an introduction to Tribology” , *Heinemann, UK* 1973.
- Braga F., Dolce M., Ferrigno A., Laterza M., Marotta G., Masi A, Nigro D and Ponzo F., (1997), “Indagine sperimentale per la valutazione delle caratteristiche meccaniche di isolatori elastomerici armati ad elevato smorzamento, VII Congresso Nazionale L'ingegneria Sismica in Italia, Taormina.
- Brzeski P., Pavlovskaja E., Kapitaniak T. and Perlikowski P., (2015), “The application of inerter in tuned mass absorber”, *International Journal of Non-Linear Mechanics*; **70**, 20–29.
- Buckle I. and Mayes R., (1990), “Seismic isolation history: application and performance - a world review”, *Earthquake Spectra*, **6**, 161–201.
- Campbell T. I., Pucchio J. B., Roeder C. W. and Stanton J. F., (1991), "Frictional Characteristics of PTFE Used in Slide Surfaces of Bridge Bearings", *Proc. 3rd World Congress on Joint Sealing and Bearing*

-
- Systems for Concrete Structures, Toronto, Ontario, Canada, Vol. 2 of Pre prints (published by the National Center for Earthquake Engineering Research, Buffalo, NY), 847-870.*
- Campbell T.I. and Kong W. L., (1987)“PTFE Sliding Surfaces in Bridge Bearings”, *Ministry of Transportation and Communications, Ontario, Canada, Report ME-87-06.*
- Cancellara D. and Pasquino M., (2011), “Proposal for a passive seismic control device: H.D.H.S.I. (High Damping Hybrid Seismic Isolator)”, *Proceedings of the 8th International Conference on Structural Dynamics, EUROLYN 2011 Leuven, Belgium, 4-6 July 2011.*
- Carlos C. S. And Héctor S. S., (2008), “Seismic Response Of Cylindrical Tanks For Oil”, *The 14Th World Conference on Earthquake Engineering October 12-17, Beijing, China.*
- Carslaw H.S. and Jaeger C., (1959), “Conduction of Heat in Solids”, *2nd Edition, Oxford University Press, London, UK.*
- Caspe M., (1984), “Base isolation from earthquake hazards: and idea whose time has come”, *In VIII World Conference on Earthquake Engineering, San Fransisco, CA.*
- Castaldo P., Palazzo B. and Della Vecchia P., (2015), “Seismic reliability of base-isolated structures with friction pendulum bearings”, *Engineering Structures; 95, 80-93.*
- Caughey T.K., OKelly M.E.J., (1965),“Classical normal modes in damped linear dynamic systems”, *Journal of Applied Mechanics, 32, 583-588.*
- Chalhoub M. and Kelly J., (1990),“Earthquake simulator testing of a combined sliding bearing and rubber bearing isolation system”, Tech. rep., *Earthquake Engineering Research Center, University of California, Berkely, CA., Report No. UCB/EERC-87/04.*
-

- Chang K. C., Hwang J.S. and Lee G.C., (1990), “Analytical model for sliding behavior of Teflon-stainless steel interfaces”. *Journal of Engineering Mechanics*, ASCE **116**(12), 2749-2763.
- Charleston A.W., Wright P.D. and Skinner R.I., (1987), “Wellington Central Police Station, Base isolation of an Essential Facility”, *Proc. Pacific Conf. on Earthquake Engineering*, Vol. **2**, Wairekei, New Zealand.
- Chemicals Americas inc; (2007), “Physical properties of Fluon, unfilled and Filled PTFE”, *Technical Service Note F12/13 AGC*
- Chen M. Z. Q., Papageorgiou C., Scheibe F., Wang F.-C., and Smith M., (2009), “The missing mechanical circuit element,” *IEEE Circuits and Systems Magazine*, Vol. **9**, no. 1, pp. 10–26.
- Chopra A.K., (2012), “Dynamics of Structures (4th edn)”, *Pearson Prentice Hall. USA*.
- Computers and Structures Incorporated (CSI). SAP2000 v. 17. Berkeley, California, 2013.
- Constantinou M., Mokha A. and Reinhorn A.R., (1990) “Teflon bearings in base isolation II: Modeling”, *Journal of Structural Engineering*; **116** (2), 455-474.
- Constantinou M.C., Tsopelas P., Kasalanati A. and Wolff E.D., (1999), “Property modification factors seismic isolation bearings”, *University at Buffalo, Buffalo, NY*, Report No. MCEER-99-0012.
- Cuomo G., (2007), “Effetti di carichi verticali elevati sul progetto dei dispositivi di isolamento sismico”, *PhD Thesis Università degli Studi di Napoli Federico II*.

- De Domenico D. and Ricciardi G.,(2017) “ An enhanced base isolation system equipped with optimal tuned mass damper inerter (TMDI)”, *Earthquake Engineering Structural Dynamics*, 1-24.
- De Domenico D., Ricciardi G. and Benzoni G., (2018), “Thermo-mechanical coupled analysis of friction pendulum seismic isolators under bidirectional excitation”, submitted to *Engineering Structures*, **106**, 131-147.
- DeMontalk R., (1932), “Shock absorbing or minimizing means for buildings. U.S.” *Patent No. 1,847,820 (New Zealand Patent Granted 1929)*.
- Den Hartog J.P., (1934), “Mechanical Vibrations”, *McGraw-Hill, New York*,
- Derham C., Kelly J. and Tomas A., (1985), “Nonlinear natural rubber bearings for seismic isolation”, *Nuclear Eng. Design*, **84(3)**, 417–428.
- D.M. 14 gennaio 2008, “ Nuove norme tecniche per le costruzioni”, *Ministero delle Infrastrutture, Italy*.
- Dolce M., Cardone D. and Ponzo F., (2001), “Comparison od Different Passive Control System for R/C Frames through Shaking Table Test”, *Proc. 5th World Congress on Joints, Bearings and Seismic System for Concrete Structures, Rome, Italy*.
- Dolce M., Ponzo F.C., Goretti A., Moroni C., Giordano F., De Canio G., Marnetto R., (2008), “3D Dynamic Tests on 2/3 scale masonry Buildings retrofitted with different System”. *Proc. 14th World Conference on Earthquake Engineering, Beijing, China*.
- DuPont-Fluoroproducts, (1996), “Teflon, PTFE, properties handbook”, *Tech. Rep. H-37051-3, DuPont*.

- Ebnesajjad S., (2000), “Fluoroplastics Volume 1”, *Non-Melt Processible Fluoroplastics. Plastics Design Library*.
- Eringen A. C., (1980) “Mechanics of Continua”, *Robert E. Krieger Publishing Company, Huntington, NY, USA*.
- Eröz M. and DesRoches R., (2008), “Bridge seismic response as a function of the Friction Pendulum System (FP) modeling assumptions”, *Engineering Structures*; **30**, 3204-3212.
- Ettles C.M.M., (1986), “Polymer and elastomer friction in the thermal control regime”, *ASME Journal of Tribology*; **108**, 98–104.
- Eurocode 8, (2003), “European Committee for Standardization: design of structures for earthquake resistance – part 1: general rules, seismic actions and rules for buildings”, *Brussels, Belgium*.
- Fenz DM, Constantinou MC., (2006), “Behavior of the double concave Friction Pendulum bearing.” *Earthquake Engineering and Structural Dynamics*; **35**:1403-1424.
- Forni M., (2011), “Seismic isolation of nuclear power plants”, *ENEA, Italy in Japan*.
- Furinghetti M., Casarotti C. and Pavese A., (2014), “Bi-directional experimental response of full scale DCSS devices”, *Second European Conference on Earthquake Engineering and Seismology, Istanbul, Turkey, August 25-29*.
- Garrido H., Curadelli O. and Ambrosini D., (2013), “Improvement of tuned mass damper by using rotational inertia through tuned viscous mass damper”, *Engineering Structures*; **56**, 2149–2153.
- Gartner B. J. and Smith M. C., (2011), “Damping and inertial hydraulic device”, *February 7, US PatentApp. 13/577, 234*.

- Glover A. R., Smith M. C., and Houghton N. E., (2009), “Forcecontrolling hydraulic device,” International Patent Application No: PCT/GB2010/001491.
- Gómez C., Avilés A., Bilbao A., Siepe D. and Nawrotzki P., (2012), “E-ELT Seismic Devices Analysis and Prototype Testing”, *Proc. SPIE 8449, Modeling, Systems Engineering, and Project Management for Astronomy*, Vol **8449** 18; DOI:10.1117/12.925001.
- Gu A., Liang G. and Yuan L., (2009), “Novel preparation of glass fiber reinforced polytetrafluoroethylene composites for application as structural materials”, *Polymers for Advanced Technologies*, **20**, 39–42.
- Hibbit et al., Abaqus, Karlsson and Sorenson, (2003), “Abaqus theory manual v. 6.14” U.S.A.
- Ho K. and Krempl E., (2002), “Extension of the viscoplastic theory based on overstress (VBO) to capture non-standard rate dependence in solids”, *International Journal of Plasticity*, 851–872.
- Housner G., Bergman L., Caughey T., Chassiakos A., Claus R., Masri S., Skelton R., Soong T., Spencer B., and Yao J., (1997), “Structural control: Past, present, and future”, *Journal of Engineering Mechanics*, ASCE **123**, Special Issue.
- Hu Y. and Chen M.Z.Q., (2015), “Performance evaluation for inerter-based dynamic vibration absorbers”, *International Journal of Mechanics and Sciences*; **99**, 297–307.
- Izumi M., (1988), “State-of-the-art report: base isolation and passive seismic response control”, *In IX Conference on Earthquake Engineering, Tokyo, Japan*, Vol. **8**, pp. 385-396.
- Jaeger J.C., (1943), “Moving sources of heat and the temperature at sliding contacts”, *Proc. R. Soc. New South Wales*, **76**, 203-224.

- Jurukovski D. and Rakicevic Z., (1995), “Vibration base isolation development and application”, In *Tenth European Conference on Earthquake Engineering, Duma, Ed., Balkema, Rotterdam*, 667–676.
- Kashiwazaki A., Mita R., Enomoto T. and Akimoto M., (2008), “Three-dimensional Base Isolation System Equipped with Hydraulic Mechanism”, *Transactions of the Japan Society of Mechanical Engineers Series C*, Vol. **66(2000)** n° 648, 2616-2621.
- Kelly J., (1986), “Seismic base isolation: review and bibliography”, *Soil Dynamic and Earthquake Engineering*, **5**, 202–216.
- Kelly J., (1990), “Base isolation: linear theory and design”, *Earthquake Spectra*, **6(2)**, 223–244.
- Kelly J., (2002), “Seismic isolation systems for developing countries”, *Earthquake Spectra*, **18(3)**, 385–406.
- Kelly J. and Quiroz E., (1992), “Mechanical Characteristic of Neoprene Isolation Bearings”, *Report N. UCB/EERC-92/11, Earthquake Engineering Research Center, Berkeley, CA*.
- Kelly J. and Tsztoo D., (1977), “Energy absorbing devices in structures under earthquake loading”, In *6th World Conference on the Earthquake Engineering New Delhi*, Vol. **2**, 1369-1374.
- Kelly J., Skinner R. and Heine A., (1972), “Mechanisms of energy absorption in special devices for use in earthquake resistant structures”, *Bulletin of the New Zealand National Society for Earthquake Engineering*, **5**, 78–89.
- Kelly J.M. and Konstantinidis D.A., (2011), “Mechanics of rubber bearings for seismic and vibration isolation”, *A John Wiley & Sons, Ltd., Publication*.

- Kelly T., (2001), “Base isolation of structures, design guidelines”, *Tech. rep., Holmes Consulting Group Ltd.*
- Kumar M., Whittaker A.S. and Constantinou M.C., (2015), “Characterizing friction in sliding isolation bearings”, *Earthquake Engineering and Structural Dynamics*; **44**,1409-1425.
- Lazar I.F., Neild S.A. and Wagg D.J., (2014), “Using an inerter-based device for structural vibration suppression”, *Earthquake Engineering and Structural Dynamics*; **43**,1129–1147.
- Lion A., (1977), “On the large deformation behavior of reinforced rubber at different temperatures”, *Journal of Mechanics Physics and Solids*, **45**, 1805–1834.
- Lissia S., Casarotti C., Pavese A. and Dacarro F., (2012), “Experimental response of full scale curved surface sliders equipped with high dissipation sliding material”, *15th World Conference on Earthquake Engineering, Lisbon, Portugal, September 24-28.*
- Lomiento G., Bonessio N. and Benzoni G., (2013), “Concave sliding isolators performance under multi-directional excitation”, *Ingegneria Sismica*, **30 (3)**.
- Lomiento G., Bonessio N. and Benzoni G., (2013)“Friction model for sliding bearings under seismic excitation”, *Journal of Earthquake Engineering*; **17**, 1162-1191.
- Marian L. and Giaralis A., (2014)“Optimal design of a novel tuned mass-damperinerter (TMDI) passive vibration control configuration for stochastically support-excited structural systems”, *Probabilistics Engineering Mechanics*; **38**,156–164.
- Massey B. S., (1997) “Mechanics of Fluids”, Chapman & Hall, London, UK, 6th edition.

- Medeot R., (1991), “The Evolution of Aseismic Devices for Bridges in Italy”, Proceedings of the 3 World Congress on Joint Sealing and Bearing System for Concrete Structure”, *National Center for Earthquake Engineering Research, State University of New York at Buffalo, New York, USA*, **Vol. 2**, pp. 1295-1320.
- Miller K., (1999), “Testing Elastomers for Hyperelastic Material Models in Finite Element Analysis”, *Rubber Technology International*.
- Mirza Hessabi R. and Mercan O., (2016), “Investigations of application of gyro-mass dampers with various types of supplemental dampers for vibration control of building”, *Engineering Structures*, **126**, 174-186.
- Mokha A., Constantinou M. and Reinhorn A., (1990), “Teflon bearings in base isolation. part I: testing”, *Journal of Structural Engineering*, **116(2)**, 438–454.
- Moon B.Y., Kang G.J., Kang B.S., Kelly J.M., (2002), “Design and manufacturing of fiber reinforced elastomeric isolator for seismic isolation”, *Journal of Materials Processing Technology*, 145-150.
- Mosqueda G., Whittaker A.S. and Fenves G.L., (2004), “Characterization and modeling of friction pendulum bearings subjected to multiple components of excitation”, *Journal of Structural Engineering*; **130(3)**, 433-442.
- Mostaghel N., (1984), “Resilient-friction base isolator”, *Department of Civil Engineering, University of Utah, Salt Lake City, UT.*,. Report No. UTEC 84-097.
- Mostaghel N. and Khodaverdian M., (1987), “Dynamics of resilient-friction base isolator (R-FBI)”, *Earthquake Engineering and Structural Dynamics* 1987, **15**, 379–390.
- Muscolino G., (2001), “Dinamica delle Strutture”, *McGraw Hill*.

- Naeim F. and Kelly J., (1999), “Design of Seismic Isolated Structure: From Theory to Practice”, *Wiley and sons*.
- Nagashima I.; Kawamura S., Kitazawa K. and Hisano M., (1987), “Study on a base isolation system”, *Proceedings of the 3rd Conference on Soil Dynamics and Earthquake Engineering*, Princeton University, Princeton, NJ, 22–24 June 1987.
- Nestovito G. and Occhiuzzi A., (2016), “Implementation of smart-passive dampers combined with double concave friction pendulum devices to retrofit an existing highway viaduct exploiting the seismic early warning information”. *Engineering Structures*, **120**, 58-74.
- Ogden R. W., (1997), “Non-linear Elastic Deformations”, *Dover, New York, USA*.
- Panchad V. R. and Jangid R. S., (2008), “Variable friction pendulum system for near-fault ground motions”, *Structural Control and Health Monitoring*, **15**, 568-584.
- Papageorgiou C. and Smith MC.,(2005), “Laboratory experimental testing of inerters”, *Proceedings of the IEEE conference on decision and control*, **44**; 3351–56.
- Pietrosanti D., De Angelis M., Basili M., (2017) “Optimal design and performance evaluation of systems with Tuned Mass Damper Inerter (TMDI)”, *Earthquake Engineering Structural Dynamics*; DOI: 10.1002/eqe.2861.
- Pranesh M., and Sinha R., (2000), “VFPI: an isolation device for aseismic design”, *Earthquake Engineering and Structural Dynamics*, **29**, 603–627.
- Quaglini V, Bocciarelli M, Gandelli E and Dubini P., (2014), “Numerical assessment of frictional heating in sliding bearings for seismic isolation”, *Journal of Earthquake Engineering*; **18**:1198-1216.

- Reaveley L.R., Mayes R.L. and Sveinsson B.I., (1998), “Seismic Isolation of a Four Story Flight Simulator Manufacturing Facility”, *Proc. 9th World Conference on Earthquake Engineering, Tokyo, Japan*.
- Riul C., Tita V., de Carvalho J. And Canto R.B., (2012), “Processing and mechanical properties evaluation of glass-fiber-reinforced PTFE laminates”, *Composites Science and Technology*, **72**, 1451-1458.
- Robinson W., Gannon C. and Meyer J., (2006), “A sliding bearing with an elastic restoring force”. *Bulletin of the New Zealand Society of Earthquake Engineering*, **39** (1), 81–84.
- Robinson W.H. and Tucker A.G., (1977), “A Lead-Rubber Shear Damper”, *Bulletin of New Zealand National Society of Earthquake Engineering*, **Vol. 10**, N. 3, 151-153.
- Robinson W.H. and Tucker A.G., (1983), “Test Results for Lead-Rubber Bearings for the William M. Clayton Building, Toe Toe Bridge, and Waiotukupuna Bridge”, *Bulletin of New Zealand National Society of Earthquake Engineering*, **Vol. 14**, N. 1, 21-33.
- Rubin M.B., (2009), “On evolution equations for elastic deformation and the notion of hyperelasticity”, *International Journal of Engineering Science*, **47**, 76-82.
- Saitoh M., (2012), “On the performance of gyro-mass devices for displacement mitigation in base isolation system”, *Structural Control Health Monitoring*, **19** (2), 246-59.
- Siepe D. and Nawrotzki P., (2015), “Horizontal And Vertical Isolation Of Seismic And Aircraft Impact”, *14th World Conference on Seismic Isolation; Energy Dissipation and Active Vibration Control of Structures*.

- Skinner R.I., Kelly J.M. and Heine A.J.H., (1975), “Hysteretic dampers for earthquake resistant structures” *Earthquake Engineering and Structural Dynamics*, **3(3)**, 287–296.
- Skinner R.I., Robinson W.H. and McVerry G.H., (1993), “An Introduction to Seismic Isolation”, *John Wiley & Sons*, Chichester, England, 1993.
- Smith M.C., (2002), “Synthesis of mechanical networks: the inerter”, *IEEE Transactions on Automatic Control*, **47(10)**, 1648–1662.
- Smith M. C., (2008), “Force-controlling mechanical device,” U.S. Patent 7 316 303, Jan. 8.
- Smith M. C. and Wagg D.J., (2016), “A fluid inerter with variable inertance properties”, *EACS - 6th European Conference on Structural Control*.
- Stachowiak G.W. and Batchelor A.W., (2005), “Engineering Tribology”, *Elsevier Butterworth-Heinemann, Dordrecht, Netherlands*.
- Staudacher E., Habacher C. and Siegenthaler R., (1970), “Erdbebensicherung in Baum”, *Neue Zürcher Zeitung, Technik*.
- Su L., Ahmadi G. and Tadjbakhsh I., (1991), “Performance of sliding resilient friction base isolation system” *Journal of Structural Engineering*, **ASCE 117**, 165–181.
- Swift S. J., Smith M. C, Glover A. R., Papageorgiou C., Gartner B. and Houghton N. E., (2013), “Design and modelling of a fluid inerter”, *International Journal of Control*, **86(11)**, 2035–2051.
- Tabor D., (1981), “Friction-The Present State of Our Understanding”, *J.Lubrication, Techn.*, **ASME**, Vol. **103**, 169-178.
- Taniguchi T., Der Kiureghian A. and Melkumyan M., (2008), “Effect of tuned mass damper on displacement demand of base isolated structures”, *Engineering Structures*; **30**, 3478–3488.

- Tarics A.G., Way D. and Kelly J.M., (1984), “The implementation of Base Isolation for the Foothill Communities Law and Justice Center”. *Technical Report No. RTA-84, San Francisco, California.*
- Taylor A., Lin M. and Martin J., (1992), “Performance of elastomers in isolation bearings: a literature review”, *Earthquake Spectra*, **8(2)**, 279–303.
- Trovato D., (2013), “Degradation of dissipative Characteristics of Friction Pendulum Isolators due to Thermal Effect”, *PhD Thesis Politecnico di Torino.*
- Tsai C.S., Chen W.S., Chiang T.C. and Chen B.J., (2006), “Component and shaking table tests for full-scale multiple friction pendulum system”, *Earthquake Engineering & Structural Dynamics*; **35**,1653-1675.
- Tsai H.C., (1995), “The effect of tuned-mass dampers on the seismic response of base-isolated structures”, *International Journal of Solids and Structures*; **32**, 1195–1210.
- Tsuda M., Tamashiro K., Sasaki S., Yagai T., Hamajima T., Yamada T. and Yasui K., (2009), “Vibration Transmission Characteristics Against Vertical Vibration in Magnetic Levitation Type HTS Seismic/Vibration Isolation Device”, *IEEE Transactions on Applied Superconductivity*, VOL. **19(3)**, 2249- 2252.
- Ueda M., Ohmata K., Yamagishi R. and Yokoo J., (2008), “Vertical and Three-Dimensional Seismic Isolation Tables with Bilinear Spring Force Characteristics (For Which a A-Shaped Link Mechanism Is Used)”, *Transactions of the Japan Society of Mechanical Engineers Series C*, Vol. **73(2007)** n° 735, 2932-2939.
- UNI EN 1998-1:2004, Eurocode 8: Design of structures for Earthquake Resistance, Part1: General rules, seismic actions and rules for buildings.

- UNI EN 1337-1:2000, Structural bearings – General design Rules.
- UNI EN 1337-2:2004, Structural bearings- Part 2: Sliding Elements.
- UNI EN 1337-3:2005, Structural bearings- Part 3: Elastomeric bearings.
- UNI EN 15129:2009, Anti-Seismic Device.
- Wright F., (1977), “An Autobiography: Frank Lloyd Wright”, *Horizon Press, New York*.
- Wang F-C., Hong M-F. and Lin T-C., (2010), “Designing and testing a hydraulic inerter”, *Proceedings of the Institution of Mechanical Engineers, Part C: Journal of mechanical Engineering Science*, **225**: 66-72.
- Wang F-C. and Su W.-J., (2008), “Impact of inerter nonlinearities on vehicle suspension control,” *Vehicle System Dynamics*, **vol. 46**, no. 7, 575–595.
- Way D. and Howard J., (1990), “Seismic Rehabilitation of the Mackay School of Mines with Base Isolation”, *Earthquake Spectra*, **Vol. 6**, No. 2.
- Xiang P. and Nishitani A., (2014), “Optimum design for more effective tuned mass damper system and its application to baseisolated buildings”, *Structural Control and Health Monitoring*; **21**, 98–114.
- Xueyuan Y. and Jianping W., (2014), “Design and numerical simulation of the disk spring vertical isolation device”, *Applied Mechanics and Materials*, 501-504.
- Yang J.N., Danielians A. and Liu S.C., (1991), “Aseismic hybrid control systems for building structures”, *Journal of Engineering Mechanics*; **117**, 836–853.

Zayas V., Low S. and Mahin S., (1987), “The FP earthquake resisting system”. *Earthquake Engineering Research Center, University of California, Berkeley*, Report No. CB/EERC-87/01.

Zeng H., Zhao J. and Wang K., (2013), “Design and theoretical studies of pulsatile hydraulic vertical isolation device”, *Advanced Materials Research*, Vol. **619**.